Optical spectroscopy of HMX reaction regimes

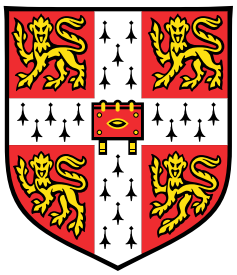

Olivia J. Morley

Department of Physics
University of Cambridge

This thesis is submitted for the degree of
Doctor of Philosophy

Emmanuel College

July 2021

Declaration

I hereby declare that except where specific reference is made to the work of others, the contents of this thesis are original and have not been submitted in whole or in part for consideration for any other degree or qualification in this, or any other university. This thesis is my own work and contains nothing which is the outcome of work done in collaboration with others, except as specified in the text. This thesis contains fewer than the 60,000 words stipulated by the Degree Committee for Physics and Chemistry.

Olivia J. Morley
July 2021

Optical spectroscopy of HMX reaction regimes

Olivia J. Morley

Abstract

A detailed study on the visible light emission from multiple granular HMX reactions has been completed. New techniques for measuring the reaction properties were devised, both directly and indirectly from the results gained from using optical spectroscopy.

Two different impact initiated deflagration reactions were performed. Improvements were made to the fallhammer sensitivity test to allow for more quantitative measurements, and the Split Hopkinson Pressure Bar (SHPB) was used for the first time to purposely initiate deflagration, providing better measurements of the energy present during initiation. Using the greybody emission, the temperatures of these reactions were measured as 3900 ± 400 K and 2900 ± 200 K respectively. Building a time-dependent pyrometer showed a constant temperature throughout the main reaction period. The significant difference between the two temperatures inspired the addition of a mass spectrometer to investigate the products from each reaction. The results showed the two reactions did not resemble variants of an 'ideal' deflagration reaction, and so identical chemistry should not be assumed to be present in both.

Optical spectroscopy also showed the existence of a spectral peak in deflagration due to emissive sodium impurities. The peak was red-shifted under the pressures of the reaction, and the calibration curve of the red-shift was calculated. The functional form of the shift has a dependence on pressure and temperature in agreement with Lindholm-Foley collisional theory, allowing the pressure to be calculated optically from position of the shift. This was achieved with a streak spectrometer, where time-dependent measurements of the temperature (using greybody emission) and pressure (using the sodium peak) from the same source of light were made.

Finally, detonation of HMX was examined. The detonation pressure and velocity were measured as a function of initial density, and found consistent with models of shock conservation and Group Interaction Modelling. High temperatures of 7000 K were recorded from the greybody emission, with the light emitted from mechanical high pressure void collapse dominating over the heat produced from the chemical reaction. These temperatures were not affected by the density of the HMX bed, but instead the size of the voids present. Larger particles increased the size of the voids, leading to higher temperatures and decreased light scattering, with the inclusion of sodium absorption features.

Acknowledgements

This research was conducted in the Fracture Group at the Cavendish Laboratory, and would not have been possible (or enjoyable!) without the help and support from many individuals. Avik Chakravarty completed his Ph.D. in the same group in 2004, and my thanks to his family who so generously have donated funds in his memory to allow others like myself to continue and expand upon his research.

I would also like to thank Emmanuel college, an absolutely amazing community who were there for me during both my undergraduate and graduate days, and who also kindly provided funding for my research. Also my thanks to QinetiQ for providing financial support as well as their knowledge into energetic reactions.

I am deeply thankful to David Williamson for his supervision; knowing exactly what to do, finding where the lab equipment has wandered off to, providing advice and generally helping me when I needed it. My thanks to all the others in the Fracture group for their willingness to help and share their knowledge (and the crossword tea breaks), especially Nick and Lewis for their support and advice, and Kieran and Mike for all the fun discussions we've had.

My thanks as well to those in the wider community; the MolE food vans crew, my housemates at 84, badmintime, and the MIRT gang – your moral support was much needed and appreciated!

Table of contents

Publication list

The following publications have been made from this thesis at time of writing:

1. O. J. Morley and D. M. Williamson. Pressure and temperature induced red-shift of the sodium D-line during HMX deflagration. *Commun Chem*, 3(13), 2020.

2. O. J. Morley and D. M. Williamson. Influence of reaction rate on optical emission of HMX. *NTREM Conference Proceedings*, 2019.

3. O. J. Morley and D. M. Williamson. Investigating the evolution of the optical emission spectra of HMX with reaction regime. *AIP Conference Proceedings*, 2272, 2020.

Chapter 1

Introduction and background

1.1 Introduction

Research into energetic materials has a long history at the Cavendish Laboratory. From 1948 over 60 theses have been written on these materials, over a range of different topics, from material properties to damage and initiation. One of the longstanding instruments developed for such research was the optical drop-weight, a modified version of a hazard safety test that initiates energetic materials by dropping a mass onto the sample. With the addition of glass anvils that bracketed the energetic material under test, the optical drop-weight therefore allows the visual evolution of initiation to be observed [1].

By 2016 a gated visible light spectrometer was added as a diagnostic to this apparatus [2]. Shown in figure 1.1, the emission spectrum of PETN and HMX initiated in the drop-weight contained a strong spectral peak just above 590 nm. A similar peak had been observed by N. Taylor when studying impact initiated ammonium nitrate [3]. In both cases, the peak was tentatively assigned to belong to nitrogen de-excitation by photoemission, and the reports at the time did not take the investigation further.

Motivated by such a result, the aim of the research presented here became to investigate the light emission of energetic reactions. This would not only allow the spectral peak in impact initiated deflagration to be identified - the earlier hypothesis of nitrogen emission has now been discarded - but also to explore the field of optical emission in these complex reactions. Overall, two main goals were present.

Firstly, to characterize and understand the optical emission measured in a range of reactions. This meant properly designing an experiment to capture the light, and to scientifically explain the results gathered. This would allow knowledge to be built of what to expect when conducting optical spectroscopy on future energetic reactions.

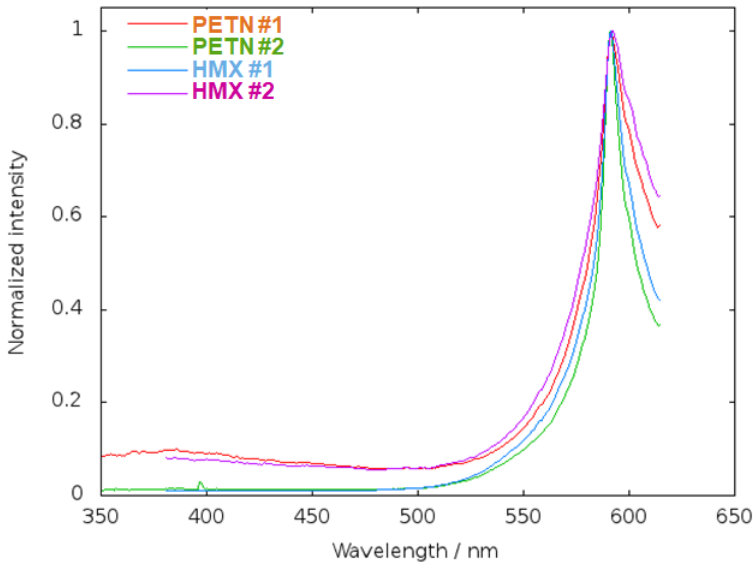

Fig. 1.1 The unknown spectral feature that was observed in the reaction light of PETN and HMX under initiation by impact, with the data provided by Dr. David Williamson.

Secondly, once the first goal was complete, to determine the uses of such spectroscopy. Once the features of the reactions are known, to what extent could they be used to measure properties of the reactions? This goal would not only determine whether optical spectroscopy was a useful technique for these regimes, but also provide new understanding on the reactions measured, increasing the insight into the underlying physics behind the observable and measurable behaviour.

The physical background for understanding optical emission from energetic reactions can be split into two components. The first concerns itself with the energetic reactions themselves, with discourse on areas such as what energetic materials are, what types of reactions exist and what properties each has. The second component is the discussion on optical emissions; what key features would one expect in a wavelength spectrum, and how these features depend on external stimuli. This chapter explores these relevant areas of physics, and the background required for the research to be understood.

1.2 Reactions of energetic materials

Energetic materials have violent exothermic reactions, with the material reacting to form many gaseous product species. For example, in the case of the organic explosive HMX, which is the main focus for this research, the idealised 'complete' reaction would be $HMX \rightarrow 4CO + 4H_2O + 4N_2$ [4]. However, in reality, there are a large number of alternative reactions,

with local conditions dictating which are preferred [5]. These local conditions and different chemical pathways, along with the rate the reaction propagates at and the type of initiation, lead to a large range of different regimes being present. This research distinguishes between three regimes:

1. Burning. The materials can be burnt in flames under room temperature and ambient pressure conditions. This is a simple combustion – oxidation – reaction, rather than the material decomposing. It can be compared to similar simple flame tests. The reaction occurs at atmosphere pressures of 0.1 MPa over millisecond timescales.

2. Deflagration. The material is initiated and reacts under moderately confined conditions, with the presence of self-induced pressurization, with pressures of order 1 GPa. This reaction progresses at subsonic velocities, limited by the speed of sound in that material, and propagates due to the heat transfer from the reaction. The characteristic timescales are faster, occuring over microseconds.

3. Detonation. In contrast, detonation is defined as a reaction which propagates at supersonic velocities with a shock front supported by the medium in front of the reaction. Rather than heat transfer, the reaction is initiated by this shock front, which is then reinforced by the reaction products. Detonation is the most extreme regime, with pressures of order 10 GPa and timescales of hundreds of nanoseconds.

Detonation, therefore, can be studied using shock physics, and has theory developed from this principle (section 1.2.3). In comparison, deflagration is a more loosely defined phenomena – a reaction that is 'not-detonation' as it does not involve shock waves. This leads to a wider range of conditions, and a less unified theory.

1.2.1 Energetic materials

The term energetic materials covers explosives, propellants and pyrotechnics, called energetics due to the fast and violent reactions that characterise these materials. Pyrotechnics is an umbrella term for a chemical energy driven effect which is not primarily rapid pressurisation. Pyrotechnic materials are designed for sensory results, such as the bright long-lasting colours observed in fireworks and flare-guns or smoke production for obscurants. In contrast, propellants are used for fuel, with a controlled energy release over a time-period, and therefore aiming for a slower burn reaction compared to a fast detonation. Whereas, explosives can be thought of as a one time compact energy source which is released very quickly, with detonation often being the aim when used.

Explosives can be split again into primary and secondary explosives. When a reaction occurs in a primary explosive it cannot be quenched; it will go to completion each time and will always detonate. In contrast, secondary explosives do not always result in detonation or complete deflagration as the reaction can be stopped before it completely consumes the material. Primaries are typically inorganic, such as metal azides, in comparison secondaries are more likely to be larger organic molecules. Primaries are also more sensitive and so are often used in small quantities to trigger a reaction in a larger secondary explosive charge, which allows the majority of the explosives used to be the safer-to-handle secondary. This research solely uses granular secondary explosives.

There are many applications of explosives in industry. The main commercial use is in mining, with roughly 22.3 billion kg of explosives used between the years 1990 and 1999 in the United States [6]. Other applications of explosives include military and defence purposes, and explosive engineering and welding.

Explosives were used in the research presented here due to the fact they produce very high pressures and temperatures that are difficult to re-create statically in a laboratory setting. They are metastable molecules with very exothermic reactions; upon application of an activation energy they quickly react to form more numerous stable molecules. This leads to liberation of heat (and therefore an increase in temperature), and the extra molecules under confinement produce a higher pressure. These reactions therefore allow dynamic measurements of the effects of high temperature and pressure, in particular the effect on the light emission. The aim of this research was to investigate the key characteristics of the light emission during the different reaction regimes, and then to determine if and how these characteristics could be used for advancing the knowledge of the field as well as for diagnostic tools.

1.2.2 Materials used in this research

This research primarily focuses on the granular secondary explosive 1,3,5,7-Tetranitro-1,3,5,7-tetrazoctane, more commonly referred to as HMX (figure 1.2). Focusing on only one material allowed for a better comparison of different reaction regimes, allowing the evolution of light emission to be more fairly studied. HMX was first made in 1930 by Robert Bachmann, and the synthesis improved in 1949 [7] allowing greater ease of production, and so is a relatively well-documented material. This has the benefit of allowing new research to be compared to previously measured quantities, having previous knowledge of properties (such as sensitivity) to allow more ease in conducting experiments, as well as being in use so that the research produced would be of interest.

Property	Value
Density	1.91 g cm^{-3}
Detonation velocity	9.11 km s^{-1} [8]
Detonation pressure	39.5 GPa [8]

Table 1.1 Properties of the stable β-polymorph of HMX at the density of a single crystal.

As a granular material, the size and distribution of the particles is also worth noting. In this thesis, three types/batches of HMX are mentioned, with the size distributions given in table 1.2.

Type	Size distribution
A	90 ± 15 μm
C	11 ± 8 μm
B	Mix of A and C, in 75:25 volume ratio

Table 1.2 The size of and composition of Type-A, B, and C HMX according to Fleming [9].

For the majority of experiments – unless stated otherwise – HMX Type-B was used. Type-B was preferable due to concerns that steady detonation could not be sustained in low-density HMX, and a higher packing density could be more readily achieved with a polydisperse particle size distribution.

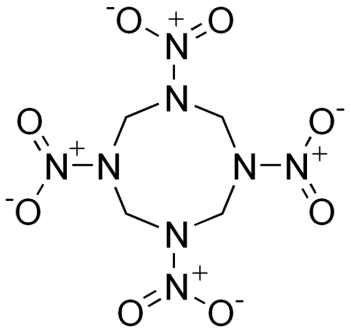

Fig. 1.2 Structure of an HMX molecule.

1.2.3 Detonation theory

Detonation propagates at shock velocities, and therefore, has its physical background in shock physics. A shock occurs when a disturbance in a medium moves faster than the speed of sound in that medium – a supersonic velocity. Before considering detonation specifically, an inert shock – one which is not supported by a chemical reaction – is considered.

For a closed system, shock propagation has to conserve mass, momentum and energy as it moves from the shocked region to the region directly in front of it (figure 1.3).

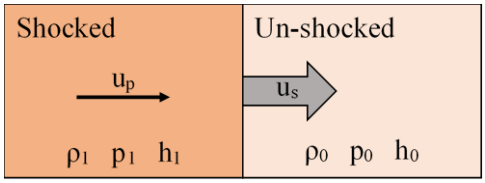

Fig. 1.3 A Shock wave travelling with velocity u_s through a medium with density ρ, particle velocity u_p, pressure p, and specific enthalpy h.

These necessary conservations lead to relationships between the system properties, the well-known Rankine-Hugoniot equations:

$$Mass\ conservation: \quad \rho_0 u_s = \rho_1 (u_s - u_p) \tag{1.1}$$

$$Momentum\ conservation: \quad \rho_0 {u_s}^2 + p_0 = \rho_1 (u_s - u_p)^2 + p_1 \tag{1.2}$$

$$Energy\ conservation: \quad h_0 + \frac{{u_s}^2}{2} = h_1 + \frac{(u_s - u_p)^2}{2} \tag{1.3}$$

Eliminating particle velocity (u_p) produces the Hugoniot equation which represents all the possible equilibrium shock states a material can be found in:

$$h_0 - h_1 = \frac{1}{2}\left(\frac{1}{\rho_0} + \frac{1}{\rho_1}\right)(p_0 - p_1) \tag{1.4}$$

This equation is material-specific, and the curves it produces are known as shock Hugoniots, commonly plotted in the pressure-volume space. The shock Hugoniots are the locii of end-point conditions possible for a single shock, which are different to the non-shock Hugoniots of a material. When the material is subject to a shock, the range of possible states changes between the non-shock and shock Hugoniots. For this reason the Rankine-Hugoniot equations are sometimes called 'jump equations'.

To find the material properties from a specific shock – the exact point on the Hugoniot - the shock properties also have to be incorporated. These shock properties are derived from the conservation of mass and momentum (eq.s 1.1 and 1.2), and constitute the Rayleigh line;

$$p_1 - p_0 = \rho_0 u_s u_p \tag{1.5}$$

Therefore, the shock state of the system is found where this Rayleigh line intersects the shock Hugoniot, shown in figure 1.4.

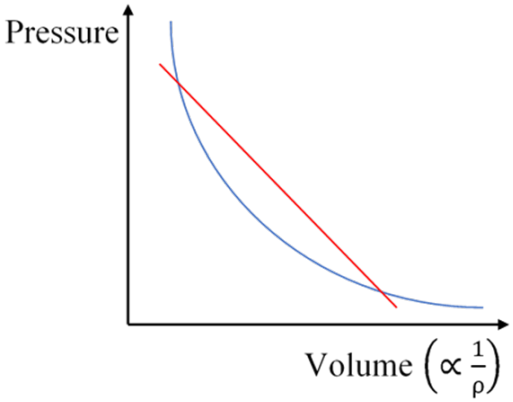

Fig. 1.4 Rayleigh line (red) intersecting Hugoniot (blue) curve plotted in pressure-volume space, resulting in two possible shock states.

This construction, built from first principles, is true for shocks in all materials and describes an inert and closed system - one with no chemical energy or heat sinks/sources. In this system, the shock will dissipate due to material releases through rarefaction waves – lowering the pressure down to ambient and destroying the shock front. To extend the theory to detonation, one must also consider the presence of the chemical reaction of the energetic material. This can be thought of as adding an extra source term, and considering two different material Hugoniots; the Hugoniot for both the unreacted material at the start and the reacted products at the end of the reaction.

C-J theory

The first detonation theory to consider is due to Chapman and Jouguet (C-J), a theory developed independently and almost simultaneously by Chapman [10] and Jouguet [11] in *circa* 1900. The C-J description considers steady state propagation of the detonation front. To be in steady state means rarefaction waves, travelling at sound speed behind the front, do not weaken the detonation front. This implies that the velocity of the explosion products – at detonation velocity - must be greater than their sound velocity.

C-J detonation is a purely mechanically based theory, with the duration of the chemical reaction not taken into account; it assumes an instantaneous reaction, and therefore an infinitely thin reaction zone at the detonation front.

As seen in figure 1.5, there is an associated pressure rise with the detonation front, called the C-J pressure. High pressures are associated with energetic reactions, reaching values of tens of gigapascals in detonation: HMX has a C-J pressure of 39.5 GPa at maximum density of a single crystal [8]. When considering that ambient pressure is 0.1 MPa, gigapascal

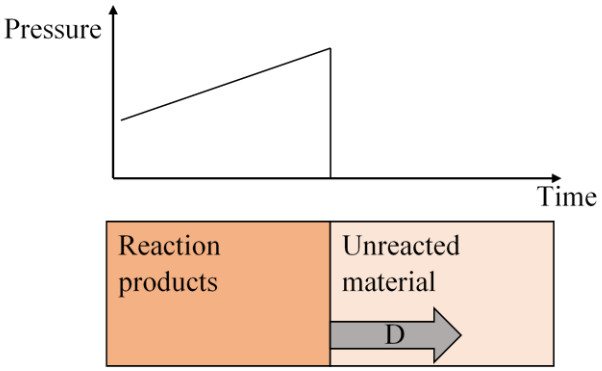

Fig. 1.5 C-J view of a detonation front passing from a shocked material into the unshocked region, and its associated pressure profile, with the assumption of an infinitely short time of reaction. The shock speed, u_s is also the detonation velocity, D.

pressures represent a very extreme condition which is difficult to induce statically in an experimental environment as it exceeds the strength of most materials that could be used for such confinement; but dynamically in detonation can be achieved with relative ease.

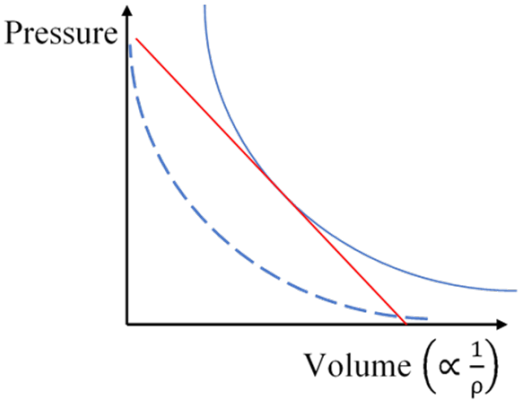

Fig. 1.6 Unreacted Hugoniot (dashed) and reacted Hugoniot (solid). The Rayleigh line lies at a tangent to the reacted Hugoniot in C-J detonation, with a single detonation state, and therefore a single detonation velocity.

Detonation describes a reaction, with the system originally in an unreacted state (on an unreacted Hugoniot shown as a dashed line in figure 1.6), which then reacts to a range of possible states described by the reacted Hugoniot. The exact state of the specific detonation is then found at the intersect of the Rayleigh line with the reacted material Hugoniot. Assuming a stable detonation with only a single detonation velocity forces the Rayleigh line to lie tangent to the reacted Hugoniot so only one possible state is produced (figure 1.6). Strong-

and weak-detonation states, where the Rayleigh line is not tangent, are possible from the construction but are not described by C-J theory.

ZND theory

A more accurate description of detonation includes a finite reaction time (and therefore a reaction length scale, or reaction 'zone'), and is known as Zeldovich-Von Neumann-Döring (ZND) detonation. Similar to the C-J theory, this was developed independently and simultaneously by Zel'dovich [12], von Neumann [13] and Döring [14] during World War II. ZND detonation takes into account the material being shocked, and then the reaction occuring over a finite time or length scale (figure 1.7). This consideration adds an initial increase of pressure to the system at the front of the detonation – a pressure spike (von Neumann spike) which thereafter then falls to the C-J pressure of the reaction zone as before.

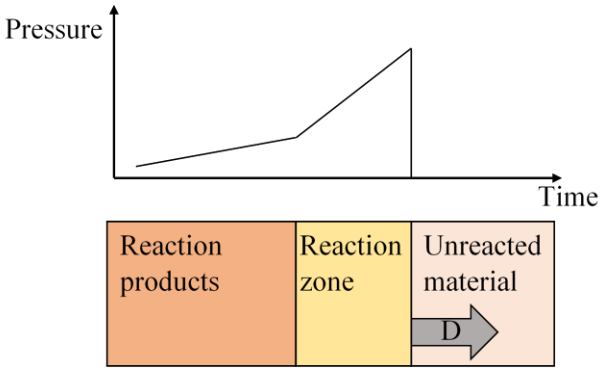

Fig. 1.7 ZND detonation front and pressure profile. With the addition of the von Neumann spike, present due to the pressure associated with the finite reaction time. The pressures and times presented are for ease of understanding and are not to scale.

This spike occurs on extremely short timescales, so that the maximum pressure it reaches is difficult to be resolved using current experimentation [15]. One of the first measurements of an early pressure spike was conducted by Duff and Houston in 1955, where they used shorting pins to measure the particle velocity of an aluminium plate at the base of a detonating column [16]. Five years later, electromagnetic gauges were used *in-situ* to measure the particle velocity [17], and this technique led to time resolutions of 50 ns for the pressure measurements [18]. The problem with embedded gauges was that simply their presence in the system would affect detonation. Switching to light interferometry methods to measure the particle velocity allowed non-intrusive measurements to be made, as well as a higher time resolution of sub-nanoseconds [19]. This technique of using light interferometry such as VISAR and PDV is now a common method of obtaining pressure wave-profiles in detonation,

allowing for better bounds on the amplitude of the von Neumann spike, however still not fully resolving the rise-time [20, 21].

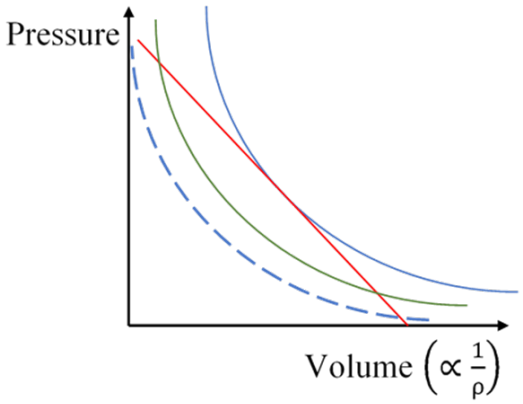

Fig. 1.8 A shocked material Hugoniot (green) and reacted (detonation wave) Hugoniot (solid blue), with the unreacted Hugoniot (dashed blue) in ZND detonation and intersecting CJ Rayleigh line (red). The Rayleigh line is formed from detonation properties, so has to lie tangent to the reacted Hugoniot like before. The position where the Rayleigh line crosses the shocked material Hugoniot corresponds to the Von-Neumann pressure spike, which is due to the additional pressures of the chemical reaction.

Shown in figure 1.8, ZND detonation considers the shocked material separate from the pre-shocked state, so another Hugoniot has to be considered, and plotted – a new curve for the shocked material about to react and one for the reacted state lying on the detonation wave, the same as before. Instead of the unreacted un-shocked material (dashed blue Hugoniot) immediately occupying a state on the reacted Hugoniot, it first occupies a point on the shocked material Hugoniot (green), occupying a higher pressure state. Then, via the Rayleigh line, the material occupies a lower pressure state on the reacted Hugoniot (solid blue), at the same pressure described by C-J theory.

For a more complete description, see Anatoly N. Dremin's book: Toward detonation theory [22].

1.2.4 Initiation of detonation and deflagration

Detonation of the material can be reached by two main mechanisms. The first is a deflagration to detonation transition (DDT), which – as its name suggests – is when a deflagration reaction under certain conditions accelerates to a supersonic speed and becomes proper detonation. When combustion starts, the hot product gases flow through the material, heating and igniting it. With an increase in burning, the resultant gases lead to an increase of pressure

in the reaction area, and this increased pressure in turns causes the rate of the reaction (combustion) to increase. The increasing pressure also causes the voids in the material to collapse, preventing gas flow and further increasing the pressure building up until detonation occurs [23]. In HMX, the run-length (amount of material) required for DDT to occur varies between 20 and 100 mm, dependent on the experiment and the porosity of the sample [24].

The second method to achieve detonation is a shock to detonation transition (SDT), where detonation starts instantaneously from an incident shock (an incident high pressure), and there is no intermediate measureable deflagration regime. With the insult to the material already occuring at detonation conditions, no run-length of material is required for detonation to be achieved. This research focused on SDT in order to keep the regimes of deflagration and detonation separate, as well as utilising less material to achieve detonation.

One interpretation of these reactions is that steady state detonation, with its single detonation velocity and one-dimensional system, is a dynamic equilibrium condition. For example, given enough material to maintain the detonation, a view taken at any time on the detonation front down the material will be indistinguishable from any other. Give the material an inert shock, such as a flyer plate, and if this produces a high enough pressure to be akin to detonation, the material will not tell the difference. Therefore, an immediate SDT occurs at the time of the shock. If the shock is larger than the one associated with detonation, this will lead to an over-driven detonation, with a higher detonation velocity. However it will decay and slow down to the steady state of detonation [22].

However, shocking below the detonation pressure will lead to a reactive response - deflagration. In time, this too will build up to form the steady state of detonation with DDT. DDT also leads to a change in the dimensionality of the system. Deflagration spreads outwards due to heat transfer, and thus is multi-dimensional. However, when transitioning to detonation, this front can then be modelled as one-dimensional axisymmetrical.

Regardless, for a reaction to begin in either deflagration or detonation, a minimum activation energy is required in the system in order to break the bonds present in the reacting species. This minimum activation energy is material dependent - a wide range of different sensitivities are present across energetic materials, even with explosives that have similar covalent bonds present in their molecular structure [25]. Coffey, Zerilli and Toton [26, 27] proposed a vibrational energy transfer mechanism (later called phonon up-pumping [28]) for energy localisation within the crystal that leads to a large increase of internal phonon modes in the explosive molecule due to phonon-phonon collisions.

The energy of these phonon modes causes dissociation of the covalent bond in the molecule, and therefore starts the reaction. Michalchuck *et al* demonstrated the link between the proposed phonon mechanism and explosive sensitivity by calculating the rate of phonon

up-pumping from the crystallographic structure and vibration mode spectrum of different explosives, and found a correlation with this up-pumping rate and the order of impact sensitivities of the explosives [29]. Therefore, knowing the crystal structure of a material allows the calculation of the up-pumping rate, and from that an estimate of the 'intrinsic sensitivity' of a perfect crystal of that material. However, this method can only provide a relative position of sensitivity compared to other explosives, and cannot account for the microstructure effects, such as defects and voids present in the crystal.

1.2.5 Hotspots

Given the ease at which reaction can occur in energetic materials, Bowden and Yoffe [30] hypothesised that the mechanical energy provided for initiation was localised into small volumes. They proposed a thermal ignition origin, where the initial mechanical energy is concentrated into a small volume which rises to a very high temperature – which they called a "hotspot" [30]. This formation allows the bulk of the material to subsequently react, as the heat produced by the combustion reaction in the hotspot is larger than the amount lost to create it, causing the reaction to spread out from the initiation point in a chain reaction. In a homogeneous material, this localisation is from the insult - such as a spark. In a heterogeneous material, such as granular HMX, the localisation and hotspot forms due to the microstructure, such as voids/cavities present.

Later experiments reinforced this hypothesis [31, 32], and in their 1974 paper, Heavens and Field [33] recorded images where these hotspots can clearly be seen as initiating the propagation of deflagration after the material was impacted. Figure 1.9 shows images from a more recent experiment of PETN deflagration at the Cavendish Laboratory [1] initiated in an optical drop-weight apparatus, where the heterogeneous initiation from clearly two separate areas (presumably each starting from small hotspots) can be seen.

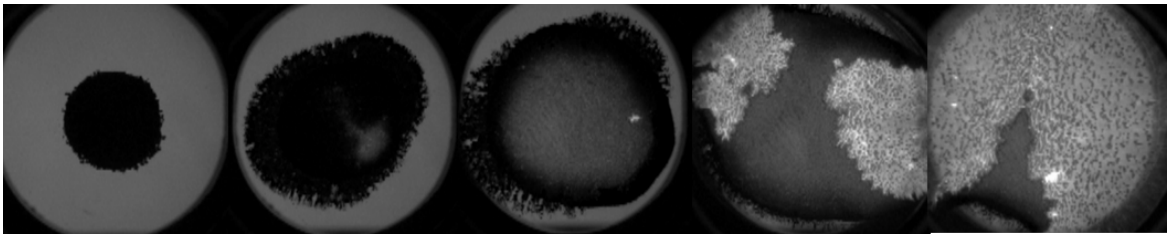

Fig. 1.9 Images from an optical drop-weight system of initiation of PETN deflagration showing the progression from a single spot to form to complete deflagration [1]. The field of view was 20 mm, with an interframe time of 7.69 μs.

There have been many proposed methods for how voids can form hotspots with the required temperatures for thermal ignition, given the mechanical input. These mechanisms are outlined below, and may be present with varying levels of importance in different experiments, as their contributions to hotspot ignition depend on a variety of factors [34]. (See section 1.2.7 for further discussion over their contribution to detonation temperature).

Adiabatic air compression

The collapsing cavities contain air – or gaseous reaction products – that rapidly decrease in volume when the pressure wave hits the cavity. Using simple thermodynamics and treating this as an adiabatic transition, this reduction in volume and increase in pressure leads to a temperature increase which could initiate reaction in the collapsed cavity.

$$\frac{V_1}{V_2} = \left(\frac{T_1}{T_2}\right)^{\frac{1}{\gamma-1}} \quad or \quad \frac{P_1}{P_2} = \left(\frac{T_1}{T_2}\right)^{\frac{\gamma}{\gamma-1}} \tag{1.6}$$

Where γ is the gamma constant ($\gamma = \frac{c_p}{c_v}$) of the collapsing gas. This constant is dependent on temperature and pressure, and over the range of conditions found in detonation, γ for air will vary from 1.2 to 1.6 [35] as shown in figure 1.10.

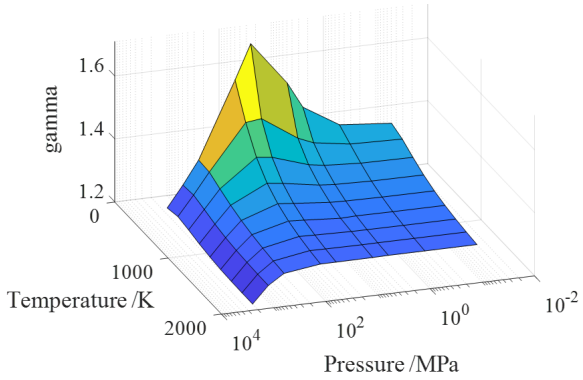

Fig. 1.10 Gamma factor of air varying with temperature and pressure with values taken from Perry's Handbook [35].

Therefore, the resulting temperature increase is more complex than one simple calculation, however an estimate can be easily made. Taking gamma as a constant value of 1.3, and the pressure of detonation to be 30 GPa into equation 1.6, results in a temperature rise from 298 K to 5500 K in the void. However, in addition to just temperature, the heat (energy) also needs to be taken into consideration, something which is not present in equation 1.6. Bowden and Yoffe estimated that the hotspots would typically have a size between 0.1 and 10 μm, and to occur on timescales of 10^{-5} to 10^{-3} seconds [30] in order to generate enough heat to support the reaction.

In experiments, the gas compression has been shown to reach temperatures needed for initiation by heat, with compressive heating of RDX by an adjacent gas showing temperatures greater than 1000 K produced, significantly above those required for initiation [36].

Jetting

As well as the purely thermodynamical calculation assuming ideal adiabatic collapse, the actual collapse of the cavity and its behaviour can be studied. Cavities do not necessarily collapse symmetrically, and a high velocity jet of material from the collapse forms. Under high enough pressures, the jet can accelerate across the cavity faster than the shock velocity, driving the rear face of the cavity into the front face and creating two volumes of high temperature and intense light emission, which can even be seen in gelatine with millimeter diameter pores and pressures of up to 3.5 GPa [37].

In detonation, the long-lived heat and higher temperatures inside the formed jet could lead to initiation. When modelling this mechanism with a pressure dependent reaction [38], both the size and shape of the cavity affected the detonation initiation, and temperatures well above the melting point of HMX (roughly 550 K [39]) could be reached. Whilst similar to the study of adiabatic air compression, in that a cavity needs to be present and subject to a high pressure shock, this description of jetting is focused on the observed behaviour of a collapse, rather than a calculation of idealised parameters. Despite this, a simple estimate of the temperature rise can be considered.

Taking the account of shock in gelatine by Bourne [37], first assume that upon impact the kinetic energy of the gelatine solely leads to a temperature rise:

$$C_v \Delta T = \frac{1}{2} u_p^2 \tag{1.7}$$

Where C_v is the specific heat capacity of gelatine at a constant volume (which is assumed similar to water, with a value of 4.16 kJ kg^{-1} K^{-1}), and u_p like before, is the particle velocity. From Bourne's experiment, investigating shock pressures of 3.5 GPa on a void 6 mm in diameter, a particle velocity of 1030 m s^{-1} was measured [37]. Using equation 1.7, this results in a temperature rise of 130 K. However, in detonation one would expect an order of magnitude larger pressure, and a hotspot of order microns, as stated above. With a higher pressure, and smaller cavity, one would expect a much larger particle velocity [37], and therefore a larger temperature rise. Taking a particle velocity of order 2600 m s^{-1} (as measured in Chapter 6), would lead to a temperature rise of 810 K, increasing the temperature of the material significantly above the melting point of HMX.

Visco-plastic work

Related to the above mechanisms, the cavity collapse can also be examined from the view of the visco-plastic work done. For the jetting described above, the initiation pressure has to be high enough so that the velocity of the jet is faster than the shock speed. At lower pressures where this is not the case, jetting does not occur, and instead plastic dissipation from the void collapse is proposed as a mechanism to cause initiation.

Spherical collapse produces large plastic strains near the surface of the cavity, which increase in temperature as the collapse occurs [40]. Once the melting point of HMX is reached, the plastic stresses disappear, as the material is no longer solid, but viscous stresses appear. These viscous forces then convert the stress energy into heat. This mechanism retains more energy because heat conduction into the surroundings is a slower process than rarefaction waves which reduce the potential energy held in tension [41].

The temperatures reached cannot be simply calculated in a single line equation, but rather are the culmination of multiple assumptions and modelling parameters. One such model predicts that this visco-plastic work leads to hotspot temperatures of up to 3000 K, depending on pore size and shape [42]. The reaction can then propagate to the bulk by surface burning, as would be expected.

Shear bands

Shear bands are a specific example of viscoplastic work, though with a focus on deformation of solid materials, rather than cavity collapse. Shear bands form when a material deforms and the thermal softening present is greater than the work hardening, with the consequence of concentrating deformation into planes. The temperature of these bands rises, dependent on the level of visco-plastic heating and the amount of heat lost by conduction. Once a material has melted, it can no longer support shear stresses and, similar to the description of visco-plastic work, any heating is viscous.

An increase in pressure increases the temperatures that can be formed in these bands, with greater than 500 °C achieved for 0.35 GPa pressures and 0.25 km s^{-1} shear velocity [43]. Therefore, given higher pressures, it is possible for shear bands, rather than plastic work surrounding cavity collapse, to achieve a high enough temperature for melt to occur.

Other

Heating due to friction between the energetic material and an additional surface can also be considered, with the maximum temperature reached dependent on the lowest melting point of the two surfaces involved. Adding foreign particles (grit) into the system with known

melting points above 500 K sensitises the explosive, adding in areas for frictional heating and transient hotspot formation [44, 45]. However, after the melt-point is reached, viscous heating occurs like above.

Other methods of deflagration and detonation initiation – such as fracture, laser or spark – are also present. The research presented below contains deflagration initiated by impact, and detonation initiated by shock. Therefore, it is not expected that these initiation mechanisms would be present in such measurements, and so there is no further discussion here.

1.2.6 Chemical reaction

For energetic materials, the reaction temperature expected from decomposition is in the 2000 – 5000 K range [4]. This can be calculated by considering the enthalpy of the reaction and the heat capacities of the molecular constituents:

$$T_{exp} = \frac{Q}{\sum C_v} + T_i \tag{1.8}$$

Where C_v are the temperature dependent heat capacities of the molecules involved, and Q is the heat produced, often called 'heat of explosion', and can be calculated from the enthalpy of formation of the different molecules. Take, for example, HMX decomposition:

$$HMX \rightarrow 4CO + 4H_2O + 4N_2 \tag{1.9}$$

Before calculating the overall temperature expected from this reactions, the heat capacities have a dependence on temperature that has to be taken into account, given the reaction is taking place at a significantly higher temperature than room temperature. So for these calculations a value of the heat capacity at 4000 K for the molecules was used, as it is the order of magnitude expected for a HMX reaction.

Given an associated heat of 1483 kJmol^{-1} for such a reaction, this leads to a calculated temperature of 4130 $\pm$ 70 K using the thermochemical properties found in J. Akhavan's book: The chemistry of explosives [4]. Other secondary explosives, such as RDX and PETN produce similar expected temperatures of 4150 $\pm$ 70 K and 4560 $\pm$ 80 K respectively.

Previous experiments that measure deflagration temperatures of these materials have recorded similar temperatures to those presented here, demonstrating that even a simple thermodynamical argument with an idealized reaction allows a reliable estimate of the temperature [46–48].

These high temperatures are believable, when considering that the overall reaction goes from a large unstable molecule of HMX to multiple common gas particles. This creation of gaseous products also suggests an instantaneous high pressure – with one molecule being

replaced with twelve. As mentioned previously, when in detonation these pressure can reach up to tens of gigapascals, however even in deflagration – where there is no shock present – pressures of order 1 GPa [33] are found due to the reaction alone, and moderate confinement of the products.

1.2.7 Shock temperatures

Shock phenomena are not limited to energetic materials, and the light emission from non-energetic granular materials is also an area of study. In particular, sonoluminescence is the process of light emission when a gas bubble suspended in a liquid collapses under an induced shock. The inert high pressure void collapse leads to an increase of thermal energy, similar to hotspot formation, and therefore a visible emission.

From this light, brightness temperatures (section 1.3.2) have been recorded of up to 17,000 K [49]. Unlike in energetic materials, the high temperatures produced do not initiate any violent reaction and there is no underlying chemical reaction – only the mechanical response of cavity collapse.

Such a high temperature seems improbable in an inert material, however this is the temperature recorded from a small hotspot, and is not the bulk temperature of the system. To achieve temperatures of 17,000 K from room temperatures using the adiabatic gas collapse equation (eq. 1.6) would require the radius of the void to decrease to a value 800 times smaller. It is this small volume that reaches such a temperature, with the light from this hotspot dominating the light emission.

When studying shock in granular energetic materials, it is important to consider the effects seen in these non-inert materials. Sonoluminescence demonstrates that a chemical reaction is not needed to record high temperatures and bright light outputs - that the material properties present in energetic compounds also have to be taken into consideration when examining the optical features. From this, it is expected that temperatures in detonation will be more complicated than just considering the chemistry alone.

Detonation temperatures

Unlike deflagration pyrometry measurements, detonation experiments are associated with much higher temperatures of around 8000 K [50–52]. This was a known and documented phenomenon by the 1970s [52], however research was limited by the technology available to study this to greater precision.

8000 K temperatures are significantly higher than that expected to be achieved in the chemical reaction taking place. However, it does not necessarily suggest a larger amount

of heat energy, only that the energy is potentially more confined. According to the Stefan-Boltzmann law (eq. 1.14), the intensity of light is proportional to the fourth power of temperature, therefore a small volume of high temperature light can dominate the spectrum. With both 8000 K and 4000 K emitters, only 6 % need to be at 8000 K for the light intensity of both temperatures to be equal. Nevertheless, another mechanism other than chemical must be responsible for temperatures above 4000 K – one that exists for detonation but not the lower pressure deflagration.

In the inert sonoluminescence mentioned above, temperatures between 6000 and 17,000 K (assuming a blackbody emission) were reached due to cavity collapse [49]. Therefore, energetic materials with cavities present will also be subject to similar material constraints as the voids in sonoluminescence experiments. Cavity collapse under high pressures is one of the main causes of hotspots (section 1.2.5). Therefore, the cavity collapse hotspot mechanisms will continue to provide still higher temperatures after the initial reaction begins, provided a large enough pressure – such as in detonation – is present.

The presence of these cavities has also been experimentally linked to the higher detonation temperatures, with research from as early as 1951 that showed intense light emission from granular materials at detonation pressures, yet negligible brightness from the detonation of plastic explosives with no 'air pockets' [53]. More recently, measurements of 4000 to 7500 K were recorded in the same material dependent on the concentration of air pores in a sample [54], and a decrease in temperature from 6000 to 4000 K when the pores were pre-compressed [55]. It can therefore be theorised that the detonation front has two radiation sources, a cooler 4000 K from chemical reaction and the dominating 7000 K from high pressure cavity collapse. In 2020, the time-dependent temperature measurements of a single HMX crystal following initiation by laser-flyer showed the initial temperature of 8000 K, which cooled to 4000 K after the high pressure shock wave had passed [56]. After 50 ns the shock front had collapsed the pores in the sample, creating small volumes of 8000 K temperatures, and the remaining source of light (and temperature) would therefore be from the 4000 K deflagration reaction that occurs, spreading out from the hotspots.

There remains some discussion over the dominant mechanism responsible for the higher temperatures measured during the cavity collapse in the high pressure detonation reaction – which of the hotspot mechanisms is most important in generating temperatures above those associated with the chemical reaction [57]?

Firstly, it is important to note that this is a different question to which of the mechanisms is most dominant in initiating hotspots. Initiation focuses on the method which can increase the temperature fastest in order to start a reaction, rather than the largest temperature reached under detonation pressures. Modelling just the initiation shows temperatures greater than

5000 K (larger than expected chemical reaction temperatures) being reached, with the dominating mechanism transitioning with pressure loading strength from plastic deformation to hydrodynamic jetting [34].

Theoretical calculations do not always account for every variable in the system, and many experimental studies on this topic have been attempted. For example, adiabatic gas compression can be experimentally tested by measuring the temperature reached when the gas compressed is composed of different molecules, as each has a specific γ ratio, and therefore a different temperature (eq. 1.6).

Chaudhri and Field investigated deflagration and showed a dependence on the type of gas found in the air pores, indicating the presence of adiabatic heating [58]. However, when researching detonation, various early studies showed that the brightness of a shock in air was dependent on the gas, but the detonation light was not [59, 60]. Filling the interstitial sites with different gases did not affect the brightness, and therefore the temperature. Indeed, other experiments performed in a vacuum also showed a bright light [61, 48]. This brightness (and high corresponding temperature) did not appear when the porosity was pressed out [54], indicating that whilst free spaces are significant in hot spot formation and high temperature detonation, the type of gas within was not.

Later considerations of those experiments also took into account that gases from the decomposing energetic material when it is shocked will fill the interstitial sites – as the chemical decomposition can produce gases in picosecond timescales [55]. More recent experiments which fill the sites with different gases contradict the earlier experiments, and do show a temperature variation [55] within the first few nanoseconds of recorded light output, suggesting adiabatic air compression does still make a measurable contribution to the temperature.

In conclusion, the experimental results are varied, but recent experiments suggest that adiabatic gas compression has some role to play in the measured detonation temperature. Whilst it is theorised to not be the dominant mechanism [34, 57], it cannot be ignored, indicating that the system cannot be accurately modelled using only one hotspot mechanism.

What can be agreed from these experiments is that the presence of gas pores/interstitial sites in the material, and their subsequent collapse under higher pressures of detonation, leads to a higher temperature than that found in deflagration where the temperature is determined from the decomposition reaction. There are many different mechanisms associated with collapse that can achieve this high temperature, and the one dominating is not clear.

1.2.8 Summary of differences between deflagration and detonation

Hotspots are crucial for the initiation of the reaction, often involving the collapse of voids present in the material, these provide heterogeneous high temperature regions where the reaction starts, and then spreads out to the bulk. Given both deflagration and detonation incorporate the same overall reaction, the total heat energy from the chemistry should be the same in both reaction regimes.

Both deflagration and detonation can be achieved with HMX and have violent and exothermic properties. Stable detonation is defined as when the reaction front propagates at a single supersonic velocity – an identifiable detonation velocity that is dependent on both the material used and the environment. This can be achieved either by direct shock (SDT) or a transition from deflagration (DDT).

The higher pressures present in detonation lead to hotter temperature measurements, due to mechanical effects such as the void collapse mechanism, which produces an increase in temperature under these more extreme pressures. These hotspots have small volumes, and even though they can reach very high temperatures, it does not mean the heat present has significantly increased. Only that the high temperature light from these small volumes dominates over any other luminence or radiance.

1.2.9 Progress in experimental research in energetic materials

In all of the above, observations proceeded theory. Experiments had to be conducted in order to first observe any new discoveries, and also to validate the hypotheses detailed by the theory. This often puts a bottle-neck on developing the knowledge of detonation and deflagration, as the experiments are limited by the available technology of the time. As the equipment improves, and new diagnostics are developed, more and more experiments are possible, allowing better understanding of the system. Below are two examples of the change of experimentation with time.

Detonation measurements

One of the earliest main diagnostic tools was the camera. From 1900, photographic plates and film have been used to image detonation waves [62]. In 1951 a rotating mirror camera was used to track the high intensity detonation front over time, recording the detonation velocity as well as investigating how the material being tested affected the intensity of the light emission [53]. Experiments were conducted into how the intensity of the light emission changed when the charge was underwater [63, 50], in a different gaseous atmosphere [59, 61], and with changing particle size [60].

With advances in the development of streak-cameras, the velocity as a function of time could be better measured. In 1961, Campbell was investigating SDT and DDT by comparing the run-to-detonation times and the changing front velocity [31]. The effects of shock pressure, double-shock and initial charge density on both the sensitivity and detonation velocity were investigated with both a streak-camera and a framing camera that managed 500 ns resolution. With datasets on run-to-detonation time and detonation velocity, proper comparisons could be made between materials, and theories on what material factors affect these detonation properties could be validated. Even 60 years later, streak cameras are still in use to compare DDT in different materials [24].

For the detonation research in this research (Chapter 6), a framing camera with a 400 ns interframe time was used to take images of the front, and could be used for a reasonable measurement of the velocity. However, in the case of stable detonation, better velocity estimates and increased time-resolution could be achieved with the use of optical fibres (or ionization pins) pressed close to the cylindrical charge, connected to fast detectors. With multiple fibres a known distance apart and faster time-resolution, the detonation velocity can be measured more easily and cheaply than with a camera, and so this method of a set number of fibres/pins is currently a common method of measuring stable detonation velocity [64–66]. A camera was still used in this research as, despite being an old technique, it provides reliable images of the detonation front, giving the first indication of any problem or change in the front propagation. Camera images also give an observation on the curvature of the detonation front, and any other non-one-dimensional effects, which diagnostics that focus on a point would not be able to measure.

However, detonation velocity was not the only property under investigation; the pressure was also an important value, and could be calculated from particle velocity, u_p, and the material Hugoniot. Early attempts to measure pressure studied the rupturing of metal foils (in 1932) [67] and crusher gauges (in 1941) [68], however were unreliable. The shock velocity, u_s, was easily measured by cameras from the position of the bright light of the detonation front with time, and there were attempts in 1956 to also measure the pressure from streak-photography using the rarefaction wave speed [51]. This did, however, assume a perfect C-J detonation.

As mentioned in section 1.2.3, the presence of the von Neumann spike was first observed in 1955 using shorting pins to measure the particle velocity [16]. Measurements of particle velocity - and therefore pressure - were improved by the addition of gauges embedded in the charge [17, 18], and then non-intrusive interferometry of a reflective surface at the base of the charge [19]. Interferometry apparatus was improved, with the invention of VISAR in 1972 [69], and then the simpler PDV in 2005 [70]. With these interferometry systems the

speed of pressure measurements is now limited by the bandwidth of the oscilloscope used to record the waveform. The PDV technique was used to measure the particle velocity, and from that the pressure, in the detonation research presented in Chapter 6.

Therefore, despite C-J theory being developed in *circa* 1900 based on the Rankine-Hugoniot equations, the basics of the theory could not be validated until detonation velocity and pressure as a function of time could be measured years later. Likewise, with ZND detonation developed in *circa* 1940, the von Neumann spike could only be observed 15 years later, and even to this day (80 years after the initial theory) measurements of the rise-time and amplitude of the spike are limited by technology and engineering considerations.

Cavendish fallhammer

Another particular example that highlights the advances made in experimentation, and the effect those had on the theory, is the impact initiation of energetic materials at the Cavendish Laboratory. One of the common themes of the research undertaken here is the adaptation of hazard and sensitivity tests already in use, changing them to more scientific diagnostic tools. Such an adaptation allows both a safe initiation of the energetic materials under study, and also immediate applications of new discoveries as the hazard tests should be well-known in industry.

In 1949, Bowden and Gurton used the impact of a falling ball to initiate PETN [71]. They discovered that distributing the explosive in an annular shape led to the compression of air inside the annulus, which then functioned as one of the newly theorised 'hotspots' mechanisms. Images to confirm the presence of the hotspots were captured by the use of transparent anvils and mirrors inside the apparatus, which had been placed inside a rotating drum of film to detect the light emission. Therefore, the first existence of hotspots in solid explosives could be confirmed. Using the same research, they established common causes of local high temperature - such as a hot wire, a spark, a grit particle (friction) or a compressed gas pocket [71].

The same ball-drop initiation was used in 1952 by Blackwood and Bowden, with the added improvement of high-speed photography in order to study the ignition of gunpowder [72]. A frame rate of 2000 frames per second was achieved, however like earlier, whilst it could capture the initiation due to the large annulus created, it could not provide a fast enough resolution for natural hotspot formation within the gunpowder grains to be observed.

By 1974, the drop-weight had been improved again, with a framing camera capable of 5 μs resolution [33]. The initiation apparatus was also changed to the now more-traditional fallhammer setup with a cuboid weight, however it was dropped onto two transparent anvils that contained the sample between them, which is not usually included for simple hazard

assessment. In turn, this design became one glass anvil in the falling weight and one in the base. The resulting images of PETN deflagration, taken using a back-lit periscope arrangement, clearly show the spread of the reaction, and the areas the original hotspots formed. Heavens and Field also attached a strain gauge to the bottom anvil of the fallhammer, and qualitatively described the shape of pressure history for multiple materials [33]. The energy absorbed by the materials upon initiation was also estimated, however it was difficult to account for all the energy present in the system.

The photographic images from this apparatus continued to be used to investigate sensitivity and hotspot formation. In 1982 Heavens *et al* concluded that multiple hotspot mechanisms are present such as adiabatic shear, adiabatic heating, viscous flow, friction, friction or shear of added particles [73]. The combination of photographs and strain gauge was also used to examine the effect of added polymer particles with the explosive sample [74].

Ten years later, the same technique was being used [75, 76]. An improved camera was implemented, and quantitative analysis on the change of radius of the sample during impact could be achieved. This visual aspect was still the main focus, as it was concluded that the reaction itself was complex and not easily quantifiable, and the images of an evolving reaction were therefore more useful than other diagnostics. That being said, other diagnostics were added. Emitted light or ionised particles were used to detect the presence of the reaction, and heat sensitive film was used to give an indication of the temperatures present and the influence of shear banding. Strain-gauges were implemented on a more traditional fallhammer with non-transparent anvils, however the focus of the research had shifted to unreacted strength and deformation of polymer-bonded explosives. From there, the better suited Hopkinson bar apparatus was used to investigate the effect of strain on the energetic samples without initiation [76], rather than studying the pressure wave that occurred upon reaction in the fallhammer.

The optical glass-anvil fallhammer continued to be developed, and by 2004 the technique of second harmonic generation was used, allowing the phase change of HMX to be observed during impact initiation [77]. In 2016, mass spectroscopy was added to the fallhammer setup, as a way of detecting the initiation through the count increase of certain product masses [2]. It was during that last round of diagnostic additions that an optical spectrometer was also included, from which this research was motivated, as introduced previously.

1.3 Light emission

With the background of energetic materials and their reactions covered above, the second area of knowledge required for the following research is the theory of light emission from

these energetic reactions, and how this emission can be measured. Optical spectroscopy concerns itself with the visible light emitted by a material, and splitting the light captured into its constituent energy levels. Normally, this is presented as a wavelength spectrum; showing the intensity of light/photons present at each wavelength across the visible range of *circa* 400 – 700 nm.

Splitting of light into constituent wavelengths is commonly associated with a triangular prism – where the refractive index of the glass causes different wavelengths to travel at different speeds through the glass. With an input of white light, the output shows the independent colour spectrum. The same effect can also be seen by utilizing a diffraction grating, which produces a series of maxima with positions dependent on the separation between the slits in the grating (d), and the wavelength of the incident light (λ);

$$dsin\theta_m = m\lambda \tag{1.10}$$

Where m is the order of the fringe seen. The grating therefore produces a series of bright maxima for each wavelength present in the light, separating the components out as required.

Using gratings is more practical than prisms due to their ability to integrate into a system and, most importantly, the fact they can be tailored to a specific requirement. The resolution for a system with N slits is calculated as:

$$R = \frac{\lambda}{\Delta\lambda} = mN \tag{1.11}$$

where $\lambda + \Delta\lambda$ is the closest wavelength to λ that can be resolved. Therefore, with a larger grating, or more lines per unit length, a larger resolving power is possible.

Once the light has been split into this wavelength spectrum, it is then possible to discern specific features. These include spectral signatures, from the presence of excited elements/molecules in the material, and blackbody radiation from the heat present.

1.3.1 Spectral

As demonstrated by familiar flame tests, when elements and molecules are burnt they emit specific wavelengths of light depending on the energy levels present, with the heat energy exciting an electron to a higher energy level and the subsequent drop to the ground level releasing a photon equal to the energy difference. Burning copper reveals a green colour, lithium burns red, and potassium purple, for example. This bright colour emission has a range of applications, such as fireworks. The emitted photons of these colours show up as sharp delta-spikes on the wavelength spectrum.

Fig. 1.11 An atom emits a photon with energy equal to the difference of its electronic energy levels. This photon energy has an associated wavelength, and so would present as a peak at that wavelength on the flame emission spectrum.

The emissivity (which can be thought of as the 'probability' or 'effectiveness' of an emission occurring) between elements varies massively, for example the single valence alkali metals having much more intense emission in general compared to other elements and molecules. The D-lines of sodium at 589 nm have a higher recorded intensity than most other spectral lines [78]; negligible impurities of only 10 ppm are needed for a noticeable emission [79]. The high emissivity of the single valence group leads most flame spectra to be dominated by the alkali metal impurities in the materials rather than the lower intensity spectra of the constituent elements expected.

Sodium and calcium (in CaO and CaOH form) are therefore present in a range of combustion measurements [80, 81], showing an intense peak at 589 nm (Na) and a collection around 554 nm (CaO) and 622 nm (CaOH) [82]. Despite these peaks having specific characteristic wavelength values, they can easily be incorrectly assigned to different elements as these highly emissive impurities are often not expected to be present in the materials being investigated. A few examples can be seen where there is a noticeable sodium peak, but it is listed incorrectly, such as an unknown radical [81], N_4^- [83] or helium [84].

Though the main focus in this research is emission spectra, the same physics applies in reverse for absorption. An unexcited (cold) element will absorb a photon of the exact energy to excite an electron to a higher energy level, which will then be released in a random direction. Therefore, there will be a net loss of photons detected at that wavelength, and will show a dip in the spectrum rather than a peak; such as the familiar Fraunhofer lines recorded in the optical spectrum of the sun.

Broadening

The spectral peaks are broadened beyond the 'delta-spikes' predicted by the single energy transition model. Independent from the environment, there is lifetime broadening of the

emission. This is due to the fact the excited state has an associated decay time, which corresponds to a broadened Lorentzian peak in the Fourier-transformed frequency space, and therefore to a Lorentzian emission trace in the wavelength spectrum.

Significant to this research, the peak is also affected by the surrounding temperature and pressure. Emission from particles that have a velocity component along the line of detection will have a Doppler-shifted frequency dependent on the particle velocity. At higher temperatures, the velocity of the particles increases due to a higher kinetic energy. As these emitting species are travelling in random directions, this leads to a larger range of frequencies which are symmetric around the central frequency. In particular, the intensity spectrum is Gaussian:

$$I(\omega) = C\,exp\left(-\frac{m(\omega-\omega_0)^2c^2}{2\omega_0^2 k_B T}\right) \tag{1.12}$$

Where m is the mass of the emitter, T is the temperature, ω the frequency, and other constants with their usual meanings.

The width is also pressure dependent. When in a gaseous state, there are frequent collisions between the emitting species and their neighbouring atoms. These collisions perturb the emitting species, and the mean time between the collisions leads to a Lorentzian profile, similar to lifetime broadening. The width is inversely proportional to the time between collisions, $\tau = \frac{b\sqrt{T}}{p}$, and so the spectral width due to collisions increases with pressure and decreases with temperature. See Laser Spectroscopy, Springer for a more complete discussion [85].

Shift

The position of the spectral peak is dependent on the energy level of the emitting species. Introducing conditions that affect the energy levels will lead to a different energy photon being emitted from the excited molecule, and therefore a different peak wavelength being observed.

One mechanism, similar to the broadening, is dependent on collisions between particles, and so the surrounding pressure. For neutral species, the dominating interaction between the emitting species and the neighbouring particles is the van der Waals potential, which is dependent on distance. At a higher pressure, the particles are closer together and so the potential – and therefore the energy difference between energy levels – changes. The energy levels have a tendency to get closer under these higher pressures, leading to a lower energy photon being released, causing a red-shift in the measured spectrum.

Charged particles, or the application of an electric field, also lead to a change in energy levels from the Coulomb interaction. The Stark shift describes both the effect of free charged particles (such as electrons or larger ions) and their interactions with the emitter, as well as the DC effect of an applied field.

A shift does not necessarily arise from the change in energy levels from the emitter. Perhaps the most well-known of spectral shifts is the Doppler shift, arising from the relative motion between the emitter and the observer. Same as Doppler broadening, it has a dependence on the speed – or temperature – of the emitting particle.

These mechanisms are revisited in more detail in Chapter 4.

1.3.2 Blackbody radiation

As well as spectral emission, light due to the heat of the solid body – blackbody radiation – is also present. This has a characteristic wavelength spectrum and intensity that solely depends on the temperature of the emitting material. From considering the amount of energy emitted at different frequencies, the spectral radiance can be calculated as:

$$R_\lambda(\lambda, T) = \frac{2hc^2}{\lambda^5} \frac{1}{exp(\frac{hc}{\lambda k_B T}) - 1} \tag{1.13}$$

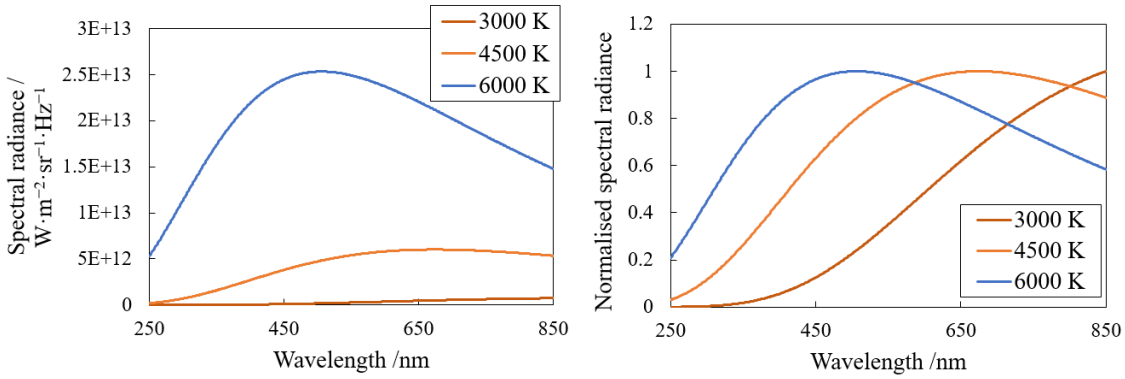

Fig. 1.12 The wavelength spectrum for three different temperatures: 3000, 4500 and 6000 K at the correct relative intensities (left) and normalised (right). Note that, as well as the increasing intensity, the peak gets narrower and shifts to the blue end of the spectrum as the temperature increases.

This function, dependent only on wavelength and temperature, is known as the Planck distribution. From this, Stefan-Boltzmann's law can be calculated, detailing that the power (intensity) of the observed blackbody light is proportional to the fourth power of temperature:

$$I = \sigma T^4 \tag{1.14}$$

Therefore, in principle, a temperature measurement can be calculated by comparing the light intensity to that with a known temperature.

If an unknown fraction of the total intensity is collected in experiments, so the intensity is no longer linked solely to the temperature, the temperature can still be estimated. The light emission of the measured spectrum will have the characteristic blackbody shape (and maximum wavelength), and so a fit to the Planck distribution can be achieved to output a temperature.

The material also won't be a perfect blackbody, and thus will have an associated material/surface emissivity factor ($\varepsilon(\lambda, T) \leq 1$) for the blackbody radiation (equation 1.13), leading to 'greybody' emission. Assuming the emissivity of the material is constant over the wavelength range, the wavelength emission spectrum can be fitted to the blackbody spectral radiance equation to determine the temperature as before, with the emissivity only affecting the intensity and not the shape of the function.

In reality, the emissivity is not a constant, and will have a material-specific dependence on wavelength and temperature. The latter dependence is important when multiple temperatures are being measured, and the former will change the shape of the greybody function over the wavelength range. Therefore, to properly to fit a greybody function to the light emission, a knowledge of the emissivity wavelength dependence is needed. This value is not known for HMX in the visible region, due to the challenges of measuring emissivity during an explosive reaction. Previous research has made the assumption that the emissivity is constant over the wavelength range [86–88], as otherwise greybody fits – and therefore, temperature measurements – would be impossible.

This technique also assumes the body is at a single temperature, and due to the T^4 dependence in the intensity, will preferentially measure the maximum temperature in the material as it will quickly dominate over other cooler emission sources. For example, as previously discussed, if radiating particles of both 8000 K and 4000 K temperatures are present, for the intensity of each to be equal, only 6 % of the emitters need to be at the higher 8000 K temperature.

In order to achieve a temperature measurement from observing the greybody radiation, the reaction will therefore require a high enough temperature as well as enough emitters so that the radiation can be significantly detected.

1.3.3 Summary

There are two main contributors in a wavelength emission spectrum. Spectral components are observed only if a certain species is present and will be positioned at a specific wavelength, though reaction conditions may affect the shape. Greybody emission will be a continuous emission across the whole spectrum, whose shape is dependent only on the temperatures present.

These features often are in competition with each other, with the conditions of the emitting particles determining which is dominant. Given the source of spectral emission is completely independent of greybody radiation, these spectral peaks are additive, and should theoretically be able to be separated from the continous greybody background.

1.4 Light emission from energetic reactions

Both the theory of energetic reactions and optical spectroscopy have been discussed. The aim of this research was to investigate the optical emission of the energetic reactions in different regimes, to understand the features seen in the emission and to, hopefully, use them to further understanding in this area.

The energetic reactions have high temperatures (*circa* 4000 K and above) and pressures (of order GPa). Therefore, the presence of any spectral lines in the optical emission would likely be broadened, and potentially shifted, under these conditions. The high temperatures, with the presence of any solid reaction products, would lead to greybody emission being present, with the peak emission in the optical range.

There would also be associated difficulties. The extreme conditions mentioned would be damaging, and so the light would have to be collected without destruction of the equipment used. Additionally, the reactions occur over short timescales, and potentially evolve over time, so a sufficient time-sensitivity would have to be implemented.

1.4.1 Previous research

Light emission has, in some form, been studied previously with regards to energetic materials. Firstly, optical spectroscopy of combustion is a well-known technique, hailing back to school flame-tests, where an element is put in a Bunsen burner and the flame goes a different colour according to what was burnt. Whilst more advanced, spectroscopy of flames is a similar process, and the flame spectra of multiple different materials has been characterized, and the common highly emissive impurities tabulated [89].

Using optical spectroscopy on flames was often to examine the chemical reactions present – which pathways were taken based on the presence of specific molecular emission in the flame [90]. Flames from propellants were examined, investigating the effects of changing propellant composition on both the optical emission and the measured reaction zone [90]. Optical spectroscopy could be used to probe reaction zone properties of propellants [91], however it became much more effective to use other types of diagnostics, such as Coherent anti-Stokes Raman spectroscopy [92–94] or Fourier Transform Infrared absorption spectroscopy [95–97]. Molecular Beam Mass spectrometry has also been incorporated for studying flame chemistry, in particular conversion of NO into NH_3 [98]. Therefore, whilst the study of flames is a large area of research, optical emission is less of a focus due to numerous other more specialised spectroscopy techniques.

Investigations into the light emission of energetic reactions are not as common as flame tests. Some of the first examinations of detonation light were film cameras that recorded images of detonation. Unfortunately, this led to a purely qualitative description of the brightness of the event. However, it was commonly accepted that the intense light of the detonation was often due to the air shock [53] rather than the detonation itself, leading to attempts to view the detonation underwater [50, 63], in order to limit such an effect. Separately, multiple experiments were performed to investigate how the detonation light depended on the gases present in the air pores [59, 99]. However, given that no spectroscopy was done to distinguish what kind of light was received, these qualitative levels of brightness could not be assumed to correspond to temperatures. For example, given the amount of sodium present in experiments [99], such an element has very emissive spectral bands that would not be distinguished from the blackbody radiation in a measurement of absolute intensity, and so would lead to an over-estimation of the temperature.

Over time, technology allowed proper spectroscopy to be used in detonation experiments. However, many spectroscopic studies of detonation were often limited to post-detonation combustion, to study the spectral signature (such as from added aluminium or copper) [100–102], the structure [103], or the temperature [46] of the resultant fireball that was created. Spectroscopically analyzing the breakout into air resulted in the high temperatures of air shock to be measured, along with the spectral emission of sodium and calcium that were observed in combustion [80]. Also, similar to the studies on flame, absorption was investigated alongside emission [104].

So spectroscopy has been used in conjunction with detonation, it has often been limited in the past to either post-detonation, or investigating specific peaks of added components, and not as a comparison to other energetic regimes. It does reinforce the high temperatures that have been observed, though these are often due to the external air shock, and not the

detonation itself. The light from external air shock originates from similar mechanisms as the previously discussed internal cavity collapse - with a large pressure from the detonation wave forcing a suddenly decrease in volume of the space. However, the internal void collapse is an intrinsic property of the detonation within the porous material, and the light emitted provides information on these hotspots. On the other hand, external air shock originates due to placement of the diagnostic equipment (with an air gap between the detonation and the measurement device) and so does not contain information from inside the detonation wave itself.

Instead of just using high resolution ($<$ 1 nm) spectroscopy, pyrometers with certain wavelength channels have been constructed in order to measure the temperature. These assume a greybody emission, and are a simple method of measuring the time-resolved temperature of the reaction. For non-steady reactions, such as the shock-to-detonation transition of nitromethane [47], the time-resolved properties were assumed to be more important than the high resolution wavelength spectrum.

At the time of writing, the Dlott group at the University of Illinois were also concentrating on light emission of energetic materials. Their research is focused on single crystals (of less than 250 μg) which are not large enough to sustain detonation on their own. Instead, detonation-like conditions are achieved by an incident laser-flyer, overdriving the crystal to simulate larger scale reactions. Taking the idea of time-dependent pyrometers to the extreme, Dlott *et al* constructed a 32-channel pyrometer for investigating the reaction of energetics initiated by laser flyer [105]. Along with a framing camera [56], this diagnostic tool allowed the temperature profile to be measured for different reaction conditions [106, 55].

As mentioned; the Cavendish Laboratory also has a brief history with studying the optical emission of energetic reactions. Both camera images of deflagration [107, 2], as well as measuring the wavelength spectrum [2, 3]. These spectra showed the inclusion of an unknown spectral peak, motivating further research.

Taking the previous research into account, the aim of this thesis was clear. The light emission from multiple different controlled regimes was to be compared, with a high wavelength resolution so both the whole optical spectrum could be observed, as well as any spectral features. This would enable any differences between regimes to be quantified and explained. For detonation, the experiment had to be designed so that it would only measure the light from the reaction front, and not from any air trapped at the surface which would be compressed by the high pressures.

Most importantly, the aim was for original, useful, research. How the optical features present could be used to quantify reaction properties, whether the light emission changed if a different initiation method was used, or the initial properties of the explosive was changed.

Therefore, a more complete understanding of the light emission could be seen, rather than limiting it to one regime or experiment.

Chapter 2

Deflagration in a fallhammer apparatus

2.1 Introduction

Previously, a very limited amount of optical spectroscopy has been conducted at the Cavendish Laboratory, where the light emission from deflagration initiated in a fallhammer apparatus was measured by a spectrometer [2]. The main feature seen in the emission spectra was a spectral peak at 590 nm. This measurement inspired the current research into the light emission of energetic materials, identifying and characterising the main features, and its evolution with different regimes.

Before embarking to measure deflagration light, the obvious first step was to investigate the spectral signatures that are observed in burning the material. Being less violent, simple combustion allowed an easier measurement to be made, and detailed the spectral contributions of the light which would likely to present within deflagration as well.

Inspired by the previous research, a fallhammer apparatus was used to initiate deflagration. This is a method which has been used to successfully measure emission light and allows the results of previous research to be properly characterised. Also, importantly, the fallhammer apparatus provides the opportunity for fast, repeatable and safe measurements of deflagration.

2.2 Optical spectroscopy equipment

The experimental setup was designed to collect as much reaction light as possible, with minimised attenuation. The light was captured using a fibre optic cable with a 1 mm diameter PMMA core, placed next to the reaction, with no interface or window that would distort the light in any way. This collection fibre optic was then collimated into a 50:50 beamsplitter [ThorLabs CM1-BS013]. Half the light was directed to a gated single-shot spectrometer

(composed of a spectrograph, gate mechanism, detector and detector interface [EG&G Princeton Applied Research. 1235 and 1235-E, 1304, 1455, 1471A]) which would measure the optical spectrum. The other half was directed to a photodiode [EOT Silicon PIN detector ET-2030] to measure the intensity as a function of time. All components were chosen with high transmission in the main optical wavelength range (400 – 700 nm).

The spectrometer was gated, and so had to be triggered in order to capture the reaction light at the right time. Given the delay between the trigger input to the spectrometer and the measurement was *circa* 200 ns, for deflagration reactions of order microseconds the spectrometer could be triggered off the reaction light itself. To achieve this, the photodiode intensity trace was connected to an oscilloscope [Tektronix DPO 5054B], which was used to trigger a pulse generator [Stanford Research Systems model DG535], which in turn triggered the spectrometer gate to open and capture the emission light over a specified duration. The oscilloscope was used to monitor the intensity and duration of the reaction light, as well as the time when the spectrometer gate was open and capturing light. Such a setup is summarised in figure 2.1.

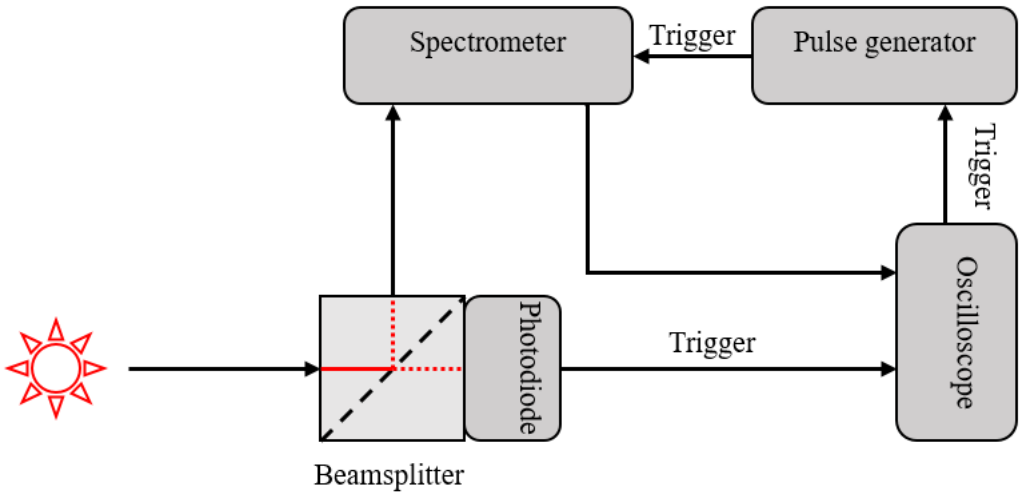

Fig. 2.1 A schematic diagram of the optical setup, showing the input light being directed to the photodiode and spectrometer, with the photodiode trace triggering the spectrometer gate to open via a pulse sent by the pulse generator.

The purpose of the spectrometer was to record the visible wavelength spectrum; splitting the light into its constituent wavelengths and detecting the respective intensities for each wavelength 'bin'. The spectrometer used (figure 2.2) was a modular system, containing a spectrograph, detector, gate control, and computer.

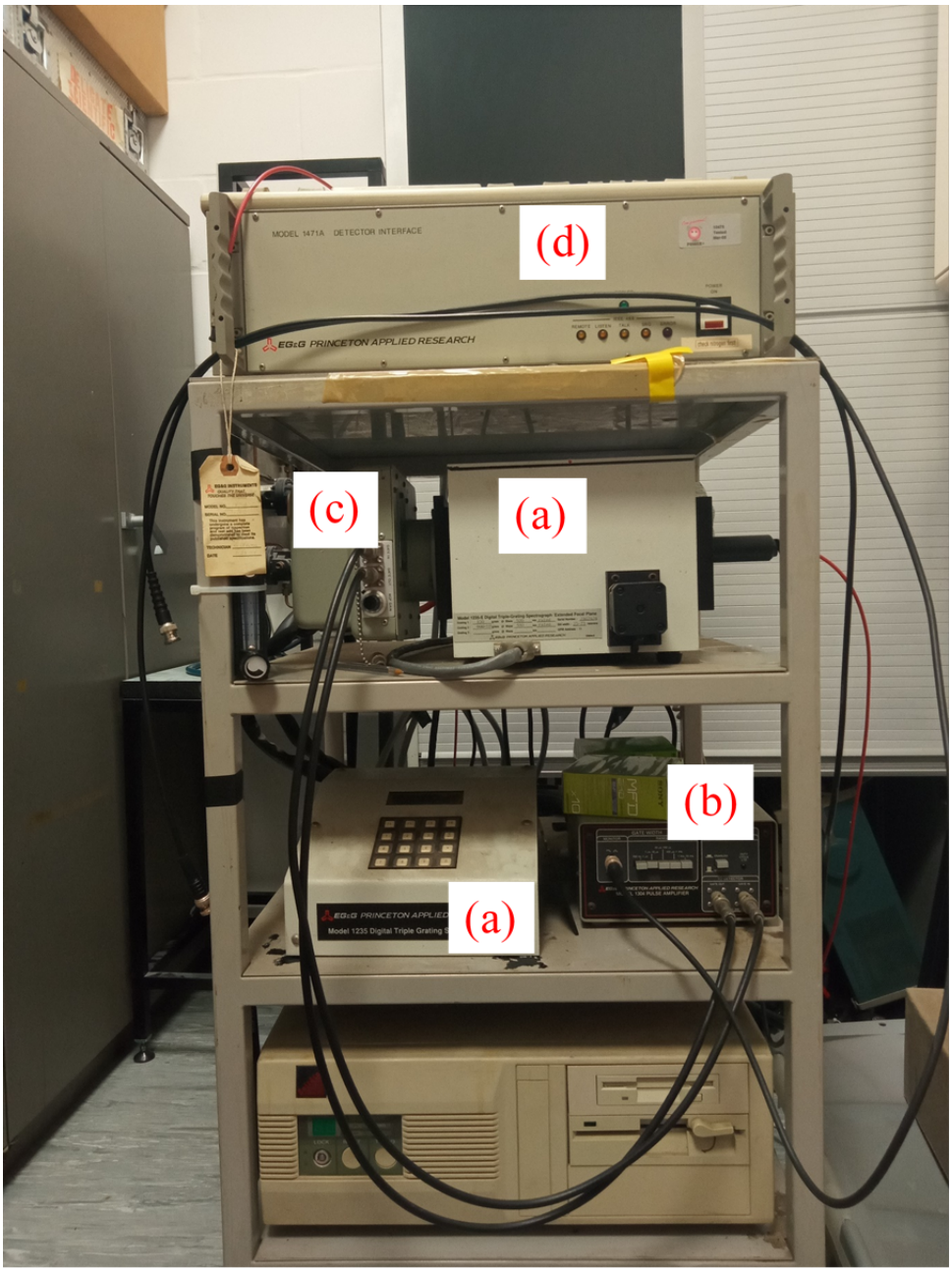

Fig. 2.2 Tower of the integrated spectrometer equipment used in the following experiments, with the spectrograph (a), gate mechanism (b), detector (c) and detector control interface (d).

As discussed in section 1.3, the light was split using a diffraction grating in a spectrograph unit. There was a choice of two gratings, one with line density 150 g mm^{-1}, allowing for a 0.6 nm resolution across the whole visible range (*circa* 500 nm), and one with a line density of 1200 g mm^{-1}, with a higher 0.06 nm resolution on a narrower range of wavelengths (*circa* 50 nm).

Once diffracted in the spectrograph, so that the different wavelengths occupied a different spatial coordinate, the light passed into the 700-pixel diode array detector. The detector was cooled to reduce thermal (Nyquist) noise, and so in order to avoid condensation in the detector, dry nitrogen was run continously through the unit when it was in use. The detector is also fitted with a microchannel plate (MCP), allowing for amplification of the detected signal, with a variable gain so that a range of different levels of light intensity could be studied. The gain took the form of a dial, from 0.0 to 10.0, in a non-linear scale that roughly followed that the intensity would double for each turn of the dial.

The number of counts measured had to be above the background noise, and the larger the measured intensity, the better the signal-to-noise ratio. However, the detector saturated at 32,000 counts, and an increase above that intensity was likely to damage the detector. Therefore, a careful balance had to be achieved between measuring enough counts to have a clear signal, and not too many to damage the equipment.

The amount of light measured could also be adjusted. The spectrometer had a gated function, so that it would collect light from when the gate opened, to the time the gate closed. The displayed spectrum would be a time-integrated measurement from the total period the gate was open for. The duration could be controlled by inputting a TTL pulse from a pulse generator into the gate control mechanism, with a width equal to that required for the gate to be open.

The spectrometer detector interface, connected into a computer running the OMAVIS software [EG&G Princeton Applied Research, OMA vision], then displayed the wavelength intensity spectrum from the measured time period.

2.2.1 Calibration method and measurements

Each optical component presented some wavelength attenuation, or biased sensitivity. In general, the equipment used had high intensity transmission from 400 - 700 nm, covering the visible light region. The level of dispersion – affecting the speed of light at different wavelengths – was negligible in the experiments, given the microsecond timescales of the reaction and the short distances the light travelled.

Thermal excitations in the detector led to dark current – electrical signal detected even when no light was inputted. As mentioned previously, the detector was chilled as part of its design to lessen this signal. However, there was still a dark current present, which was easily removed from the final intensity by taking a measurement when no light is seen by the spectrometer, so the only spectrum was from this dark current, and then subtracting it from all future measurements.

The main source of attenuation in the spectrum was due to the fibre optic cable transporting the light from the reaction to the measuring equipment. This was accounted for, along with the other optical effects from the components, by taking a calibration measurement against a known blackbody. In this case, a lamp which emitted a blackbody, C(λ), corresponding to 2856 K (NPL certified) when a specific voltage and current were supplied (7.29 V, 3.549 A). This blackbody could be theoretically calculated using Planck's equation (eq. 1.13). Measuring this blackbody with the spectrometer produced a wavelength spectrum, S(λ), with the attenuation and sensitivity of all the optical measurements included, as shown in figure 2.3. From this, a ratio of the intensities, R(λ), was calculated.

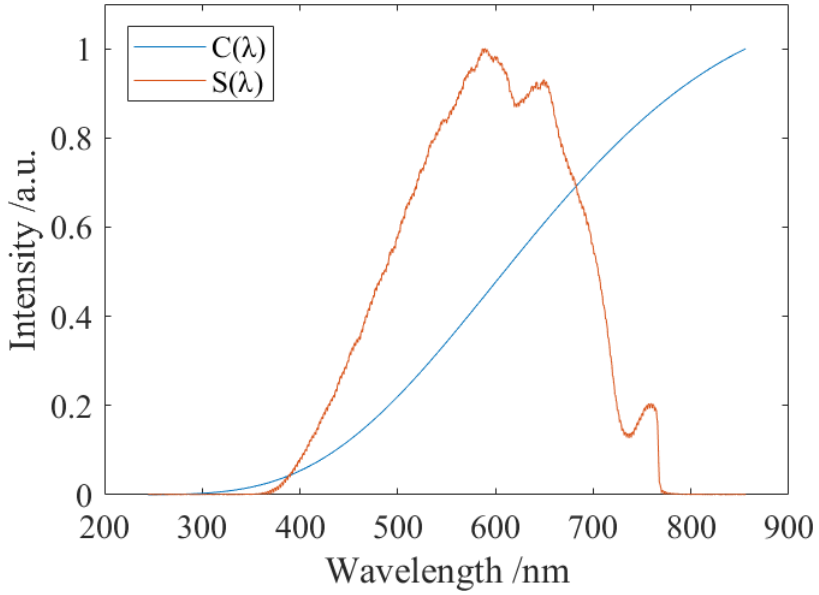

Fig. 2.3 The measured lamp spectrum (orange) compared to a calculated blackbody at the same temperature (blue). The two 'peaks' present in S(λ) are due to attenuation in the fibre optic cables used, and the overall sensitivity is due to the optical elements being designed for visible light.

$$R(\lambda) = \frac{C(\lambda)}{S(\lambda)} \tag{2.1}$$

The measured wavelengths values in the experiment would then be multiplied by this ratio, in order to remove the aforementioned attenuation and sensitivities present in the optical setup, with examples shown in figure 2.4. Due to the continual replacing of the fibre optic and modifications to the experiment, this ratio would be recorded before each individual measurement.

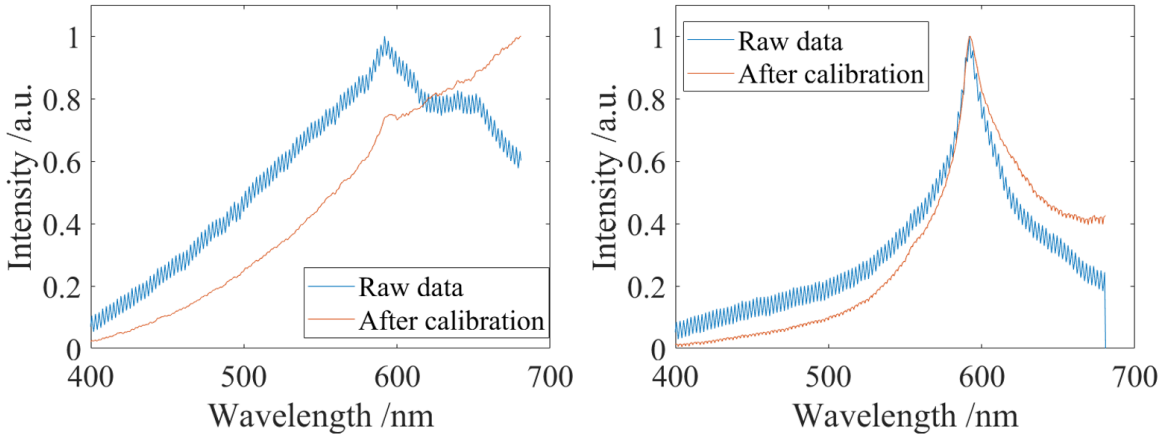

Fig. 2.4 Two examples of measured spectra before (blue) and after (orange) calibration was performed. One with a dominant spectral feature (right). Removing the high frequency and thermally activated dark current takes out small random uncertainty fluctuations and the blackbody ratio accounts for the attenuation and sensitivity across the range of wavelengths.

Given the low sensitivity of the spectrometer outside of the 400 – 700 nm range, this ratio will tend to exaggerate data lying outside the visible region. Therefore, the majority of the analysis was done within this range, where all the equipment has high sensitivity. After this calibration, the attenuation had been accounted for and the spectrum could be reliably analysed.

2.3 Ambient pressure burning reactions

Material was burnt using a butane flame which itself had negligible measured emission. In order to achieve a controlled burn, a spatula was used to hold the material above the flame, causing it to melt and then flare, emitting bright light over a few milliseconds.

The capturing fibre-optic cable was placed near the flame, close enough to measure as much light as possible without damaging the fibre. The flare of the reaction was captured by triggering the spectrometer gate to open for a few milliseconds once a higher light intensity was measured by the photodiode. Figure 2.5 shows the optical spectrum recorded from burning HMX, as well as similar secondary explosives RDX and PETN.

Seen in figure 2.5, the emission spectrum from burning was purely spectral as expected. The reaction had not reached a large enough temperature for blackbody features to be easily seen, as well as the fact the reaction was clean - completely reacting into gas products so there were comparably few solid products for a blackbody to radiate - an observation that will be revisited in Chapter 5.

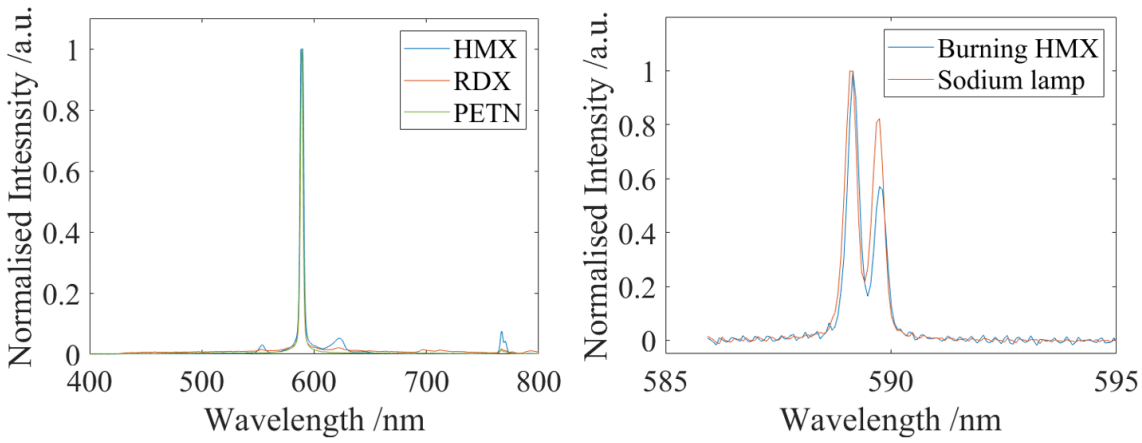

Fig. 2.5 Typical burning spectra, over whole visible range (left) with a resolution of 0.6 nm. The spectrum shows four distinct spectral emissions, with sharp lines at 589 and 770 nm, and broad emission at 555 and 620 nm. The main emission across all spectra was the 589 nm peak, which resolved into a doublet when measured with a 0.06 nm resolution (right).

The main spectral peak in all experiments, regardless of the material investigated, was the sodium doublet present at 589 nm. Using a diffraction grating in the spectrometer with a higher line density increased the resolution of the spectrum to 0.06 nm, allowing the doublet to be resolved into its two distinctive peaks at 589.0 and 589.6 nm. Comparison to a sodium lamp allowed a visible confirmation that sodium had been correctly identified.

The identification of sodium was not immediate as HMX, as well as RDX and PETN, do not, or more correctly, *should* not, contain sodium. Yet trace impurities can be expected, with sodium being the sixth most common element on Earth, and 'fresh' water containing about 20 mg per litre [108], or 15 ppm. These trace impurities dominate the spectrum because of how highly emissive they are, despite the negligible amount that would be present. Sodium can dominate burning spectra down to 10 ppm [79], and is observed in the spectral features of the majority of combustion spectra [82].

The presence of sodium in most combustion emission could also be realised by noting that the characteristic colour of their flames is the orange-yellow of 589 nm sodium. Figure 2.6 shows HMX on a clean spatula that was placed in the butane flame, which was measured as mostly sodium emission.

After identifying sodium as the main spectral feature, the other peaks were also identified as alkali metal impurities, with the potassium doublet at 770 nm and a collection of CaO and CaOH peaks at 555 nm and 620 nm. Similar to sodium, these are also common impurities seen in flame spectra [89, 82].

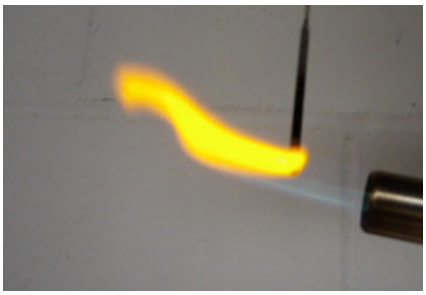

Fig. 2.6 HMX on a clean spatula placed in a butane flame. The characteristic yellow-orange of sodium can be seen. As sodium is such a common contaminant, and so emissive, it is observable in most flames.

Therefore, for the burning optical spectrum of HMX, the emission signatures of nitrogen, carbon, oxygen and other expected molecules were simply not intense enough to be seen over the impurity signatures of the alkali metals.

2.4 Fallhammer apparatus

Fallhammer initiated deflagration allowed the repeatable study of the light intensity and wavelength spectrum from the same source of light produced in a confined energetic reaction. A modified BAM-fallhammer [OZM Research. BFH-10 BAM] was used to create the impact conditions required for reaction. The energetic material was placed between two steel anvils and a weight was dropped onto this setup in order to initiate deflagration.

The BAM-fallhammer test and equipment was designed for testing the fall sensitivity of energetic materials (as specified in the EMTAP (Energetic Materials Testing and Assessment Policy) manual, test number 43 [109]). This purpose meant it is able to safely initiate deflagration, with a choice of masses (0.5 – 10 kg) and heights (up to 1 m) in order to test the potential energy from which a material initiated. This apparatus is a commercially available piece of equipment, designed so that two different laboratories could have the same test in order to fairly compare energetic materials. Shown in figure 2.7 is the BAM-fallhammer that was used at the Cavendish Laboratory for the deflagration experiments detailed below.

10 mm^3 of HMX was used, having a poured density of *circa* 0.95 g cm^{-3}. As a reaction was required each time, the weight and the height it was dropped from were chosen so the energy delivered to the material would ensure initiation was achieved. For HMX with a drop sensitivity of *circa* 7 J [110, 111], a drop height of 90 cm and mass of 2 kg was chosen, resulting in a potential energy of 18 J.

High pressures are accomplished in this system due to the ringing of the pressure waves in the anvils. The anvils (and sample) have a lower mechanical impedance than the weight that

Fig. 2.7 The fallhammer apparatus at the Cavendish Laboratory, and used in the following experiments.

falls on the top anvil, or the base underneath the bottom. Due to this impedance mismatch, the compressive waves reflect and reinforce inside of the anvils, with each reflection producing a series of 'steps' of pressure – called ringing-up. The pressure rings up to a maximum point at the time the falling weight has been completely arrested. Once the weight rebounded, the same process would occur, with a ringing-down of the pressure, leading to a half-sine pulse shape. Therefore, even with a relatively small original impact pressure, the actual peak pressure can be a lot higher.

The maximum amplitude of this half-sine is determined by the amount of stored elastic energy in the anvils. The anvils have a cross sectional area of 25π mm^2, a length of 10 mm, and were made of steel, so would have a modulus, Y, of *circa* 200 GPa. Assuming all 18 J of the falling kinetic energy (U) was transferred,

$$Y = \frac{P}{\varepsilon} \text{ and } \frac{U}{V} = \frac{1}{2} \times Y \times \varepsilon^2 = \frac{1}{2}\frac{P^2}{Y} \tag{2.2}$$

$$\therefore P = \sqrt{\frac{2UY}{V}} \tag{2.3}$$

Where P is the pressure, V the volume and ε the strain in the anvils.

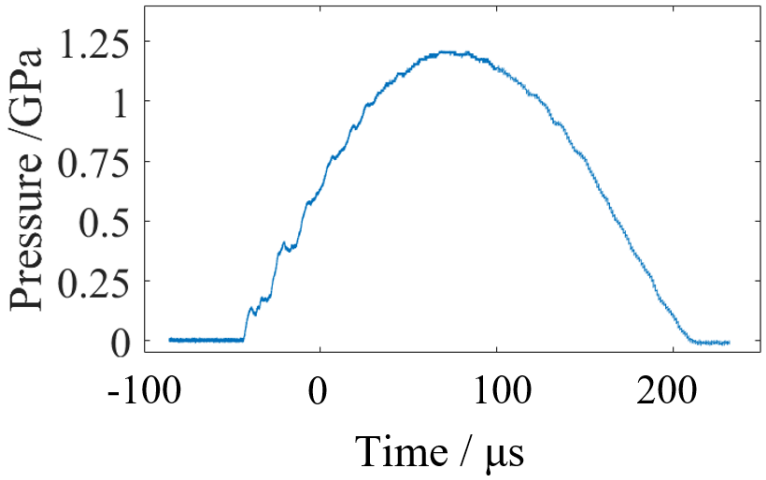

Fig. 2.8 An example of the pressure measured in the top anvil of the fallhammer against time (see section 2.4.1 for the method of measuring this pressure with a strain gauge), with an overall half-sine shape due to the ringing up of the pressure.

This results in an expected peak pressure of order 1 GPa, as seen in figure 2.8. The duration of the pulse was determined by the time it takes for the waves to reflect in the anvils. Given the multiple components present in the system, and the different impedances of the materials, determining this value would be an impractical equation. In experiments, a duration of *circa* 250 μs was observed (shown in figure 2.8).

The apparatus had been modified to allow for light capture by drilling a hole into the steel cylinder surrounding the anvils, which allowed for a 1 mm diameter PMMA fibre optic cable to be placed through and lie on the reaction plane.

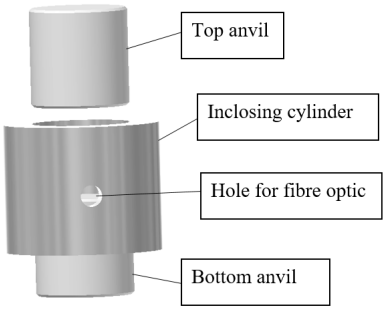

Fig. 2.9 A drawing of the anvils and cylinder setup. The weight falls onto the top anvil, crushing the material between them. Light was then collected out of the hole in the cylinder via fibre optic cable.

As the end of the fibre was flush with inner wall of cylinder, about 1 cm at the end was destroyed after each experiment which needed to be cut off and re-polished. Placing the fibre directly 'into' the reaction meant there were no additional absorption effects present due to the use of windows or similar additional interfaces.

2.4.1 Strain gauge addition

Another modification to the BAM fallhammer was the introduction of a strain gauge [Kulite Semiconductor Products, Inc. AFP-500–090] on the top anvil. The aim of this modification was to be able to measure the mechanical pressure incident on the sample (figure 2.8), rather than rely purely on the energy imparted by the falling weight. The strain gauge was placed onto the top anvil, aligned perpendicular to the falling mass, with the output connected to an oscilloscope [Tektronix DPO 5054B]. Similar to the optical system, this needed calibration before measuring, which was achieved by considering the impulse applied to the anvil.

$$Force = area \times pressure = m\frac{dv}{dt} \tag{2.4}$$

The pressure (p) measured from the gauge was converted linearly into a voltage signal $V(t)$, which was measured on the oscilloscope, $p = aV(t)$. The aim of this calibration was to calculate this proportionality constant, a. Using the above equation (eq. 2.4),

$$A\int_{start}^{peak} aV(t)dt = -mv_i \tag{2.5}$$

Where A is the cross-sectional area of the anvils (25π mm^2), m the mass of the incident falling weight and v_i is initial incident velocity. Calculating this velocity was achieved by using a Photon Doppler Velocimeter (PDV), pointed from below up towards the falling mass. The measured velocity trace would, in theory, be equal to the integral of the pressure in the anvils.

Calibration was achieved by measuring the voltage trace and initial velocity for a range of different masses and drop heights. Plotting the integral of the voltage trace measured by the strain gauge, and multiplied by the cross sectional area of the anvils, against the initial momentum of the falling mass therefore gave a straight line with gradient of 0.661 $\pm$ 0.025 V GPa^{-1}, shown in figure 2.10. Therefore, the value of a was 1.51 $\pm$ 0.05 GPa V^{-1}.

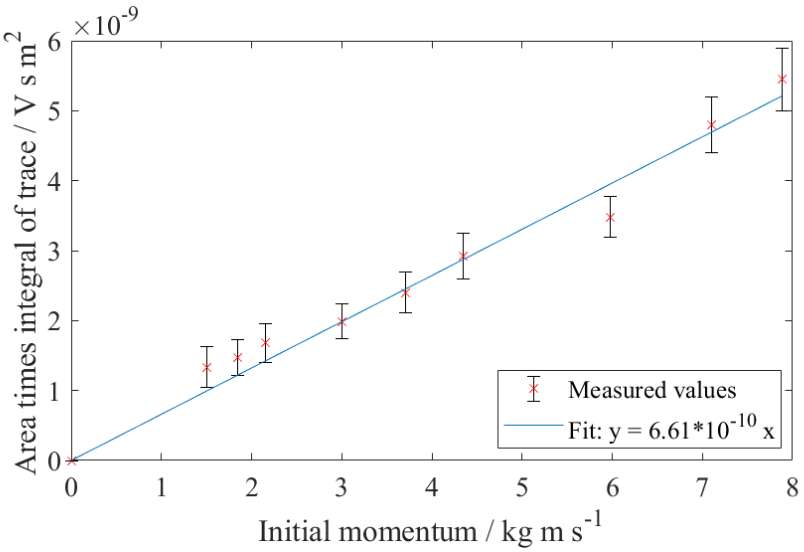

Fig. 2.10 The integral of the voltage (area under the pressure trace) was calculated from the start time to the time zero velocity was measured for each drop, with three different masses used. This was plotted against the initial momentum of the falling weight in order to calculate the calibration constant.

2.5 Results

2.5.1 Mechanical

With the addition of the strain gauge in conjunction with a photodiode, the pressure at which the reaction initiated could be measured, as well as the knowledge of whether the reaction initiated on rising, constant, or falling pressure.

Unlike the previous measurements conducted by Heavens and Field [33], there was no significant drop in pressure during the reaction time. This suggests that the pressure produced by the deflagration substitutes for the sudden loss of material supporting the anvil – implying that pressure equilibration occurs on very short timescales. To fully test this hypothesis, an independent measure of reaction pressure would be needed, with this line of inquiry conducted in Chapter 4.

The pressure that initiation occurred at was 0.60 $\pm$ 0.11 GPa across the experiments, which was similar to that measured by Heavens and Field [33]. What was interesting was the point on the loading path that the reaction initiated. In the majority (roughly 80 %) of cases, it initiated on the ring-up to maximum pressure (figure 2.11). However, on a few experiments, the reaction initiated at a similar pressure value, but on the ring-down of the pressure (figure 2.12).

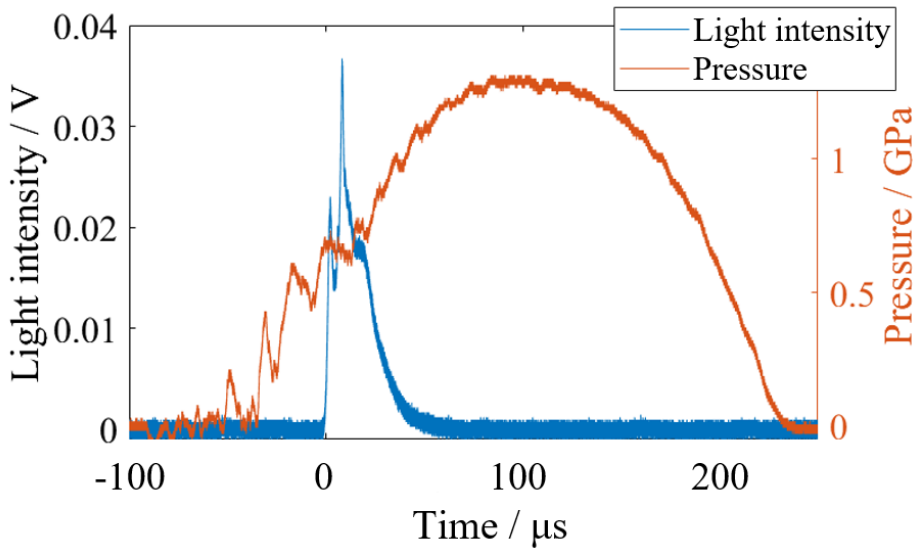

Fig. 2.11 Trace of the strain gauge along with the light intensity recorded. During the reaction the pressure stayed roughly constant, and did not drop to zero.

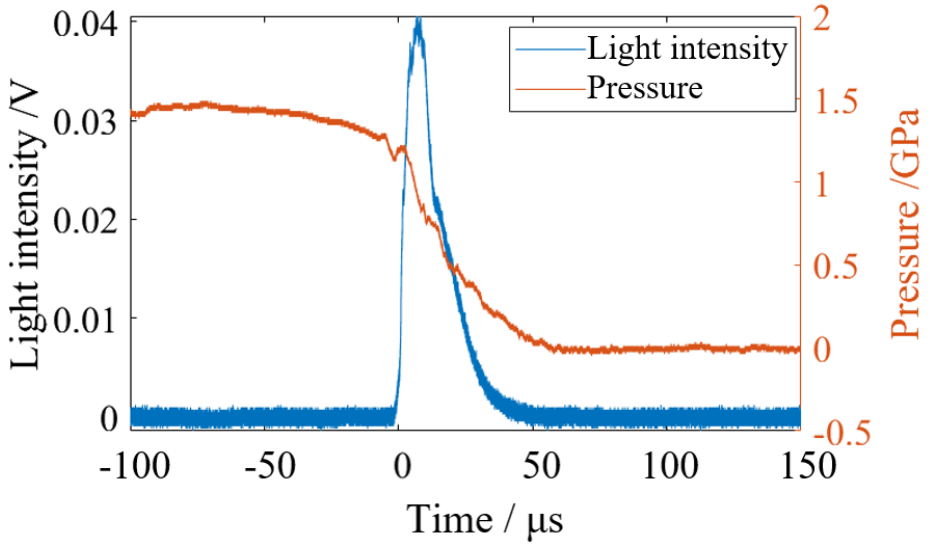

Fig. 2.12 Reaction initiates on the ring-down of the pressure for a minority of the experiments

Initiation on ring-down suggests that there is not only a simple pressure threshold to be overcome in order for initiation, but there is also a dependence on other factors, such as energy. The initiation was pathway dependent, seemingly only able to initiate on the rising and falling of the stress, rather than on the maximum.

2.5.2 Optical

From just the photodiode trace, the length of the deflagration reaction could be seen, typically ranging from *circa* 20 μs to 40 μs (figure 2.13).

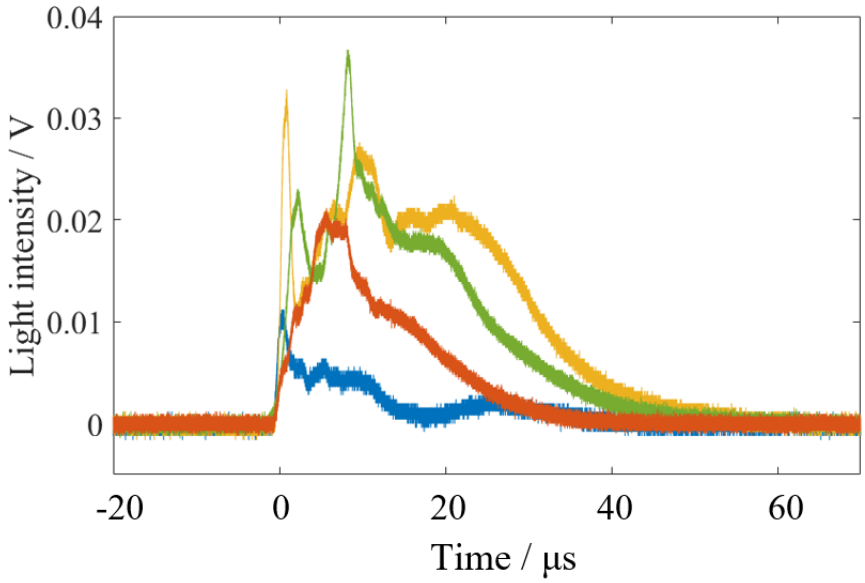

Fig. 2.13 Comparison of four different photodiode measurements observed in fallhammer deflagration. The reaction was tens of microseconds long, with the main period of light emission lasting 20 μs. Different intensities were also observed each time, despite 'identical' experimental conditions.

There were a lot of variables that were not controlled in the fallhammer apparatus, an example being the distribution of the powdered sample in the anvil. This stochastic nature was manifest in a few measureable quantities, such as the length of the reaction, the pressure - and pathway - of initiation, but most noticeable in measuring the brightness and shape of the light emission present. Shown in figure 2.13, the photodetector signal volts measured varied from *circa* 10 to 40 mV. This was partly due to the placing of the fibre-optic cable in relation to the position of the main light emission, but also shows that the fallhammer deflagration measurements were not exactly reproducible, and that multiple measurements would be needed in order to characterise any properties.

Spectral

The main feature in all the measured spectrum was the spectral emission around 590 nm (figure 2.14). From the burning spectra (figure 2.5) this can be identified as the same highly

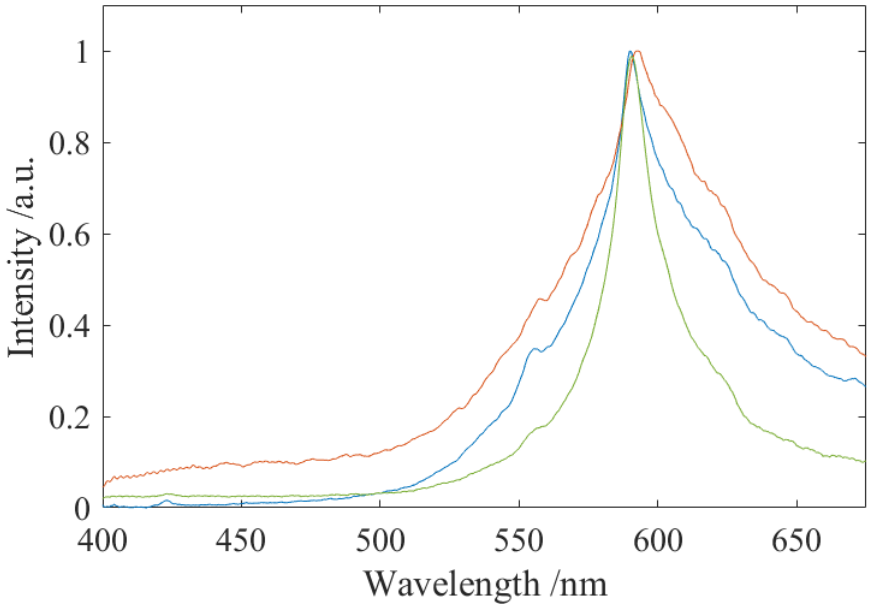

Fig. 2.14 Three example spectra from 'identical' HMX deflagration with normalized intensity. The blackbody effects are now noticeable, as well as the temperature and pressure broadened peak that dominates the spectrum.

emissive sodium impurity in the HMX that dominated those spectra. The other spectral emissions at 555 nm can, similarly, be identified as the same calcium emissions.

Past 700 nm the spectrometer sensitivity significantly falls, however potassium emission was observed from the burning spectrum at 770 nm, as shown in figure 2.5. This suggests that potassium could easily be as emissive as sodium, and so in deflagration the large broadened peak could potentially be affecting the far red parts of the spectrum.

The spectral peaks have clearly broadened, to the extent of being present in a significant portion of the visible spectrum. Given the high temperatures and pressures present in deflagration, this was not unexpected as both Doppler and collisional broadening were likely to be contributing (section 1.3.1). The width could not be used to estimate these deflagration conditions, as the two broadening mechanisms are not easily separated, and as seen in the spectrum, the peaks were not symmetric and have no clear position to measure the peak width from.

A very interesting observation was that the centre of the sodium peak was not present at the 589 nm wavelength as seen in burning (figure 2.15). The peak was consistently shifted to a larger value of 590 – 591 nm, with a mean red-shift across all measurements of 1.3 $\pm$ 0.3 nm.

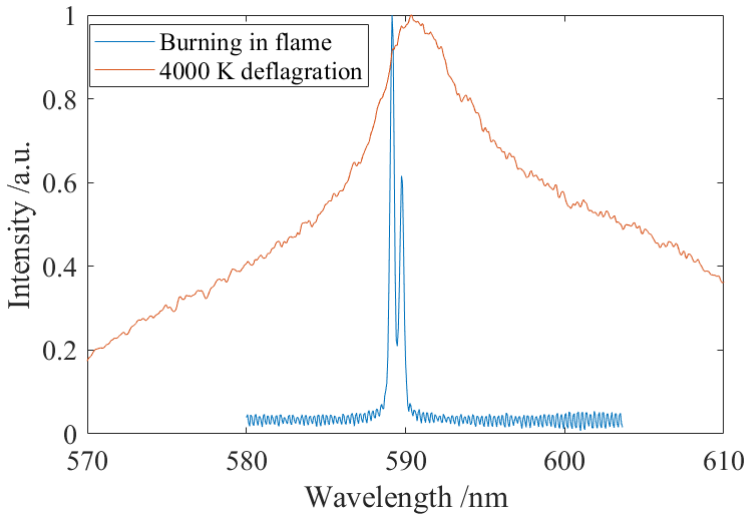

Fig. 2.15 A 0.06 nm resolution measurement of the deflagration peak compared to that of burning HMX. The peak has broadened and the centre has clearly red-shifted.

Such a shift was small, but significant, and was theorized to be caused by the high pressures present in deflagration (collisional shift). However, more in-depth theory and experiments were needed before this hypothesis could be confirmed, with a full description found in Chapter 4.

Measuring temperature

Unlike the burning spectrum, a continuous greybody emission was also present across the whole spectrum. To get a temperature measurement, a blackbody shape was fitted to the non-spectral part of the wavelength spectrum. Using a blackbody fit assumed a constant emissivity over the wavelength range used (section 1.3.2), as the dependence of emissivity on wavelength of reacting HMX was unknown at the time of writing. The assumption of a constant emissivity is common procedure for previous temperature measurements of similar energetic reactions [86–88], however will provide a source of uncertainty in the resulting temperature reported.

The non-spectral part of the emission would usually be in the region of 400 - 500 nm depending on how spectral the emission appeared, with the wavelength range for the greybody fit determined by eye. This range was run through a simple MATLAB code to fit the most accurate blackbody shape (section 1.3.2), and from that a single temperature was recovered, with a typical trace shown in figure 2.16. The range of wavelengths used was small, which meant that a single blackbody shape fit well, but the associated error was large, of order 200 K. Fitting this blackbody beyond the region of interest and across the whole spectrum, shown in

figure 2.17, illustrates how the larger wavelengths are dominated by spectral contributions and should not be used in any temperature fits.

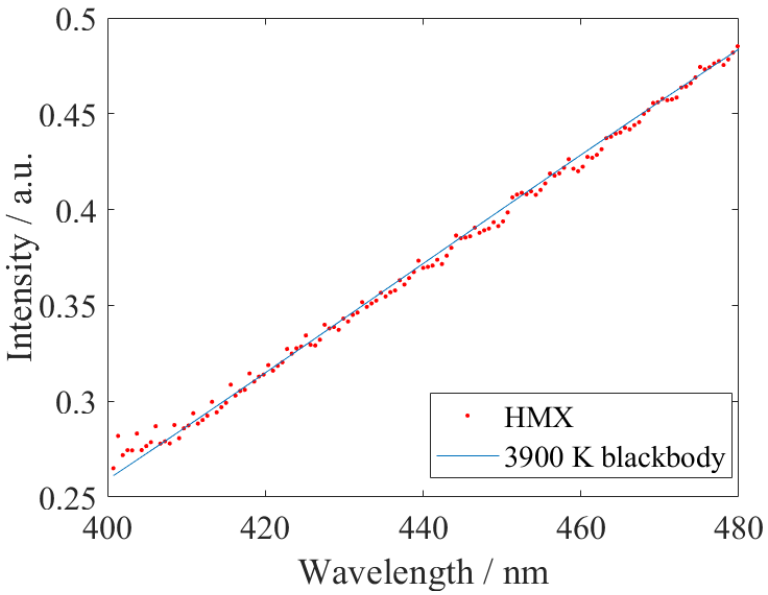

Fig. 2.16 Typical blackbody fit to the non-spectral part of the wider-range HMX deflagration emission spectrum.

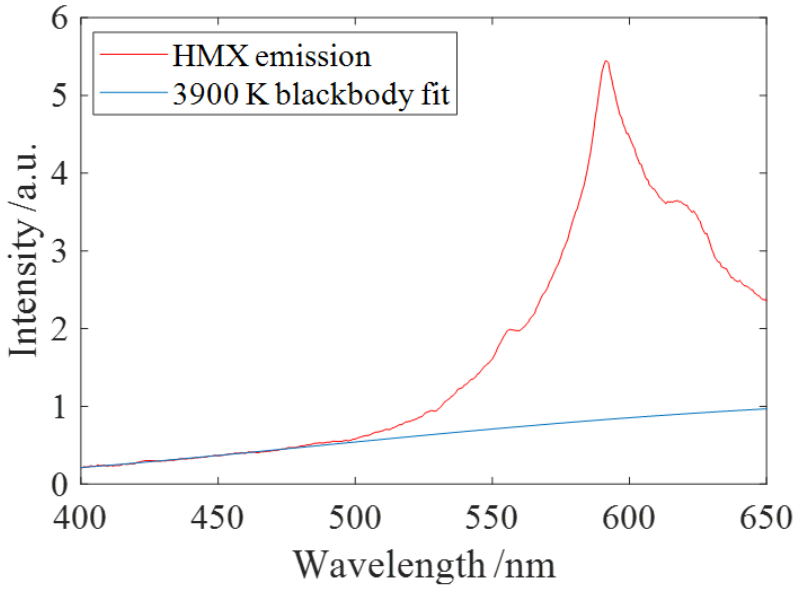

Fig. 2.17 The blackbody fitted to the 400-500 nm region extended across the whole spectrum. The spectral contributions of sodium, as well as calcium and potassium, significantly increase the intensity of the larger wavelengths, greatly deviating from the blackbody radiation.

Similar to the brightness measurements, the temperature values were very stochastic, which would be expected as the intensity of the light is dependent on the temperature. The average measured temperature was 3900 K, with the majority of measurements found in the 3700 – 4100 K range. However, there were temperatures as low as 3300 K, or as high as 5000 K, producing a large standard error of 400 K on the mean value.

This large range of temperatures suggest that there were many variables that deflagration temperature depended on, which were not all controlled in the fallhammer apparatus. Therefore, to reinforce the statement made earlier on the stochastic nature of this experiment, when measuring these properties multiple experiments and large data sets are required in order to properly analyse the results. Figure 2.18 shows the results of the 18 experiments conducted, which were sufficient to observe both the mean temperature as well as the typical range and spread of the possible temperatures.

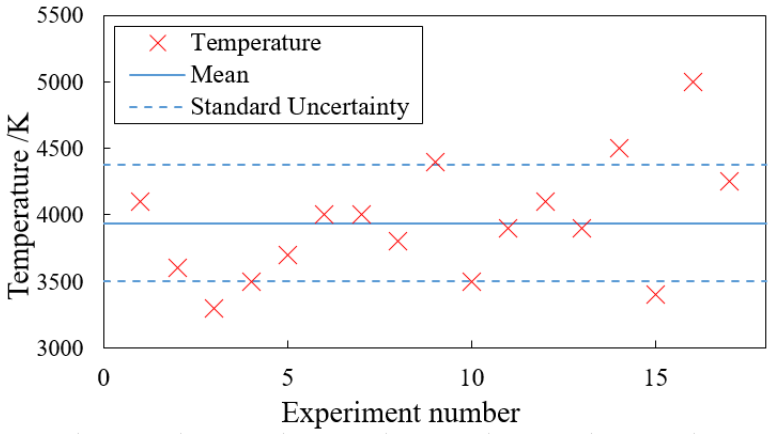

Fig. 2.18 All HMX temperatures, with mean (3900 K) and standard error (400 K) included on the graph. This assortment of measurements shows a range of more than 1000 K, indicating what a stochastic process the fallhammer initiation is.

These mean temperature was in agreement with the expected value of 4130 ± 70 K from considering the idealised chemical reaction (section 1.2.6). In fallhammer deflagration it was likely that this idealised reaction did not always occur, and therefore a lower temperature may be expected. However, as the intensity of a blackbody is dependent on the fourth power of its temperature, high temperatures have more light emission and therefore will preferentially show. So these blackbody measurements were measuring the maximum temperature reached, rather than the bulk average across the reaction, which would belong to the higher temperatures associated with the more idealised reactions.

The other complication is that, as this was measured on a single-shot spectrometer, it does not take any time evolution into account. There is no guarantee that these temperatures are constant throughout the reaction, or reflect the main temperature present. Therefore, another

diagnostic was needed to independently measure the light temperature with appropriate time resolution (section 2.6).

2.5.3 Addition of sodium

As the main spectral peak was likely due to sodium, a set of experiments adding sodium – in the form of ground-up table salt (NaCl) – to HMX in the deflagration setup was conducted. This was an attempt to force a peak, rather than rely on the negligible sodium present in HMX.

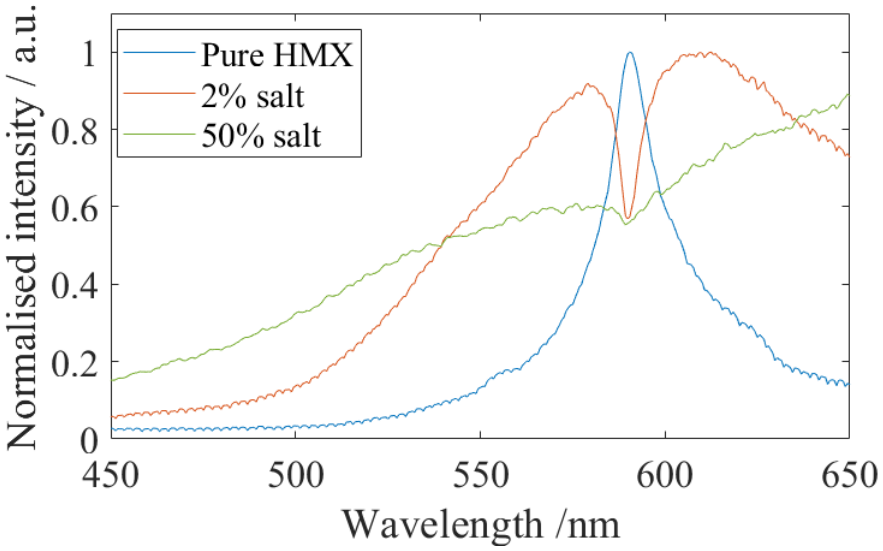

Fig. 2.19 The deflagration spectrum with increasing salt addition by volume. With increasing salt, the reaction became a thermal burn, leading a loss of emission spectral features. A clear absorption peak was also seen due to the sodium that was added around the HMX crystal rather than present in the hotspots inside the HMX. The spectrum intensity have been normalised so the shape could be more easily compared.

However, this sodium was not embedded in the HMX crystals, and so was not present at the hotspot initiation. Instead of being excited by the heat and emitting photons, it behaved like cold atoms, absorbing reaction light at 589 nm (figure 2.19). Crucially, the sodium atoms had to be colder than the reaction light (4000 K) to show absorption, but also had to be in a vapour state as solid sodium does not have these absorption lines. Therefore, the atoms had to be above the sodium vaporisation temperature of 1156 K. This implies that any 'surface' impurity that is not found within the crystal structure, and therefore not present in the hotspots, will be seen as absorption rather than emission in the optical spectrum.

As more salt was added it behaved like a fuel, leading to a longer reaction and a more blackbody spectrum, as the reaction became less 'energetic' and more of a hot burn. In this way, it is suggested that deflagration experiments where an energetic material is mixed with a binder, or is not near 100 % purity, may lead to the spectral features being destroyed as the observed light is no longer from the actual energetic reaction, but from the heat radiated from the solid products present in the reaction.

2.6 Time-resolved pyrometry

As commented above, there was no time-resolution present on the spectrometer measurements. Adding in a time-resolved pyrometer onto the setup would not only allow the temperature evolution of the deflagration reaction to be observed, but would also provide another independent temperature measurement of the system, which would be able to support – or question – the spectrometer results.

To this end, a 4-channel time-resolved pyrometer was designed and built. The building and assembling of the apparatus was carried out by Dan Braund [112], an undergraduate summer intern, who also wrote the code used to interpret the output.

The apparatus was designed with multiple aims. It firstly had to be simple and not too expensive, so it could be easily and quickly built. To achieve reliable temperature measurements, a sufficient number of intensity readings at different wavelengths would have to be taken so that a greybody fit could be applied to the data. The minimum number of wavelengths needed for this fit is, trivially, two. A better fit can be achieved with more channels, at the cost of lower levels of light collection and greater experimental complexity. As a compromise, a four channel pyrometer was envisioned.

This relationship between temperature and intensity (power) does, theoretically, allow temperature measurement based on intensity only (a one channel pyrometer). However, this has the difficulty of distinguishing between higher intensity because the source is hotter, or whether there are more emitters present. Therefore, this method was not used; as the number of emitters (total intensity of light) was very variable as the reaction progressed.

Lastly, this apparatus was designed to be able to be used on multiple different reaction regimes – so time-resolution could be applied to other deflagration and detonation reactions. Portability would therefore be useful, as well as the ability to include neutral density filters in the case of significantly brighter emission events.

The spectral contributions observed in deflagration (figure 2.17) limit the potential wavelength channels available to be used in optical pyrometry, as a significant portion of wavelengths contained a mix of greybody and spectral emissions. These spectral contributions

would likely vary in different regimes, as would the position of the peak temperature expected to measure. Therefore, the ability to pick the wavelengths of the fit – the filters used – was invaluable to building the apparatus, so it could be tailored to avoid spectral peaks whilst ensuring a high enough intensity was recorded.

2.6.1 Equipment

In summary, the aim was to produce a simple, fast and portable pyrometer which had the option to avoid certain wavelengths that may contain spectral features, and therefore be able to select and change which wavelength channels to use.

Shown in figure 2.20 is a simplified diagram of the setup, with a single fibre optic used to couple the light into the pyrometer. This was then transferred into a single connector, containing the core of four fibre optics [ThorLabs BF44LS01], splitting the input into four roughly equal contributions. This approach eliminated the use of beamsplitters, and in practice led to more light intensity by virtue of having fewer components, and therefore, less imperfect interfaces that lost light.

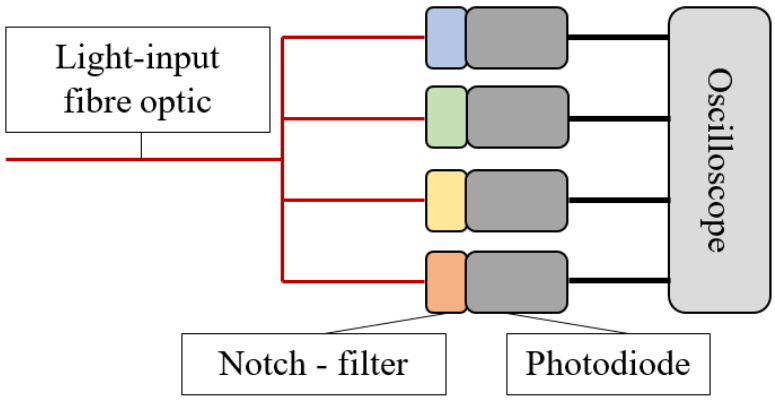

Fig. 2.20 Schematic of the pyrometer used. Fibre optics (red lines) connect the light input to four photodiodes, covered with a notch wavelength filter. The photodiodes are then connected to an oscilloscope, from where the traces are seen and retrieved.

Each of the ends of this fibre optic was connected to an amplified fast photodiode [ThorLabs PDA10A2] capable of reaching the time resolution required (with a rise time of 2.3 ns). In order to choose wavelength channels, removable notch filters were fitted in front of the photodiodes [ThorLabs FBXXX-40]. These filters had an individual wavelength

width of 40 nm in order to guarantee enough light intensity was collected, as well as having wavelength specific collimators in kinematic mounts to focus the light onto the photodiode.

In order to specify the pyrometer to fallhammer deflagration, the previous spectrometer measurements were vital. From this the spectral regions to avoid are known, as well as providing an expected temperature of 4000 K – high enough that the visible wavelength region would contain enough light intensity for a fit.

The pyrometer was calibrated in the same way as the spectrometer; measuring a verified blackbody source and using the output to form a ratio that would account for each sensitivity present in the components.

2.6.2 Results

Previous single-shot greybody fits to gauge the temperature were performed in the 400 – 500 nm region. Preliminary measurements also revealed that the likely potassium (770 nm) emission was just as intense, if not more so, than the sodium emission. As it was at a longer wavelength than normally measured with the spectrometer, this was not immediately apparent. However, inclusions of 'red' wavelength channels of 750 nm, as well as 700 nm, led to significantly increased signals in these channels and poorly fitting greybody distributions and were therefore discounted.

Accordingly, three channels at 400, 450 and 500 nm were chosen for the fallhammer deflagration experiments. The three traces from the oscilloscope were then fitted to a greybody at each time-step, allowing the temperature evolution, and overall light intensity, to be observed as a function of time (figure 2.21). The fit was only reliable once enough light was received by the photodiodes, so the measured temperature was accurate for the duration of the reaction, and loses this accuracy when the light emission returns to low signals.

Figure 2.22 shows typical temperature evolution along with intensity for two deflagration measurements. The temperature rose sharply with the main light intensity, stayed roughly constant through the high intensity region, and then (for some measurements) started to slightly fall when the light intensity falls.

Similar to the time-integrated measurements, these show a deflagration temperature for the main reaction period of 4000 ± 200 K, with the uncertainty as the standard deviation between experiments, as before. This independent confirmation of the temperature, along with the fact the value stays constant for the main period of the reaction, informs that the spectrometer was a reasonable apparatus to use for temperature measurements, despite having no time-resolution.

The roughly constant temperature gives evidence that the deflagration conditions were not rapidly changing throughout the *circa* 20 μs of reaction, despite the variations in light

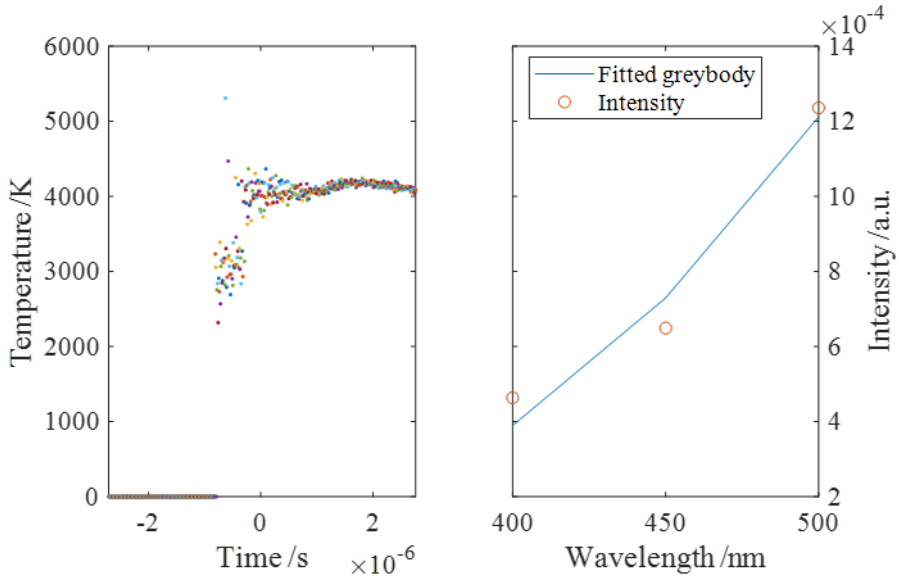

Fig. 2.21 The fitting program in the middle of a run. The time evolution of temperature observed (left) was built by fitting a greybody at each time step to the three wavelengths (right), giving the temperature at that time.

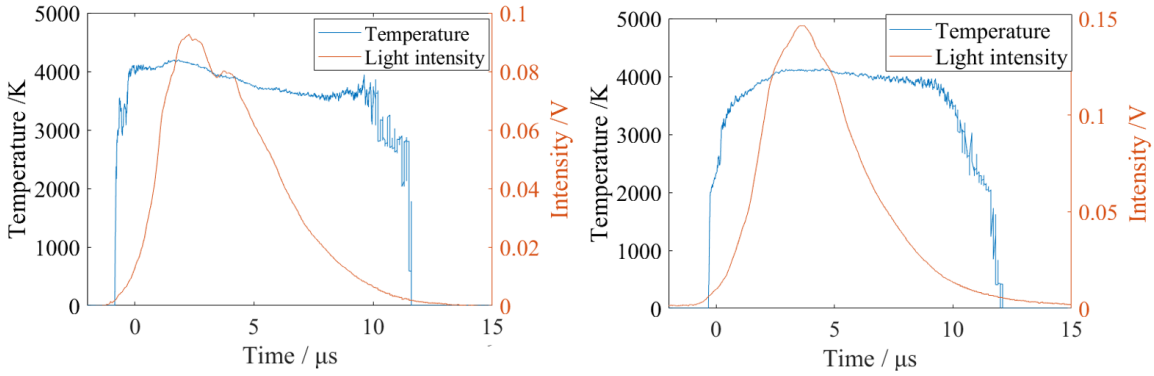

Fig. 2.22 Two typical deflagration temperature measurements with the above-mentioned optical pyrometer, overlaid with the period of light emission. The temperature rises sharply with light intensity and stays roughly constant with the main period of light emission. For the left figure, the temperature then starts to fall as the intensity falls, whereas for the right figure, it stays constant throughout.

intensity. The intensity increase was due to the number of emitters increasing at a fixed temperature, and was not due to the rising temperature of a fixed number of emitters.

This constant temperature also indicated that spectral features were not contributing to the measurement. As can be seen, the shape of the total light intensity did not affect the temperature measured, as peaks can often be seen in the light intensity, which did not have any effect on the pyrometer output. When, for interests' sake, a wavelength channel with

overlap to the spectral features was included for pyrometry measurements, the temperature erroneously followed the shape of the light intensity (similar to what one would expect from a one-channel pyrometer), due to the large systematic errors in the measurements.

2.7 Applying diagnostic technique to a traditional sensitivity test

The BAM fallhammer used in this research was developed as a commercial tool in order to measure the impact sensitivity of an energetic material, specifically following the procedure outlined by the EMTAP manual [109]. The impact sensitivity is determined using the gravitational potential energy of the mass used by the fallhammer, and the height it was dropped from. In the above research, a simple modification of a strain gauge on the steel anvils was developed, allowing the pressure-history of the impact to be determined. By conducting a normal sensitivity test using the BAM fallhammer with the added strain gauge, the usefulness of such an addition could be observed; whether the new data provided with the 'traditional' test would be helpful in furthering the knowledge of impact initiation.

Compared to the procedure detailed above, there were a few differences with the method undertaken. Firstly, the test had to comply with the standard. This meant 40 mm^3 of material would be used for each drop. Then, with the mass staying constant, the height of the drop was varied. The aim was to take multiple measurements from a range of heights, from low enough that no reaction was seen, to high enough that it was almost guaranteed each time. This would build dataset of the number of 'go' reactions at each height. In order to convert this into a continuous probability against drop-energy, Probit analysis was used (detailed below).

Secondly, RDX was used instead of HMX. Multiple drops had to be achieved at each height, each using 40 mm^3 of material, which would lead to a large total requirement of the material. As this test was an application of the developed techniques, and not directly comparable to any other measurements made in this research, it was more convenient to use RDX than the finite supply of HMX available.

The reaction was detected, as before, from the light emission. For interests' sake, the light was directly connected to the pyrometer in order to investigate whether any significant effect on the temperature could be observed during the test.

Previous research by Storm *et al* suggested an impact sensitivity of 5.6 ± 0.8 J in RDX [111]. Therefore, with a 1 kg mass, heights of 30 cm to 90 cm in intervals of 10 were chosen to provide a sufficient range for the data collected.

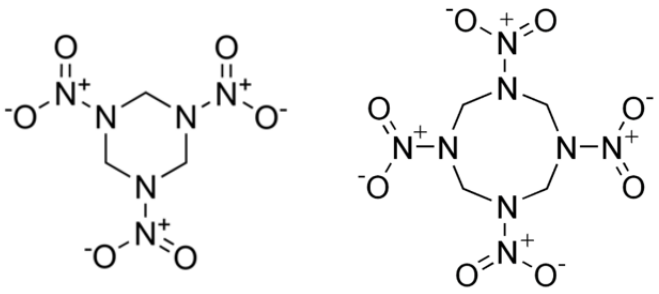

Fig. 2.23 RDX molecule (left) compared to HMX (right). As can be seen, these have a very similar structure, with RDX possessing a 3-nitrogen ring, rather than the 4-nitrogen ring present in HMX.

2.7.1 Results

Probit energy analysis

For each height chosen, a finite number of drops were conducted. The outcome of each drop was binary; either the reaction occured, or it did not. Therefore, at each height, a probability of reaction could be calculated from the number of 'go' reactions over the total times the experiment was repeated, as shown in table 2.1. Increasing the amount of drops at each height would increase the accuracy of this calculated probability, however it would also consume more time and material. A similar concern was that only a finite number of heights could be investigated. Therefore, from this dataset of calculated probabilities at set impact energies, a continuous probability distribution of the 'true' probability of reaction against the drop-energy was required.

Height /cm	Energy /J	Probability of reaction
30	2.9	0
40	3.9	0.17
50	4.9	0.33
60	5.9	0.67
70	6.9	0.80
80	7.8	0.83
90	8.8	1.0

Table 2.1 The heights, corresponding gravitational potential energy, and probability of reaction for a 1 kg mass falling on the RDX sample.

Probit analysis is a technique which, assuming normal statistics, maps discrete probabilities into a continuous normal cumulative distribution [113]. First, the probability calculated

was transformed using the inverse of the standard normal cumulative distribution that corresponds with the given probability, excluding the values of 0 and 1 for the heights of 30 and 90 cm respectively. These inverse probabilities were then plotted against the logarithm of the drop-energy shown in figure 2.24.

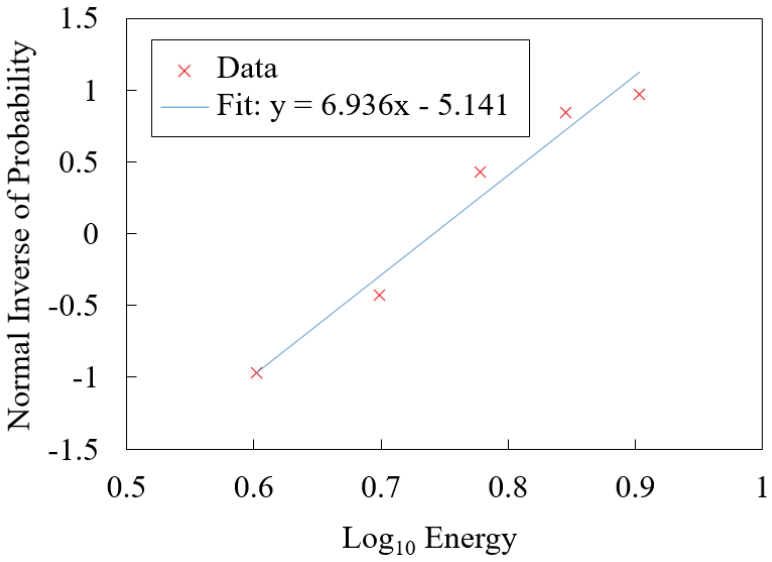

Fig. 2.24 The inverse probabilities plotted against the logarithm of the drop energies. As probabilites of 0 and 1 did not return a value, these values were excluded to form the fit. The data falls on a straight line, which both indicates that the normal cumulative probability distribution is appropriate to model the data, with the fit constants of said probability provided by the gradient and intercept of the regression line.

As can be seen, the points form a straight line, which indicates the underlying probability distribution follows normal statistics, and therefore Probit analysis is the correct choice to use to determine the continuous distribution. Therefore, the fit constants from the regression of this data were used to return the normal cumulative probability distribution that corresponds to the probabilities provided, which could then be plotted against the data collected (figure 2.25).

This distribution gives a full indication of the probability of reaction given an impact energy (drop-height). However, it does not provide a clear 'activation' energy, and the impact sensitivity is often taken as the value at which 50 % of the drops would be expected to react. In the this case, the 50 % value corresponds to an energy of 5.5 $\pm$ 0.4 J.

This sensitivity was in very good agreement with the value reported by Storm *et al* of 5.6 $\pm$ 0.8 J [111]. However, the manufacturer Eurenco also provides a sensitivity of 7.5 J [110] that is in disagreement with both. Given different impact apparatus, analysis of results and RDX batches, a range of different answers is unfortunately common.

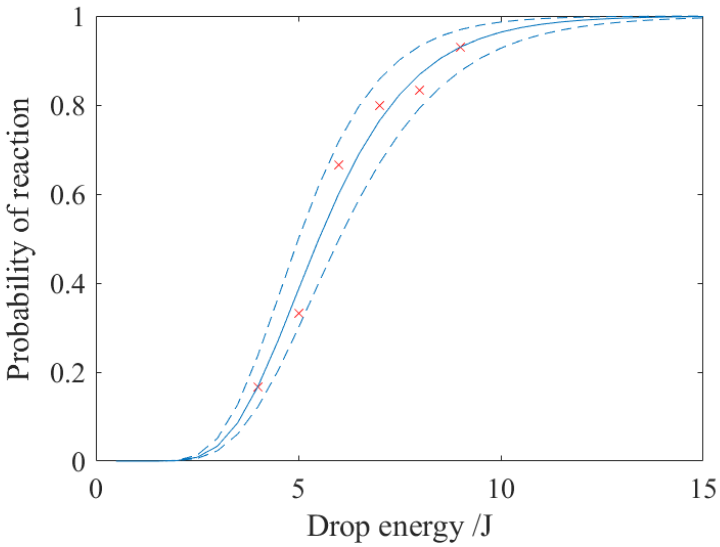

Fig. 2.25 The probability distribution (with 95% confidence limits) for the drop energies. Not enough repeat drops were conducted at 90 cm to observe a 'no-go' reaction, and so the probability of 0.93 - calculated from the fit in figure 2.23 - was included instead.

Gauge analysis

From the pressure-history provided by the gauge and the light intensity trace, the pressure at initiation can be measured. Figure 2.26 details the pressures at which initiation occured for the different drop heights.

As can be observed from the data, for every reaction the initiating pressure was above 0.41 ± 0.02 GPa, implying the existence of a threshold to reaction occuring at this value. By extrapolating the maximum pressures measured at each height (taken from the pressure-history for no reaction drops), this would imply that for heights below 33 cm (for a 1 kg mass) the falling mass does not provide a high enough force to initiate the reaction, and so no reaction would ever be observed for heights below 33 cm, or 3.2 J. This is contradictory to the traditional energy analysis, which assumes a small, but finite, probability of reactions occuring at low heights (figure 2.25).

The pressure of initiaiton also is not the same for each drop - instead varying between the threshold and the maximum possible pressure in the trace. This indicates that another threshold is present - that pressure is not the only variable upon which the reaction is dependent. One candidate for this could also be the energy absorbed.

The energy imparted by the pulse can be calculated by considering the integral of the pressure-time curve present. From the gauge-calibration before, it could be observed that the energy present from the falling weight ($\frac{1}{2}mv^2$) would be proportional to the integral of the

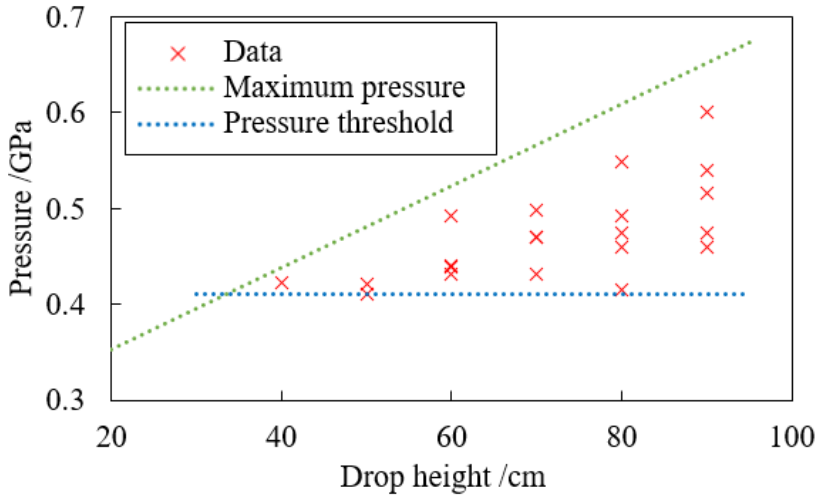

Fig. 2.26 The measured pressure for initiation against drop height. The maximum possible pressure in the pulse is shown in green, with the observed threshold - the minimum pressure observed for reaction - shown in blue. From the intersection of these lines, it implicates that no reaction will ever be observed for a 1 kg mass dropping from below 33 cm.

voltage trace squared (eq. 2.5). Taking this integral and plotting against the impact energy yielded a straight line (figure 2.27), the gradient of which could be used as the constant to calculate the total energy absorbed at the point of reaction.

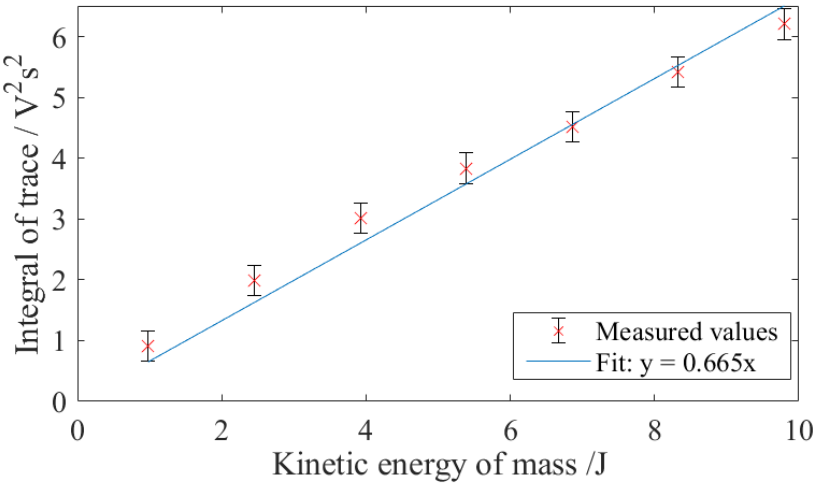

Fig. 2.27 The squared integral had a linear relationship with the kinetic energy imparted. The gradient of this relationship could then be used to calculate the corresponding energy absorbed by the time of reaction.

However, there are a number of issues associated with such a simple approach. Most importantly, there is no mechanism for energy loss - it assumes that all the energy present is represented in the gauge trace, and that the energetic material will be absorbing the provided energy. However, other loss mechanisms may be present, such as heating the anvils, or deformation of the equipment.

Consider, for example, a hypothetical experiment where the reaction did not occur. Utilising the method above and calculating the whole area under the curve would result in a calculation that all the energy provided by the falling weight had been absorbed by the sample. Such a conclusion would be unphysical. With the weight falling on the sample, the energy calculation represents the stored elastic energy of the material as it is compressed, which would then be released in tension when the weight rebounds off the anvil. Therefore, it should not be assumed that this energy would be completely absorbed by the energetic sample in order to react.

Despite these problems in the method, a rough energy estimate could still be achieved, with figure 2.28 showing the results of the above energy considerations on the RDX samples.

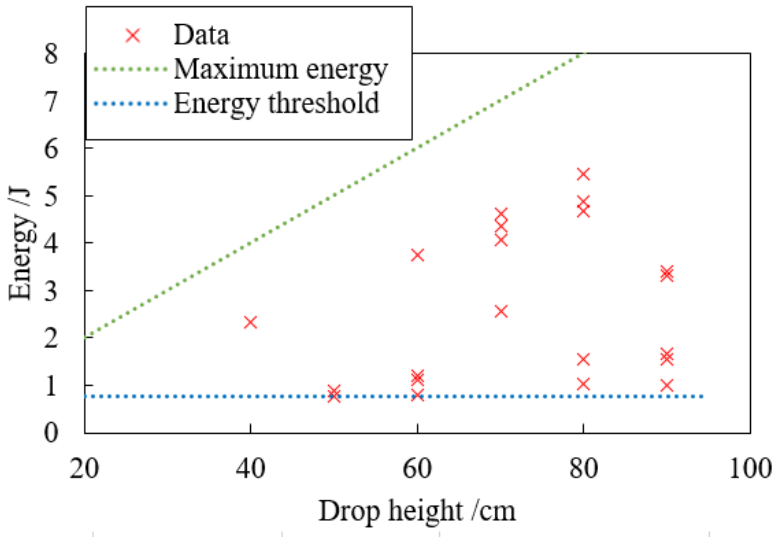

Fig. 2.28 The maximum possible energy available for initiation against drop height. Treating the system in an identical fashion to the pressure, the maximum possible energy delivered by the pulse is shown in green. The inability to distinguish other energy in the system, and therefore extract the exact energy absorbed by the material leads to difficulties in using this method for calculating energy sensitivity. For example, the higher energies for each drop correspond to initiation on ring-down, whereas the lower energy reactions occurred nearer the start of the pulse, leading to a large range of values. As the energy calculated was dependent on the pressure, a minimum threshold was also observed.

The energies recorded with the heights show some similarities with the pressure results. As the drop-height increases, the increased force on the anvils leads to higher possible energies. However, at all heights a lower bound of 0.76 ± 0.1 J is also present. This would be expected, as the energy is calculated from the pressure, and so these are linked variables.

The problems associated with calculating the energy in this fashion could also be observed. As discussed, integrating the curve only provides a measurement of the maximum possible total energy in the system, and not the amount actually absorbed by the material. When the reaction occurred on 'ring-up' of the anvils, the integral would return a lower energy value compared to when the reaction occurred at similar pressures on the 'ring-down'. Figure 2.29 shows these two behaviours, as observed from supposedly identical experiments, from the mass-drop height of 80 cm.

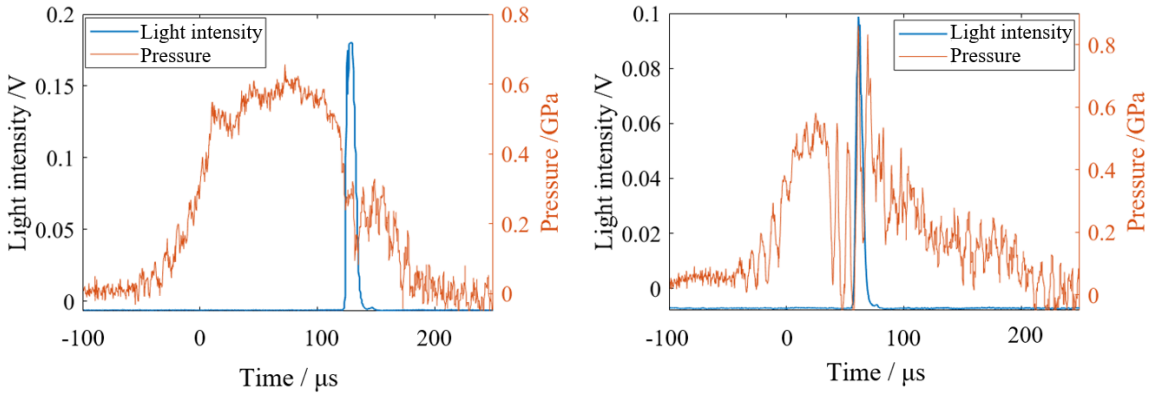

Fig. 2.29 Example pressure-history traces for two drops from a height of 80 cm. Both experiments had identical procedure and method, and initiated a reaction, however the histories are very different. The trace on the left shows a much smoother ring-up, and the reaction occuring on the ring-down slope, accompanied by a moderate pressure drop. Occuring on ring-down, this led to a large possible energy absorption. Whereas the trace on the right shows a much more oscillating pressure, with a drop down to zero just before the main light emission on ring-up, and then a pressure spike during the period of main reaction. For the second case, the drop in pressure was never observed for experiments that did not initiate, and so the pressure recorded for initation was taken before the drop occured.

Both of these reactions initiate at almost exactly the same pressure. However, without a reliable method of accounting for all the energy of the system, little could be said about the absorbed energy of each reaction. As observed for the HMX reactions in section 2.5.1, the initiation of RDX always occurred on the ringing of the pressure, and never on the maximum pressure. This behaviour suggests a link between the likelihood of the reaction and the shape of the pressure pulse – rather than just an absolute value.

Another interesting observation was the shape of the pressure history. As seen in figure 2.29, the shape of the increasing pressure was different, with a much smoother ring-up for the experiment with the later reaction. Other differences can be seen, such as a pressure drop at the time of reaction for some experiments but not for others. From figure 2.29, one trace shows a moderate drop in pressure for the reaction, which then stays constant, whereas the second shows a large oscillating pressure behaviour, dropping immediately before the reaction and then increasing again during the period of light emission. These variations were present in all drops at all heights - there was no 'typical' pressure trace for the RDX sample having a mass dropped on it.

There are multiple reasons for this level of variation - afterall, the total fallhammer setup is a complicated system. Whilst the same amount of RDX was used each time, the compaction and deformation of the material was not controlled, with the chance of some crystals slipping between the anvil and the guiding cylinder. Also the guiding cylinder tolerance was discovered to have an effect. If the fit of the cylinder was too tight, it would still allow the anvils through it without trouble when clean, however would more often lead to the anvils becoming stuck in the cylinder during experiments; therefore some of the measured pressure would be applied to the cylinder and anvil setup rather than the explosive. Added to this was the previous point that the energy loss mechanisms are not known, and therefore different amounts of energy could be absorbed by the sample in each experiment, with no method of explicity measuring this amount. All these features would add to give the different pressure-history traces observed each reaction.

It is likely that this wide variation in the pressure-history was leading to the stochastic nature of the fallhammer tests, and the wide sigmoidal curve of the probability of reaction at different heights. Therefore, controlling this initiating impact force, and the pressure-history of the sample, may be more important to understanding initiation, as it would lead to repeatable experiments being managed. In addition, using apparatus that accounts for all the energy of the system - both that applied to the sample and also released - would allow a value of the energy absorbed by the sample to be better calculated. Then, a true, reliable, sensitivity value could be calculated rather than simply taking the drop-energy or even the pressure-threshold.

In a similar manner, the recorded temperatures were very varied for all heights, pressures and energies, with no discernable pattern. For interest, the temperature measurements were similar to HMX, with an average temperature of 3900 $\pm$ 300 K and a range of 1000 K.

2.7.2 Summary

A standard impact sensitivity test was run on RDX according to EMTAP [109] guidelines, with the addition of a strain gauge. From the probability of reaction at multiple drop-heights, the traditional sigmoidal 's'-curve of chance of reaction at different drop energies was constructed using Probit analysis. This allowed the energy for which there was a 50 % chance of reaction to be calculated as 5.5 ± 0.3 J.

The strain-gauge measurements allowed a pressure threshold of 0.41 ± 0.02 GPa to be observed across the drop-heights used, which led to the conclusion that for low enough drop heights - below 33 cm (3.2 J) - a reaction would never be seen. However, from the behaviour of where the reaction occurs on the pressure curve, there was clearly more than just a pressure or energy threshold that needed to be overcome. Multiple reactions initiated on the downslope of the pressure curve, after a period of peak pressure and energy, which remains a curious feature.

The stochastic nature of the fallhammer could be due to the stochastic nature of the pressure-histories observed. Therefore, with a more controlled system, and a repeatable impact insult, it could be possible to lessen these large variations.

2.8 Conclusions for fallhammer deflagration

The impact initiated deflagration optical emission spectrum in HMX was measured, showing a mix of spectral and greybody features. Away from the spectral features, the greybody emission follows the Planck distribution, allowing the temperature of HMX to be determined as 3900 ± 400 K. Despite being very stochastic, this reflects the temperature expected from a theoretical calculation of the chemical energy released in the reaction.

Independent pyrometry measurements verify the fallhammer deflagration temperature of 4000 ± 200 K with a three-channel pyrometer measuring the intensity at 400, 450 and 500 nm. These measurements showed a roughly constant temperature throughout the main light emission period.

The pressure in the anvils was in agreement with previous similar measurements, however it did not show a drop of pressure when the reaction occurred, suggesting that the pressure of the reaction was in equilibration with the initiation mechanical pressure. The high pressure, along with the temperature, led to the expected broadening of the sodium spectral emission across a significant portion of the wavelength spectrum. This sodium peak had also shifted by a few nanometers, possibly due to the high pressure reaction.

The inclusion of a strain gauge could also be applied to investigate the behaviour of initiation in a standard fallhammer sensitivty test. Initiation of RDX showed similar behaviour

to the HMX, initiating on the ring-up or ring-down of the pressure. The reaction occuring only at pressures greater than 0.41 ± 0.02 GPa contradicts fitting a sigmoidal probability of reaction curve to the energy of initiation, as this threshold implies no reaction will ever occur for impacts below a certain energy.

2.8.1 Further research

The reaction was investigated with both a high spatial resolution spectrometer, and a time-resolved pyrometer. The inclusion of a streak spectrometer would allow the whole spectrum to be time resolved, allowing a better view of the evolution of the reaction and the light emitted. This line of research is presented in Chapter 4.

Deflagration is not a well-defined reaction, and therefore has multiple possible conditions. The large variations in the pressure-history and impact of the fallhamer, even between 'identical' experiments, also likely affected the repeatability of the results gained. In the next chapter, another initiation method which was more repeatable was investigated using the same diagnostics to discover what was consistent between deflagration reactions, and what would be different.

The spectral shift was also further investigated in Chapter 4, with a closer examination of the dependence of the red-shift on pressure and temperature.

Chapter 3

Deflagration in a Split Hopkinson Pressure Bar

3.1 Introduction

The previous chapter discussed deflagration initiation of HMX by use of a falling weight – a technique which is common for sensitivity tests. The fallhammer imparts pressures of order 1 GPa over a timescale of a few hundred microseconds. Such mechanical properties are also able to be achieved in a Split Hopkinson Pressure Bar (SHPB), and so this apparatus should theoretically be able to initiate deflagration in the same material.

The aim was to, firstly, investigate the feasibility of such an ignition in HMX as this would – at the time of the experiment – report the first instance of using such an apparatus to purposely attempt and investigate ignition. A SHPB has been used previously to investigate HMX, however the focus was on the high strain rate mechanical properties [114–116], and not on initiating a deflagration reaction.

Utilising a SHPB would provide many advantages other than just testing to see if it can initiate HMX. By providing another route to deflagration, it would allow comparisons to be made with the fallhammer results, detailing the extent to which the apparatus used to cause the reaction can influence the measured properties. This would provide more detail on the process of deflagration, and the different properties it can create. When handling energetic materials, accidental initiation is unlikely to be due to conditions identical to those in a fallhammer (with a weight falling on the material placed between two hardened steel anvils), and so investigating different initaition methods would provide more detail on the range of deflagration reactions, allowing more accurate simulation of different scenarios, leading to a better understanding of safely handling these materials.

The SHPB also has other advantages over the fallhammer apparatus, as it is a piece of equipment designed for measuring material properties of a range of different samples, rather than just testing sensitivities. The pressure applied to the sample can be more readily controlled, and quantitative descriptions of the pressure imparted, reflected and transmitted from the sample can be measured. This would allow the pressure-density history to be known, as well as providing a method to calculate the elastic energy absorbed by the sample before initiation. In summary, it is a piece of apparatus that was designed for testing material properties, and therefore is a more controlled, and more diagnostic tool than the fallhammer was designed to be.

3.2 Equipment

3.2.1 Split Hopkinson pressure bar

The Hopkinson Pressure bar, named after Bertram Hopkinson who first published papers on the system in 1914, was devised in order to measure high strain-rate properties of the detonation of gun-cotton [117]. Later, he experimented with the pressure produced by firing a rifle bullet at the apparatus [118]. After his death in 1914, the Hopkinson bar was then reviewed by Landon and Quinney [119] in 1923, and brought back into interest in the United Kingdom by the second world war. Taylor [120] and Kolsky [121] both used it to investigate the high rate mechanical properties of materials, and it has continued to be a popular piece of equipment to this day for such testing and experimentation [122]. This current research brings the Hopkinson bar back to its roots in energetics, but focused on initiation.

The SHPB investigates the high strain rate properties of a sample. This is achieved using a series of co-axial bars; the striker, input, and output bar and the momentum trap (figure 3.1).

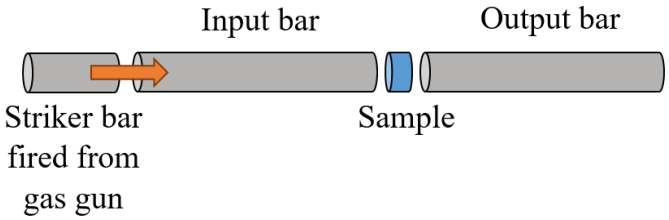

Fig. 3.1 Diagram of the components of a SHPB apparatus, not to scale. In the experiments described below, a 70 mm striker bar was used in conjunction with 240 mm input and output bars and *circa* 300 μm HMX sample. The diameter for all bars (and sample) was 12.7 mm.

A gas gun fires the striker bar at the input bar, launching a pressure wave which travels down the input bar and is incident on the sample. The sample in turn hits the output bar, which then hits the momentum trap. With bars constructed of the same material, the impedance mismatch between the different bars is minimal. Therefore, the system behaves like a Newton's cradle, with the pressure wave travelling through the bars (and sample), until it reaches the momentum trap, which travels away from the bars. If no sample is inserted, the pressure wave is fully transmitted (no reflection) due to the matched impedance.

The velocity of the striker bar was measured by placing a light gate at the end of the gas gun barrel. The light gate consisted of two lasers a known distance apart, shining into a detector. The time between the first laser being cut off and the second was recorded, and from this the velocity of the bar could be known.

For the aim of initiating HMX, the properties in the SHPB were chosen to be similar to those present in the BAM fallhammer test. Based on the fallhammer pressure trace shown in Chapter 2, this led to the design of the SHPB to reach 1 GPa pressures, and a 100 μs duration of applied force. The shape of the pressure pulse in the SHPB would, however, take the form of a top-hat rather than the half-sine seen in the fallhammer.

Setup

The measured pressure on the sample - present in the input bar - is determined by the collision of the striker bar. Assuming that the bars have the same specific impedance, Z, then the pulse takes a top-hat shape, with the pressure amplitude equal to:

$$P = \frac{Zv}{2} \tag{3.1}$$

Where v is the velocity of the striker bar. The duration of this top-hat pulse, τ, is determined by the time it takes for the wave - travelling at the sound speed c - to travel the length of the striker bar and then reflect back again. So the duration is calculated as:

$$\tau = 2\frac{l_{striker}}{c} \tag{3.2}$$

Therefore, these two quantities can be controlled by both the material that the bars are made of (Z and c) as well as the dimensions of the striker bar and the velocity it is fired at.

Another material consideration was the yield strength. The SHPB was planned to reach a deflagration initiation pressure of order 1 GPa, and therefore the bars used had to still have elastic behaviour in this regime. Therefore, Maraging 350 steel alloy bars were chosen, as they had a yield strength of 2.4 GPa. These bars had a sound speed of 4882 m s^{-1}, and a specific impedance of 39483160 kg m^{-2} s^{-1}.

For these properties, to reach 1 GPa would require a velocity of the striker bar of *circa* 50 m s^{-1}, and to have this last for 100 μs would require a striker bar length of 240 mm. The initial length used was 150 mm, which was then lessened to 70 mm after initial experiments determined that longer durations for the pulses were not required, and the shorter length meant that less pressure in the gas gun was needed to reach the required velocities for high pressures in the bars. The input and output bars had lengths of 240 mm, and every bar had the same diameter of 12.7 mm.

With this setup, the initiation conditions in the SHPB were comparable to the fallhammer with two main differences. Firstly, that the speed of the striker bar was an order of magnitude larger, at 50 m s^{-1}, rather than the falling weight velocity of *circa* 3 m s^{-1}. Secondly, due to the impedance match of the bars, there would be no ringing, rather the pressure pulse would be a top-hat shape.

Energetic material

The same HMX as in the fallhammer was used, however a larger volume of 40 mm^3 was inserted, given both the larger diameter present in the SHPB and to ensure that initiation would occur. Being a horizontal system rather than vertical meant care had to be taken when loading the material into the sample area. To achieve this, a sleeve was made (figure 3.2) which fit over the sample loading area, so that HMX could be inserted, then the bars pushed together and turned so the material was evenly distributed.

This led to a thickness of HMX of *circa* 300 μm, measured with a traveling microscope, and therefore a volume (for 12.7 mm bar diameter) of *circa* 38 mm^3; close to the volume of HMX inserted by the measuring spoon. Therefore, the HMX was at a similar loose packed density to that observed in the fallhammer.

To capture the light, a hole was drilled in the sleeve and a PMMA core fibre optic was inserted (the same as used before). This was then moved over the point of initiation so that the fibre optic was planar to the reaction in the same way as for the fallhammer apparatus.

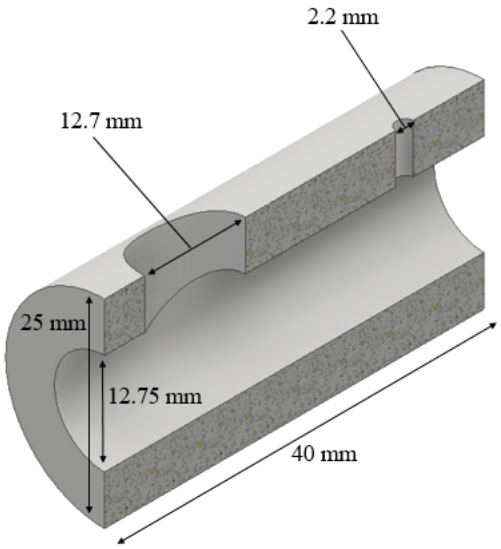

Fig. 3.2 Cross section view of the enclosing sleeve, with a tight fit to the bars to increase confinement (outer diameter of 25 mm and inner of 12.75 mm). The larger hole allowed HMX to be inserted between the bars, and then moved aside so that the fibre optic inserted into the smaller hole would be incident on the reaction.

Bar diagnostics

Measurement of the pressure pulse in the input and output bars was required. In the Cavendish SHPB, this is traditionally done using strain gauges [Kulite model AFP-500-090] attached to each bar. These would output the pressure experienced as a voltage, positive for compression and negative for tension. Therefore, a calibration measurement had to be carried out before the experiment so that the output could be converted into a pressure.

To achieve calibration, the striker bar was fired with increasing pressures, and therefore with greater velocities. These velocities, measured on the light gates, were then used, along with the bar impedance, to calculate the expected pressures in the bar (eq. 3.1). The voltage on the bar could then be plotted against the calculated pressures (figure 3.3), with the gradient of the graph providing the calibration constant.

The gauges were first calibrated up to relatively low pressures of order 0.1 GPa, showing an expected linear trend. This was due to the fact the gauges were not designed to withstand high gigapascal pressures, and were liable to breaking. However, increasing the force applied to 1 GPa showed that this linear calibration would not hold (figure 3.4), and that instead a cubic fit was more appropriate. As the following experiments would occur at gigapascal pressures, the assumption of linearity was therefore discarded and the gauges were calibrated to the higher stresses.

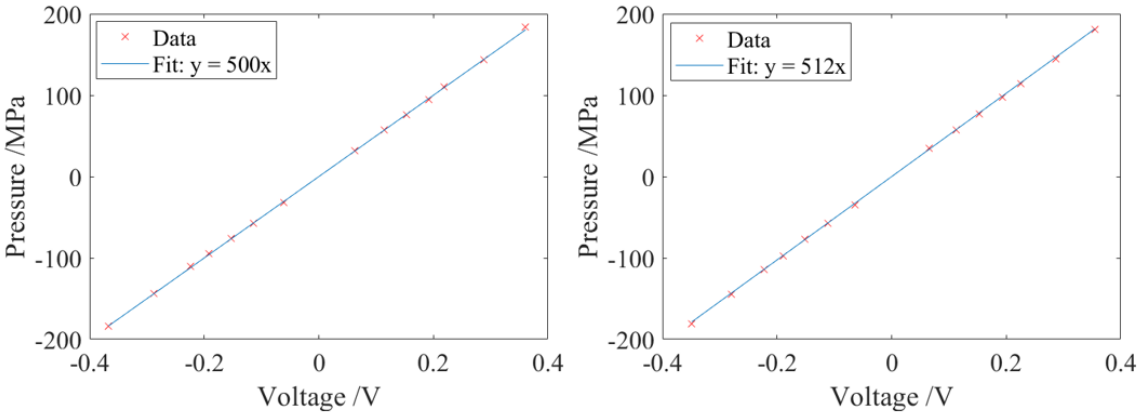

Fig. 3.3 Strain gauge calibration curve for the input (left) and output (right) bar. The gauges on each have slightly different properties, as evidenced by the different fits of the data.

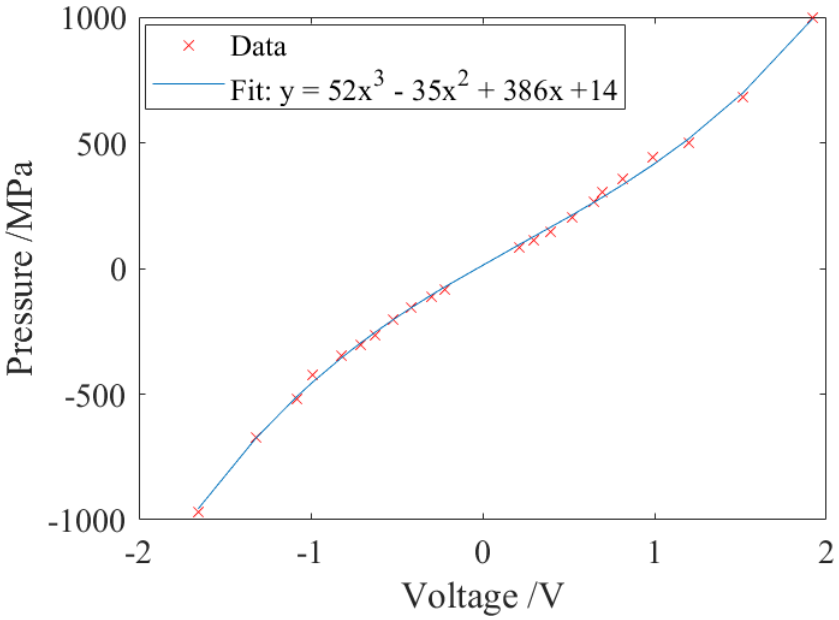

Fig. 3.4 An example of the calibration re-done to 1 GPa strains to show the non-linearity as the pressure increases.

.

A few experiments with the gauges were used, however there was a 50 % failure rate at these high pressures of *circa* 1 GPa, leading to the gauge needing to be replaced. The unreliability of the gauges meant another method of measuring the pressure in the bars was required which would be reliable under these velocities.

A method of calculating the pressure was measuring the particle speed of the associated pressure pulse in the input and output bars themselves. To this end, a Photon Doppler

Velocimeter (PDV) was used [123], and the speeds obtained directly converted into pressure using equation 3.1. The PDV diagnostic uses laser interferometry to measure the speeds. A 1550 nm laser is directed from a fibre optic at a reflective surface, leading to the reflected laser pulse being collected by the same fibre optic and interfering with the incident laser light. If the surface is moving, the reflected laser light will be Doppler shifted, and will therefore create a beat frequency waveform when it interferes with the incident light. This beat frequency is proportional to the speed of the surface normal to the directed laser light.

In order to make a measurement, the laser from the PDV fibre had to reflect from the moving object with a component parallel to the velocity, and be reflected back into the PDV. The bars were painted with retro-reflective paint in order to allow this reflection, and the PDV fibre optic was placed at a 30° angle to the bars. If placed completely parallel, there would be no reflection back into the PDV, and if placed normally no component of the laser would be parallel the velocity of the bars, and thus record no motion. 30° insured there was enough light reflected to be measured, as well as a high enough component of speed was measured.

A disadvantage of using the PDV was that it measured an absolute velocity, a scalar property. This meant that it was not possible to determine if the bars were in tension or compression, as could be achieved with the strain gauge.

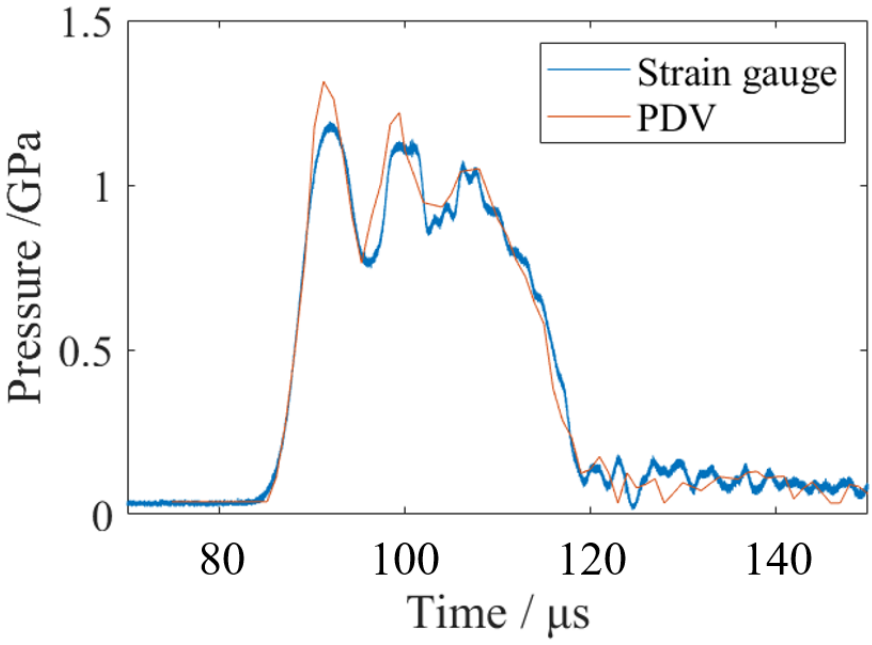

Fig. 3.5 Comparison of strain gauge measurements to PDV measurements – there is good agreement between these techniques in terms of overall pressure measured. However, the strain gauges have both positive and negative values, as well as more data and a smoother fit, providing more detail for the pressure pulse.

The pressure pulse measured by both the strain gauges and PDV (figure 3.5) could be compared to that measured for a fallhammer (figure 2.8). Where the fallhammer had a half-sine shape, the SHPB had a top-hat profile. The oscillations observed in this top-hat pulse were due to Pochammer-Cree dispersion – the wave speed is dependent on frequency, and so these sinusoidal oscillations are seen, especially in high-frequency/short time signals such as the ones measured in this experiment [124]. Pochammer-Cree dispersion is especially noticeable when many frequencies are present; such as in the case of a square wave which is composed of an infinite Fourier series. For a single frequency sine wave, these oscillations would not be present.

The pulses in the Hopkinson bar could also be shaped. For instance, a thin 500 μm copper shim inserted between the striker bar and the input would lead to a ramping wave shape (figure 3.6). Other shapes could also potentially be formed, such as using a spherically ended bar to achieve a half-sine pulse shape.

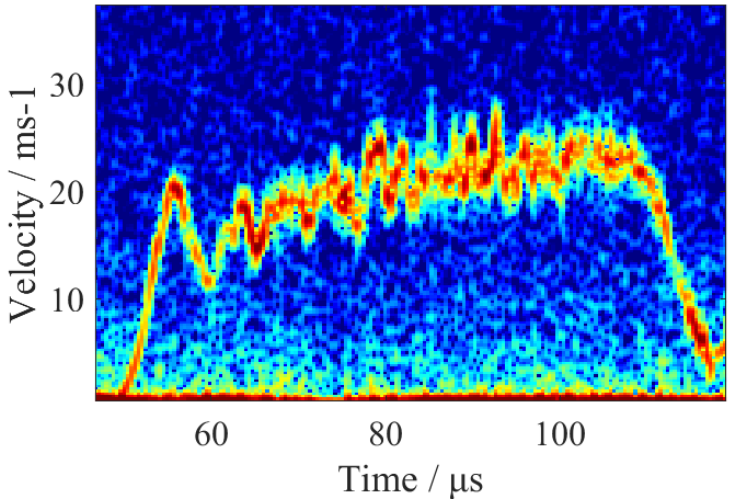

Fig. 3.6 An example of the raw PDV velocity data of the pressure pulse when a ramping pulse was used. A copper shim was inserted before the input bar, causing a rise in velocity 15 to 23 m s^{-1}.

Given that the fallhammer deflagration initiated on either ring-up or ring-down, this suggested that there was a degree of pathway dependence present. The ramping wave profile would allow conditions more similar to the ringing in the fallhammer to be observed, and to allow a test of whether there existed an absolute pressure threshold - initiation occurring at the same value, either on the ramping wave or the top-hat - or whether there was any pathway dependent behaviour, so that the initiation conditions were affected by the shape of the pulse.

Optical measurements

To allow for comparison between the different initiation regimes, exactly the same procedure was taken with the spectrometer. The fibre optic carried the light into the spectrometer and photodiode as detailed in Chapter 2, and was calibrated by measuring the known blackbody of the same calibrated lamp.

The first measurements were done using the spectrometer; once the emission spectrum was known, the pyrometer could then be used (section 2.6), selecting wavelengths that would not contain any spectral emissions.

3.2.2 Calibration of gas gun pressure with striker bar velocity

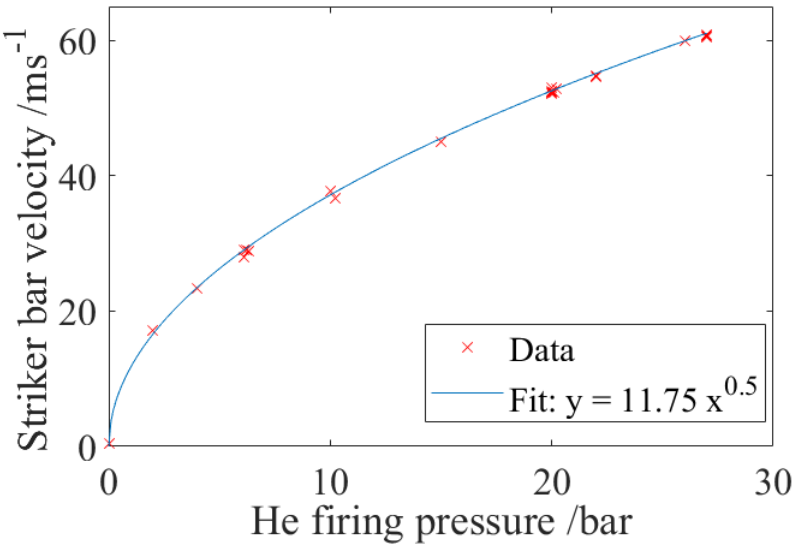

Fig. 3.7 The calibration curve of helium firing pressure against striker bar velocity, for a 150 mm length striker bar.

Compressed helium was used to launch the striker bar from the gas gun, with a controllable pressure. The aim was to calibrate the pressure in the gas gun with the striker bar velocity at the light gates. The calibration curve (figure 3.7) shows that the required speed for 1 GPa (*circa* 50 m s^{-1}) could be achieved at helium firing pressures of around 20 bar.

The above calibration was for the 150 mm striker bar length. The same calibration was also measured for the 70 mm length, which had the advantage of reaching the required velocity at a lower firing pressure, and thus could reach higher velocities more easily, at the cost of a reduced duration pulse.

3.3 Results

3.3.1 Mechanical

The Split Hopkinson Pressure Bar was able to initiate HMX at pressures above 1028 ± 18 MPa. In the event of a successful reaction, the material completely reacted and the emission light was clearly observed, both on the photodiode (figure 3.8) and also in person.

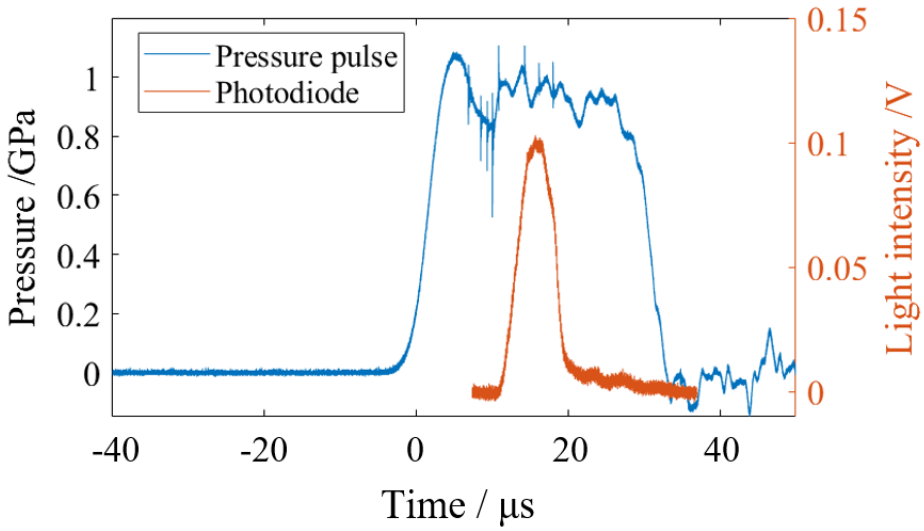

Fig. 3.8 Photodiode trace of reaction light emission against the pressure pulse from the bar impact in the sample.

The initiation success was dependent on the amplitude of the pressure pulse; as seen in figure 3.9, there was a clear threshold present at 1028 ± 18 MPa, with initiation achieved almost every time above this value, except for two outliers at *circa* 1040 MPa.

This measured pressure was almost double that observed in the fallhammer (at 600 MPa), the first evidence that measured impact sensitivity was dependent on the shape and rate of the applied pulse. The sensitivity graph also shows a very sharp step in comparison to the traditional energy sensitivities curves observed in fallhammer experiments – where, as shown in section 2.7.1, a sigmoidal curve is constructed as the probability of reaction gradually increases with energy [125, 126]. Whereas, the sudden success once the pressure increases above *circa* 1 GPa in the SHPB shows a much clearer threshold – indicating that the pressure of the impact in the SHPB is potentially a good measure of sensitivity.

In other words, deflagration in the SHPB displays much less stochastic behaviour compared to that seen with the fallhammer, having repeatable experiments with a calculable and more binary threshold of reaction.

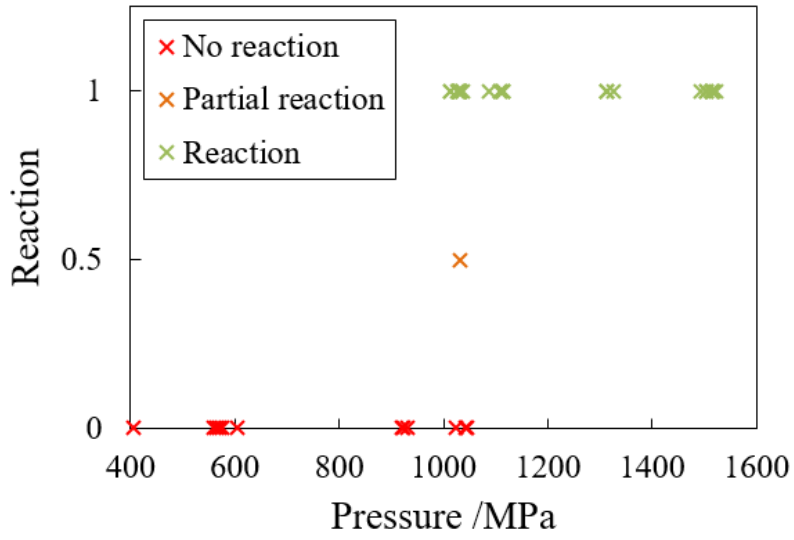

Fig. 3.9 Initiation success against bar pressure. There was one partial reaction, where not all the material reacted, as shown in orange. A clear threshold for reaction to occur can be seen at *circa* 1030 MPa.

The pressure values shown here were recorded from the PDV measurements, as the strain gauges broke for roughly half of the measurements. However, it was the glue holding them to the bars which led to them breaking, rather than the gauges themselves failing, so these could likely be used in future, if a different technique was used to attach them to the bars.

Ramping pressure

Given that there seemed to exist a clear pressure threshold, ramping pulses were used to investigate this behaviour. Curiously, against expectations, there was never an observed reaction that occurred for such a ramping pressure. Eight pulses, ramping through 0.7 GPa to 1.2 GPa as shown in figure 3.10 were performed, and no reaction ever detected.

Such a result was surprising, as it appeared inconsistent with the other measured behaviour seen by HMX. In particular, with the fallhammer it was observed that the reaction only occured on the rising or falling pressure wave, the opposite behaviour of what was witnessed in the SHPB. In previous experiments with a top-hat pulse, the reaction took *circa* 10 μs after the pressure pulse was incident to react (figure 3.8), and so the amount of time spent over the pressure threshold of 1.03 GPa in the ramping wave should have been enough to initiate, if a pressure threshold was all that was required.

Much like the fallhammer, this evidence against a pressure threshold implies a dependence on the shape of the pressure pulse, and other variables that were not controlled. For example,

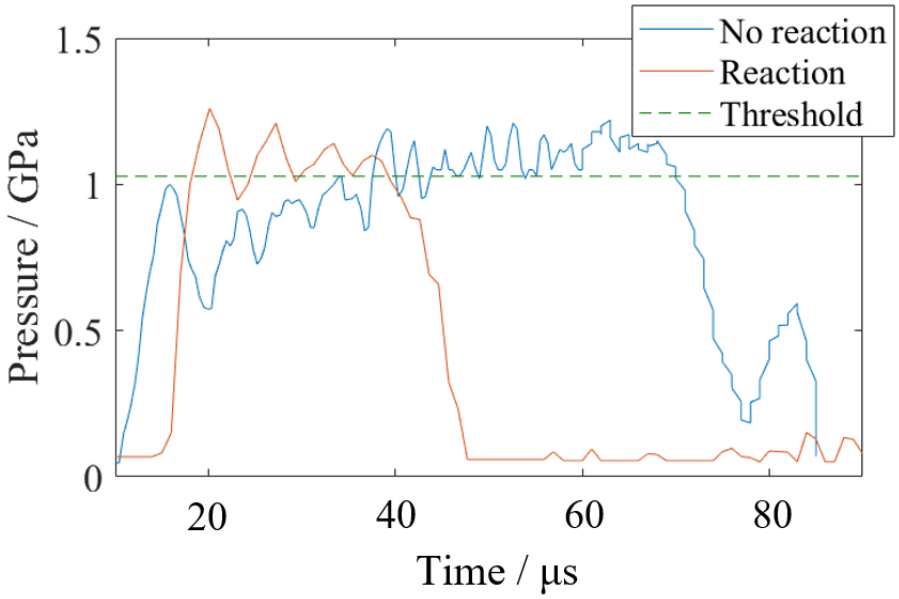

Fig. 3.10 The profile of the ramping pressure wave which did not lead to initiation, against a shorter constant top-hat profile that did. Even though the ramping pressure reaches the pressures that led to successful initiation, no reaction occurred.

there could also be an energy threshold as well as pressure to be overcome. Such a conclusion is obvious when considering the first results from SHPB initiation – that the pressure required was almost double that for the fallhammer, immediately showing that the pulse shape has some effect on the initiation conditions observed.

Energy considerations

The energy in the bars was measured by considering the area under the pressure pulse. However, it was imperative to know whether the pulse was in compression or tension to properly calculate this value, as it depended on force, F, a vector quantity. This meant the PDV traces could not be used, as they only recorded the speed of the bars, and not the velocity. Therefore, a few experiments were done with the strain gauges attached in order to correctly calculate the overall energy involved. As mentioned previously, these only had a 50 % chance of survival, and so were less efficient.

$$E = \int F dl = \int \frac{F^2}{ZA} dt \tag{3.3}$$

Where A is the cross-sectional area of the bars, and the speed $v = \frac{F}{ZA}$ could be positive (heading right) or negative (heading left). Therefore, to keep compression and tension, the energy equation was modified:

$$E = \int \frac{F \mid F \mid}{ZA} dt \tag{3.4}$$

The energy absorbed by the sample could be calculated by considering the energy in the original pulse, minus the sum of the transmitted and reflected waves (figure 3.11).

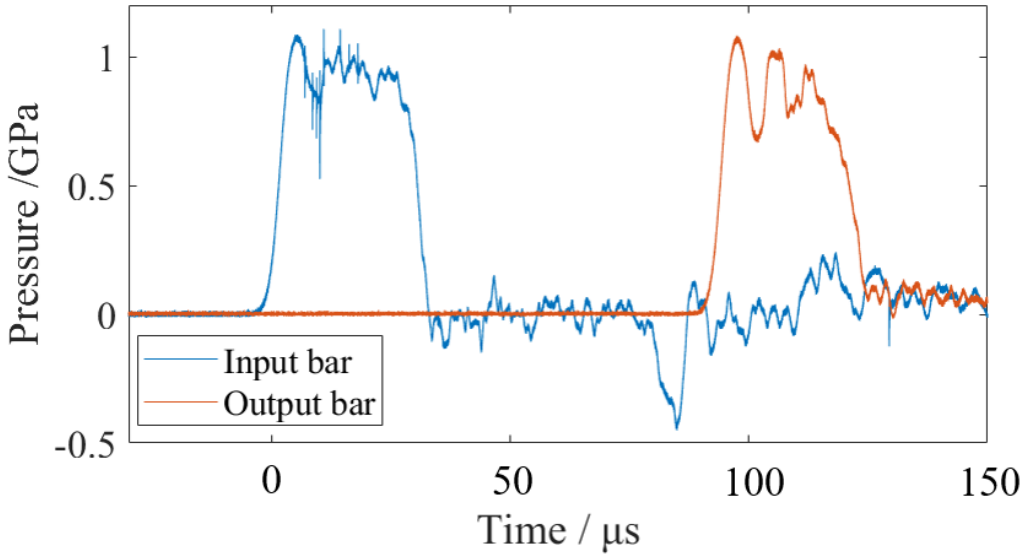

Fig. 3.11 The original and reflected pulse measured in the input bar, with the transmitted pulse measured in the output bar.

The input bar trace - after the incident pulse has impacted - contains both the negative tensile reflected pulse and the positive compressive reaction pulse. The output bar trace contains both the compressive transmitted pulse, and a compressive reaction pulse equal to that in the input bar.

$$Integral_{input} = -E_{Reflected} + E_{Reaction} \tag{3.5}$$

$$Integral_{output} = E_{transmitted} + E_{Reaction} \tag{3.6}$$

Therefore, taking the input bar trace after the incident pulse, integrating it according to equation 3.4, and subtracting this integral from the output bar integral, will leave only the reflected and transmitted energies. The reactive energy from the sample will cancel out.

$$E_{absorbed} = E_{Incident} - (E_{transmitted} + E_{reflected}) = Integral_{Incident} - (Integral_{output} - Integral_{input}) \tag{3.7}$$

This calculation gave the energy absorbed by the sample in order for a reaction to occur, allowing comparison to the fallhammer sensitivity.

Property	Value / J		
Incident energy	110	105	107
Energy absorbed	9.0	7.5	8.1

Table 3.1 The calculated energies present in the pulses for three HMX reactions for which the gauges survived.

The incident elastic energy should be the same as the kinetic energy of the striker bar, which had a value of 111 ± 2 J, and so was in reasonable agreement. From table 3.1, the mean energy absorbed by HMX could be calculated as 8.2 ± 0.8 J. The error on each measurement could be estimated by considering the trace of the gauges for a reaction that did not go, with the assumption the energy absorbed by the sample was negligible. By doing the same analysis yielded a value of 0.6 J, providing an error for the calculation.

The absorbed energy value of 8.2 ± 0.8 J was of order of the reported impact sensitivity in the fallhammer apparatus of 6.4 J [111], and was calculated explicitly rather than statistically. However, this fallhammer impact sensitivity varies between experiments, with Storm *et al* [111] measuring the above value of 6.4 J, and the sensitivity recorded by Eurenco (manufacturer) [110] was stated as 7.5 J, and so there is not a definitive impact energy sensitivity at the time of writing. Therefore, the mean calculated value of 8.2 ± 0.8 J in the SHPB was in reasonable agreement with previously reported impact sensitivity values which had been measured in the fallhammer apparatus.

This agreement between the apparatus implies that there exists an activation energy in order for initiation to occur, which is not dependent on the method of initiation. However, such an activation energy would have obvious limits, otherwise any low force applied for a long enough time would lead to a reaction. Whilst there was also a required pressure for initiation, indicated by the sharp threshold at *circa* 1 GPa measured, the difference of this value to that of the fallhammer suggests such a 'pressure threshold' would be apparatus-dependent.

Power considerations

Another variable that is useful to consider is the power: the energy delivered per unit time. This is difficult to measure in the fallhammer, due to the difficulty in in accounting for all the energy, but is possible to calculate in the Hopkinson bar. From equation 3.3, it can be seen that the power is easily calculated:

$$\text{Power} = \frac{F^2}{ZA} = \frac{AP^2}{Z} \tag{3.8}$$

Therefore, the presence of a pressure threshold of 1028 ± 18 MPa (figure 3.9) implies a power threshold is present at 3.39 ± 0.06 MW. This threshold makes physical sense; below the power threshold the rate of energy accumulation (the rate of heat increase) is lower than the energy (heat) loss mechanisms in the system and so the HMX sample cannot ever gain enough required energy to react. This explains why even very long duration impacts - such as pressing HMX into a higher density - do not lead to a reaction, as the power imparted to the energetic is too low for it to retain the energy.

The power of the impact was calculated from the energy launched into the sample - the incident energy of the input bar impact minus the reflected energy - which was delivered in 27.8 μs. For the dataset above, this led to a mean imparted power of 80.5 ± 1.6 MW, far above the perceived threshold calculated from the pressure. However, not all of that energy was absorbed by the HMX, the presence of a transmission wave in the output bar (figure 3.11) clearly shows that energy passed through the sample. By comparing the incident energy to the absorbed energy (table 3.1), only 7.6 ± 0.5 % of the available energy was absorbed by the material, with the absorbed power equal to 6.14 ± 0.12 MW. Therefore, in order to properly understand the power (or energy) threshold, a knowledge of both the power (energy) imparted to the sample is needed, as well as the efficiency of the material itself to absorb the energy. Different energetic materials (or the same material with a different microstructure) will require different activation energies for reaction, but may also have different efficiencies in absorbing the imparted energy.

As well as a power threshold, this treatment of the results implies a secondary requirement; a loading duration threshold. Provided the impact delivers a high enough power to the sample, the energy will increase over time. Therefore, the duration of the impact has to be long enough so enough energy can be delivered. Similar to a long duration, low power (pressure) impact, no reaction will occur with a very short high power (pressure) impact, as the energy accumulated during the loading was not enough for the reaction to proceed.

As observed in figure 3.8, in the SHPB with a 70 mm striker bar, the reaction repeatably occured and finished around 20 μs before the end of the loading pulse. Therefore, these

experiments were consistently above the 'loading duration' threshold that was required for the reaction. This resulted in the very clear pressure threshold being measured, where every impact above the required pressure had enough time to accumulate the required energy for reaction. In order to test the hypothesis of the loading duration threshold, further research would be needed examining impacts with shorter striker bars.

3.3.2 Optical

With the differences observed in the mechanical properties in initiation, the question was whether these differences would affect the light emission. The time of reaction, from the photodiode traces (figure 3.8) shows a reaction duration of *circa* 15 μs, of similar timescale to that witnessed in the fallhammer.

Spectrometer

Figure 3.12 shows the emission from the visible spectrum of SHPB HMX deflagration, taken by the spectrometer.

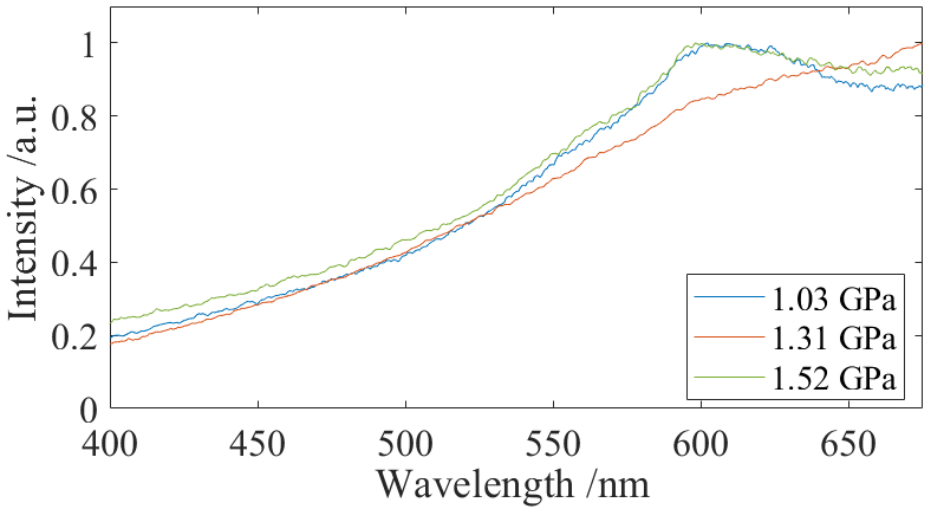

Fig. 3.12 Three examples of the visible emission of HMX deflagration, initiated in a SHPB, with a 0.6 nm resolution across the whole spectrum and normalised to the maximum value. Three spectra are shown, from an initiation pressure of 1.03, 1.31 and 1.52 GPa respectively, though the overall shape and features were similar. Whilst mostly consisting of greybody emission, a sodium peak could still be seen.

The spectrum is obviously different from that measured in the fallhammer deflagration. The continuous greybody emission was more dominant, having a higher intensity in compari-

son to the sodium emission line, which was still observed, however was no longer such a significant feature. Unlike the sodium emission, which was present in every spectrum, the other molecular emission lines – belonging to calcium – were not strong enough to be seen over the greybody radiation in any SHPB emission.

This increased greybody emission meant more wavelengths could be used to estimate the temperature, producing a more reliable measurement. However, for a fair comparison to the fallhammer, the same 400 – 500 nm region was used from the spectrometer measurements to fit to a Planck distribution (figure 3.13). This was because the experiment would most likely contain a range of temperatures present as the reaction is heterogeneous, with the cooler temperature blackbodies having a higher intensity in the 'red' region compared to the hotter temperatures peaking in the 'blue'. By including more 'red' regions – such as 700 nm, the regime would contain relatively cooler temperatures, which could affect the overall temperature measurement and not allow for a good comparison with the fallhammer results.

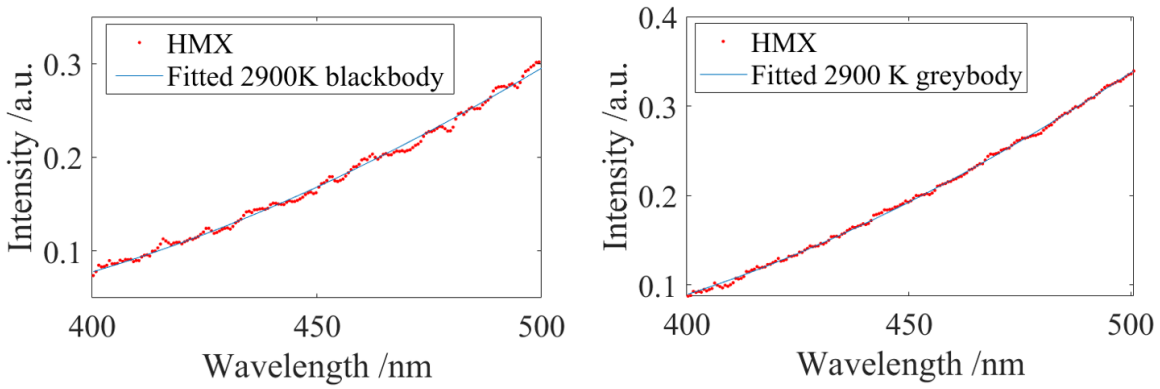

Fig. 3.13 Greybody fits to the 400 – 500 nm region of the wavelength spectrum for two different SHPB deflagration measurements.

Extending the blackbody over the whole wavelength range (figure 3.14) demonstrates how much more dominant the blackbody radiation is for the SHPB emission, with the more red wavelengths past the spectral peak also in agreement with the blackbody fit. Across all the spectra, a mean temperature of 2900 $\pm$ 200 K was measured for SHPB deflagration, as shown in figure 3.15.

The measured temperature was significantly lower than the 3900 $\pm$ 400 K seen in the fallhammer deflagration. Despite similar initiation conditions, a difference of 1000 K was seen in the temperatures, as well as the presence of increased greybody emitters in the sample.

An explanation for such observations could be that the higher pressure of initiation (and the input pulse having a constant top-hat shaped high pressure rather than the ring-up

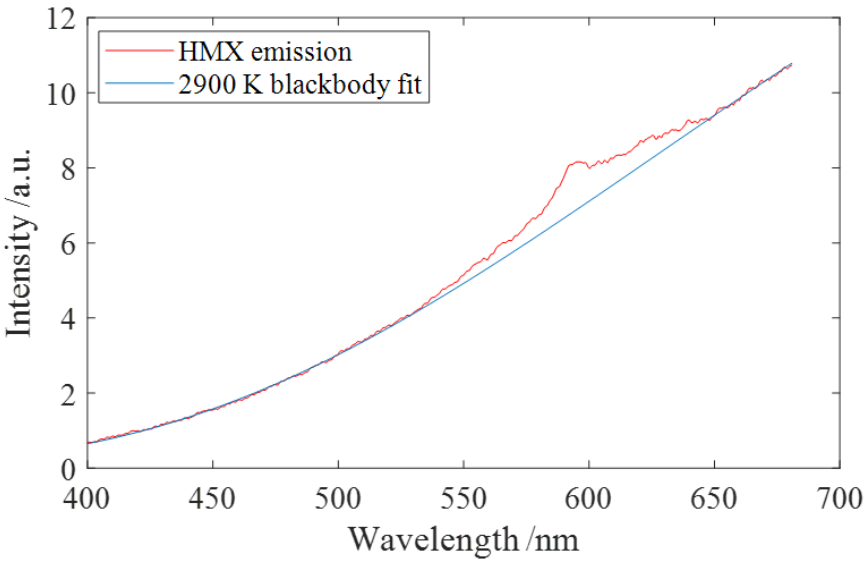

Fig. 3.14 The blackbody fit extended over the whole visible range. The SHPB spectrum has a much better agreement with blackbody radiation compared to previous fallhammer results, with deviation observed for only 50 nm either side of the sodium peak.

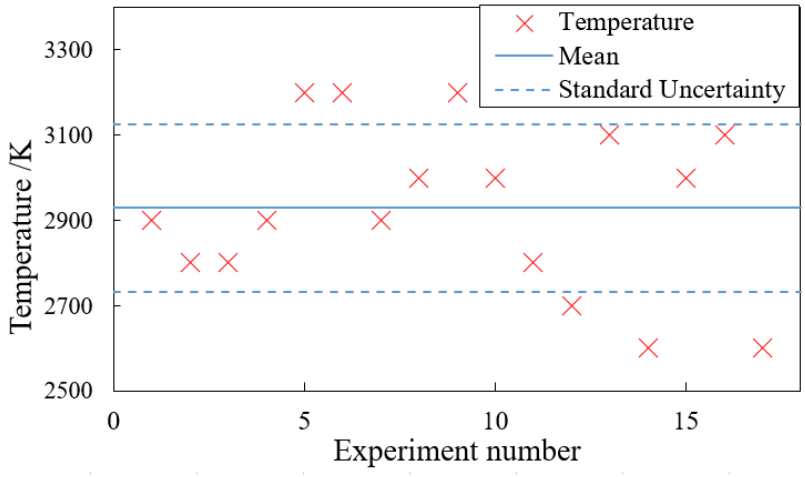

Fig. 3.15 The measured temperatures of 17 SHPB deflagration reactions, with a mean of 2900 K and standard deviation of 200 K.

observed in the fallhammer) leads to changes in the chemistry. For example, the increased pressure leading to another chemical reaction favouring more solid products rather than the ideal HMX decomposition (eq. 1.9). With more solid products formed, the greybody radiation would increase due to the presence of more solid emitters, and less dominant spectral lines - like the calcium observed in fallhammer deflagration - would have too low an intensity to be observed relative to this greybody emission. The heat - and therefore

temperature - would also be lower as the reaction took a less exothermic pathway under the higher pressures. Chapter 5 details the results of using a mass spectrometer to investigate this hypothesis.

Sodium peak shift

Though not as strong, the sodium emission peak was still present in all the spectra measured. Like the fallhammer, it had red-shifted, however the amount shifted was significantly larger, with shifts of 4 nm and above. An increased shift observed for a higher pressure, and lower temperature, reaction was of interest as it could potentially allow a new measurement of reaction conditions based on spectral red-shift. This avenue of research is presented in Chapter 4.

Pyrometer

The pyrometer would allow an independent measure of the SHPB deflagration temperature, as well as investigating whether any time dependence was seen in measured values. From the spectrometer results (figure 3.14), there are many more wavelength channels that could be chosen for the pyrometer, as the sodium emission line is much less dominating. Therefore, four channels were chosen, two in the blue at 450 and 500 nm, and two in the red at 700 and 750 nm. This range allowed a better fit over the whole spectrum, whilst still avoiding the 590 nm sodium region. This was different to the fallhammer pyrometry, as the advantages of a better fit over the whole visible spectrum with four channels outweighed the disadvantage of being a different method and no longer a completely fair comparison, as well as the fact the larger wavelengths still had good agreement to the fit performed in the blue region (figure 3.14).

The pyrometer measurements in figure 3.16 show similar behaviour to that seen in the fallhammer deflagration. The temperature was roughly constant over the main period of light emission, falling off in some measurements once the light started to decrease. The measured temperature across the experiments was 3100 $\pm$ 250 K, in agreement with the spectrometer results, confirming a lower temperature present in SHPB deflagration, compared to the 4000 $\pm$ 400 K measured in fallhammer pyrometry.

Specific similar characteristics can be seen, with an example shown in figure 3.17. In both the fallhammer and SHPB, one pyrometer reaction had some light emitted at the beginning of the reaction with a temperature 1000 K hotter than what would be expected before the main period of light emission. The only major difference was the temperature scales were 1000 K cooler in the SHPB than the fallhammer.

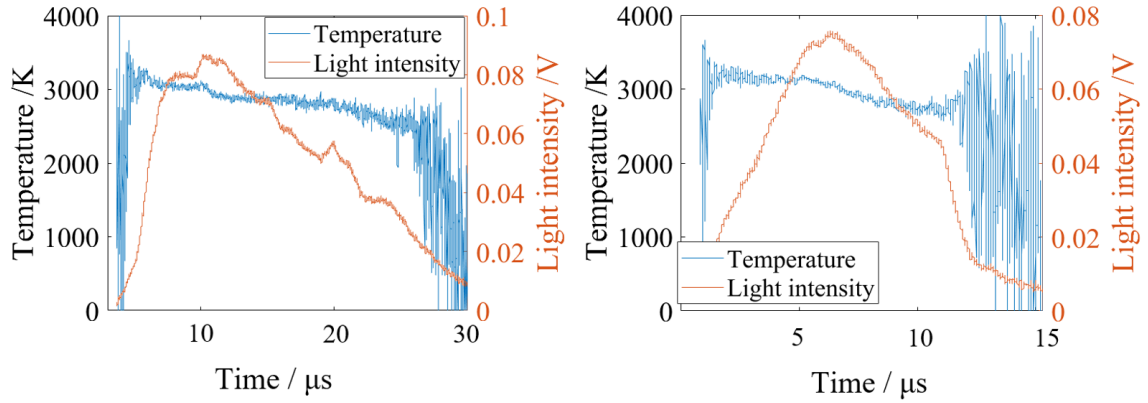

Fig. 3.16 Two traces of the SHPB pyrometer readings. These confirm the temperatures measured by the spectrometer, whilst having behaviour similar to those measured in the fallhammer.

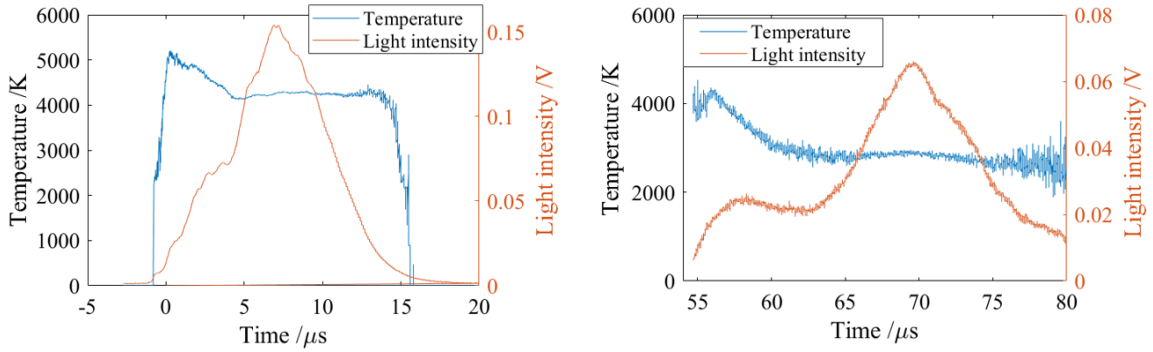

Fig. 3.17 A fallhammer (left) and SHPB (right) trace showing a similar pattern - with the main reaction occurring at constant temperature, however light at the start reaching a temperature 1000 K higher than the main reaction.

These measurements indicate that there are still underlying similarities present in the deflagration reactions, as well as the constant temperature through the main light emission period and the duration of the reaction, which are not dependent on the initiation method.

Another important comment for the temperature was that, other than being cooler, the standard error and range of results of the temperature measurements was also lower than that of the fallhammer. Similar to what was mentioned above with the sharp threshold for initiation pressure, this indicates that the SHPB deflagration was a lot more reproducible and an overall less stochastic process that the fallhammer.

Temperature comparisons to fallhammer

In summary, the typical wavelength spectrum for both the fallhammer and SHPB deflagration, as well as the burning spectrum, are seen in figure 3.18. This highlights the competition between spectral and greybody emission, with the burning and fallhammer deflagration dominated by the sodium emission, and the SHPB by the greybody from solid particles.

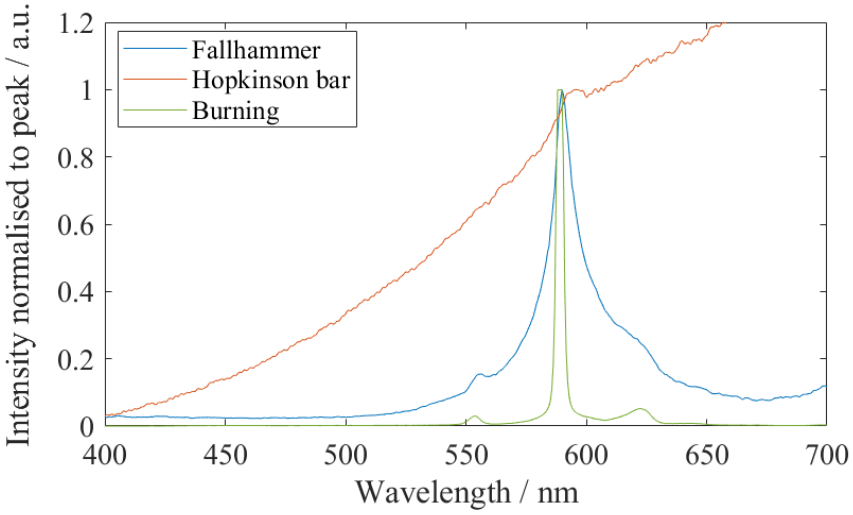

Fig. 3.18 Typical optical emission as seen in the fallhammer, SHPB, and burning. Both deflagration regimes have significantly more greybody emission than simple burning, though all retain the sodium peak.

The temperatures measured also demonstrate the differences caused by changing the initiation method. The comparison in the blackbody fit can be more easily observed when observing the 400-500 nm region of both the fallhammer and SHPB at similar intensities (figure 3.19). The hotter fallhammer appears more linear, and has a lower increase in intensity across this range, as these wavelengths are closer to the peak of the 3900 K blackbody (740 nm), compared to 2800 K radiation (1040 nm). Figure 3.20 shows the overall temepratures measured by both the spectrometer and pyrometer for both initiation methods.

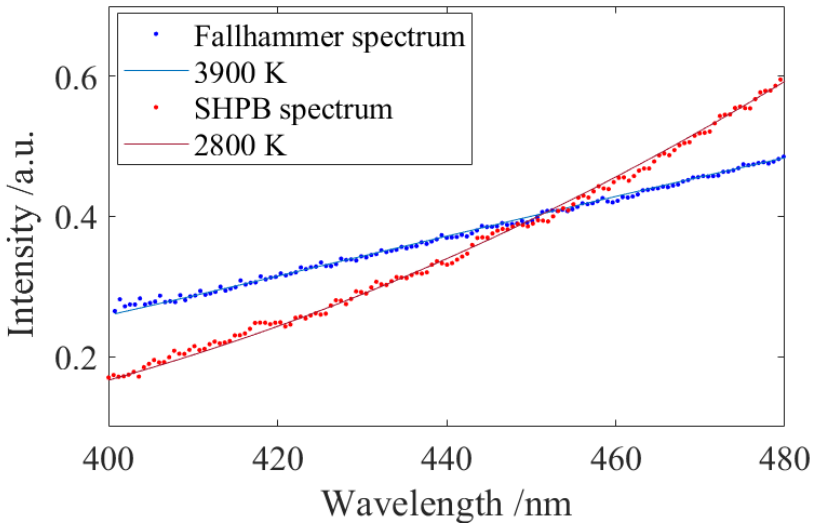

Fig. 3.19 The emission spectrum in the 400-500 nm range for the fallhammer and SHPB deflagration, displayed at comparable intensities. The cooler SHPB emission more than doubles in intensity over this range, whereas the fallhammer has a less extreme increase.

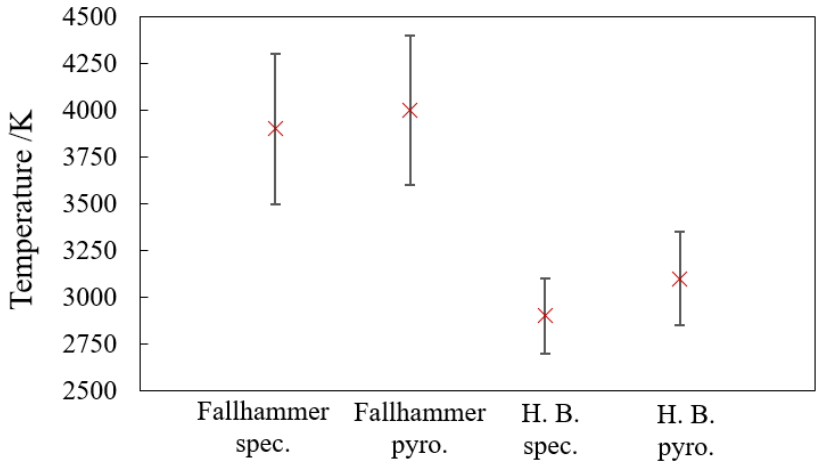

Fig. 3.20 The temperature measurements taken by the spectrometer and pyrometer for the fallhammer and SHPB deflagration, with standard error bars.

3.4 Applying developed technique to other materials

This chapter dealt with developing a new experiment for initiating deflagration in HMX, with similarities to the well-known and commonly used BAM-fallhammer impact sensitivity test. For HMX, the SHPB showed initiation at a higher pressure, but with similar absorbed energy, to the fallhammer. Given the importance of knowing the sensitivity of explosives for

their safe handling, the results of a new 'sensitivity-style' test are of use to the energetics community.

In order to better understand the comparison between the two methods of initiation, materials other than HMX were studied to observe whether the 'standard' order of sensitivities still held in the SHPB, and whether the behaviour measured in HMX was standard to this type of energetic. To this aim, RDX and PETN were chosen.

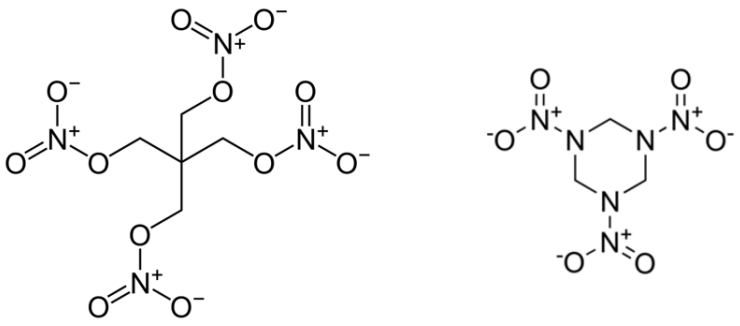

Fig. 3.21 Structures of PETN (left) and RDX (right).

As can be seen in figure 3.21, these two materials are chemically very similar to HMX. They are both in-use and well documented granular secondary explosives. Given their characteristics, no change in the setup or method of the experiment was required.

In order to investigate the sensitivities, both the energy and pressure were measured. Like before, the incident energy impacting the sample, along with that absorbed was measured, with the absorbed energy compared to the 'known' value obtained in the fallhammer tests, as stated in table 3.2. The initiation pressure was also measured, in order to determine if, and how, it varied between materials.

Material	Impact sensitivity /J
HMX	6.4
PETN	3.0
RDX	5.9

Table 3.2 The reported sensitivities of HMX, PETN and RDX as observed in the BAM impact test from 25 drops [111].

Another property that was investigated was how the time to reaction – the length of time elapsed between the initial applied force and the reaction light observed – depended on the applied mechanical pressure.

3.4.1 Results

Pressure

Similar to HMX, the speed of the striker bar was varied in order to establish the required pressure for initiation. The results for PETN, RDX and the above measured HMX are shown in figure 3.22.

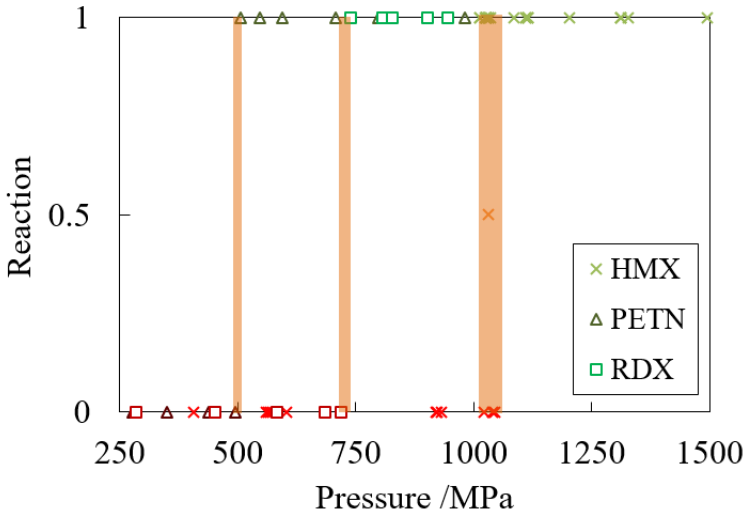

Fig. 3.22 Initiation success against pressure measured in the bar for PETN, RDX and HMX. The orange areas show the pressure initiation threshold for each material.

These pressure thresholds were measured as (508 $\pm$ 10), (724 $\pm$ 16) and (1028 $\pm$ 18) MPa for PETN, RDX and HMX respectively. As was measured before, the conditions for a reaction to occur or not are seen to be sharp, with a relatively well-determined pressure required in order to initiate the material.

The order of sensitivities presented in table 3.2 holds, with PETN more sensitive (requires lower pressure for initiation) than RDX, which in turn is more sensitive than HMX. It is worth remembering that the ramping pressures did not initiate HMX above the 'established' pressure threshold (section 3.3.1), which means that these results could not neatly be assigned to a pressure sensitivity value. However, the sharp transition between an initiation and not in all materials, and the agreement in sensitivity ordering, suggests that pressure does play a role in initiation and is still a relevant property to measure for establishing sensitivities.

Energy

As discussed, strain gauges were used instead of PDV in order to reliably calculate the energies involved. Using the same analysis technique as described above for HMX resulted

in calculated absorbed energies of (4.2 $\pm$ 0.3), (5.6 $\pm$ 0.8) and (8.2 $\pm$ 0.8) J for PETN, RDX and HMX respectively. Table 3.3 summarises these results, along with the impact sensitivities measured by Storm *et al* [111].

Material	Pressure threshold /MPa	Energy absorbed /J	Impact sensitivity /J [111]
HMX	1028	8.2	6.4
PETN	508	4.2	3.0
RDX	724	5.6	5.9

Table 3.3 Summary of the pressure of initiation, calculated absorbed energy and independently measured impact sensitivity in a fallhammer test [111]. Reasonable agreement was seen between absorbed energy and the impact sensitivity.

The absorbed energy was in reasonable agreement with the reported fallhammer energy impact sensitivity. As stated before, these values are not the only measurements of impact sensitivity, with fallhammer results varying between experiments and laboratories. This problem – of disagreements between seemingly 'identical' experiments – could potentially be resolved by the use of the SHPB method detailed here. With the energy calculated explicitly, rather than relying on the statistics derived from multiple drops, and all the energy present in the system accounted for (whereas in the fallhammer an unknown factor would be transmitted and lost), the SHPB results should be more reliable across different laboratories.

The conclusion of such agreement between the SHPB and impact tests led to the hypothesis of an energy threshold (activation energy) for deflagration, with certain limits for long-term low-force events. This theory could also be tested by considering the time to reaction – if the material needed a specific energy in order to initiate, the reaction would therefore react more quickly when a higher force/pressure was applied.

Time to reaction

Fortunately, the Hopkinson bar allowed the time to reaction to be easily calculated. The light gates positioned just in front of the input bar were used to measure the striker bar velocity, and also to trigger the oscilloscope for the strain gauges. Therefore, the time for the pressure pulse to enter the input bar was known. With the known speed of the pulse in the bar, the time of arrival at the sample was then simply calculated. Subtracting the time of arrival from the time the light was first detected on the photodiode gave the time it took for the reaction to occur after the pulse arrived.

Figure 3.23 shows this time to reaction against the applied mechanical pressure.

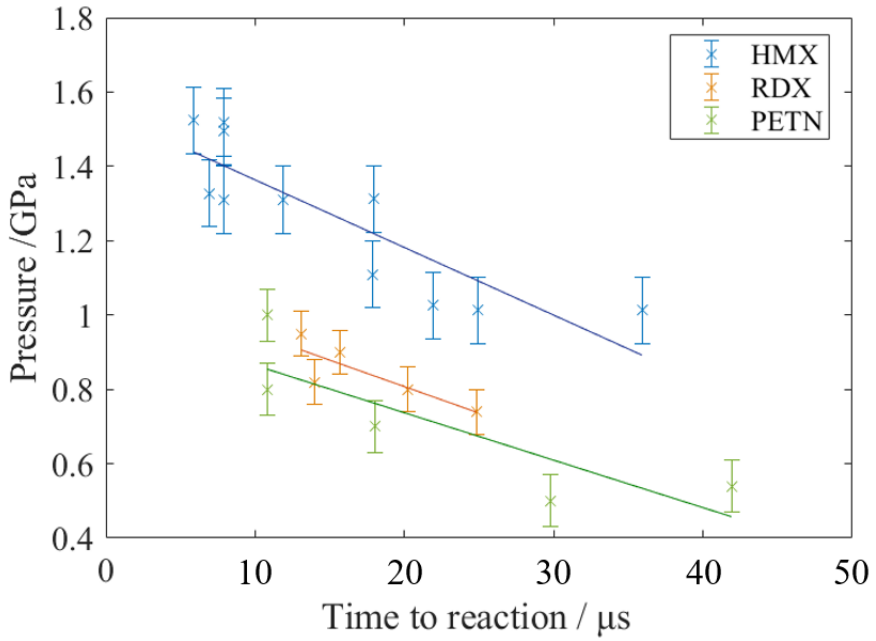

Fig. 3.23 Time to reaction against the applied pressure in the input bar. As the pressure increases, the time for the reaction to occur decreases.

The general trend of the data shows that as the input pressure increases, the time to reaction decreases, as predicted by the theory of an energy threshold. This is because the available energy to be absorbed by the sample depends on both the size of the pressure incident on the sample, as well as the duration; mathematically the energy is proportional to the integral of the square of the pressure wave with time (eq. 3.3). Therefore, if a specific amount of energy is required for a reaction (an energy threshold), increasing the incident pressure means less time has to pass in order to achieve the same energy calculated for a smaller pressure over a longer time. Therefore, as shown by figure 3.23, the incident pressure would be inversely proportional to the time to reaction.

3.4.2 Summary

The results gained for HMX proved themselves to be repeatable in other energetic materials, with a sharp pressure threshold to initiation present (for top-hat pulses) with values in HMX, PETN and RDX which agreed with the established order of sensitivity PETN>RDX>HMX. Whilst there might not be a simple pressure threshold (as ramping pulse experiments show), this result shows that the top-hat initiation pressure could function as a sensitivity measurement.

The calculated absorbed energy also was in relative agreement with the values determined by impact in the fallhammer. These fallhammer values do not account for all the energy in the system – as is the case in the SHPB calculations. The consistency between results was also an encouraging sign that energy could be used as a function of sensitivity, with a threshold similar across apparatus.

This energy threshold hypothesis was supported by the time to reaction decreasing with increasing applied pressure – with increasing force, the required energy was reached more quickly. However, such a hypothesis would clearly have limits, as reaction does not occur for long-time low-force events. Therefore, a power threshold might be more useful to consider instead.

3.5 Conclusions

The deflagration initiated by a Split Hopkinson Pressure Bar was investigated, and compared to that observed in a more traditional fallhammer apparatus. The pressure threshold for initiation was very narrow at 1.028 GPa, though did not initiate for a pressure wave ramping through this value. The value of the initiation pressure was larger in the SHPB than that seen in the fallhammer, but also showed evidence of pathway dependence given the non-initiation of the ramped pulses. The calculated energy deficit for these pulses showed an absorption of 8.2 $\pm$ 0.8 J, similar to the reported sensitivity in the fallhammer, however calculated explicitly rather than statistically.

The same behaviour was observed in RDX and PETN initiation in the SHPB, with a lowering 'pressure threshold' for the more sensitive energetics, and the absorbed energy in reasonable agreement with fallhammer impact sensitivities. However, these results reinforced the notion that pressure alone was not a good indicator of sensitvity as the measured time to reaction also decreased with increasing the applied pressure, consistent with the idea of a required activation energy (energy threshold), rather than just a specific pressure.

The emission spectrum also showed differences, with more greybody emitters relative to sodium than seen in the fallhammer, and a lower measured temperature. A reason for this could be the higher pressures leading to more solid products formed in the reaction, leading to a less exothermic reaction. Such a hypothesis was investigated, with the results shown in Chapter 5.

In summary, the optical emission for deflagration had some similarities: there would be a mix of spectral and greybody emission, the reaction would last of order 10 μs, and the temperature would be constant. However, the differences seen reflect on the differences present in the initiation method. Therefore, one must be very careful when comparing

'deflagration' experiments, as each experiment/laboratory would have different initiations and conditions.

The SHPB initiated deflagration had a large advantage over the fallhammer, as it was a lot more controlled. There was a clear pressure threshold, less variation in temperature and more calculations and diagnostics could be added, such as the energy absorbed by the material. It provided a more repeatable (less stochastic) experiment with potential to be expanded further.

3.5.1 Further research

The theory of extra solid products created in SHPB deflagration could be tested by the addition of a mass spectrometer onto the Hopkinson bar and the BAM fallhammer. This allow the concentrations of the reaction products to be measured, to see if there was a significant increase in soot for the Hopkinson bar. Such a line of enquiry is presented in Chapter 5.

The pressure pulse could undergo further shaping – investigating the effect of a half-sine or the effect of a long-duration short-amplitude pulse compared to one with a short-duration long-amplitude. These different shapes could be tailored to provide more information on the effect the shape of the pulse has on initiation, without changing the apparatus and diagnostics.

The Hopkinson bar could also be used to investigate a range of other energetic materials and even potentially test the sensitivity of traditionally insensitive materials which have difficulty being initiated in a drop-weight apparatus due to ceiling constraints. This would introduce an independent sensitivity measure compared to the fall energy, one that allows easier comparison. It could also be used to investigate the damage in materials, and the effect that it has on sensitivity.

Chapter 4

Spectral red-shift

4.1 Introduction

The previous measurements of deflagration show a particularly interesting feature. In the fallhammer apparatus, the sodium spectral peak was very noticeable in deflagration light, present for roughly half the visible spectrum. This can be seen as an annoyance, as the peak can present a challenge for pyrometry measurements that fit the light emission to a greybody, and any competing spectral emissions distort the fit. However, its presence is not something that should just be dismissed as a feature to avoid; the previous measurements on deflagration noted that the centre of the sodium peak was not found at the ambient emission wavelength of 589 nm. Repeating the deflagration measurements in a Hopkinson bar resulted in a red-shift of the sodium again, but this time the shift was roughly double the value that was seen in the fallhammer.

Unlike the more noticeable spectral broadening, caused by the high temperatures and pressures, this shift mechanism is not as commonly measured. Such a measurement provides an opportunity to focus on this observed red-shift; to both research the mechanisms present that may be causing such a shift, and to test whether any of these known theories could accurately model the measurements made. The following chapter details this process, from the discovered theories, to the experiments designed, and the conclusions received from them.

For a more concise description of the research in this chapter, see the resultant publication [127].

4.2 Theory

In section 1.3.1, a brief discussion of possible shift mechanisms was discussed in the context of spectral features seen in optical emission. These mechanisms include the Doppler, collisional (pressure) and Stark shift. Given the fact that the shift increased at higher pressures, the initial prediction was that the collisional shift would be responsible, but it was worth calculating order-of-magnitude estimates for the contributions of each shift mechanism, in order to see whether it was significant and should be considered.

The estimates would be compared to the deflagration measurements in the previous chapters. These show a red-shift of order 1 nm experienced by sodium emission at 589 nm, in reaction conditions of order 4000 K and 1 GPa.

4.2.1 Doppler

The Doppler shift is likely the most well-known of spectral shifts, often associated with astrophysical applications, and is a consequence of the emitting object moving relative to the observer. Consider an object emitting radiation with wavelength λ_s (distance between the wavefronts). Each wavefront travels at the speed of light, c, but the observer also is moving towards the emitter at speed v. From the observer's reference frame, the total distance the wavefront has travelled in the time for one period, t_0, is:

$$ct_0 = \lambda_s - vt_0 \tag{4.1}$$

Rearranging for t_0 gives;

$$t_0 = \frac{\lambda_0}{c} = \frac{\lambda_s}{c}\left(1 + \frac{v}{c}\right) \tag{4.2}$$

Which relates the observed wavelength, λ_0, to the emitted one, λ_s, for non-relativistic speeds.

In deflagration containing sodium, the highest particle velocity achievable was estimated to be the detonation velocity, equal to 9 km s^{-1}. This is significantly smaller than the speed of light, and so the observed wavelength and shift can be calculated using the non-relastivistic formula above:

$$\lambda_0 = 589.3 \times \left(1 + \frac{9 \times 10^3}{3 \times 10^8}\right) \text{ nm}, \quad \lambda_0 - 589.3 = 0.018\,\text{nm}. \tag{4.3}$$

A shift of 0.018 nm is below the resolution of the spectrometer, and negligible compared to the 1 nm shift observed.

More importantly, this result assumes that the emitting sodium atoms all have the same velocity – travelling normally towards the observer. However, in deflagration, the particles would be moving in all directions, there is no intrinsic bias to the system. Particles moving away from the observer would produce Doppler shifts that cancel out the ones moving towards. Therefore, the outcome is a symmetric broadening rather than a single shift.

This logic, with the fact that the maximum observed shift is significantly smaller than the measured one, means the Doppler mechanism can be discounted.

4.2.2 Stark

The Stark effect refers to the splitting of energy levels under the influence of an electric field. Unlike the Doppler shift, an estimate for the shift in peak cannot easily be determined with a simple formula. Instead, comparisons to previous experiments and data-sets were used, considering both the overall electric field that may be present (DC effect), as well as the effect of electrons produced in the reaction conditions.

Firstly, to consider the DC effect, a value of the expected electric field present in deflagration, and the shift it would cause in sodium, was required. Similar to considering the Doppler effect, the electric field present in detonation was used to gain a maximum expected shift present in deflagration. From Tasker, Lee and Gustavson [128], detonation from an HMX based material would produce an electric field of order 10 kV cm^{-1}. When considering previous measurements of the DC Stark shift in sodium D2 lines, an electric field of this magnitude would result in a red-shift of order 2×10^{-5} nm [129], and so would clearly not be a measurable effect in this research.

However, the Stark shift can also be considered in terms of electron density, and the shift due to the increased potential between the charged particle and the emitting atom. Data-sets of the expected red-shift for electron densities have been compiled [130], and therefore the magnitude of the shift in deflagration could be estimated, if the electron density could be calculated.

The Saha ionization equation details the level of ionisation of a gas, given the temperature, T, and ionisation energy, ε, and therefore provides the electron density, n_e.

$$\frac{n_e^2}{n - n_e} = \frac{2}{\lambda^3}\frac{g_1}{g_0} exp\left(\frac{-\varepsilon}{k_B T}\right) \tag{4.4}$$

Where n is the total gas density, k_B is the Boltzman constant, g_0 and g_1 are the degeneracy state of the ground and excited states of the atom, and λ is the thermal de Broglie wavelength of the electron;

$$\lambda = \sqrt{\frac{h^2}{2\pi k_B m_e T}} \tag{4.5}$$

which depends on the Planck constant, h, mass of the electron, m_e, and temperature. To gain an estimate of the electron density in deflagration, the temperature of 4000 K was used, and the total gas density $n = 10^{22} cm^{-3}$ from the ideal gas equation. The ionisation energy was approximated as that of air, given the idealised reaction products would be similar (eq. 1.9), with a value of 14 eV. Assuming the degeneracies have the same order of magnitude, this predicts an electron density in deflagration of *circa* $5 \times 10^{15} cm^{-3}$. From the datasets of Stark shift against electron density [130], this would correspond to a red-shift of order 10^{-4} nm in the 589 nm line of sodium, an order of magnitude larger than the DC effect, but still significantly smaller than the measured value.

Both the DC and the electron effects taken separately predict a shift negligible compared to the measured 1 nm. Stark shifts for charged molecules, rather than just electrons, are also a reported phenomenon. Calculations to determine the density of these charged molecules – using dissociation energies rather than ionisation – were not undertaken. This is, firstly, because the exact chemical composition is unknown, and would start to complicate the equations more. Secondly, the reported shifts for molecules are not nearly as well-known as for electrons [130].

These reasons increase the difficulty of calculating the Stark effect for molecules, but it is also worth considering the theory that the Stark shift was built upon. The Stark effect is primarily used, and associated, with investigating the effect of the electronic contribution, with an addition for more massive charged particles as an extra consideration. It is a semi-classical theory that predicts how charged particles will affect the energy levels of the emitting species; an evolution on the classical collisional theory (see next section) [131] with added detail on electronic charge contributions, and focusing on the less massive electrons rather than ions.

Once these more massive charged particles are included, the collisional aspects – focusing on the van der Waals potential instead of the Coulomb – become more important and cannot be ignored completely. Therefore, instead of focusing on these contributions from the Stark approach, with increasingly more complex equations and unavailable data, it becomes more practical to consider the shift from the collisional theory angle instead.

4.2.3 Collisional

The basis of collisional theory considers the van der Waals interaction between two species, and how the potential between them is a function of distance, which itself is a function of density, and therefore pressure. This interaction can be approximated by Lennard-Jones potential, V_{LJ};

$$V_{LJ} = V_m \left[\left(\frac{r_m}{r} \right)^{12} - 2 \left(\frac{r_m}{r} \right)^{6} \right] \tag{4.6}$$

Where r is the distance between the particles, and V_m the minimum value of the potential, found at r_m. A graphical representation, shown below (figure 4.1), demonstrates how the energy difference between the ground and excited energy level will be dependent on how close the neighbouring molecules are (how high the pressure of the perturbing species is).

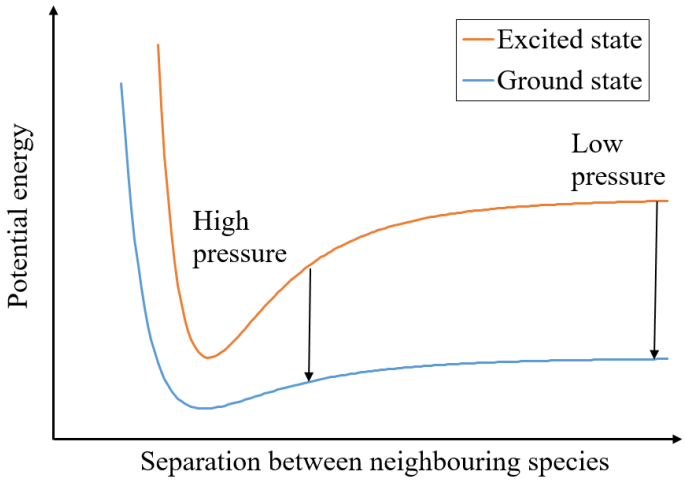

Fig. 4.1 Simple diagram illustrating the difference in photon energy emitted, related to the potentials of the emitting species, and the distance between the emitting species and the neighbouring perturbing atoms. At lower separation distances (higher pressures) between the gas species, the difference between the excited and ground energy levels is lower for the emitter, thus the photon released in light emission would be red-shifted in comparison to the high separation (low pressure) photon.

Previous experiments that measured the peak shift in sodium [132–134] focused on flame spectroscopy, and the increase in red-shift when the density of the surrounding gas species was increased. In comparison, the aim of this research was to investigate the link between the pressure of the reaction and the shift, and to measure the shift in the significantly more violent deflagration reactions. Therefore, the theory that was developed following these experiments was studied in order to predict the contribution of collisional effects on the shift.

Lindholm-Foley

Lindholm-Foley collision theory is a framework that describes this collisional effect. It incorporates the work of Margenau, whose experimental results of red-shift with increasing density [133–135] could not be explained by Lorentz collisions, which predicted collisional broadening, but not a shift [136].

In order to gain an approximate value of the shift, the technique used by Fletcher and McDaniel [137], itself based on Traving [138], was followed.

Firstly, the potential experienced by the particles was approximated to be a dispersive interaction. Based on the Lennard-Jones potential for van der Waals, it incorporates the r^{-6} term; assuming that the particles are far enough apart that the potential is purely attractive and the repulsive r^{-12} term is insignificant at these distances.

The dispersive potential often is represented in the below form [139],

$$V(R) = -\frac{2V_m r_m^6}{r^6} = \frac{C_6}{r_6} = -\frac{3}{2}\left(\frac{E_A E_B}{E_A + E_B}\right)\frac{\alpha_A^0 \alpha_B^0}{(4\pi\varepsilon_0)^2}\frac{1}{r^6} \tag{4.7}$$

Where C_6 is the constant associated with the r^{-6} term in the potential, ε_0 the vacuum permittivity, E_A and E_B are the ionization energies of the interacting molecules, and α_A^0 and α_B^0 are the respective static polarizabilities.

The next approximation applied was that the system can be described in the impact limit, which assumes a lower density condition. This limit assumes that only one collision occurs at a given time, and each collision is an independent event, meaning particles with larger initial distances to the perturber are not considered. In higher density scenarios, where the collisions can no longer be treated as independent, the static limit would apply.

The impact limit was chosen in order to achieve an estimate of the collisional shift, but was not done so on the basis that the system had a low density, as deflagration has a high associated pressure. Like many theories concerning line-shift, Lindholm-Foley collisional theory also details how the line-width would behave in a given scenario, considering the effect of broadening over a larger range of energies/wavelengths. Whilst the impact and static limit are presented as the low- and high-density (or slow- and fast-collision) limits respectively, there is another consequence that is not considered.

The two limits – or, more accurately – the two collisional types present in the system, have different effects on the line profile. The impact theory collisions have a larger impact on the inner part of the line profile – around the centre of the emission, whilst the 'wings' of the emission are better approximated by the static theory collisions [138]. As this research was primarily concerned with the line-shift and not the line-width, it was therefore apparent that the impact theory approximation should be used. However, given that it is a low-density

limit, it might lead to the theory starting to fail as reaction pressure increases – leading to an intrinsic high-pressure limit in the theory.

Using the dispersive r^{-6} potential, Traving [138] showed that the expected line-shift according to Lindhom-Foley collision theory in the impact limit would be:

$$\Delta f_s = \frac{2.94}{2\pi}(\Delta C_6)^{\frac{2}{5}}\langle v^{\frac{3}{5}}\rangle n \tag{4.8}$$

Where Δf_s is the frequency shift in Hz, and n is the density of all perturbers. v is the speed of the perturbing molecules, with the average speed given by $\langle v\rangle = \sqrt{\frac{8kT}{\pi m}}$, where m is the mass of the molecules (taken to be the average mass of molecules in air). ΔC_6 refers to the difference in the experienced potential C_6 of the excited state of the emitting species compared to that of the ground state, divided by the Planck constant. From the equation detailing the dispersive potential (eq. 4.7), this value is calculated as:

$$\Delta C_6 = \frac{3E_p}{2h}\frac{\alpha_p^0}{(4\pi\varepsilon_0)^2}\left[\frac{E_{A,L}\alpha_{A,L}^0}{E_{A,L}+E_p} - \frac{E_{A,U}\alpha_{A,U}^0}{E_{A,U}+E_p}\right] \tag{4.9}$$

Where E refers to the ionisation energy of the perturbers (E_p), and the sodium atom ($E_{A,L}$ for the lower energy state and $E_{A,U}$ for the upper). Similarly, α^0 refers to the polarizabilities of the states as before.

Assuming a Maxwellian distribution of velocities [138], where $\langle v^{\frac{3}{5}}\rangle = 0.891\langle v\rangle^{\frac{3}{5}}$, the average speed of the perturbing gas stated above can be inserted into the equation 4.8, leading to the shift having a dependence on temperature to the power of 0.3. The number density, n can also be inserted from the ideal gas equation ($P = nKT$), which leads to an overall frequency shift of:

$$\Delta f_s = -2.18\times 10^{23}(\Delta C_6)^{\frac{2}{5}}\frac{P}{T^{0.7}}\ \text{Hz} \tag{4.10}$$

With an observed dependence on the temperature T, and pressure P, of the enviornment. The frequency shift is related to that in the wavelength, $c\lambda^{-2}\Delta\lambda \approx -\Delta f$, and so the wavelength shift can be determined as:

$$\Delta\lambda_s = 2.18\times 10^{23}\frac{\lambda^2}{c}(\Delta C_6)^{\frac{2}{5}}\frac{P}{T^{0.7}}\ \text{m} \tag{4.11}$$

Sodium emission in deflagration conditions

From equation 4.11, the wavelength shift is dependent on the properties of the specific emitting atom. The calculation requires the energy of polarisation for the perturbing molecules, the energy levels of sodium and the polarizability of all the states. There is also a wavelength

dependence, which was made equal to the central wavelength observed in sodium emission of 589.3 nm.

The exact chemical composition of the perturbing molecules in deflagration was unknown. It was assumed that they would overall have behaviour comparable to air, firstly because it is probable that air was trapped in the voids that collapsed to form hotspots. Also, the reaction products in an idealised reaction, which would also likely be present, would be similar to air.

Table 4.1 details these properties that were used in the calculation of the collisional shift of sodium in deflagration.

Property	Value
E_p	14.86 eV [137]
$E_{Na,L}$	5.14 eV [78]
$E_{Na,U}$	3.03 eV [78]
α_p^0	1.72 $(4\pi\varepsilon_0)$Å^3 [137]
$\alpha_{Na,L}^0$	24.1 $(4\pi\varepsilon_0)$Å^3 [129]
$\alpha_{Na,U}^0$	50.2 $(4\pi\varepsilon_0)$Å^3 [129]

Table 4.1 The ionisation energy and polarisations of the perturbing gas (air), and the excited and ground state of sodium.

Inserting these values into equation 4.9 and 4.11, led to a predicted red-shift in sodium of:

$$\Delta\lambda_s = 883\frac{P}{T^{0.7}}\ \text{GPa}^{-1}\ \text{K}^{0.7}\ \text{nm} \tag{4.12}$$

For the deflagration conditions of 1 GPa and 4000 K, this corresponds to a shift of *circa* 3 nm, which is in agreement with the observed shift in previous measurements. This predicted value indicates that added contributions from the Stark effect are not required, and that treating the perturbers as neutral atoms is sufficient.

There are a few underlying approximations present to reach this answer. First, that the interaction can be purely described as a dispersive r^{-6} potential. Secondly, that the chemical reaction itself is an idealised one-step reaction with products that have properties similar to air. And thirdly, that the impact regime was suitable for describing the system. Therefore, there is an associated uncertainty with the above calculation due to the deviations in the actual experiment to the theorised one. Such an uncertainty would be more easily found by doing the experiments, than attempting to calculate here.

4.2.4 Theoretical conclusions

The order of magnitude estimations for collisional shift, as detailed by Lindholm-Foley theory, are consistent with the previous experimental results that detailed a red-shift of a few nanometers in deflagration. Further experiments would be required to investigate the relationship between reaction pressure and red-shift of the sodium line, and to test whether the predicted $PT^{-0.7}$ functional form would be observed in the data.

Not only would these experimental results test the Lindholm-Foley collisional theory, but would also, independently of any theory, provide the relationship between sodium red-shift and pressure in deflagration reactions, providing a calibration for optical pressure measurements.

Before conducting such experiments, there was another mechanism to be aware of. Despite not being previously attempted in deflagration (or with sodium emission), utilising a peak-shift to measure pressure has been common practice in another area of physics, which is worth discussing before determining the behaviour of sodium emission in deflagration.

4.3 Ruby fluorescence

In deflagration, the pressure dynamically reaches a value of order 1 GPa. To reach such conditions statically a diamond anvil cell could be used, with the basic outline of such an apparatus shown in figure 4.2.

In order to determine the pressure experienced in the cell, the peak shift of ruby is measured, and compared to the calibrated values. Unlike sodium emission, this is a fluorescence reaction, with the ruby excited by a laser, and occurs in solid rather than vapour state. The ruby red-shift has been calibrated to pressures of 150 GPa [140], significantly higher than even reached in detonation. The shift can be estimated by determining the behaviour of Cr ions in Al_2O_3 when a pressure is exerted, relying on energy matrices first calculated by Tanabe and Sugano [141, 142] and was first utilized to measure pressure in a diamond anvil cell in 1972 [143].

A diamond anvil cell could not be used to calibrate the sodium peak shift seen, as this apparatus was designed for increasing the pressure in solid, or liquid, samples. Burning sodium could not easily be introduced into the equipment, and statically held at a high pressure.

However, ruby could be added to the deflagration experiment more easily. To achieve this, a small chip of ruby was ground into powder in a press. Being one of the hardest substances, plates of tungsten carbide were used to crush the ruby, so it could be added to the sample of HMX. The particles produced in the powder had to be smaller than the height of the HMX

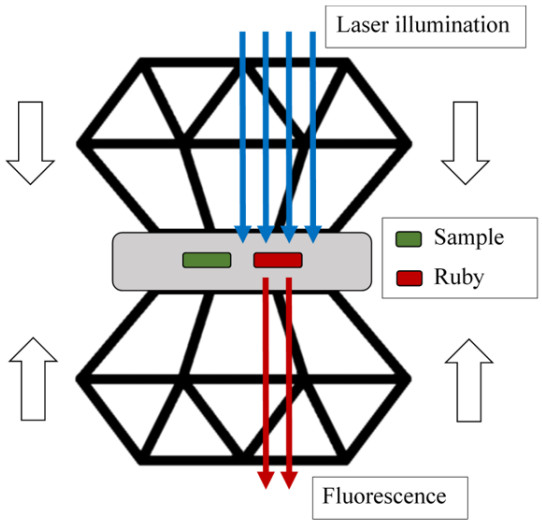

Fig. 4.2 Diagram of a diamond anvil cell. The two diamonds compress the sample (either a solid or liquid) in the surrounding gasket. A piece of ruby is included in/next to the sample and subject to laser illumination. The 694 nm fluorescence is then captured by a spectrometer.

sample in the fallhammer; if not, the weight would fall on them and be supported, leading to no initiation.

The ruby was excited by a 532 nm laser with a *circa* 70 mW power output, incident through a fibre optic placed in plane to the sample, opposite the fibre collecting the light emission. However, the level of fluorescence seen was not bright enough to be measured on the microsecond timescales of the reaction, let alone above the intensity of the deflagration itself.

This attempt of using the shift of ruby under pressure did not work. However, the idea is still valid and could be revisited, if a method of increasing the signal of the ruby fluorescence was achieved. Regardless, another method of measuring the pressure in the reaction, independent of optics, had to be applied.

4.4 Experiments

The aim was to collect a set of sodium peak measurements, and the associated reaction pressures, from both the fallhammer and Hopkinson bar apparatus in order to create a calibration dataset, and to test the accuracy of Lindholm-Foley theory.

Measuring the sodium peak centre could be achieved with ease from the spectrometer measurements. Therefore, a reliable method of measuring pressure had to be included into the experimental setup.

The mechanical input pressure was measured by use of a strain gauge, as previously described in Chapter 2. This measurement allows ease of comparison to Hopkinson bar deflagration, which measures the mechanical pressure acting on the sample using PDV velocity readings on the input bar (section 3.2.1). In the approximation that the pressure equilibrates infinitely fast, the initiation pressure is equal to the reaction pressure, and these measurements can be assumed to be the pressure experienced by the sodium. However, this approximation cannot be assumed true in deflagration immediately; an independent measurement of the dynamic gas pressure was needed to confirm the relationship between initiation and reaction gas pressure.

4.4.1 Dynamic pressure measurement

To measure the gas pressure, a dynamic piezo-electric gauge designed to withstand up to 6 GPa [Kistler Type 6215] was included in the experimental setup. Seen in figure 4.3, the Kistler gauge was added on the plane of the deflagration reaction, similar to the fibre optic. The gauge contains a quartz piezo-electric sensor designed to ensure that it not only survives being next to a deflagration reaction, but can be repeatedly used. This sensor directly converted the incident gas pressure into a voltage, allowing for clear determination of the reaction pressure.

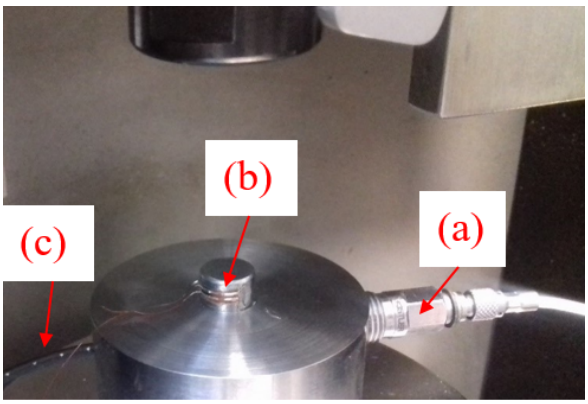

Fig. 4.3 A Kistler 6215 dynamic gas pressure gauge (a) inserted into the fallhammer apparatus. The strain gauge (b) is attached to the top anvil, with the black fibre optic (c) collecting the reaction light.

However, this relies on the assumption that there was no volume change accompanying the change in pressure. Whereas, in the fallhammer configuration, the reaction gas expands before reaching the pressure gauge. This means the output pressure has to be corrected, according to the volume change associated with this expansion.

$$\frac{P_1}{P_2} = \left(\frac{V_2}{V_1}\right)^{\gamma} \tag{4.13}$$

$$\frac{P_{measured}}{P_{reaction}} = \left(\frac{V_m}{V_m + V_v + V_g}\right)^{\gamma} \tag{4.14}$$

Where V_m is the volume of material, V_v, the space in the fallhammer setup it can expand into, and V_g the dead space in the Kistler gauge, equal to 10 mm^3.

An overal volume of 15 mm^3 of granulated HMX was inserted in each experiment. During initiation this material would be compressed, increasing in density and decreasing in volume. From the Hopkinson bar experiments, a thickness of 0.16 mm after compression was measured, the corresponding thickness in the fallhammer (taking into account the diameter of the setup and the original volume material used was different) would be of order 0.10 mm. This would lead to a volume at point of initiation, V_m, of 7.6 mm^3.

The highest uncertainty was related to the expansion of the gas pushing the steel cylinders up. Given the fibre optic was likely to be blown out, providing an avenue for air to escape at the height of 1 mm, the amount of expanding gas volume can be estimated as the volume of the enclosed cylinder from the compressed HMX to the height of the blown fibre. This leads to an expansion volume of 71 mm^3.

Altogether this will lead to the actual reaction pressure of:

$$P_{reaction} = (24 \pm 2) P_{measured} \tag{4.15}$$

Figure 4.4 shows typical traces of these measurements, with the calibration and moderation done. The mechanical pressure was taken when the reaction occurred, and stayed constant over the period of light emission. There was a delay between the immediate reaction and the produced gas reaction pressure, so the gas pressure was recorded at the first major maximum in the trace. Figure 4.5 details the comparison of the mechanical pressure against the gas pressure in order to examine the hypothesis of fast pressure equilibration.

From figure 4.5, a clear correlation can be seen, with the measured values almost identical. Constraining the dataset to go through the origin results in a measured gradient of 1.02 $\pm$ 0.04.

These results support the approximation that pressure will equilibrate sufficiently fast so that the mechanical strain gauge values are good indicators of reaction gas pressure. This allows initiation pressure to be used as pressure of reaction for these deflagration experiments. The measurement of initiating mechanical pressure was more favourable to use than the dynamic gas pressure, as the uncertainty involved in calculating the change in volume was

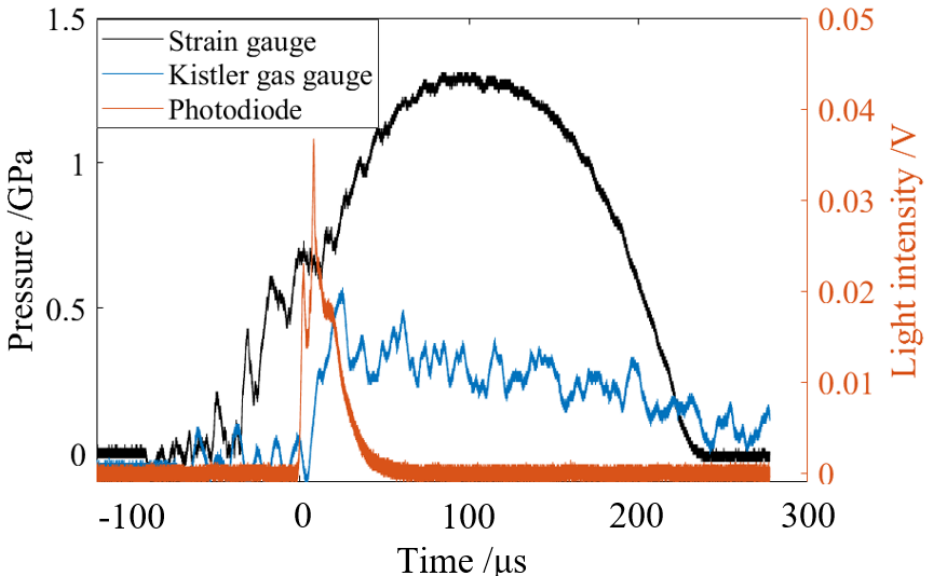

Fig. 4.4 Example trace showing the recorded mechanical pressure (black), the gas pressure (blue), and the reaction light (orange). For calculations, the initiation pressure was taken at the point of reaction - when the photodiode light intensity suddenly rose - and gas pressure was taken at the first maximum, which occured just after the reaction light was recorded.

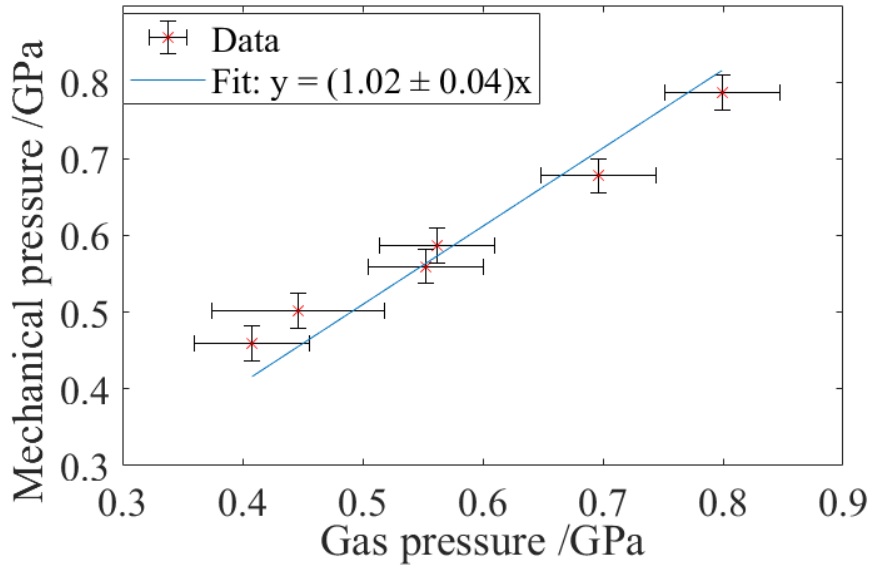

Fig. 4.5 The initiating mechanical strain pressure plotted against the maximum of the dynamically measured gas pressure. A strong linear correlation, close to unity, can be observed in these measurements. The best fit was constrained to pass through the origin. Error bars relate to the uncertainty of determining the maximum pressure reached, and the calculated uncertainties from the calibration and converting voltages to pressure.

high, and varied from experiment to experiment. Whereas the mechanical pressure had a much lower uncertainty, both in the fallhammer and the Hopkinson bar, and was more readily available to be calculated.

4.4.2 Red-shift

Having confirmed from the experimental setup detailed above that the red-shift and pressure of sodium could be measured in the fallhammer, an initial measurement of the relationship (figure 4.6) could be made between these variables, assuming the temperature was roughly constant.

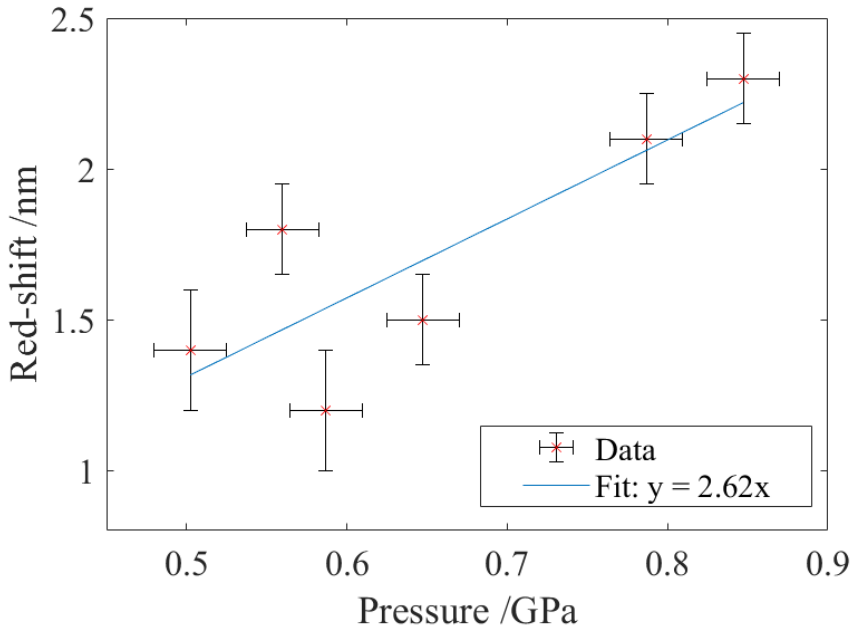

Fig. 4.6 The relationship between the reaction pressure and the associated shift from the central 589 nm sodium emission in the fallhammer apparatus. A linear relationship was seen, as predicted by Lindholm-Foley theory, as the temperature was roughly constant across the reactions.

The predicted linear relationship with pressure (equation 4.12) was seen, provided a constant temperature. But it was clear from this data that the range of pressures and shifts measured was small. The initiation pressure in the fallhammer apparatus was reasonably constant at 0.60 ± 0.11 GPa, and there was no simple process to increase or decrease this value. Therefore, it was necessary to include more data.

Hopkinson bar initiation allowed, firstly, higher initiation pressures (up to 1.5 GPa) to be reached. It also permitted more control over the exact pressure, as the pulse was a top-hat

function, meaning the reaction could not initiate on the 'ring-up' to the maximum pressure, and so will proceed at the value determined by the velocity of the striker bar. Including the data would therefore provide data in the 1 – 1.5 GPa range, extending the size of the possible dataset of values.

Two other advantages were present with using the Hopkinson bar deflagration data. One was that the pressure was automatically calculated in the experimental setup, so no further change to the experiment was needed. The other was that the measured reaction temperature in this initiation was different (section 3.3.2). Therefore, inclusion of this data would allow a better test of the collisional theory, as the shift would no longer be considered linear with pressure, but follow the $PT^{-0.7}$ relationship described above. The temperatures of the fallhammer and Hopkinson bar reactions also were required for this construction, however these could be calculated from the same spectrum as the shift, using the greybody emission in the 400 - 500 nm range as before.

Following the same methods detailed in chapter 3, the red-shifts in the Hopkinson bar at pressures 1 – 1.5 GPa, and temperatures of *circa* 3000 K, were measured. Along with the fallhammer results, these were plotted against the functional form detailed by Lindholm-Foley.

From figure 4.7, it can be seen that the data are consistent with collisional impact theory:

$$\Delta\lambda = 950PT^{-0.7}\ nm \tag{4.16}$$

with a constant of proportionality equal to 950 ± 30 GPa^{-1} K$^{0.7}$ nm. This value was calculated with linear regression, and constrained to pass through the origin. The result marks the first time that a spectral shift has been calibrated for deflagration conditions, and therefore allows a completely original diagnostic technique of measuring the reaction pressure purely from the visible light emission.

Not only do the results match the functional form of collisional theory, the constant of proportionality is remarkably close to the predicted value of *circa* 880 GPa^{-1} K$^{0.7}$ nm (eq. 4.12). Considering the approximations present in the calculated value, such as only assuming a van der Waals interaction was present and the chemical reaction was an idealized one-step process, these results show that even a basic consideration of Lindholm-Foley theory provides a sufficient description of the occurring process. Further corrections, such as the Stark effect for considering charged perturbers, are not necessary at this stage.

At the higher pressures in figure 4.7, a potential upward curve (deviation from linear) can be seen, though it is still within error, which could hint at the start of the high pressure limit to the theory – possibly a consequence of using the impact theory assumption. Once a

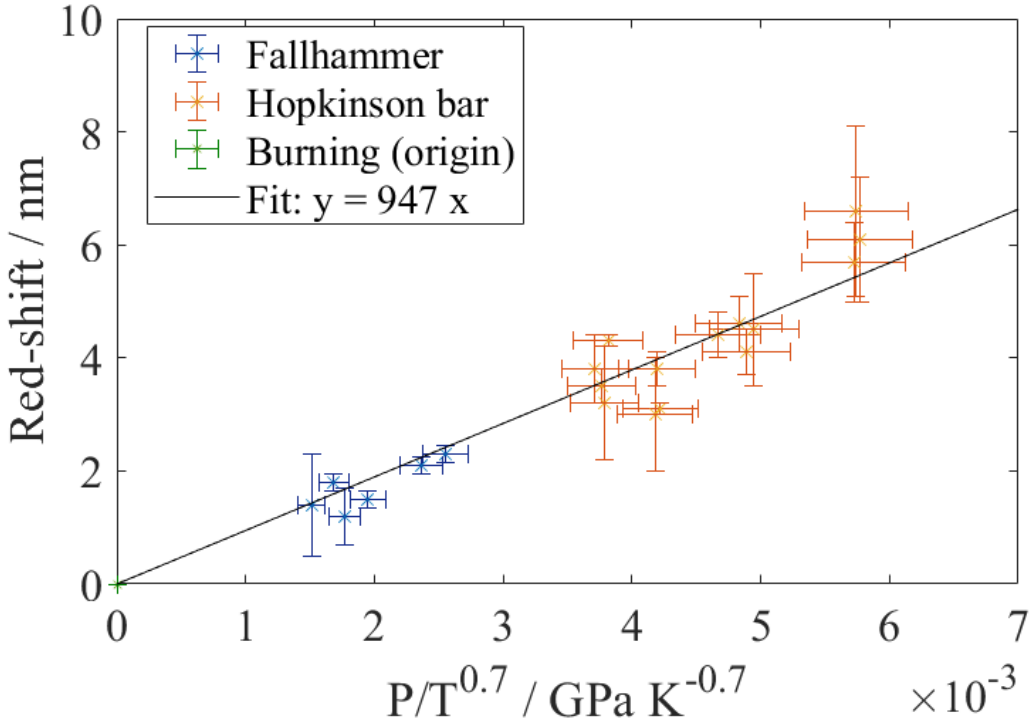

Fig. 4.7 The relationship between the measured pressure and temperature, and red-shift, of the sodium doublet across the three regimes of burning (green at origin), fallhammer (orange) and Hopkinson bar (blue) deflagration. Vertical error bars show the uncertainty of peak centre, and horizontal errors were calculated from the uncertainties in pressure and temperature measurements, with the assumption these were random uncoupled errors, and therefore could be combined in quadrature.

high enough pressure is reached, the molecules would be close enough together that quantum exchange interactions that had previously been neglected would start to become significant.

For curiosity, the expected shift for detonation can now be calculated. For single crystal HMX detonation with a pressure of 40 GPa and a temperature of 7000 K, the expected sodium peak red-shift from this calibration would be 77 nm - significantly more noticeable than in deflagration.

4.5 Summary on red-shift calibration

Following preliminary measurements that showed a red-shift in the sodium emission, the physical mechanisms of why a shift would occur were explored. Of these mechanisms, the collisional shift, specifically Lindholm-Foley theory, predicted shifts in deflagration of the same order of magnitude as those observed previously.

Experimentally determining the shifts, reaction pressures and temperatures resulted in a calibration curve that allows for the pressure of the reaction to be determined based on optical methods alone. This produces a measurement of pressure that is at the point of the reaction and is from the same light source as the temperature measurement as well as being simple, non-intrusive and fast.

These measurements also showed a relationship in agreement with Lindholm-Foley theory. The shift had the theoretical $PT^{-0.7}$ dependence, and a constant of proportionality of 950 GPa^{-1} $K^{0.7}$ nm, close to the 880 that was roughly calculated. The agreement shows that Lindholm-Foley is sufficient to describe the red-shift of sodium in deflagration conditions, and the approximations hold true. As a general collision theory, it can also be applied to other emitting species that may be present in a high pressure reaction, and so is not limited to sodium.

4.6 Applying technique with a streak spectrometer

With the above conclusion that pressure could be measured alongside temperature by studying the light emission, the next obvious question was whether this could be implemented. All the measurements of the wavelength spectra had been taken with a time-independent integrated spectrometer. However, if a time-dependent spectrum was recorded, the change of peak shift - and therefore, the change in pressure - could be examined during the deflagration reaction. The pyrometer built for temperature measurements (section 2.6) had the required time-resolution, but only used four wavelength channels. Therefore, a different piece apparatus was needed which had both the time-dependence of the pyrometer and the wavelength resolution of the spectrometer.

Such a diagnostic tool would be a streak-spectrometer - quite literally, a spectrometer which is connected to a streak unit, allowing the spectrum at different points in time to be measured, rather than just an integrated count over time.

4.6.1 Equipment

The spectrometer part of the apparatus - splitting the input light into the wavelength spectrum - was effectively just a newer model of the previous one [Princeton Instruments SP-2300]. However, rather than connecting this straight to a detector like before, the output was connected to a streak camera unit [Optronis Octoscope]. The multiple parts added a complexity, as they were not all controlled through one interface like the previous apparatus.

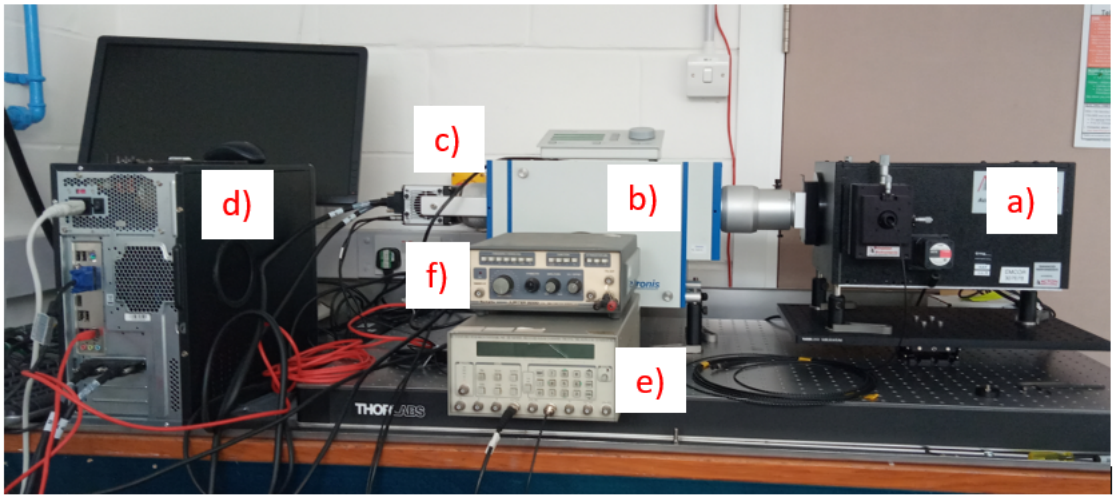

Fig. 4.8 The assembled streak spectrometer. The spectrometer (a) contained the input for the light emission, and split this into the spectrum. Then, the light passed through the streak unit (b) to the detector (c). The control software and results were present on a separate computer (d). A delay generator (e) was used to trigger the various parts of the assembled system, as each had associated delays. These delays were determined with the use of a controlled pulse into an LED from the pulse generator (f).

The completed setup of the streak-spectrometer is shown in figure 4.8. Given both the size of the assembled equipment, and the difficulty moving it, it was used to measure the deflagration in the fallhammer only.

The output of the spectrometer was manually connected to the streak camera opening, and so the wavelengths had to be calibrated anytime the equipment was moved, or the grating was changed or shifted on the spectrometer. This calibration was simple, as a spectral lamp with known peaks could be used. In particular, mercury was used as it had four clear peaks located from 405 nm to 579 nm. With 0.3 nm resolution from 400 to 650 nm, the wavelength resolution and range was comparable to the previous measurements. With the same technique as before, the intensity attenuation due to the optical components was accounted for using a lamp with a blackbody of known temperature.

Calibrating the timings was more challenging. Due to the multiple parts of the system, the internal delays to start the camera exposure and to start the streak unit were independent. With the use of an LED connected to a pulse generator to simulate the timings of a deflagration reaction, it was determined that the camera needed a trigger between 4 and 9 milliseconds (for a 10 ms exposure) before the light emission, and the streak unit had a delay of 375 μs after the camera was triggered for streak speeds of 10 μs mm^{-1}. This speed would allow a time resolution of 0.15 μs.

Given the millisecond delay for the camera, this cannot be triggered from the light emission, or even the rise in the strain gauge. Instead, the only part of the system that occured on a longer time-scale which could be used for triggering purposes was the falling weight. Therefore, a light gate was installed on the fallhammer system. When the weight broke the light, this would trigger a delay generator [DG535 Stanford Research Systems], which in turn would trigger the camera, and then the streak system.

By performing multiple drops with the light gate installed, the average time between this trigger and the reaction was measured as 17,890 $\pm$ 80 μs. This was for the reactions that occured on the ring-up of the pressure pulse - the minority that initiated on ring-down would not be captured. For a streak speed of 10 μs mm^{-1}, the total time the window of detection would be open for was 200 μs. With this window of opportunity, and the variations from the speed of the weight and time to reaction, only a fraction (roughly 50 %) of the reactions were able to be captured. As the experiments are easily done, this success rate is tolerable for the overall efficiency.

The total delays of the system, and the expected window of measurement, are summarised in figure 4.9.

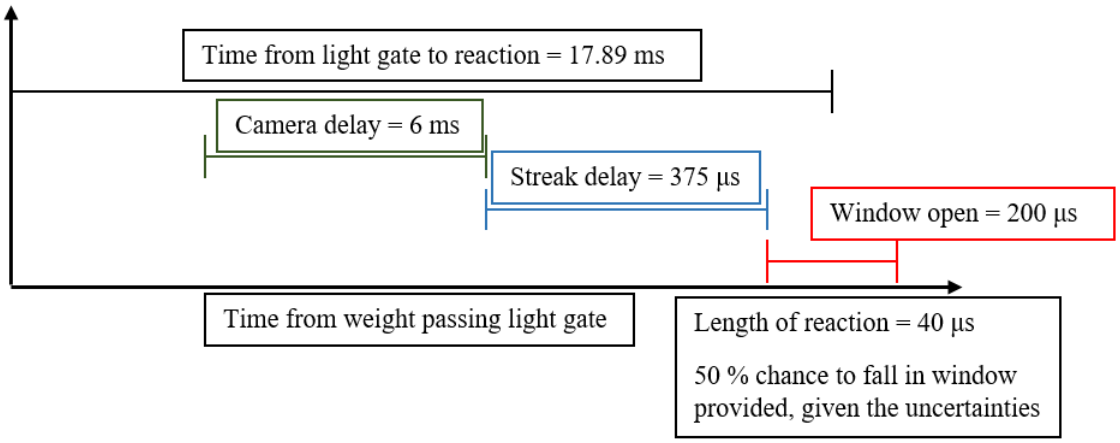

Fig. 4.9 The delays between the weight passing the light gate, and those intrinsic to the streak and camera system. These are not to scale, but provide an indication of the time needed to trigger the independent parts of the system, as triggering off the light or the strain gauge would be too fast.

With the equipment calibrated, it could then be used for measurements. However, it should be noted that the signal-to-noise (STN) ratio was lower than for the gated spectrometer. With the gated spectrometer the light over a larger period of time would be added together, and therefore just by the virtue of the streak spectrometer having time resolution, the individual frames of shorter time duration will be more noisy. Both these detectors had MCP plates

in order to increase the gain - the intensity - of the signal. For the gated spectrometer, a reasonable STN ratio was achieved with the gain levels available. However, even with the maximum value on the streak-detector, the STN was still low. Adding together nearby frames would increase this ratio, at the cost of the time resolution. Therefore, a balance had to be found in the analysis in order to achieve measurable data with an acceptable time resolution. In practice, this limited the resolution to 0.7 μs.

4.6.2 Fallhammer deflagration

With the high-resolution spectrum known at different points in time, both the temperature (from greybody fitting as before) and the pressure (using eq. 4.16) could be measured to observe their evolution with time.

Firstly, as shown in figure 4.10, the temperature results confirmed the previously measured pyrometer readings. The same technique as discussed in section 2.5.2 was applied for the temperature fits - a greybody was fit to the wavelengths that did not contain any spectral features (400 to 500 nm), and this was repeated for each point in time similar to the pyrometer measurements (section 2.6.2).

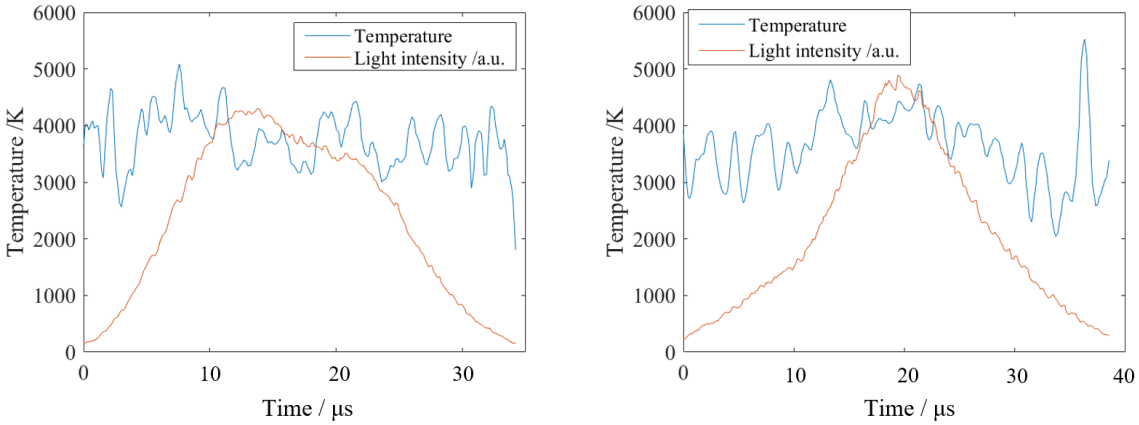

Fig. 4.10 The temperature (blue) and light intensity (red) of the reactions for two measurements with the streak camera. A greybody was fitted to the non-spectral part of the spectrum at each point in time. The large oscillations observed here, compared to the more smooth pyrometer results, were due to the noise present in the data, as the signal strength was not so large.

These two traces were typical across the dataset. Similar to the pyrometer measurements of the fallhammer these show a constant temperature across the period of main light emission. However, due to the significantly higher noise present in the streak-spectrometer, the uncertainty in the fit leads to the much larger oscillations observed in figure 4.10. These

oscillations are unwanted artefacts in the data, however they do provide a useful insight into the error associated with the temperature measurements, with the traces in figure 4.10 showing a total range of almost 1000 K during the main reaction period. With all the data, a mean temperature of 3900 $\pm$ 400 K was recorded for these measurements, in agreement with the previous measurements of 3900 $\pm$ 400 K and 4000 $\pm$ 200 K (Chapter 2).

The new technique added for these measurements was the pressure calculated from the shift of the centre of the sodium peak. At each point in time, the centre of the sodium peak was measured and the shift from 589.3 nm was recorded (fig. 4.11).

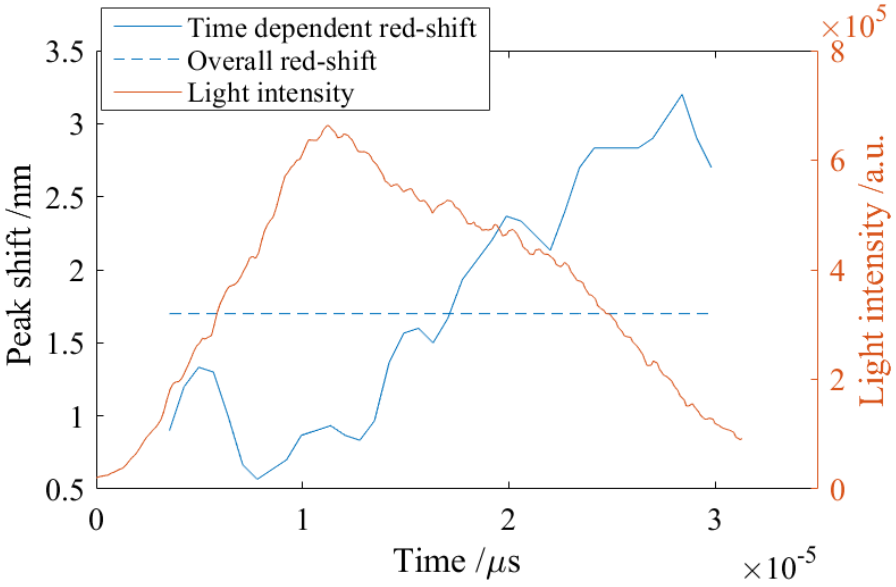

Fig. 4.11 The red-shift of the sodium peak (solid blue) and the light intensity (red) against time. The dashed blue line represents the centre of the sodium peak for the integrated count of all the time-spectra; what would be recorded for the previous gated spectrometer. All peak centres were recorded with an uncertainty of 0.1 nm.

In order to convert these shifted wavelength values into pressure, the above newly determined calibration ($\Delta\lambda = 950PT^{-0.7}$ nm) was applied. For each point in time the simultaneously measured temperature value, as determined by the greybody fit at the 'blue' end of the spectrum, was used in this calculation. Figure 4.12 shows two examples of the shift-calculated pressure, alongside the period of light emission, and the pressure of initiation from the strain gauge (the temperature is not shown in order to reduce the complexity of the graphs).

Unlike the temperature readings, there was not a 'typical' pressure trace, however there was a consistent pattern that was observed. In all cases there was a general rise in pressure with time. Shown in figure 4.12, these two results show the most increase of the rise

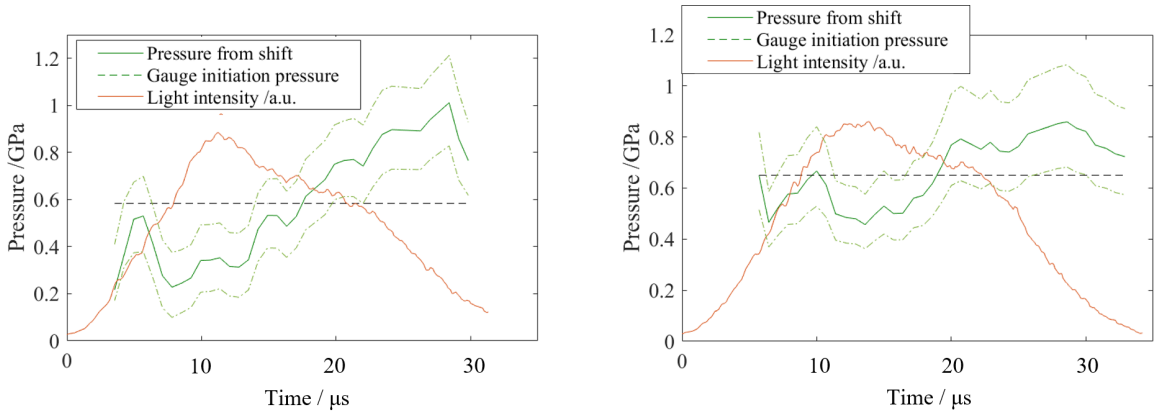

Fig. 4.12 The pressure calculated from the peak shift (solid green) at each point in time, compared with the initiation pressure according to the strain gauge (dashed dark green). The standard error on the pressure, calculated from the uncertainty in the temperature, calibration and peak shift, is also displayed (dot-dashed green). No pressure calculations are shown for times that no clear peak could be seen; for the low intensity measurements at the beginning and end of the reaction. For all readings, the average peak-shift pressure was in close agreement to the initiation pressure, and showed an increase during the reaction.

in pressure (left), and the least (right), with all results showing this trend towards higher pressures at later times. This would be expected, as the reaction would continually be producing moles of gas, which would be increasing the pressure over time.

With measurements of both temperature and pressure, and the dependence of the pressure measurement on temperature, the next obvious question was whether any pattern emerged between these two variables.

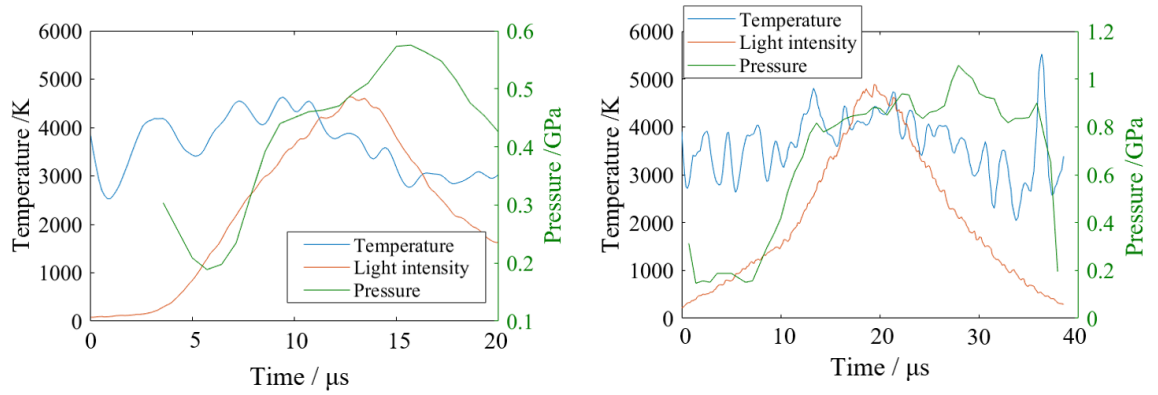

Fig. 4.13 The temperature and pressure during the main period of light emission. On the left shows the only experiment of six in which the temperature was not constant throughout the reaction, and falls during the pressure rise. On the right shows a more typical trace, with the pressure having no obvious effect on the temperature. Overall, no link was observed between these two variables.

Figure 4.13 shows two examples of the temperature and pressure over time. In the left reaction, a 'crossover' was observed, with the increasing pressure of the reaction occuring with a fall of the temperature - exactly the behaviour that would be expected with the higher-pressure Hopkinson bar deflagration showing lower temperatures. However, this was not a common trend, as in all other cases the temperature remains constant during the main period of light emission as mentioned above. As observed in the right reaction of figure 4.13, it was more often the case that there was no link between the pressure and temperature readings - that the temperature would often remain roughly constant whilst the pressure would rise. Save for an outlier, the data suggests that the pressure change during the fallhammer reaction was not enough to significantly effect the measured temperatures.

4.6.3 Summary on using streak spectrometer

A streak spectrometer was assembled in order to obtain a both a time dependence and a high spectral resolution of the light emission. Greybody fits to the low-wavelength non-spectral contributions gave temperature readings in agreement with those previously measured by the gated spectrometer and the 3-channel pyrometer. However, due to the lower signal-to-noise observed in the streak-spectrometer, the results obtained had larger variations and uncertainty.

The streak-spectrometer did allow the position of the sodium peak with time to be known, and therefore the behaviour of pressure with time from solely optical techniques. These measurements showed a trend of a pressure rise during the reaction, with the value averaging out to the mechanical initiation value obtained by the strain gauge. No significant pattern was observed between the temperature and pressure of the reaction.

With a higher signal-to-noise ratio, this data would become more accurate. However, even with this setup, it shows that time-dependent measurements of pressure and temperature can be made from just the light emission.

4.7 Conclusions

A new technique for allowing time-dependent reaction pressure measurements based solely on deflagration light was discovered, calibrated and verified.

With the different deflagration regimes from the fallhammer and the split Hopkinson pressure bar, the red-shift of the sodium emission was found to be in agreement with Lindholm-Foley theory, proving that this collisional based theory still holds as a good approximation under gigapascal pressures. Using the equation $\Delta\lambda = 950PT^{-0.7}$ nm, this new technique was used successfully in conjunction with a streak spectrometer to track the

pressure of the fallhammer deflagration reaction using only the optical light for the first time. These measurements showed a rise in pressure with time, accompanied by the known constant temperature.

Being based on a universal collision theory, the red-shift equation can be used on any system that emits some spectral light, as long as the diagnostics provide the resolution to observe a shift of the spectral peak. Being non-intrusive, simple and having instantaneous time-dependence, the method has a large advantage, allowing pressure measurements in systems that previously had difficulty in achieving such results.

4.7.1 Further research

The calibration graph constructed could be extended by considering other materials. The Hopkinson bar has a maximum initiation pressure of 2 GPa, if using maraging steel bars, and a minimum initiation of 1 GPa for HMX. In the fallhammer, all the reaction pressures recorded were similar, and all were done using the same batch of HMX. Using a different material, such as PETN or RDX, would also produce a high pressure deflagration reaction and would also show sodium emission in the spectrum (as sodium was observed in the burning spectrum of PETN and RDX in figure 2.5), but would initiate at lower pressures (Chapter 3). As the conditions of deflagration were important, not the molecule used to create them, including studies of deflagration on other energetic materials should increase the possible range of the calibration.

Taking advantage of the time-dependent nature of the peak shift, the experiments could be applied further than measuring the peak position in a simple fallhammer deflagration. The technique could be applied to more complex systems, such as a deflagration-detonation-transition reaction. As the deflagration progresses, the pressure could be dynamically measured at each point until detonation is achieved.

Given the relative simplicity of the method, it could be applied to any combustion reaction at high pressure, regardless of whether energetic materials are present, as long as the spectral emissions are seen.

Chapter 5

Mass Spectroscopy

5.1 Introduction

In Chapter 3, optical measurements of deflagration in a Split-Hopkinson Pressure bar (SHPB) were taken and compared to those measured in the fallhammer equipment from Chapter 2. The two main differences seen in the optical spectra were the increase in greybody radiation from solid particles and the significantly lower temperature in the SHPB deflagration. A hypothesis for this result was that the initiation conditions in the SHPB were causing the chemistry of the deflagration to change – that the reaction pathway was affected due to the constant higher pressure present to favour different reaction products. These would lower the expected temperature of the overall reaction as the enthalpy (energy) of formation of these reaction products would differ from the idealised products, as well as potentially producing more solid particles which would radiate the greybody emission.

When theorizing the reaction of HMX, the initiation method is often not taken into account [4, 144], such as in section 1.2.6, where the 'ideal' reaction was stated independent of conditions. In order to properly simulate deflagration, the 'normal' chemical pathway of the reaction is an important part of the modelling process, and therefore, if it is dependent on initiation method, such information would be essential in order to provide accurate simulations of different deflagration scenarios. After all, most accidental initiations in real-life do not occur in a fallhammer (or SHPB) -like environment, with a small amount of material between two hardened steel anvils. Therefore, to increase the safety in handling and using energetic materials, the 'typical' deflagration reaction has to be understood, and should not be assumed to be the same for all situations.

Considering the reaction chemistry, it is obvious that external conditions such as temperature, pressure and material quality would affect the reaction pathway and products [145, 146]. In addition, there is a precedent in reactions of energetic materials that the type of reaction

(whether detonation, deflagration or decomposition) does change the chemical pathway, and therefore, observed products [147]. Also, previous research into the decomposition chemistry at different pressures (1 and 68 atmospheres) showed a change in the released products [146, 148]. Therefore, with deflagration instead of decomposition, a change of initiation method (and therefore a different pressure) would most likely affect the chemistry, which could be determined by examining the reaction products. Whether this change in the chemistry was significant or measurable - as the optical spectroscopy would suggest - was the motivation for the following experiments.

In order to test the hypothesis that the reaction was significantly changing, a mass spectrometer was attached to both the fallhammer and the SHPB during a deflagration reaction. This was reminiscent of previous experiments done at the Cavendish [107, 2], where a mass spectrometer was used as another diagnostic to determine if a material had reacted by monitoring the mass increase of likely reaction products. The main goal for this experiment was to compare the products of the two initiation methods, in order to test the hypothesis that the overall HMX chemical reaction between the two was different. The intent here was not to fully describe the chemistry of the reaction, but to do a relatively simple test to determine whether any differences could be observed in the chemistry by investigating the intensity of a few reaction products masses.

Other experiments were also conducted. Before comparing the two deflagration regimes, the mass spectrum could capture the products of decomposing HMX, allowing a different regime to be compared to deflagration. Also, both RDX and PETN were initiated in the fallhammer to determine if different secondary explosives could be distinguished from the measured products.

5.2 Method

5.2.1 Equipment

A quadrupole mass spectrometer [Hiden Analytical RC PIC Quadrupole] was used along with a vacuum system designed and built by Andrew Jardine and Sue Gymer. The vacuum system was required as the mass spectrometer operates at low pressures of order 10^{-6} bar, and so a series of pumps were needed to lower the room pressure of 1 bar down to this value.

Shown in figure 5.1, the input tube (a) was connected next to the deflagration reaction, where the products would enter and then pass into the first chamber (b) kept at pressures of order a milibar by the first pump (c). They would then pass onto the second chamber (d) held

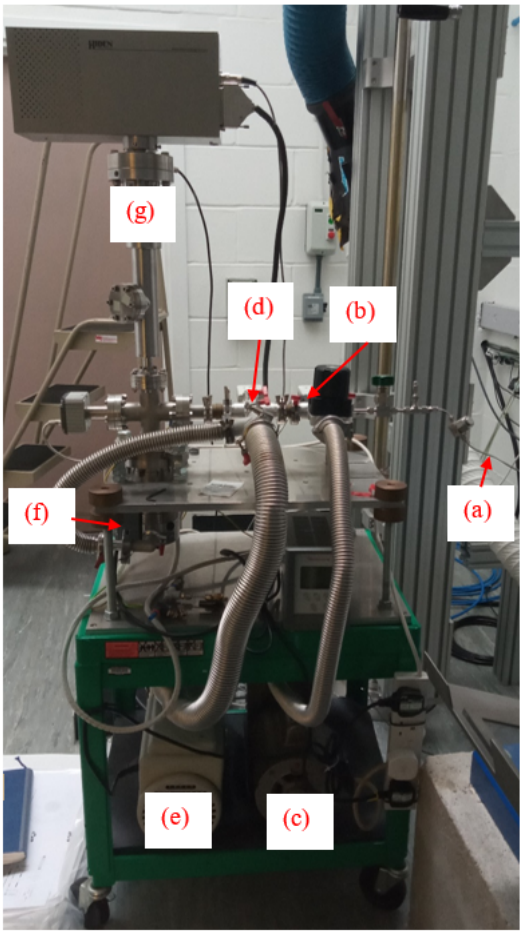

Fig. 5.1 The combined vacuum system and mass spectrometer used in these experiments, see body of text for the descriptions of the components labelled.

at 10^{-2} mbar by the second pump (e). Finally, a turbo pump (f) kept the vacuum around the mass spectrometer (g) at 10^{-6} mbar, where the products would be detected.

As would be expected, the process of travelling from the reaction to the mass spectrometer was considerably slower than that of the light, and the mass spectrometer had a time resolution of hundreds of milliseconds. This meant it would not immediately detect particles, nor provide a good estimate for the time the reaction took - it is a post-reaction integrated result. Therefore, it was not triggered from the reaction like the other diagnostics. Instead, it started detecting before the reaction occurred, and then turned off manually when it was done - typically a process taking 30 seconds.

Similar to the optical spectrometer, the mass spectrometer had a variable voltage gain, to allow for different intensities to be measured. This had to be well controlled to allow for enough counts to be seen, but not too many to saturate the detector.

With the variable gain, as well as other uncontrolled variations – most importantly, the fact not all of the products from each reaction would be captured in the equipment – meant that the absolute number of counts would not be meaningful from experiment to experiment. Instead, the reaction products would be compared by measuring the increase in counts from multiple masses within the same experiment. From this, the proportion of each mass present in the products was calculated for each reaction that occurred, which could then be compared with others.

5.2.2 Gas collection

In order to collect the gases produced in deflagration, a technique similar to what was done in the previous experiments was used. A hole was drilled in the side of the sleeve surrounding the reaction. Instead of fitting in an optical fibre or gas gauge, this was used to connect the mass spectrometer input tube to the reaction plane of the experiment.

Both the fallhammer anvils and SHPB bars would not be a closed system under vacuum, and so relied on the assumption that enough of the products would be captured through the mass spectrometer to be reliably detected. The remainder could escape out around the anvils/bars, or potentially with the optical fibre if it was blown out. However, given the identical setup on both the fallhammer and the SHPB, such an arrangement would not affect one more than the other.

5.2.3 Choice of masses

Noted above, the experimental setup means that not all of the created reaction gases would be captured. Along with the variable gain setting on the mass spectrometer this means that recording the total number of counts for each mass would not be an accurate representation of the system. Instead, working on the assumption that the escaped gas would have the same molecular makeup as the captured gas, the increase in counts for multiple masses as a percentage of the overall count increase would be considered.

Such a method required the mass spectrometer to detect at least two different masses in the same experiment, though the more that could be measured, the better the comparison would be. To accurately calculate a count increase meant that the signal intensity had to be high enough so a significant increase over the background could be detected, however not too high that it would saturate the detector. Comparing different masses in the same experiment – with the same gain setting – meant that the chosen products had to have a similar intensity, otherwise the count increase of the weaker intensity product would be negligible.

There were other constraints on which products to pick. Figure 5.2 shows the typical background of air, showing high intensity peaks at water ion masses (16, 17 and 18 for O_2^-, OH^- and H_2O), as well as nitrogen (28 for N_2) and oxygen (32 for O_2). Therefore, these masses could not be chosen to monitor the reaction as they were so abundant in air that the increase due to the reaction would not be significant.

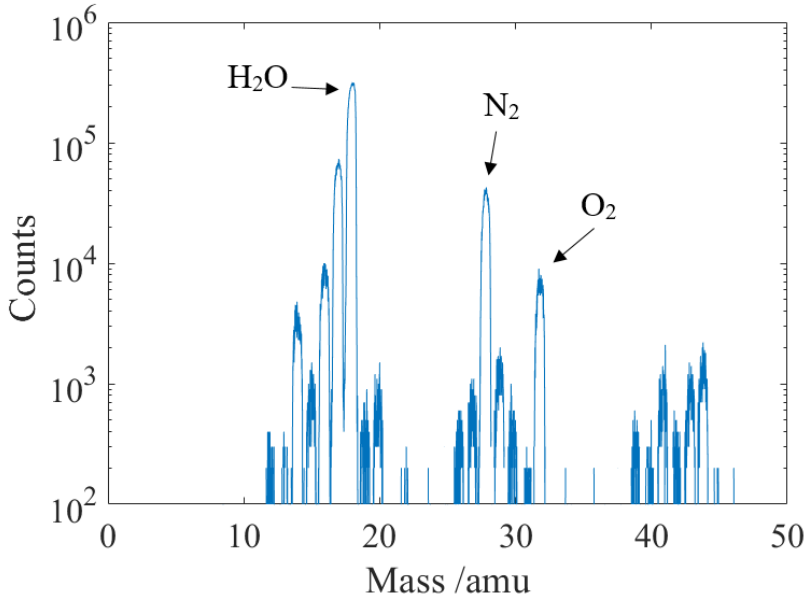

Fig. 5.2 The background air spectrum of masses from 4 to 50 amus. Counts above 10^6 should be avoided to avoid damaging the detector. The major peaks in air of H_2O, N_2 and O_2 have been labelled.

Mass /amu	Product(s)	Comments
12	C	Measurable
14	N ion	Major component in air
16	O ion, NH_2 ion, CH_4	O ion major component in air
17	OH ion, NH_3	OH ion major component in air
18	H_2O	Major component in air
28	N_2, CO	N_2 major component in air
30	NO, CH_2O	Measurable
32	O_2	Major component in air
44	CO_2, N_2O	Measurable
46	NO_2	Weak signal

Table 5.1 The masses, and the corresponding molecules, as observed in the preliminary mass spectrometer experiments into finding the right masses to detect in deflagration.

Table 5.1 details the common possible masses of reaction products that would be seen in HMX deflagration, and whether they would be suitable for study. Three masses were identified; masses 44 (CO_2 and N_2O), 30 (NO and CH_2O) and 12 (C) all had a comparable count intensity, so a measurable increase in counts could be seen in all three in the same experiment with the same gain setting.

Two other points should be considered. First, the mass spectrometer used did not have the mass resolution to determine the difference between CO_2 and N_2O, nor NO and CH_2O. Therefore, it would be impossible to distinguish or identify which of these products was made. Secondly, masses could fragment on the filament, and so the peaks could be due to a larger molecule fragmenting, e.g. C from a CO_2 molecule rather than from the reaction itself. However, this fragmentation should be the same from experiment to experiment and so would not affect the comparison being made.

5.3 Decomposition

The materials were first reacted in air to examine the reaction products before observing deflagration. However, in an attempt to lessen any unwanted masses to be detected, the material was not burnt over a butane flame. Instead, 10 mm^3 of material was placed on a high resistance wire, which was then heated up by applying a large voltage, causing the material to melt and react. An inverted funnel connected to the mass spectrometer then collected the products.

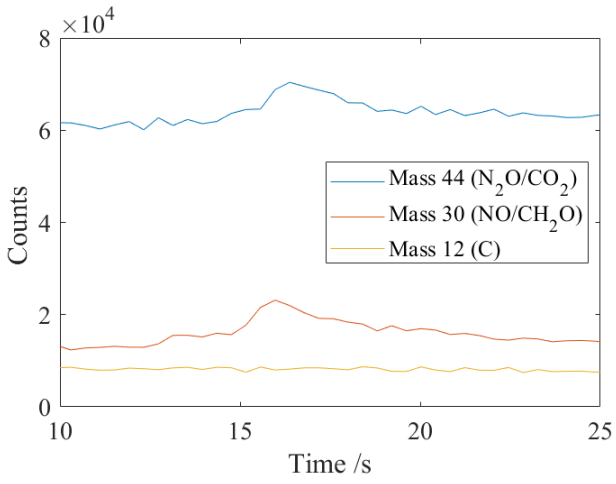

Fig. 5.3 The counts of the three masses against time, where the increase due to the reaction can be seen starting at 14 seconds, with the peak at 16 s. From this trace, it is clear that mass 30 and 44 show a large increase of counts, whereas mass 12 showed no significant change.

Figure 5.3 shows a typical trace from the mass spectrometer of HMX decomposition. The background value of each mass was calculated by taking an average of the counts before the reaction. Then, this value was taken away from the maximum value in order to establish the increase of counts upon reaction. The total increase in counts for all three were added together, and the proportion of each was calculated from the total increase, as shown in table 5.2.

	44 amu (CO_2 and N_2O)	30 amu (CO and CH_2O)	12 amu (C)
Proportion /%	38.6 ± 1.8	57.5 ± 1.0	3.8 ± 0.9

Table 5.2 The proportions of each mass in the decomposition reaction.

The error in each individual count increase was determined by considering the fluctuations in the 'constant' background signal away from the peak. This resulted in a percentage uncertainty of roughly 2 % for the largest signal (mass 44) and a 4 % percentage error for masses 30 and 12. Therefore, the uncertainty reported in table 5.2 was due to the spread of data, rather the individual measurement uncertainty. The measured ratio of masses was similar to those measured by Oyumi and Brill [148]. In both cases, a larger quantity of mass 30 (CH_2O and NO) than mass 44 (CO_2 and N_2O) was present.

With these results, it showed that the mass spectrometer could pick up measurable count increases due to the HMX reaction, and gave an indication of the intensity of counts – and the voltage gain required – that would be observed for deflagration.

5.4 Fallhammer

In order to achieve consistency between the fallhammer and SHPB deflagration, 40 mm^3 of HMX was used in both. This increase (from the previously used 10 mm^3) also increased the observed signals in the mass spectrometer, because more material reacting meant more reaction products which would be detected.

The experiment was run a total of eight times, to ensure that enough data would be accumulated, but also with an intention to minimise the amount of HMX used. Both the mass spectrometer and the pyrometer were attached to these experiments, to measure the overall average proportion of reaction products, and also to investigate whether the temperature of the reaction (as measured on the pyrometer) had a dependence on the reaction products observed.

Table 5.3 details the average proportions of each of the same masses as used in the above experiments.

	44 amu (CO_2 and N_2O)	30 amu (CO and CH_2O)	12 amu (C)
Proportion /%	80.0 ± 2.3	10.8 ± 2.8	9.2 ± 1.8

Table 5.3 The proportions of mass 44, 30 and 12, and the standard deviations, from eight deflagration experiments in the fallhammer apparatus.

The error in the measurement was the same to that reported in the decomposition experiments as the background behaviour did not change, and so the reported uncertainty in table 5.3 was due to the spread of the results over eight experiments.

Immediately, it is clear the products are significantly different from those observed in decomposition/burning. This is clear evidence that the 'ideal' or dominant reaction pathways between deflagration and decomposition are significantly different. The largest difference is the increase in mass 44 in the fallhammer experiments – with deflagration producing a higher proportion of either CO_2 or N_2O, compared to NO and CH_2O. The higher pressure environment in deflagration would favour a lower reaction pressure according to Le Chatelier's principle - that changes in the conditions of a system (such as pressure) would lead to an opposing change in the reaction in order to achieve a more equilibrium state. This lower reaction pressure could be achieved by the creation of fewer moles of gas. By producing the larger gas molecules of N_2O rather than NO/N_2 in the higher pressure deflagration, this would lead to the overall creation of fewer gas moles from each HMX mole, and so a lower pressure in the reaction products.

Likewise, it can be seen from table 5.3 that the proportion of free carbon atoms in the reaction products increased. This could be a higher fragmentation of larger molecules into carbon, however it could also be seen as evidence of Le Chatelier's principle, as solid carbon would lead to a lower pressure than a gas molecule. Despite carbon not being included in the 'ideal' reactions, the formation of this element in energetic reactions through other chemical pathways is well known, and there have been many studies on the properties of this 'detonation soot' [149–154]. The condensed carbon in the soot often was described as having a complex composition, with many different morphologies present [151, 152]. However, it was noted that the amount of soot produced - and the compoisition - was influenced by environmental conditions and peak pressures of the reaction [150, 153].

Therefore, only from the average proportions of a small fraction of the total reaction products, it is clear that deflagration chemistry is different from decomposition – with either a different chemical pathway present, or the same available pathways with different ratios of probability of occurring.

Such a result, as mentioned above, had previously been observed [147], with the same decrease of NO (and increase of CO_2) seen. Therefore, the mass fractions measured from the

decomposition (table 5.2) and fallhammer deflagration (table 5.3) confirmed a previously known measurement, as well as provided a comparison for when the SHPB would be used for initiation.

5.4.1 Temperature dependence

When different products are created in a reaction, the overall released energy would vary, due to the difference in enthalpy of formation of the various products. As noted before (Chapter 2), the fallhammer experiment is very stochastic, with a wide range of temperatures. The use of a mass spectrometer measuring simultaneously with the pyrometer allowed the temperature to be compared to the proportion of masses, and determine whether there was a correlation present – whether changes in temperature could be linked to the changes in the proportion of these three masses.

Figure 5.4 shows the results of plotting the proportion of each mass against the recorded reaction temperature from the main reaction period.

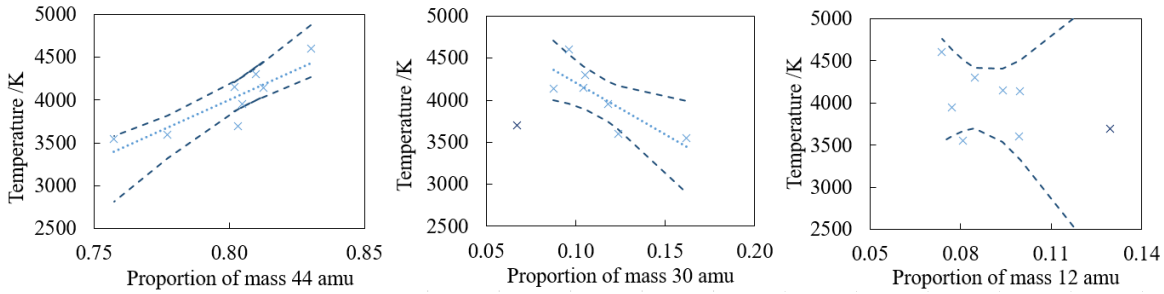

Fig. 5.4 The dependence of temperature on the proportion of each of the three masses investigated. Linear regression was performed to indicate the trends present in the data, with 95 % confidence limits shown. Mass 44 showed a strong positive correlation and mass 30, accounting for one outlier where significantly more mass 12 was produced, showed a negative correlation with temperature. No significant correlation was observed between mass 12 and temperature.

Mass 44 (CO_2 and N_2O) shows a clear correlation with temperature, with an increase in the proportion present with a higher temperature. Whereas, with the exception of one outlier (at 3700 K, where less mass 30 and more mass 12 was present than expected), an increase in mass 30 is associated with a lower measured reaction temperature. Mass 12 - carbon - did not show any significant correlation with temperature.

Table 5.4 details the enthalpy of formation of the molecules for the chosen masses. With a larger enthalpy of formation, more energy would be required in order to make the product, and so the available energy for heat/temperature would be lower. Comparing the carbon

Molecule	Enthalpy of formation / kJ mol^{-1} [78]
CO_2	-393.5
N_2O	83.0
NO	90.3
CH_2O	-179.2
C	0

Table 5.4 Enthalpies of formation, taken from NIST [78], of various molecules of reaction products.

products (CO_2 and CH_2O) separately from the nitrogen ones (N_2O and NO), it can be seen that the mass 44 products have a lower enthalpy than those of mass 30, therefore leading to a higher temperature of the reaction – as observed.

To test this, a mass spectrometer with better mass resolution would be required. However, the aim of these experiments was not to determine the entire chemistry of the reaction, but rather to see whether changes in the reaction properties could be experimentally verified against the chemistry. The correlation observed in the fallhammer data shows a definite correlation between products and temperature – indicating that the measured temperature was a result of the chemical reaction, as previously assumed. And therefore, that the wide variation in reaction temperature in the fallhammer was due to changes in the 'overall' chemical reaction occurring in the HMX deflagration.

5.4.2 Comparing different energetic materials

Before the mass spectrometer was moved to the Hopkinson bar deflagration experiment, it was kept on the fallhammer in order to test another hypothesis. HMX, RDX and PETN are all granular secondary explosives with similar properties. The 'ideal' decomposition reactions (eq. 5.1 – 5.3) show that the reaction products have the same proportions for HMX and RDX, however PETN has a noticeable difference in that CO_2 is also present in 'ideal' decomposition [4]:

$$HMX \rightarrow 4CO + 4H_2O + 4N_2 \tag{5.1}$$

$$RDX \rightarrow 3CO + 3H_2O + 3N_2 \tag{5.2}$$

$$PETN \rightarrow 2CO + 3CO_2 + 4H_2O + 2N_2 \tag{5.3}$$

It would stand to reason that there would also be variation in the non-ideal reaction products; in those produced by different chemical pathways. Therefore, eight drops were also performed in the fallhammer with RDX and PETN in order to see if the mass spectrometer results alone would be enough to distinguish between energetic materials.

Material	44 amu (CO_2 and N_2O)	30 amu (CO and CH_2O)	12 amu (C)
HMX /%	80.0 ± 2.3	10.8 ± 2.8	9.2 ± 1.8
RDX /%	85.1 ± 1.8	8.7 ± 2.2	6.2 ± 2.0
PETN /%	91.4 ± 1.1	4.0 ± 1.4	4.7 ± 1.1

Table 5.5 The average proportions of each masses for HMX, RDX and PETN from eight fallhammer deflagration reactions.

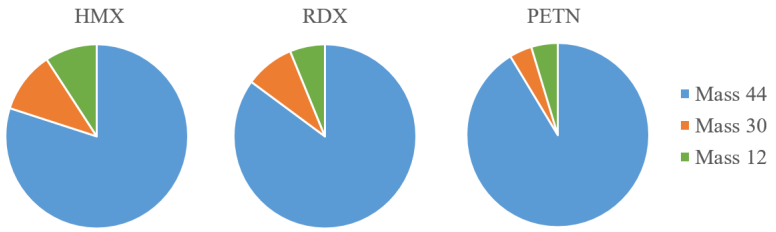

Fig. 5.5 A graphical representation of the proportions of each mass present in the fallhammer deflagration products of HMX, RDX and PETN.

From table 5.5, it was seen that there was a significant difference in the proportions of the three products – which can also be seen graphically in figure 5.5. From HMX, to RDX, to PETN, the proportion of mass 44 increases, with the resulting decrease in mass 30 and 12.

This increase in CO_2 was expected for PETN, as CO_2 is present in the ideal decomposition reaction (eq. 5.3), however what was also interesting was that HMX and RDX were distinguishable, indicating that the non-ideal pathways are different. The overall trend of the proportion of masses produced matches the order of impact sensitivity as observed in section 3.4. A possible explanation of these results is that as RDX initiates at a lower pressure, it could therefore favour the production of less solid products (mass 12), and therefore an increase of the gaseous CO_2 and N_2O.

Regardless, it was clear that by using simple mass spectrometry, and only a few product masses, the different energetic materials could be reliably distinguished.

5.5 Hopkinson bar

In the fallhammer, the average proportion of the masses was measured, along with the temperature dependence on the slight variations of each mass proportion between 'identical' experiments. Exactly the same set of experiments were run again in the SHPB in order to allow a comparison between the two initiation methods. Table 5.6 details the average proportions of each of the same masses.

	44 amu (CO_2 and N_2O)	30 amu (CO and CH_2O)	12 amu (C)
Fallhammer /%	80.0 ± 2.3	10.8 ± 2.8	9.2 ± 1.8
SHPB /%	84.0 ± 2.9	8.0 ± 3.4	8.0 ± 2.1

Table 5.6 The proportions of mass 44, 30 and 12, and the standard deviations, from eight deflagration experiments in the SHPB apparatus.

As can be easily observed, there was no significant difference between the proportions of the masses observed in the fallhammer compared to the SHPB, despite the large difference in reaction temperature.

However, firstly, it should be re-iterated that this solely means the combined counts of CO_2 and N_2O (and NO and CH_2O) were similar, so it cannot be assumed the concentrations of each molecule were similar. More importantly, as shown with the fallhammer data, the masses detected varied with the temperature measured, with a reasonable range present. Therefore, the average products detected should not be considered independent of the temperature of the reaction. Instead, the data points should be examined in product-temperature space and then compared in order to comment sensibly on the results.

5.5.1 Temperature dependence

Firstly, just the Hopkinson bar products were considered in order to examine whether the same temperature dependence was seen for the masses.

As shown in figure 5.6, similar to the fallhammer, a correlation can be seen between mass 44 and temperature and a strong negative correlation was measured between mass 30 and temperature. However, unlike the fallhammer, a potential positive correlation with carbon and temperature was seen. Similar to the argument above, this positive carbon correlation suggests that the higher pressures of the Hopkinson bar lead to a more favourable environment for the production of solid products, as this would lead to less gas moles – and therefore a lower pressure in reaction products – to be achieved.

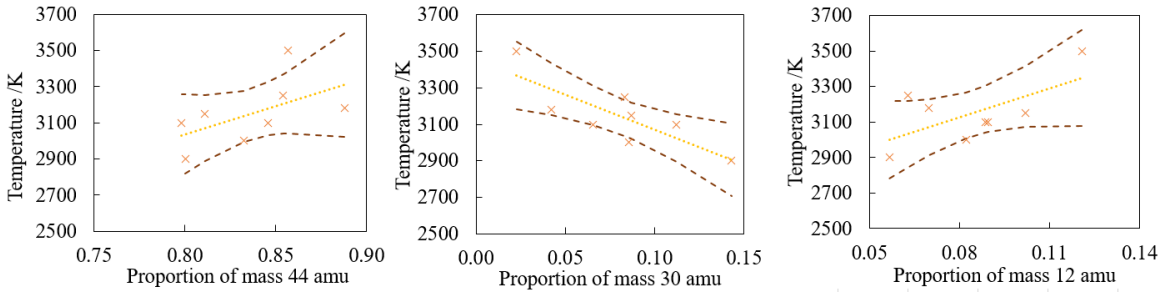

Fig. 5.6 The dependence of temperature on the proportion of each of the three masses investigated, with linear regression done in an identical fashion to the fallhammer data.

5.5.2 Comparison between initiation methods

Figures 5.7 and 5.8 compare the data of the fallhammer to the SHPB in the same space.

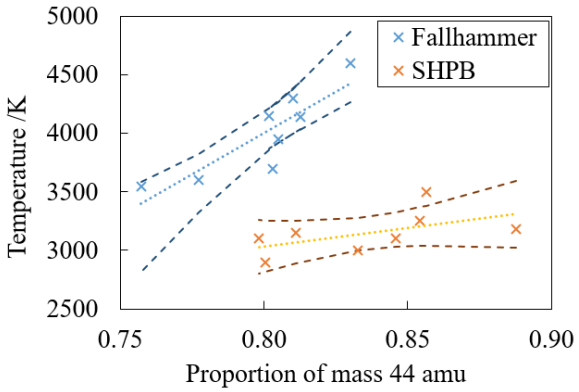

Fig. 5.7 The dependence of temperature on the proportion of mass 44, comparing the fallhammer data to the Split Hopkinson Pressure bar (SHPB).

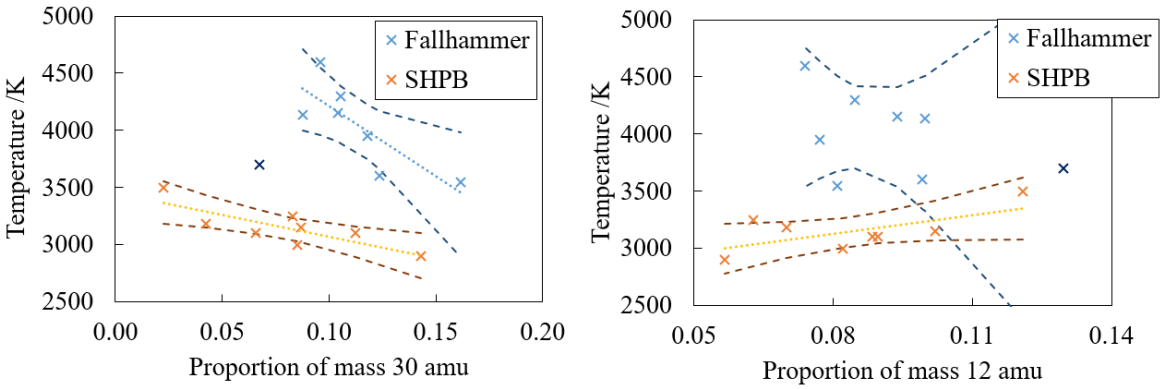

Fig. 5.8 The dependence of temperature on the proportion of mass 30 and mass 12, comparing the fallhammer data to the Split Hopkinson Pressure bar (SHPB).

For masses 44 and 30, although the general trend is the same, the data points for the two different initiation methods do not overlap in this product-temperature space and instead form independent groupings. The lower temperature SHPB initiation had a higher (on average) mass 44 production, and lower mass 30, contrary to what the individual trend of mass production and temperature indicate.

If these two different deflagration reactions had the same 'ideal' chemical equation – or same 'typical' pathways – it would be expected that the data points would meet – that the data from both experiments would lie on the same product-temperature trend-line. In such a case, the SHPB deflagration (which initiated the HMX reaction at a higher pressure) could have been modelled as a high pressure (and low temperature) deviation from the fallhammer deflagration. Instead, the data sets are independent in the space, with no transition nor overlap. This indicates that the chemistry between these experiments was different – or, at least, the same possible reaction pathways were present but with consistently different proportions. For example, a dominant chemical pathway in the fallhammer which leads to a high temperature and higher mass 30 produced might be negligible in the SHPB. Despite similarities in the reaction products, the fallhammer reaction always accessed a higher exothermic pathway, or one requiring a lower activation energy, than the SHPB counterpart.

The trend seen in the carbon products also strengthens this conclusion. Comparing the fallhammer results to decomposition, the higher pressure SHPB shows a more favourable environment for solid carbon production – as the temperature increased with more carbon production, unlike in the fallhammer, where no correlation was seen. This would also suggest other solid products would be favourable to be produced, therefore creating the higher greybody radiation as observed in optical spectroscopy (section 3.3.2).

The fact that both initiation methods show the same temperature dependence on mass 44 and 30, as well as the fact the average proportions of the three masses were not significantly different, indicates that the chemistry in both would be similar. It is important to remember, however, that despite how small the difference in the chemistry might be, the consequences of this difference was vast. For example, the measured temperature of the reaction was (on average) 1000 K different. Therefore, despite the similarities, the chemistry cannot be assumed to be the same - or at least, the variation between the reactions cannot be assumed to be a small perturbation. This conclusion should be considered when modelling or simulating deflagration under different initiation methods, as just a slight change leads to large measurable differences in the resulting reaction.

5.5.3 Comparison between deflagration and decomposition in product-temperature space

Shown in figures 5.7 and 5.8, the proportion of masses 44 and 30 amu had an observable relationship with the temperature of the reaction. With the previously measured decomposition products (table 5.2), knowing the temperature of this reaction would allow decomposition to be compared to both these deflagration reactions. The temperature of HMX flames at atmospheric pressures has been measured multiple times, with values within the range of 520 to 700 K [155–158]. Assuming a temperature of 610 ± 90 K, figure 5.9 shows the results of the addition of deflagration in product-temperature space.

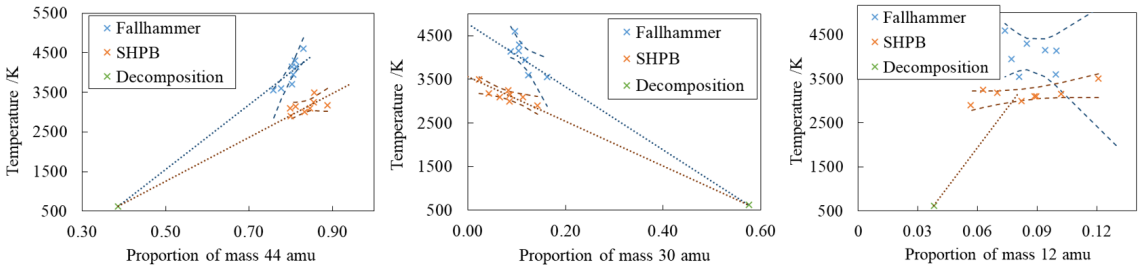

Fig. 5.9 The product-temperature space for the two deflagration reactions as before, with the added decomposition results. For masses 44 and 30, this added point is in agreement with the correlation observed between the proportion of mass and temperature that was already established.

With mass 44 and 30 amu, there is good agreement between the position of the decomposition data on the product-temperature space with the possible (within error) trends of both the fallhammer and SHPB datasets. This implies that decomposition can possibly be thought of as the low-pressure (or atmospheric pressure) variant of both of these deflagration reactions. Increasing the pressure under which decomposition occurs leads to a higher temperature of the flame [155], which could be used in further research to provide more data between the lower temperature decomposition and the higher temperature deflagration.

There was no agreement between the decomposition measurement and the deflagration results of mass 12 amu. This was expected with the fallhammer data as there was no obvious trend between product and temperature for this mass. Likewise, the SHPB data did not have a large gradient – measuring roughly the same intensity of mass 12 for each temperature, and, unlike the previous two masses, the ratio of mass 12 in decomposition was similar to that measured in deflagration.

The data for mass 12 amu provided no obvious dependence between the ratio of carbon produced and temperature. This could be due to the chemistry: that there are many pathways

with different enthalpies that produce roughly the same amount of carbon. Alternatively, the difference in behaviour between this mass and the two larger ones could be due to the experiment, such as molecules fragmenting in the mass spectrometer, and so both the carbon products and carbon fragments from larger molecules were being measured.

Future research using the mass spectrometer, where the experiment is conducted under vacuum and more mass species can be monitored, would allow a better understanding on which molecule production has the largest effect on the temperature of the reaction. This, in turn, would help enable the actual chemical pathways present in deflagration to be realised.

5.6 Conclusions

In summary, the mass spectrometer was attached to previously described energetic reactions, using three carefully chosen masses of reaction products. This allowed, firstly, different types of secondary explosives to be distinguished solely by the proportions of these three different masses detected upon the reaction.

The main aim was to compare the deflagration of HMX observed in both the Hopkinson bar and the fallhammer. Both deflagration reactions showed that the temperature of the reaction – as measured by the pyrometer – correlated with the production of mass 44 (CO_2/N_2O), and had a negative correlation with mass 30 (NO/CH_2O). These trends were also in agreement with the products and temperature of HMX decomposition, giving evidence that decomposition reaction chemistry can be thought of as the atmospheric pressure variant of the deflagration reaction. In contrast, mass 12 (carbon) had no strong correlation with temperature.

Despite the fact the average proportions of the masses had no significant difference, the two data-sets did not overlap in product-temperature space. On average, the hotter fallhammer produced less mass 44 and more mass 30 than the cooler Hopkinson bar deflagration. This indicates that the ‘typical’ chemical reaction is different for these two methods, or at least have different probable reaction branches, with the fallhammer consistently accessing more exothermic chemistry. Therefore, a typical deflagration chemical reaction cannot be assumed across all initiation methods and experiments.

Changes in the initiation method are enough to significantly affect the chemistry, which in turn leads to the higher pressure Hopkinson bar deflagration having a much lower reaction temperature. It also potentially leads to more solid products present in the reaction products, causing the more dominant greybody radiation observed in the optical spectrum.

Therefore, when modelling, simulating or comparing experimental results for deflagration, the initiation method should be taken into consideration. The different mechanical conditions

present are driving different reaction pathways, and the chemistry, though similar, cannot be assumed to be exactly the same. This change in chemistry leads to large differences in the temperature, as observed in Hopkinson bar deflagration. However, considering only three masses were considered, these results do not completely describe the chemistry, only prove that the initiation conditions and prevailing environment have a significant and measurable effect.

5.6.1 Further work

The obvious further research that could be done would be using a higher resolution mass spectrometer, so that the same mass products could be differentiated. Also, the experiment could be done in a proper vacuum, or in an inert argon atmosphere, so that primary products such as N_2 and H_2O could also be investigated. If the product gas was also trapped and collected, the whole mass spectrum of the products could be observed, rather than a transient measurement of three masses. This would allow the proper chemical pathways to be considered and worked out, so the actual chemistry could be known.

The mass spectrometer could also be attached to other energetic reactions, such as a laser-flyer deflagration, or deflagration initiated by friction or spark rather than impact. This would broaden the investigation on how the chemistry in deflagration depends on initiation, and which reactions have the most similarities (or differences). Detonation could also be examined in order to examine how the chemical pathways vary between detonation and deflagration. Considering the differences observed between decomposition and deflagration, it stands to reason that detonation would be very different again.

Chapter 6

Detonation

6.1 Introduction

After investigating burning and deflagration, the natural extension of the research was the last regime: detonation. This is the most violent reaction, with higher expected pressures and temperatures and shorter timescales involved. The aim was to design a detonation experiment that would reliably measure detonation velocity, pressure and temperature. Using the same HMX as in previous experiments, the light emission could then be compared to the less violent reaction emission spectra. Then, the system could be altered to investigate detonation behaviour upon changing the initial microstructure of the HMX (varying the density and particle size).

Unlike deflagration, detonation has some predicted behaviour based on shock physics. C-J and ZND detonation (section 1.2.3) could be used to model the characteristics of detonation, and the expected values of velocity and pressures could be estimated. However, the behaviour and dependences of temperature - a property that can be measured based on the light emission as previously shown - are not as well researched.

Given the more extreme conditions, designing experiments to safely measure detonation properties was more difficult. Deflagration could be achieved with a small volume of HMX, whereas steady detonation required enough material to support the shock front, increasing the size of the experiment and reaction. The experiments, above all else, had to be safe for all involved. Secondly, the diagnostic equipment also had to repeatedly survive the higher pressures in order to achieve any measurements, as well as be fast enough to accurately capture the faster timescales involved.

6.2 Calculating detonation properties

Detonation is a complicated reaction with many different processes happening simultaneously. The aim was to simplify the reaction as much as possible in order to gain rough estimates of the detonation velocity and C-J pressure, as well as how their behaviour changes with porosity/density. This model of detonation behaviour could then be applied to experimental results in order to test the accuracy of the data, and the assumptions present in the model used.

It was beneficial to see how far a look from first principles could be taken, and how accurate the answers could be calculated without added complications or empirical equations from other experiments. Therefore, the first approach of modelling was based on the shock conservation laws (eq. 1.1 - 1.3).

6.2.1 Shock conservation detonation model

First, the absolute values of detonation velocity and CJ pressure at 100% theoretical maximum density (TMD) HMX was considered, before any density changes could be added. These are both well-known properties (table 1.1), with measured values of 9.1 kms^{-1} and 39.5 GPa respectively.

Properties at maximum density

In order to estimate a velocity, a timescale and distance are required. In this instance, the aim was to determine the maximum possible velocity, and so intrinsic properties of the energetic molecule were chosen – bond lengths and the associated vibrational frequencies. For secondary explosives such as HMX, the nitro group - NO_2 - is a common feature and was used for these estimates.

This group has an average bond length of 1.224 Å[159] and a vibrational frequency of the N-O stretch of *circa* 1545 cm^{-1} wavenumbers ($\tilde{\nu}$) [160]. Calculating the potential maximum velocity that this group can have (and, therefore, achieving an upper bound on detonation velocity) was achieved by multiplying the bond length (d) by double the frequency (f). The factor of two is because this is the time it takes for one atom to affect its neighbour, rather than a full oscillation.

$$Velocity = 2 \times f \times d = 2 \times c \times \tilde{\nu} \times d = 11.37\, kms^{-1} \tag{6.1}$$

The calculated value of 11.37 km s^{-1} is clearly different from the measured values of nitro-group explosives (such as 6.90 in TNT, 7.35 in TATB, 8.65 in RDX and 9.11 in HMX

[8]). However, it is remarkably close despite all the approximations used, with dependence only on the properties present in the molecular scale of the nitro group. This approach – limited by the molecular vibrations – also agrees with the fact that across energetic materials a limit of 10 km s^{-1} seems to exist for detonation velocity, as the reaction cannot physically propagate faster based on the molecules present.

For pressure, a similar molecular based approach was taken, based on the chemical reaction producing 12 moles of gaseous products for each mole of solid HMX. Using the ideal gas equation, $PV = nRT$, and assuming a bulk temperature of 4000 K, this leads to an estimated pressure of 2.58 GPa, an order of magnitude lower than the 39.5 GPa expected for this reaction. This is because of the high concentrations involved; the ideal gas equation volume needs to be modified to include the size of the gas molecules: $P(V - nb) = nRT$, where b is a gas constant equal to 3.19×10^{-5} m^3 mol^{-1} for oxygen [161], for example. However, the value of b is calculated at ambient conditions and such an estimate leads to the model breaking down, as the predicted volume of the gas molecules becomes larger than the original volume, leading to an unphysical negative pressure. This is due to compression effects of the pressure on the atomic orbitals not being taken into account, and treating the molecules like hard spheres instead.

The reactions conditions were outside the limits of these simple gas equations. Therefore, the problem was approached using the shock conservation equations (eq. 1.1 - 1.3).

$$P = \rho \times u_p \times u_s = \rho_0 \times u_s^2 \times \left(1 - \frac{\rho_0}{\rho}\right) \tag{6.2}$$

Where, as before, ρ is the density of the material, u_p is the particle velocity and u_s is the shock velocity - and also equal to the detonation velocity D. Unfortunately, there is no simple estimate for the change of density (ρ compared to ρ_0) upon the materials being shocked. If the density increase was taken as very large, this would lead to an estimated pressure in HMX of $P = 1910 \times (9110)^2 = 160$ GPa, which is an order of magnitude too large for what would be expected. Therefore, the actual equation for the change of density with an applied shock had to be known (eq 6.3), which could only be achieved by empirically deriving them from experiments. From assembling multiple experimental measurements of the density of the material upon shock, Johansson and Persson found the following relationship between the shocked density and original density of HMX [52];

$$\rho = 0.14 + 1.26 \times \rho_0 \, g \, cm^{-3} \tag{6.3}$$

With this formula, the pressure at 100% TMD (1.91 g cm^{-3}) can be calculated as;

$$P = 1910 \times (9110)^2 \times \left(1 - \frac{1.91}{2.5466}\right) = 39.6\ GPa \tag{6.4}$$

Which is exactly the value expected. However, as stated above, it relied upon doing the experiment in order to gain a function of the density change, and so is a superficial - and indeed, circular - conclusion. Unlike the estimate for absolute detonation velocity, a simple first-principles approach was not possible to achieve a roughly correct estimation of the pressure. A method of estimating the density change, and therefore the detonation pressure, based on atomic/intermolecular compression using a Group Interaction Modelling (GIM) approach is discussed in section 6.2.2.

The values were calculated with the assumption of 100% TMD – no porosity present in the material. The motivation from here was to add another variable into the equations, and determine how the velocity and pressure would act with a decrease in density of the material, or equivalently, an increase of pores. With a decrease of explosives present in the sample, replacing it with air, it can trivially be assumed that the detonation velocity and pressure would decrease.

Velocity density dependence

Experimentally, the dependence of velocity on initial density is well known. Numerous sets of data show a rough linear decrease of velocity with density, in multiple different energetic materials [52]. Roughly linear repeatable dependence possibly suggests the dominating physics is simple, despite the large complexity of the detonation reaction.

To that effect, the velocity at each density can be estimated solely based on the proportion of energetic material in the material, and the shock velocity in both the HMX and the air. The total distance travelled (d) is the sum of the distance in HMX, and that in air. The proportion of distance in HMX was defined to be equal to the actual density of the material divided by the maximum density of HMX, which made the assumption that the material was isotropic, and that length scale is not important – that the density is the same regardless of the scale used.

$$d = d_{HMX} + d_{air} = \frac{\rho}{\rho_0} + \left(1 - \frac{\rho}{\rho_0}\right) = 1 \tag{6.5}$$

The time to cross each regime (t) is dependent on the speed of the shock (c) in each. The speed in HMX was simply taken as 9.11 km s^{-1}, the detonation velocity at 100% TMD, which ensured that the model reached the correct value at high limit, however requires knowledge of this velocity beforehand.

$$t = t_{HMX} + t_{air} = \frac{d_{HMX}}{c_{HMX}} + \frac{d_{air}}{c_{air}} \tag{6.6}$$

Therefore, the shock speed in air was required. Calculating this shock speed relies on the Rankine-Hugoniot equations presented in Chapter 1 (eq. 1.1 - 1.3), with an added detail. For this system, there were three different regimes instead of two: the driving gas (just reacted HMX), the gas being driven (air at ambient conditions before the shock wave), and the shocked air between these two states. Of these three states, the temperature and pressure of the driving gas and the driven gas are known (table 6.1), however the properties of the shocked air - the middle state - are unknown.

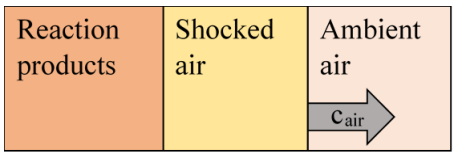

Fig. 6.1 The regimes of air required to calculate the speed of the shock in air (c_{air}). The reacted HMX shocks the air, which then starts to drive the non-shocked ambient air.

	Driving gas	Driven gas
Temperature	4000 K	300 K
Pressure	39.5 GPa	0.101 MPa

Table 6.1 Properties of the gases involved

The speed of the shock could be calculated using the mass and momentum conservation laws (from the Rankine-Hugoniot equations);

$$c_{air}^2 = \frac{p_2 - p_1}{\rho_1 \left(1 - \frac{\rho_1}{\rho_2}\right)} \tag{6.7}$$

Where the subscript 1 refers to the air before the shock wave (driven gas), and the subscript 2 to the shocked air, rather than the driving reacted HMX. The ratio of densities could be calculated, provided the assumption the air is a perfect gas, with $h = c_v T + \frac{p}{\rho}$ and $v = \frac{RT}{p}$. The driven gas is at ambient conditions, and so can be assumed perfect. However, as discussed previously, such an assumption starts to break at higher pressures. For the method presented here, the assumption is still used on the shocked gas, as such a treatment provided a physical and reasonable result, with the knowledge that this would provide a level of uncertainty to the calculation. The ratio of densities of the shocked and driven gas is therefore;

$$\frac{\rho_2}{\rho_1} = \frac{1 + \frac{\gamma+1}{\gamma-1}\frac{p_2}{p_1}}{\frac{\gamma+1}{\gamma-1} + \frac{p_2}{p_1}} \tag{6.8}$$

Where gamma represents the specific heat ratio. Therefore, in order to calculate the speed of the air shock, the only properties needed were the pressures in the shocked and unshocked air. The shocked air pressure could be determined by considering the conservation equations of mass, momentum and energy across all three regimes, including the driving HMX reaction product gas. This leads to a considerably more complicated form than the previously done equations as three regimes are being considered instead of just two.

For ease of time, the Wisconsin Shock Tube Laboratory online calculator was used [162]. This tool followed the conservation laws and gas equations presented above, with a full description of the method offered by Anderson's book: Modern Compressible Flow with Historical Perspective [163]. The driving gas was taken to be the HMX reactions products at a temperature of 4000 K and with the assumption they would behave similar to air. Inputting different driving gas pressures allowed the air shock velocity as a function of driving pressure (detonation pressure) to be calculated (figure 6.2).

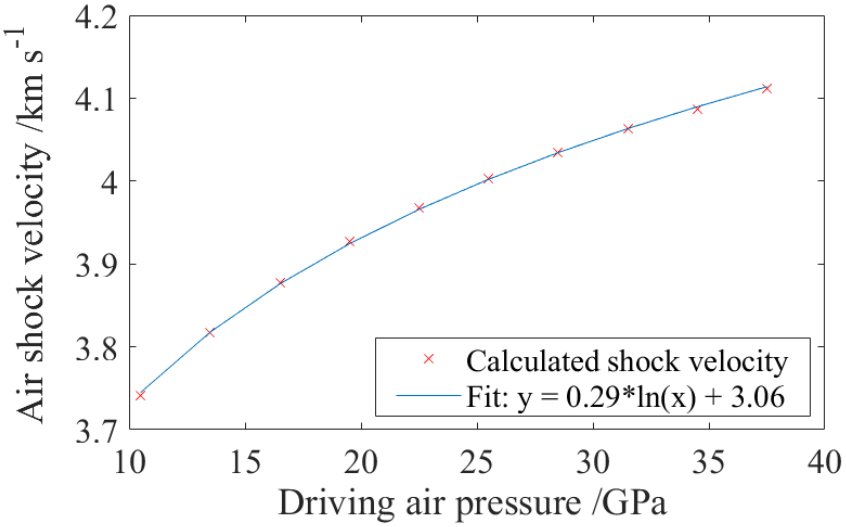

Fig. 6.2 The calculated shock speed in air as a function of driving gas (detonation) pressure for a driving gas temperature of 4000 K. The data was well described by a log function, which is a reasonable function for approximation as the velocity will drop to zero when the driving air pressure is equal to the ambient air pressure, and there will be a theoretical maximum velocity that the air can support, which it will tend towards at higher pressures.

Given the dependence of air shock speed on detonation pressure, an expected decreasing pressure with lower density HMX, would also cause the air shock speed to decrease. However,

this level of detail was not required for a rough estimate, and so the detonation pressure expected at 100% TMD was used (39.5 GPa). This resulted in an air shock speed of 4.1 km s^{-1}, and therefore the detonation velocity behavior with HMX density could be plotted based on equation 6.6. Figure 6.3 shows this relationship, having the roughly linear decrease as expected. When compared with previous experimentally measured detonation velocity in HMX [164], the model shows reasonable agreement, with a matching gradient but slightly lower values. However, when compared to the results achieved in this thesis (see below), a much better agreement is seen.

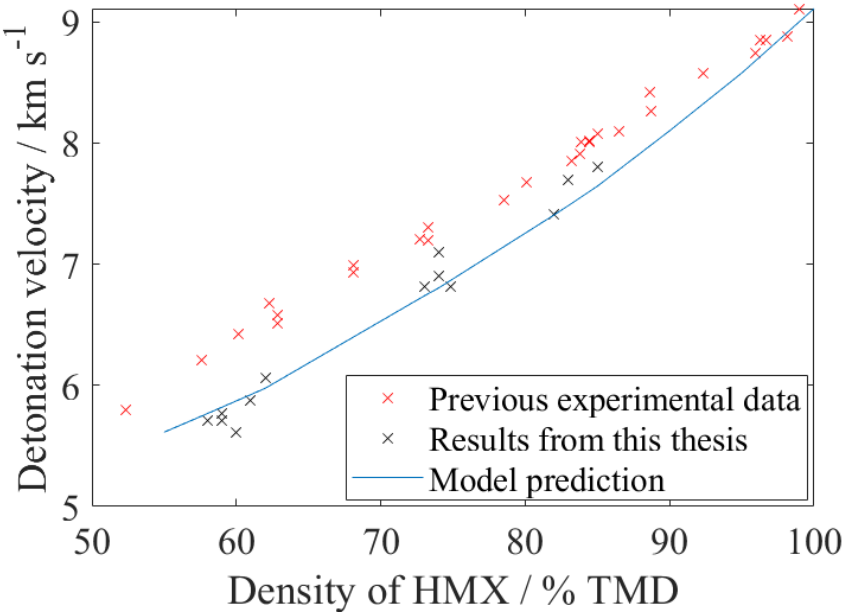

Fig. 6.3 Calculated detonation velocity at different values of HMX density using the shock conservation model, and compared against experimentally measured values at different densities of HMX in a 25 mm diameter column [164] as well as the results mentioned below in this research. Very good agreement can be observed.

The knowledge of the dependence of pressure with density would allow a more accurate estimation, but for a simple exercise, the calculations described above give a reasonable predicted behaviour, provided the velocity and pressure at 100% TMD are known.

Pressure density dependence

With a simple model of how detonation velocity depends on HMX density, the obvious next step was to attempt a similar method for the detonation pressure – especially as this relationship would improve the accuracy of the velocity calculation.

Equation 6.2 details the pressure dependence on density and detonation velocity. Therefore, the pressure at different densities can be calculated by changing the initial density (ρ_0), and using the corresponding detonation velocity at each density. Given the rough detonation velocities calculated above, and the empirical formula for estimating the density change (equation 6.3), the pressure as a function of density could then be known, shown in figure 6.4.

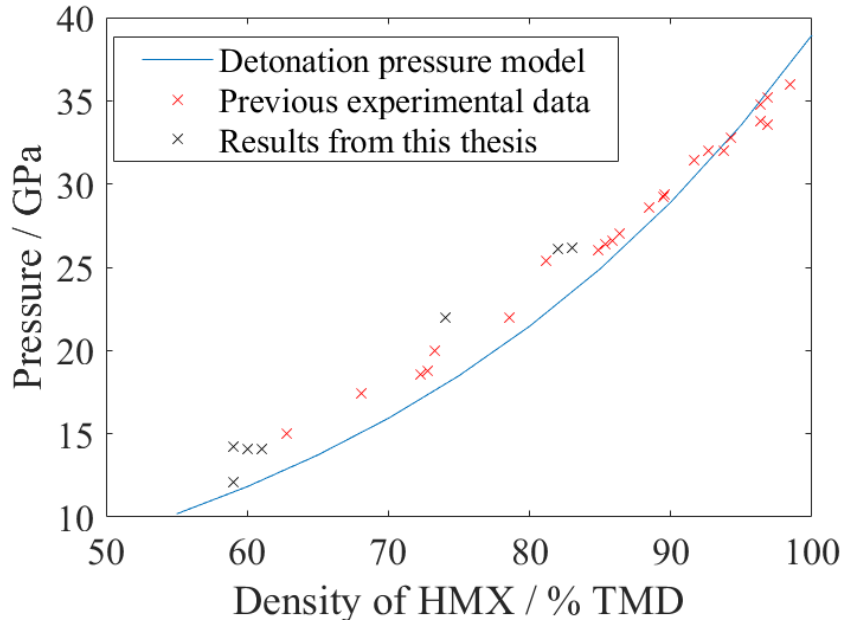

Fig. 6.4 Calculated detonation pressure from the shock conservaton model at different values of HMX density, using density-dependent detonation velocity values and the empirically determined density change in HMX upon detonation. This is compared to experimentally measured pressure in an HMX column, from the same experiments that measured the velocity with density as stated above [164], as well as the results achieved in this research.

Compared to previous experimental research, this simple shock model shows good agreement, especially at the higher density values. The pressure-density relationship can then be formatted into the calculation for detonation velocity, and repeated, theoretically growing more accurate with each iteration. However, with the other large approximations present in these calculations, there are likely larger sources of uncertainty present. Regardless, this does allow a simple prediction of the relationship between detonation properties and density as shown in figures 6.3 and 6.4.

The main problems associated with this model was that it could not accurately predict the 100% TMD detonation properties, and that the pressure calculations relied on empirically

determined density changes during the detonation process. With this in mind, a second model was considered.

6.2.2 Group Interaction Modelling (GIM)

The theory presented in the above section was based on shock physics, using conservation equations in order to predict behaviour of detonation properties. This methodology is well established, however there was another approach that was explored. The theory presented below follows the work of Porter on Group Interaction Modelling (GIM) [165], which was further developed by Gould and Cullis [166].

An approach to modelling energetic materials is to examine the intermolecular forces between the separate molecules, in a methodology more commonly used to describe polymer chains. The equation of state is dependent on the interactional energy between the chains, or in this case, the energetic molecules. This energy is a van der Waals potential, which depends on the distances present between the chains, and so is dependent on volume change. In an energetic material, the detonation pressure compacts the material and collapses any present voids, increasing the density at the shock front and therefore decreasing the volume – and distance – between constituent parts. Therefore, starting from a van der Waals potential provides an equation of state where the energy change, and therefore pressure, can be linked to this change of volume.

This model relies on the assumption that HMX, and its reaction products, can be described by the interaction energy equation of state. Detonation is treated as the moment at which the HMX molecules dissociate into their reaction products, accompanied by a sudden release of energy. By knowing the dissociation energy of the HMX, the conditions (volume change during dissociation/detonation) which led to this energy production can be calculated through the interaction energy equation of state, and then used to calculate the corresponding pressure that occurs at the same time as this energy release, as outlined below.

Treating the system as situated in an energy minimum – a quantum mechanical well – allows the interaction potential to take a Lennard-Jones form [166]:

$$E = E_{coh}\left(\left(\frac{V_o}{V_d}\right)^4 - 2\left(\frac{V_o}{V_d}\right)^2\right) \tag{6.9}$$

Where E_{coh} is the cohesive energy of the material, which in HMX is equal to 140,000 J mol^{-1} [166]. V_d is the volume of material during detonation and V_o represents the volume of the molecules at which the interaction energy is minimised which is equal to 161 cc mol^{-1} in HMX [166].

This relative change in volume upon detonation can be determined by considering the exotherm energy released from HMX dissociation, which is equal to 1.64 MJ mol^{-1} [167]. Assuming this energy is equal to only the interaction energy, this value was substituted into equation 6.9. Therefore, the volume ratio that would be required during detonation was calculated as: $\frac{V_o}{V_d} = 2.136$.

Pressure at 100% TMD

Once the equation of state is known, the pressure can be calculated by taking the derivative of the energy with respect to volume at a constant temperature. This results in the pressure taking the form of:

$$P = \frac{4E}{V_o}\left(\left(\frac{V_o}{V_d}\right)^5 - \left(\frac{V_o}{V_d}\right)^3\right) \tag{6.10}$$

Where E represents the absolute energy of the amorphous product system at ambient temperatures. This energy can be represented as a sum of the cohesive energy, the thermal heat, H_T, and the configurational energy, H_c [166]:

$$E = E_{coh} - H_T - H_c \tag{6.11}$$

The thermal heat can be calculated simply by considering the degrees of freedom, N, present using the equipartition theorem:

$$H_T \approx \frac{NRT}{2} \tag{6.12}$$

Taking the products produced in the HMX reaction (H_2O, CO and N_2), the diatomic gases have 5 degrees of freedom per molecule, and water has 6. This leads to a total of 64 degrees of freedom that are present in the products. The thermal heat is determined from the temperature under which the dissociation occurs (as equation 6.10 was achieved by differentiating the energy at a constant temperature). In this model, the HMX is treated as suddenly dissociating, and so the temperature would therefore be at *circa* 300 K, giving a thermal heat of 80,064 J mol^{-1}.

The configurational energy is less obvious. This term refers to whether the material is amorphous or crystalline. In detonation, the products formed have no configuration and so Group Interaction Modelling [165] is used to provide an empirically derived approximation of the energy of the products dependent on the cohesive energy and thermal heat only:

$$E = 0.89E_{coh} - H_T \tag{6.13}$$

Using the value of 140,000 J mol^{-1} for the cohesive energy as stated above, with the calculated thermal energy, the total energy, E of the reaction products is therefore equal to 44,530 J mol^{-1}.

This value can be substituted into equation 6.10, along with the change of volume, $\frac{V_o}{V_d}$ = 2.136, to calculate a detonation pressure of 38 GPa, which is in good agreement with the experimentally determined value of 39 GPa.

Velocity at 100% TMD

Taking the assumption that the system is analogous to a one dimensional lattice with spacing a, mass of molecules m and spring constant k between the molecules, the natural frequency of oscillations, ω can be stated as:

$$\omega = \sqrt{\frac{k}{m}} \tag{6.14}$$

From the frequency of the oscillations, the speed that this disturbance takes is equal to $a\omega$. With the density, $\rho = \frac{m}{a}$, and pressure, $P = k\delta a$, the speed can be written as:

$$c = a\sqrt{\frac{k}{m}} = \sqrt{\frac{P}{\rho\,\delta a/a}} = \sqrt{\frac{P}{\rho\,\Delta V/V}} \tag{6.15}$$

Where the change of volume is $\frac{\Delta V}{V} = 1 - \frac{V_d}{V_o} = 0.532$ for HMX detonation. Therefore, when a shock passes through the system, the shock speed (in Eulerian coordinates - the reference frame of the current wave compression) is equal to this speed c, which is dependent on the pressure, density and change of volume of the shock. However, this is not equal to the detonation velocity D. In order to calculate D, this requires the shock speed to be in the reference frame before the shock front (Lagrangian coordinates), which is achieved by adding c to the particle velocity u_p.

The relationship between the particle velocity u_p and the velocity c can be found by considering the volume change after a shock passes through the system. The initial volume of material, $c\delta t$, is compressed by the particle velocity following the shock by the volume $u_p\delta t$. Therefore, the particle velocity can be found as:

$$u_p = \frac{\Delta V}{V}c = \sqrt{\frac{P\Delta V/V}{\rho}} \tag{6.16}$$

With the particle velocity known, the detonation velocity $D = u_p + c$ can be achieved. Using the above calculated pressure of 38 GPa, the relative volume change of 0.532, and the density of HMX of 1.91 g cc^{-1}, u_p was equal to 3.25 km s^{-1} and c equal to 6.11 s^{-1}.

Therefore, the detonation velocity was 9.36 km s^{-1}, in reasonable agreement with the documented velocity of HMX of 9.11 km s^{-1}.

Property	Value
E_{coh}	140,000 J mol^{-1} [166]
$E_{dissociation}$	1.64 MJ mol^{-1} [167]
H_T	80,064 J mol^{-1}
$E_{products}$	44,530 J mol^{-1}
V_o	161 cc mol^{-1} [166]
$\frac{V_o}{V_d}$	2.136
$\frac{\Delta V}{V}$	0.532
Density	1.91 g cc^{-1}
Pressure	38 GPa
Velocity	9.36 km s^{-1}

Table 6.2 A summary of the properties used and calculated for HMX detonation following the GIM framework

Density dependence

Following the GIM approach provided accurate estimations for detonation of a single crystal of HMX at 100% TMD. Like before, once the values of a single crystal of HMX was known, the aim was then to calculate how these values changed with initial starting density, in an attempt to fit them to previous data.

The pressure was reliant on the volume of the material, the energy per unit mole, and the relative change of volume upon detonation. In order to change the density, a new unit cell could be considered, with a ratio of empty space to HMX crystal. For example, for an 85% TMD initial density, a 'mole' of material would consist of an 85:15 split between HMX and empty space/air.

This decreases the energy per mole, whilst increasing the volume:

$$E_{85\%} = 0.85 E_{100\%} \tag{6.17}$$

$$V_{85\%} = \frac{1}{0.85} V_{100\%} \tag{6.18}$$

Assuming the relative volume change in detonation was the same, the above changes lead to a relationship between pressure and initial density that is similar to that derived using the shock conservation model, as shown in figure 6.5. The advantage of the GIM approach

is that it calculates the change in volume using energy dissociation measurements, which does not require previous detonation experiments to be done, unlike the empirically derived density relationship used in the shock conservation model.

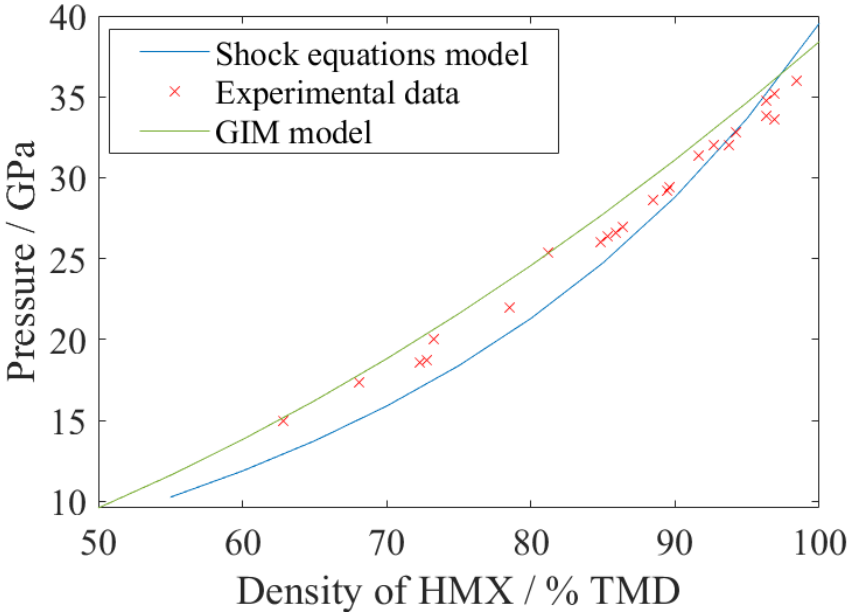

Fig. 6.5 The new GIM model compared with the one derived from conservation equations (figure 6.4.), where it can be seen to also be in good agreement with the experimental data.

There is reasonable agreement with the previous shock conservation model in terms of overall behaviour, as well as very good agreement with the experimental data, especially at lower densities. With the GIM predictions agreeing with the experimental data, this shows that Group Interaction Modelling – and using a Lennard-Jones equation of state - was a good model to use for detonation.

In order to calculate the GIM detonation velocity, the detonation pressure, change of volume, and density were required. Therefore, the pressure has to be calculated first using the GIM model as it is required for calculating the velocity. The relative volume change was assumed to be the same for all densities.

However, if the density present in the velocity equations (eq.s 6.15 and 6.16) was altered to reflect upon the decreasing initial density, the predicted dependence of the detonation velocity did not match with experiments. If the density was kept constant at 1.91 g cc^{-1}, the relationship between calculated velocity and density was in better agreement with the experimental data at high densities, just by inserting the lower pressure values into equations (figure 6.6).

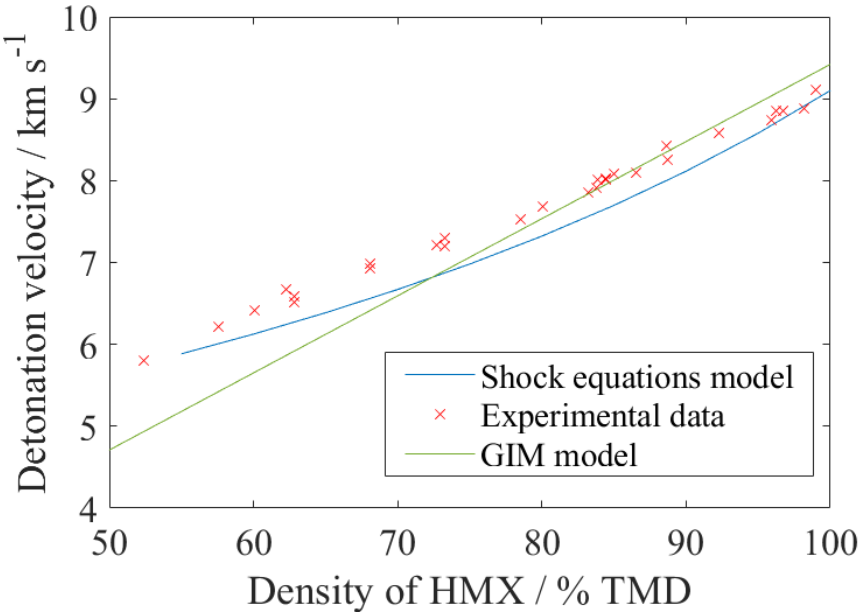

Fig. 6.6 Including the new GIM calculations against the previous model (figure 6.3) shows that whilst the GIM model matches the experimental data at higher densities; it starts to deviate away from both the experimental data and the shock derived model below 70% TMD. This could be due to the fact the GIM model is a continuum model, that does account for voids, which will be more present at lower densities.

An argument could be made that these calculations were only considering the velocity in the crystals themselves (at 100% TMD), and not the air-spaces. In actual detonation, the crystals will not be arranged periodically with air gaps between them, but rather would be in contact with each other. For the detonation to spread, it will therefore likely go crystal-to-crystal, rather than 'jumping' the air gap, which would lead to a constant density.

Therefore, whilst GIM allows the detonation velocity to be accurately predicted for high densities, it depends upon this constant density approximation to be made. However, GIM uses a continuum model, and so it makes sense that it cannot properly handle the presence of local voids. It does, however provide a good estimate for the velocity at 100% TMD. This value could then be used in shock conservation model, which, as observed in figure 6.6, provided a better model of the detonation velocity when considering the range of densities involved, as this can account for the discontinuities in the porous system.

Summary

In conclusion, GIM treats the HMX crystals on a molecular basis, with a potential based on distance between the species, and detonation defined as the moment of sudden dissociation.

This approach allowed good evaluation of the detonation properties at 100% TMD, as well as the relationship between pressure and initial density. In comparison, the shock conservation approach managed a good estimate for the detonation velocity varying with density, using the simple argument based on air shock speeds.

Despite being a complicated reaction, the fact that these models both had agreement with previous research shows that detonation can be reasonably accurately modelled using very different methods and assumptions. Either model, or a combination of both (such as taking the 100% TMD values from GIM and using them in the shock conservation model), has the potential to be a useful comparison to future experimental data.

6.2.3 Other models

As would be expected, various models of detonation have been created with significantly more detail, depth and complexity than the examples presented above. It has been an active area of research for decades, with multiple different focuses and aims, improving each year as more experimental data is gathered and as the amount of technology/computing power increases. Below are a few examples of the calculations done in the past for modelling detonation.

In 1968, Kamlets and Jacobs used large datasets of detonation properties, leading to their three empirical equations to calculate detonation pressure, p, and velocity, D [168] .

$$\phi = NM^{0.5}Q^{0.5} \tag{6.19}$$

$$p = 15.58\rho_0^2\phi \tag{6.20}$$

$$D = 1.01\phi^{0.5}(1 + 1.30\rho_0) \tag{6.21}$$

Where N is the number of gaseous moles produced in the detonation reaction per gram of explosive, M is the average weight of these gaseous products, and Q is the chemical energy of the detonation per gram of explosive [168, 52].

These were derived from experimental data, producing simple equations for the detonation velocity and pressure to allow a relatively accurate estimate of detonation properties for any energetic material.

More recently, larger computer codes have been implemented such as CHEETAH and EXPLO5. These are thermochemical codes that account more fully for the chemistry of the system, rather than just the detonation properties. EXPLO5, for example, is based on

the chemical equilibrium of steady state detonation, using a Bickett-Kistiakowsky-Wilson equation of state (BKW EOS) for the gas molecules, and a Cowan-Fickett EOS for the solid ones [169]. The BKW EOS is a variation on the ideal gas law, with added terms fitted to experimental data in order to account for the failings of the ideal gas law under such conditions. The Cowan-Fickett EOS also uses experimental data to fit the solid particle behaviour, indicating the level of complexity present in detonation that empirical data is required to increase model accuracy.

As experimental work increases, so do the models in order to more accurately reflect the physics. Following on from the discussion of the importance of hotspots in initiating reactions, continuum phenomenological based burn models are including terms in order to account for the hotspot influence on reaction rate. A well-known example is the Lee-Tarver model [170], based on the equation of state of the unreacted explosive as well as the reacted products, which remains a popular choice for detonation modelling. There are multiple other continuum models, which use numerous different physical bases to simulate the complexity of detonation [171]. Two common examples with very different approaches are the aptly named Forest Fire model [172], which has a reaction rate only dependent on pressure, and CREST [173] which is entropy driven.

Initiation can also be modelled directly from hotspots themselves, using the mechanisms discussed in section 1.2.5. An example would be Frey [43] investigating shear bands, or Khasainov using visco-plastic collapse as the dominant hotspot mechanism [41]. Such models can be combined with the continuum burn models mentioned above to form hybrid models, such as Kim's model [174] which incorporates viscoplastic pore collapse for initiation, followed by growth modeled using a similar approach to Lee and Tarver.

This discussion only briefly touched on all the theoretical research that has been done, and that is still ongoing. However, it does establish the importance of experimental data for the continuation of modelling. Firstly, in that experimental data is required to initially parameterise the model, and secondly that another independent dataset would be needed to validate the conclusions drawn by the model. The use of light emission to further investigate the properties of detonation would bring more knowledge about the reaction to the modelers, and hopefully lead to a more accurate description being formed.

6.3 Method

The aim was to investigate steady-state detonation. To achieve this, the experiment was designed as a column setup, as shown in figure 6.7, with the column made of polymethyl

methacrylate (PMMA). PMMA was chosen as it was transparent, so a camera could be used to image the inside of the column during the reaction.

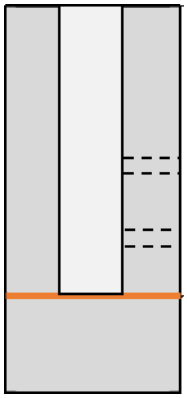

Fig. 6.7 Diagram of the design of the detonation column, made of PMMA with a large enough diameter to support detonation, holes bored through the outside to insert fibre optic cables and a copper sheet for reflecting PDV laser.

Given the objective to measure only detonation light, the reaction would be initiated by a detonator in order to start a Shock-to-Detonation Transition (SDT). The alternative, a Deflagration-to-Detonation Transition (DDT) would consume a large quantity of HMX in the run up to detonation, as well as providing unwanted deflagration light. Therefore, a PETN-boosted detonator [RP-501] was used to initiate detonation. This is a high-voltage detonator, and required the presence of a 5 kV capacitor bank in order to set it off.

The diameter of the column had to be above the critical diameter of HMX in order for detonation to be sustained; a value of *circa* 6.5 mm [175]. For ease, the diameter was designed to be the same as that of the detonator - 7.5 mm - so that it could be inserted at the top of the column and stay in a co-axial position with the HMX.

As well as having a critical diameter, the HMX also needed to have a high enough density, measured as a percentage of the Theoretical Maximum Density (TMD) of a single crystal, to support the detonation wave. This critical fraction was unknown for the experiment, and so the HMX was pressed in order to increase its density. Before pressing the fibre optic cables were inserted into the holes shown in figure 6.7, and glued in place so that the HMX would be pressed against the end of the fibre with no air gap present.

Type-B HMX was used for pressing as it was polydisperse. This meant it could be pressed to densities above the maximum packing fraction for spheres (74% TMD) as the smaller particles would fit into the gaps made by the larger ones. Therefore, the polydisperse material can achieve higher densities under lower applied pressures, and so is safer to use. The press at the Cavendish Laboratory has reinforced steel doors that were closed when the pressure on the material was applied in order to provide a barrier if the material reacted during the

pressing process. The procedure was to measure in *circa* 0.20 g of HMX, and press it at the chosen pressure. This was then repeated until the required height was produced, ensuring that the HMX had a homogenous density along the length of the column.

The pressure applied to press the HMX was low enough that the PMMA column did not deform, but high enough to produce the desired density. For 25 MPa applied in the press, a density of 82% TMD was achieved, high enough that the column would detonate. This constituted the upper bound on the density; for safety and practicality. This pressure could be reduced later, so that a lower density column could be pressed in order to investigate density effects.

At the base of the column, a thin sheet of copper of thickness 30 μm was glued onto the PMMA with an epoxy, and then a 4 mm PMMA disc glued on the bottom. This was to provide a reflective surface that would allow PDV measurements to occur at the base of the HMX charge. PMMA was used because it was transparent and also because the refractive index of PMMA is the same for the shocked and non-shocked material (no 'window correction' is required) [176], and therefore the velocity of the PDV laser - and the following particle velocity measurements of the copper from this laser light - will not be affected by the PMMA material properties under shock. Figure 6.8 shows the column fully prepared before an experiment.

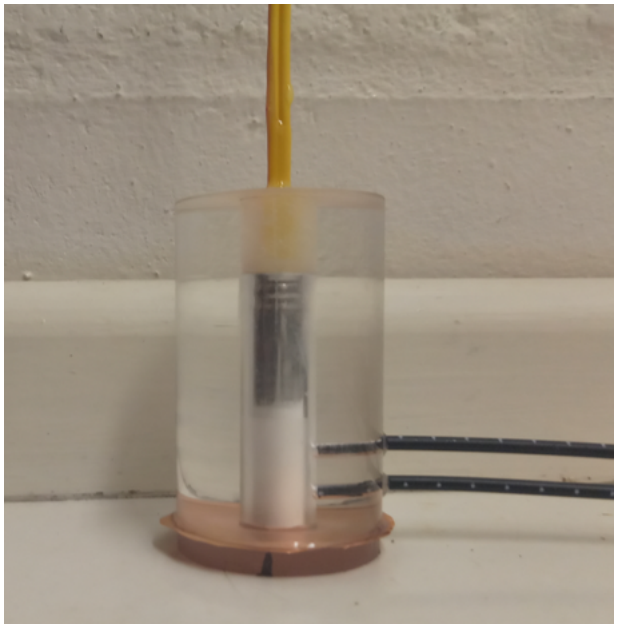

Fig. 6.8 Photograph of the column assembled, with the detonator inserted at the top, touching the pressed HMX, fibre optics inserted and glued in place, and with the copper at the base.

The initial distance from the detonator to the first diagnostic – the top fibre optic - was 10 mm to allow for a steady detonation to be reached, with a 10 mm gap between the fibre optics, and 10 mm from the bottom. After initial testing, these lengths were reduced to 7, 6 and 5 mm in order to lessen the amount of HMX used.

For detonation, the column was then placed in a steel box with a volume of *circa* 0.125 m^3 to contain the explosion and limit the potential damage to the surroundings. A port on the side allowed the fibres and high voltage cable to be connected outside the box, and PMMA windows could be placed on the side of the box in order to see inside.

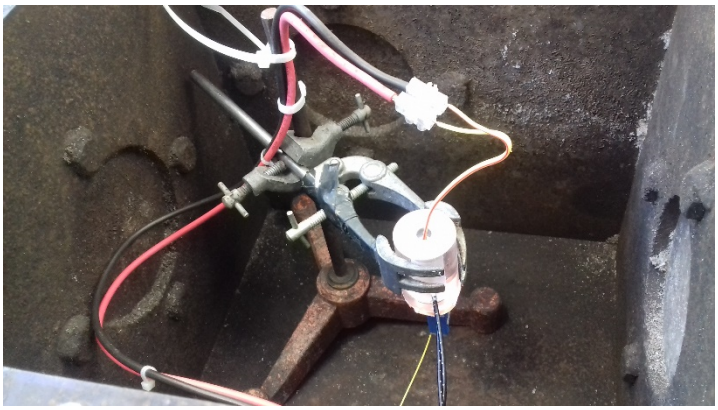

Fig. 6.9 The setup inside the detonation box before the lid was secured down. The column was held by a retort stand and clamp at a level from which the camera could take a picture through the front PMMA window. The fibre optics for the spectrometer and PDV were taken through the port to the side. Another PMMA window was placed opposite the front window, so a flash lamp could illuminate the setup.

6.4 Equipment

6.4.1 Spectrometer

The same gated-spectrometer from the previous deflagration experiments (Chapter 2) was used for detonation measurements. The main difference between its use was the timescales involved. In deflagration, the microsecond long reaction time meant that the spectrometer could be triggered off the reaction light increase, and still capture the majority of the light emission as the time for the signal to be received, and the gate to open, was of order 200 ns.

However, in detonation the time of light emission itself was of order 200 ns, and so the spectrometer was not fast enough to measure the light from the same source that triggered it. Therefore, two fibre optics were required. The first (upstream) fibre optic was connected to a fast photodiode [EOT Silicon PIN detector ET-2030], which measured the light intensity.

The rising light from this first fibre triggered the pulse generator [Stanford Research Systems. DG535] to open the spectrometer gate, so that it would be open to catch the light as it passed the second (downstream) fibre optic.

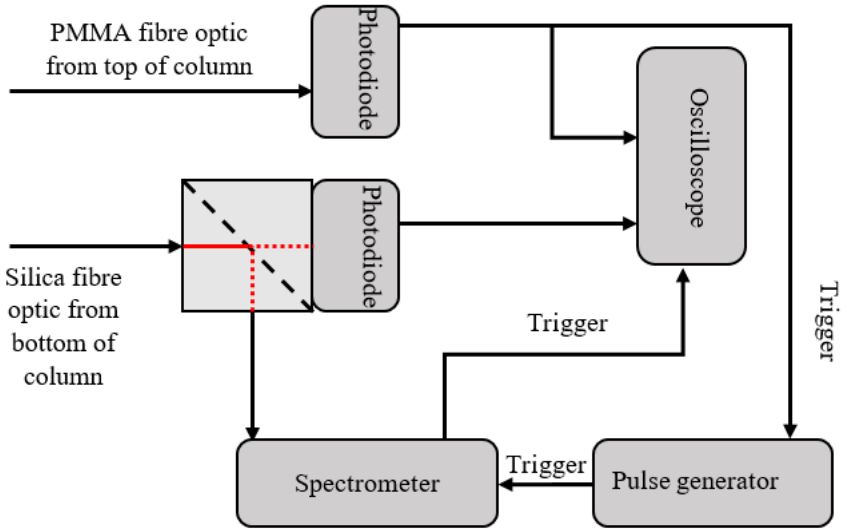

Fig. 6.10 Diagram of the equipment used to capture the detonation light.

The second fibre optic was, after the first experiment, situated 6 mm below the first. Using a maximum detonation velocity of 9.11 km s^{-1}, the earliest time it would reach the second was 700 ns later, enough time for the spectrometer gate to open. Given the unknown detonation velocities involved, the spectrometer gate was open for a period of 2 μs – allowing for a velocity between 3 and 9 km s^{-1}, with a large window to ensure all the light was captured.

As mentioned above, the fibres had been glued into the column, and the HMX pressed against them. This was to ensure that the only light measured was from detonation – a narrow field of view meant only the light from the front as it passed would be captured, and the air shock would be minimal. The ends of the fibre would be destroyed, but they could be cut and re-calibrated before each experiment.

Another complication that arose was the increased electrical noise that was produced by the capacitor bank discharging. This noise would trigger the spectrometer prematurely if the equipment was close enough. To prevent this, the spectrometer tower was moved into another room 15 m away where the noise was lessened enough to not affect measurements. However, this increased distance meant the attenuation in the fibre optics became a more

significant problem. Figure 6.11 demonstrates the level of attenuation present in a 1 m fibre optic and one 10 m long.

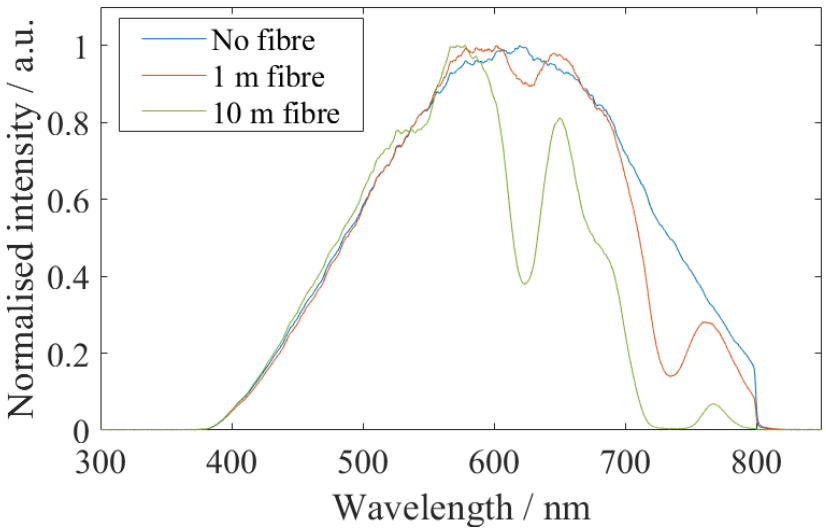

Fig. 6.11 A blackbody lamp measured by the spectrometer through no fibre optic, a 1 m cable and a 10 m cable of PMMA cored fibre optic. The absorption by the cable can be seen to dramatically increase as the length of cable used increases.

The fibre optic used in these experiments had a 1 mm PMMA core, meaning it could easily be destroyed and cut back without fracturing a long length of the core. However, the absorption levels in this fibre were large compared to a 1 mm silica core fibre optic. Therefore, to have fibre which could both be placed next to a detonation reaction as well as limiting the attenuation present, a 15 m length of silica fibre was used to connect the spectrometer to the room the detonation box was in, which was then coupled into a 1 m length of PMMA cored fibre next to the detonation. The combination of the permanent fibre and the sacrificial fibre meant the attenuation levels were similar to that measured for the deflagration experiments, without risking the length of silica fibre.

The calibration was then achieved in the same manner as before, with the spectrum of a known blackbody measured through every optical element. Once this measurement was done, the sacrificial fibre could be glued into the detonation column.

6.4.2 Pyrometer

After the spectrometer was used to gain the emission spectrum, the channels of the pyrometer could be chosen to avoid the presence of any spectral peaks. Once the filters were chosen, the

pyrometer was calibrated in the usual way by measuring the spectrum of a known blackbody, as detailed in previous chapters.

The pyrometer was not as sensitive to electrical noise as the spectrometer, so could be placed closer to the detonation experiment. Another advantage was that, since the pyrometer measured the light intensity with photodiodes connected to an oscilloscope, it could be triggered off the detonation light as the oscilloscope would pre-record. Therefore, it could be connected to the top fibre optic and the light intensity used to trigger the spectrometer, which was connected to the bottom fibre optic.

6.4.3 Camera

A fast framing camera [IVV invisible. Vivitar] was used to take pictures of the setup before and during the column detonation. The column was back-lit by a flash lamp as the short exposure time of the camera meant that little light intensity was captured. After the capacitor bank was discharged – and the detonation started – the flash lamp and camera were carefully timed to catch the detonation event. The camera took 12 images with an exposure of 30 ns, each 400 ns apart so that the whole column detonation would be captured.

Figure 6.12 shows the column before the experiment, and the typical images received during the detonation event. These images both allowed the velocity to be measured from the passage of the front, and to prove that the detonation was steady down the column - that it wasn't accelerating or decelerating. Additionally, the pictures provided information on how far through the HMX the detonation light carried, and the relative brightness of the different experiments.

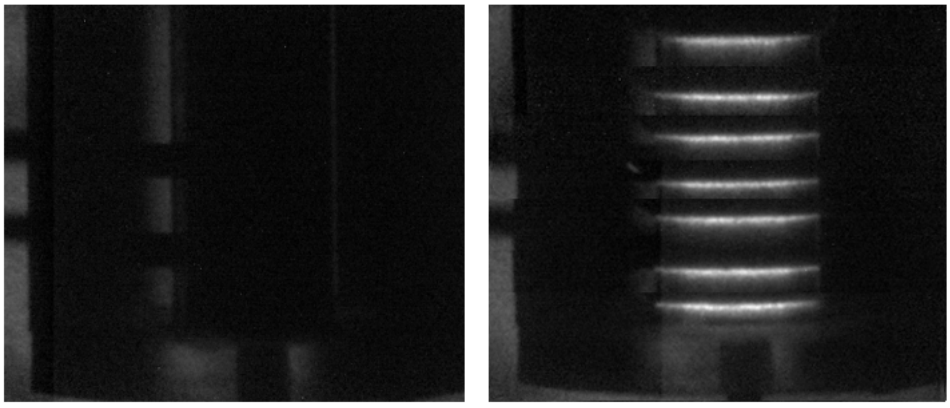

Fig. 6.12 The column before detonation, and a combination of 7 frames taken 400 ns apart during the experiment. The bright line shows the presence of the hot and emissive detonation front, moving down the column at detonation velocity.

6.4.4 PDV

The Photon Doppler Velocimeter (PDV) was used to measure the detonation C-J pressure [177]. The PDV, homebuilt in the Cavendish Laboratory, was developed in order to measure fast particle velocities, based off the original device conceived by Strand *et al* [70]. It uses heterodyne techniques, with a laser of wavelength 1550 nm pointed at a reflective surface of the object from which the speed was required. The reflected laser returns and interferes with the original one. If the reflected surface is moving, the reflected signal will have a Doppler shifted frequency, and thus the interference would produce a beat frequency proportional to the velocity, which can then be measured.

The PDV was used with the fibre carrying the laser pointed vertically up at the centre of the column, travelling through 4 mm of transparent PMMA to reflect off the 30 μm thin copper sheet at the bottom of the pressed HMX. This measured the particle velocity, u_p, present at the copper-PMMA interface, from which the pressure could be found by using Goranson's equation (eq. 6.22) [178]. This is derived from the conservation of mass and momentum at the HMX-PMMA interface, using the Rankine-Hugoniot equations and the Rayleigh line (equation 1.5) discussed in Chapter 1.

$$P = \frac{1}{2} u_p (\rho_{HMX} D + \rho_{PMMA} u_s) \tag{6.22}$$

Where ρ is the density for the HMX and PMMA, D the detonation velocity, and u_s the shock speed in PMMA. The shock speed in PMMA had a relationship with the particle speed, found using the Hugoniot for PMMA. This is an empirically derived Hugoniot, but commonly available given the popularity of using PMMA in shock experiments. Suceska, in his book: Test Methods for Explosives [178], defined this relationship between shock and particle velocity in PMMA as:

$$u_s = 1.524 u_p + 2.579 \tag{6.23}$$

Therefore, in order to calculate the pressure, a simultaneous measurement of detonation velocity, D, and particle velocity, u_p, was required. Given the size of the expected particle velocities, an oscilloscope with a large enough bandwidth was needed in order to measure these values. The presence of the von Neumann peak leads to extremely high velocities that cannot be resolved even with a high-bandwidth oscilloscope, meaning the C-J velocity, and therefore C-J pressure, was the value of detonation pressure recorded.

With a PDV based on the Doppler shift of the reflected light, an expected shift in frequency of the laser would be:

$$\Delta f = \frac{2u_p}{\lambda} \tag{6.24}$$

For a maximum expected particle velocity of 3 km s^{-1}, and a laser wavelength of 1550 nm, this corresponds to a required measureable frequency of *circa* 4 GHz. Therefore, a 6 GHz TDS 6604 Tektronix oscilloscope was utilised for these measurements.

6.5 Results

Successful steady state detonation was achieved, with the camera images confirming that the velocity of the detonation front was supersonic and constant down the column.

6.5.1 Velocity

A better estimate of the velocity than using the camera images could be gained from the time it took for the front to travel 6 mm between the two fibre optics. Figure 6.13 shows the photodiode traces from the top and bottom fibre optic. By overlaying the two light emissions, the time taken for the front to travel, and therefore the velocity, could be found.

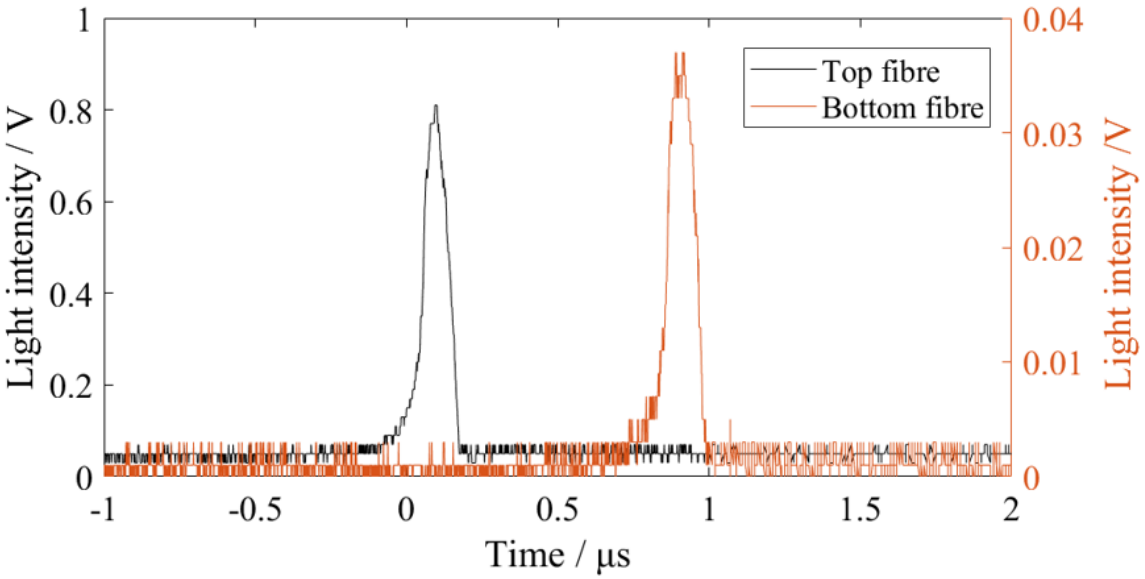

Fig. 6.13 Oscilloscope traces for the photodiode measurements from the top and bottom fibre optic, separated by 6 mm. The bottom fibre optic had less intense light as that optical path had many more interfaces, and split the light with the spectrometer.

From the trace, a velocity of 7.41 $\pm$ 0.18 km s^{-1} was calculated, as would be expected for 82% TMD HMX from the models detailed above (figure 6.6).

6.5.2 Pressure

The trace received on the PDV oscilloscope was run through an in-house program written by N. Taylor in order to gain the particle velocity with time (figure 6.14). The trace shows very little of the von Neumann peak, limited by the oscilloscope bandwidth, and so the C-J particle velocity was estimated from where the gradient in the peak changed [91] [177], and in practice this was very close to the peak itself.

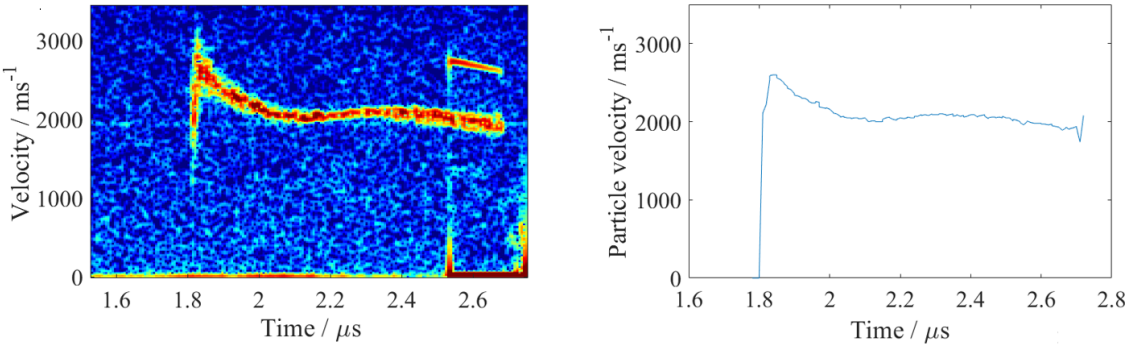

Fig. 6.14 The particle velocity with time, with the raw (left) and extracted (right) data. As can be seen there was an increase to *circa* 2.7 km s^{-1} at the time the detonation front hit the copper sheet. The large oscillation at later times were mostly likely from the fibre moving, or release waves in the PMMA, and so are artefacts in the trace. Regardless, these occur after the peak.

With a measured C-J particle velocity of 2.61 km s^{-1}, this corresponded to a shock velocity of 6.57 km s^{-1} in the PMMA. These values were then included into equation 6.22, along with the detonation velocity of 7.41 km s^{-1} and the density of the HMX at 82% TMD, to produce a measured detonation pressure of 25.4 $\pm$ 0.8 GPa. Similar to the measured velocity, this is in agreement with the model predictions for 82% TMD HMX (figure 6.5).

6.5.3 Spectrometer

The gate was open over 2 microseconds to ensure that the detonation front was captured, as the velocity was not known and the aim was to capture the whole 200 ns front. Little light emission was detected by the photodiode after the front had passed (figure 6.13), and so keeping the gate open for a longer period was continued in later experiments as the extra

non-detonation light that would be detected with respect to the light from the front was minimal.

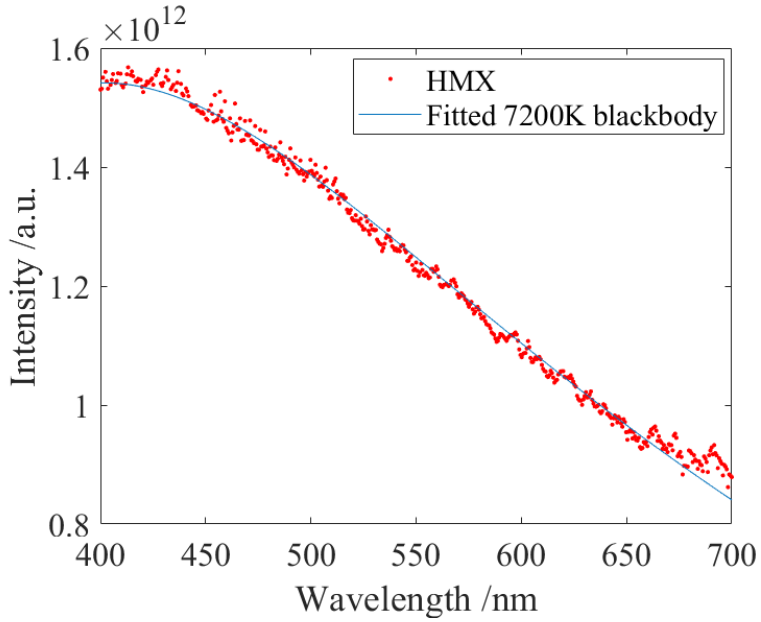

Fig. 6.15 Emission spectrum from detonation, with a greybody fit applied across the whole range. No spectral features – either emission or absorption – were seen, and a single temperature fit of 7200 ± 200 K could be calculated from the data.

The emission spectrum, shown in figure 6.15, was significantly different from the previous measured emission light. No spectral features were present, either as emission or absorption peaks. The higher pressures and temperatures present would have broadened these out, and the increased temperatures would have also significantly increased the blackbody intensity (eq. 1.14).

The emission was therefore completely formed of greybody radiation, allowing a fit across the whole range of wavelengths. A single temperature fit of 7200 ± 200 K was found to fit the range well, indicating that the measured light did not have a large continuum of temperatures present.

The value of 7200 K was significantly higher than that measured in deflagration, in agreement with past experiments into detonation temperature [50–52, 54]. This value, larger than could be achieved from the chemical reaction alone, was likely from the void collapse under high pressure discussed in section 1.2.7. Being 82% TMD, a lot of voids would be present in the detonation so a larger temperature would be expected for such an experiment.

6.5.4 Pyrometer

Once the spectrometer had confirmed that the emission spectrum was purely greybody, the pyrometer could then be used to investigate the change of temperatures present. Filters at 450, 500, 700 and 750 nm were used for the greybody fit, given there were no spectral features to avoid and a larger range fit with more points would lead to a more accurate temperature.

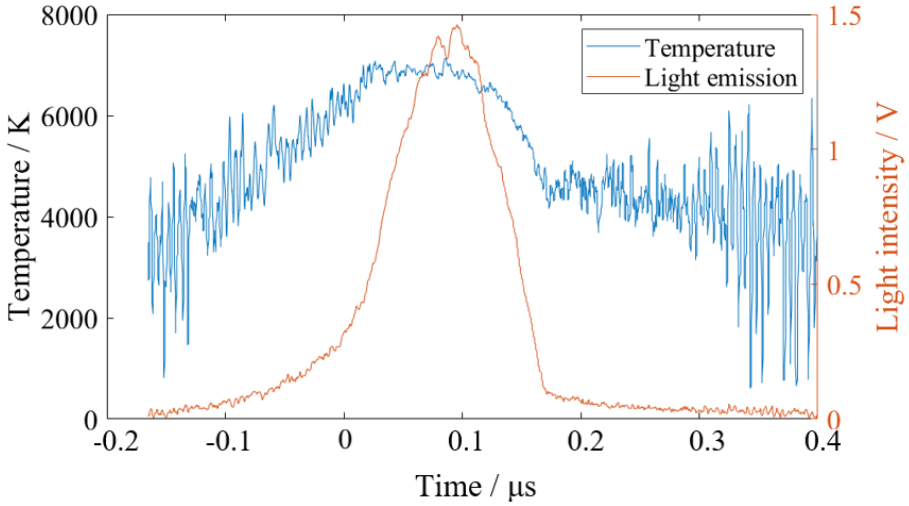

Fig. 6.16 The greybody temperature of the detonation front with the times of main light emission. After the front has passed, the temperature does start to decrease down to lower temperatures.

The time-resolved measurement in figure 6.16 independently confirms the temperature of 7000 $\pm$ 300 K for the main period of light emission. As before, the accuracy of the measurements lowers as the light intensity decreases, and so only the temperatures for the main reaction time were trusted.

After the main reaction of high temperatures, the value starts to drop. Assuming the ZND detonation model, after the pressure front the reaction zone would be present, with deflagration reactions occurring. Therefore, it would be expected that the temperature would fall to deflagration temperatures of *circa* 4000 K in this time. However, in these detonation reactions the high pressure likely destroys the fibre optic before the deflagration reaction zone arrived and a constant deflagration temperature could be recorded.

Other recent experiments that note high temperature detonation include those done by B. P. Johnson *et al* in 2020 [56]. In their laser-flyer detonation experiment on a single crystal of HMX they note a high temperature of 8000 K which lasts a few nanoseconds before the deflagration (and chemistry-driven) temperatures of 4000 K are measured. There are multiple reasons why these experiments note the two different expected temperatures, whereas the

above method does not. Firstly, as mentioned, the fibre optic in the column setup is destroyed so cannot record past a particular point.

More importantly is the amount of material being considered. In column detonation, the fibre optic captures a wide angle of a shock wave passing through multiple crystals of HMX. This indicates that the light measured is not from one single reaction from start to end, but from the addition of mutliple different detonation hotspots that are combining together with the result that the brightest light - that from the hot 7000 K at the start of detonation - always dominates in the combined spectrum. The advantage of the laser-flyer initiation of one crystal is that the collecting fibre optic is not destroyed, and would record the complete evolution of only one hotspot site, thus showing the two regimes. However, over-driving a single crystal of HMX to detonation-like properties using the shock from a laser flyer is not the same as detonation (which is well known to require a critical diameter of material in order to support the detonation), and the question remains whether the same properties would be observed. Regardless, both experiments do show the high temperatures present in detonation that could not be achieved from the chemical reaction alone.

6.5.5 Summary

The experiment detailed above proved that the velocity, pressure and temperature of detonation could be measured for the same column. The high temperature of 7200 K was measured independently by both the spectrometer and pyrometer.

Property	Value
Velocity	7.41 ± 0.18 km s^{-1}
Pressure	25.4 ± 0.8 GPa
Temperature (spectrometer)	7200 ± 200 K
Temperature (pyrometer)	7000 ± 300 K

Table 6.3 Measured properties of 82% HMX detonation in a 7.5 mm diameter column.

This high temperature was attributed to void collapse inside the HMX due to the high pressures present. However, it was also possible that the measured light was from the air shock – air adiabatically compressed under high pressures, producing high temperatures – from a gap of air directly in front of the fibre that had not been fully removed. Or, that the pressure wave breaking the fibre, causing PMMA to release bright light, could be causing such temperatures.

6.6 Air shock

To be confident of measuring detonation light before the pressure wave hits the fibre, a new configuration was used. This involved the pyrometer directly straight up at the bottom of the detonation column (in the place of the PDV fibre). The side fibre optic cables were still used, to match the timings of the pyrometer to the camera images taken, so that it could be determined when the pressure wave hit the fibre.

The column was prepared with no copper sheet in place. Instead, the 4 mm PMMA disc had a hole drilled through, and the fibre optic glued in place at the bottom of the column. The HMX was not pressed for such an experiment, but was a tapped density of 60% TMD. The next section details more properties of tapped densities compared to pressed.

This configuration would allow the detonation light, travelling through the unreacted HMX, to be measured before the pressure wave hit the fibre. The results in figure 6.17 show the detonation light temperature before the fibre was hit with the shock front and another, larger temperature, from where the fibre was destroyed. The camera pictures confirm the timings, with the second large temperature readings corresponding with the image capturing light in the fibre optic (figure 6.18).

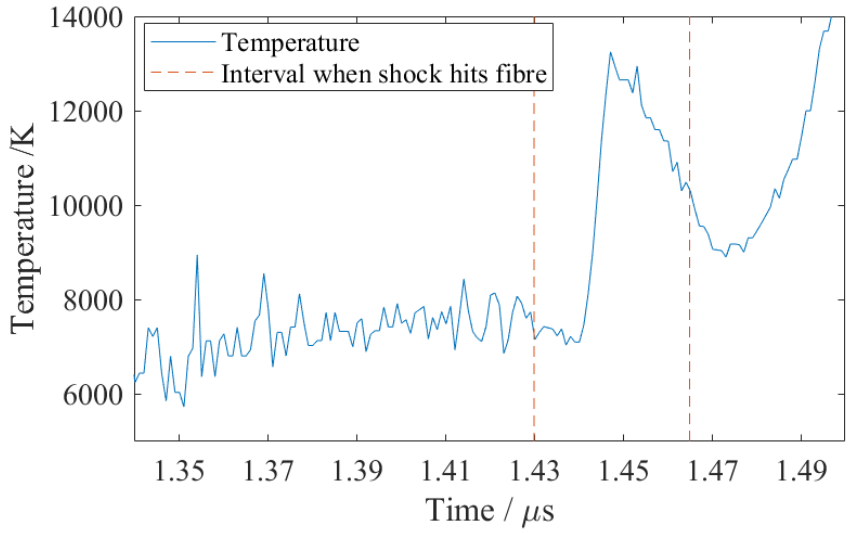

Fig. 6.17 The pyrometer measurements showing the 7500 K of detonation light for a tapped density measured before the much larger temperature of 12,000 K when the pressure wave hits the fibre. The interval shown represents the time, with associated uncertainty, at which the shock wave would have reached the fibre.

The earlier measured temperature of 7500 K from the detonation front was measured before the shock hit the fibre, confirming that the above measured temperatures were not

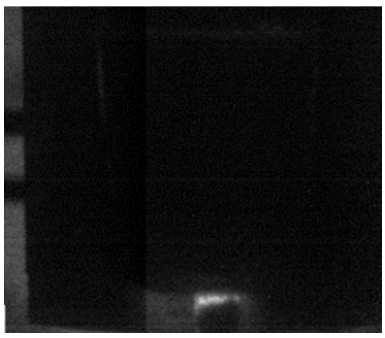

Fig. 6.18 The camera image of the detonation front hitting the fibre optic connected to the pyrometer at the bottom of the column. Bright emission was seen, comparable to the HMX detonation (figure 6.12), but not from the detonation itself.

from the 12,000 K air shock. Therefore, the side-on configuration could be trusted to be measuring the detonation light and, therefore, temperature.

6.7 Density series

Once the detonation experiment had been confirmed able to measure pressure, velocity and temperature, the next area to investigate was how these properties depend on the initial density of the HMX. Detonation pressure and velocity dependence on HMX had been measured previously [164], however the measured effect on hotspot temperature had not. With the assumption that the temperature reached has a large dependence on microstructure, requiring interstitial pores in the material to reach temperatures above those associated with the chemical reaction (section 1.2.6), it is not an unreasonable assumption that the initial density will affect such a quantity.

As the material is pressed to higher densities, the overall 'space' of air pores diminishes. This results in the pores decreasing in size, number density, or both. Microstructure studies on HMX pressed to three different densities indicates that both the size and total number of voids is decreasing [179]. Decreasing number density would result in fewer pores that emit the high temperature light, resulting in a cooler measured temperature as the relative proportion, compared to the lower 4000 K temperature, is lowered. However, as mentioned above, the pressure of the detonation is higher, which, given pores of a constant size, would increase the temperature. Therefore, it is not clear what the 'expected' density-dependent function the temperature would take.

What is known are the extreme values – the temperatures of 100% TMD (single crystal) and of low TMD deflagration. In the limit of low densities, detonation fails and so the temperature will be that of deflagration. For single crystals, the temperature will also be

close to that of deflagration – there are no pores left to collapse, so the high temperature mechanisms do not exist, thereby leading to that expected from the chemical reaction. From the measurements taken so far, this produces a triangle shape – starting at 4000 K, rising to 7000 K at 80 % TMD, then falling to 4000 K again.

The aim of the following series of measurements was to probe the temperature at a range of different densities – from 85% TMD (highest achievable in the press using current methods) to tapped densities of *circa* 60% TMD. An experiment designed to measure pressure, velocity and temperature would allow the density dependence on measured temperature to be known, whilst also confirming the behaviour of velocity and pressure.

6.7.1 Method

Exactly the same setup and method was used as detailed above, with the only difference being the density of HMX in the column. The highest density was 85% TMD, which was achieved by applying 25 MPa of pressure in the press. This pressure was reduced to 12 and 6 MPa to produce columns with *circa* 70% TMD, and then a tapped density of *circa* 60% TMD was produced as the lowest value to be used in these experiments.

6.7.2 Velocity

Figure 6.19 shows the detonation velocity measured from the different density columns, showing a linear relationship of $D = 0.081\rho + 0.95\ km\ s^{-1}$ with density measured as a fraction of the theoretical maximum density (TMD). This behaviour was in good agreement with the previously measured HMX velocity, as well as both the shock conservation and GIM model that was constructed in section 6.2. These two models start to diverge at the lower densities, however as there is no significant divergence of either from the data, it is not immediately clear which would be more accurate for densities lower than 60% TMD, as such densities could not be achieved with the current experiments.

As discussed previously, the GIM model relied on an assumption that the shock only travelled through crystals and not through the air gaps. In comparison, the shock travelling through the air gaps was the basis of the shock conservation model. Despite such a contradiction, the agreement between the data measured from the experiments and the models validates the approach taken by both models, as well as the strength of the results themselves. The GIM approach had another advantage of that it could accurately predict the velocity at 100% TMD, whereas this value was needed for the shock conservation model.

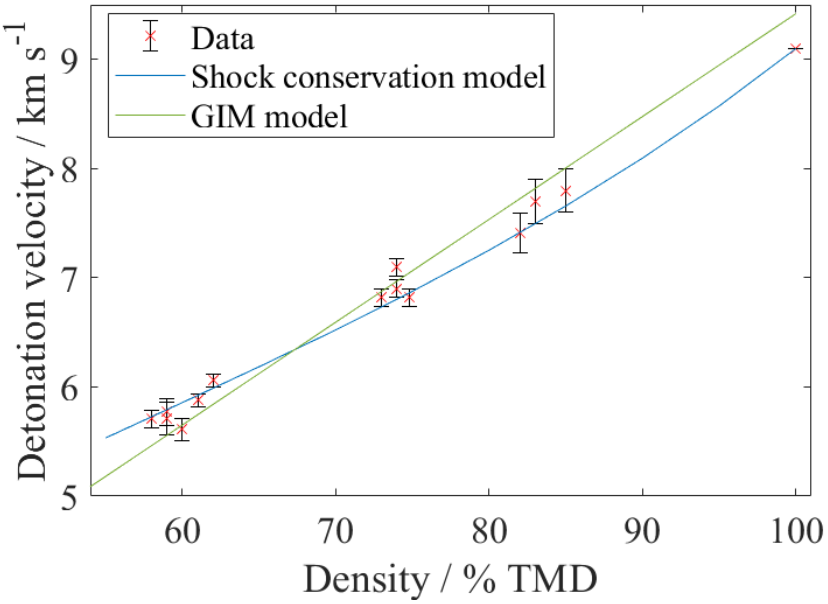

Fig. 6.19 The detonation velocity against percentage TMD showing a rough linear relationship. The value at 100% TMD was included to allow the upper bound to be observed. It was also compared to the shock conservation and GIM models detailed in section 6.2. Both models fit the data, however at the lower densities, the modes start to diverge from each other.

6.7.3 Pressure

Likewise, the pressure also showed a roughly linear response of $P = 0.60\rho - 23$ GPa, shown in figure 6.20. It was clear from the data that the model constructed from shock conservation equations (section 6.2.1) underestimated the detonation pressure, whereas the GIM approach (section 6.2.2) had accurately predicted the pressure, as shown in the close agreement with the experimental results.

Overall, it can be concluded that the effect of density on detonation pressure and velocity in the experiments showed the expected behaviour, with the GIM approach accurately calculating the pressure and velocity relationship with density, and the shock conservation model accurately predicting the velocity dependence. However, these quantities had been measured previously, and it was the effect of density on temperature that was, therefore, more interesting.

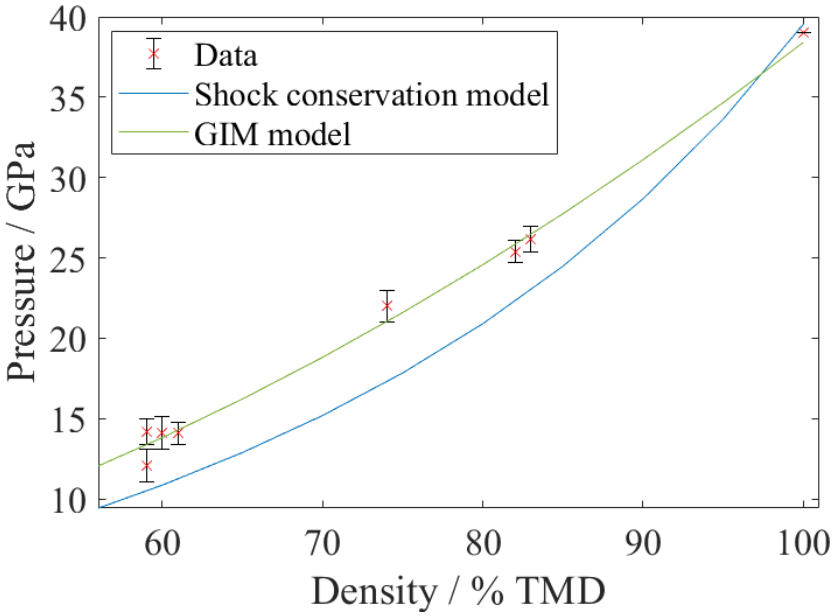

Fig. 6.20 The detonation pressure against percentage TMD showing a rough linear relationship. Like above, the value at 100% TMD was included as well as a comparison to the models detailed in section 6.2. Unlike the detonation velocity, the GIM predictions for the pressure proved more accurate than the shock conservation model.

6.7.4 Temperature

For 70 to 85% TMD - densities achieved through pressing - the measured temperature stayed constant at 7000 $\pm$ 200 K. A slight outlier at 82% TMD measured a lower value of 6600 K, but in all cases, a greybody fit gave good agreement with the whole spectrum, allowing a confident temperature to be reached. The corresponding pyrometer measurements were also in agreement, showing that for the pressed densities, the percentage TMD had no obvious effect on the measured temperature.

In the case of the tapped HMX, the wavelength spectrum shown in figure 6.21 could not have a single good greybody fit across the range, indicating the presence of more than one blackbody shape, and therefore not a single dominating temperature unlike the other detonation measurements. Also, the best fit showed an increase in temperature to 7500 K.

The Planck distribution produces different shapes dependent on temperature, with a larger intensity towards the blue wavelengths at higher temperatures. Therefore, a fit across the smaller wavelengths would contain relatively more high temperature emission, and produce a hotter measurement. Using this fit across the wavelengths (figure 6.22) of the 400 -500 nm range therefore provided an estimate of the hottest temperature in the light – in this case, belonging to temperatures of *circa* 8000 K.

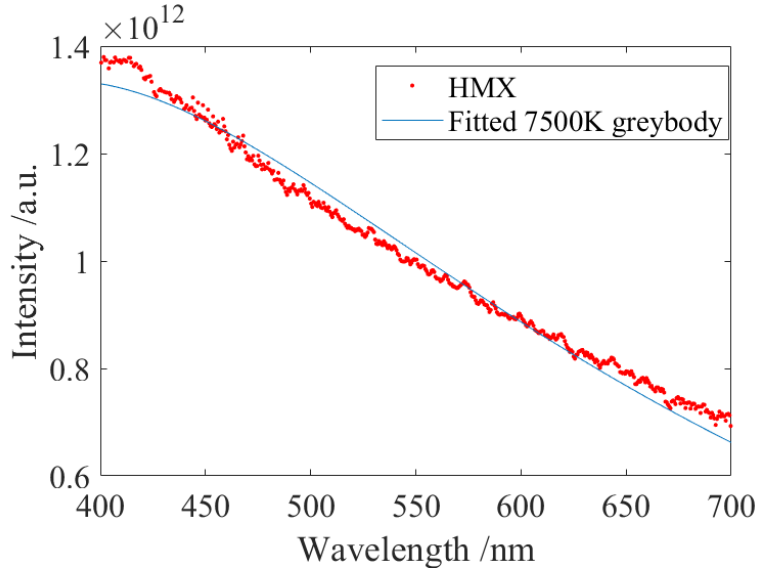

Fig. 6.21 Unlike the previous measurements of light emission, the tapped density wavelength spectrum did not allow a good greybody fit across the range of optical wavelengths. The best fit temperature of 7500 K clearly does not fit the data as well as previous fits.

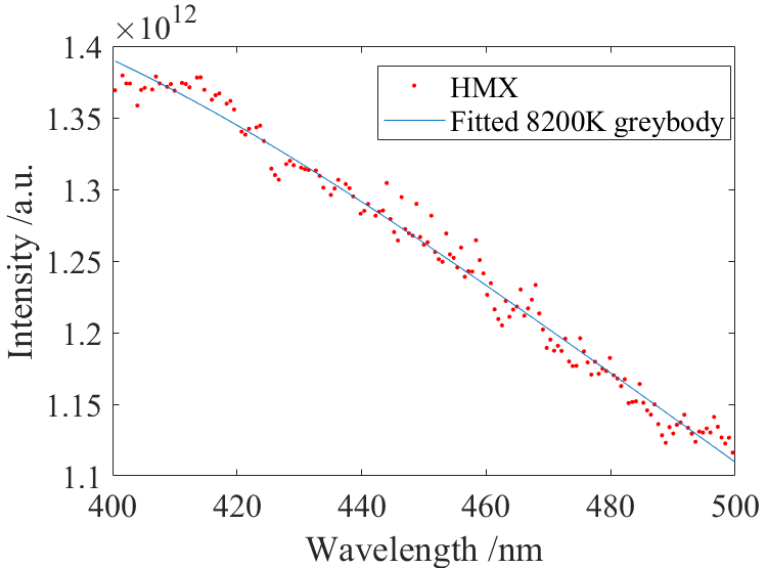

Fig. 6.22 A 400 – 500 nm fit resulted in a temperature of 8200 K being measured.

Once the hottest temperature was known, another temperature fit could be done, but this time with the algorithm adjusted so that it was fitting a Planck intensity added onto the 8000 K temperature. This provided a second greybody temperature of *circa* 3700 K – what one would expect in deflagration – and a much better fit across the range, as observed in figure 6.23.

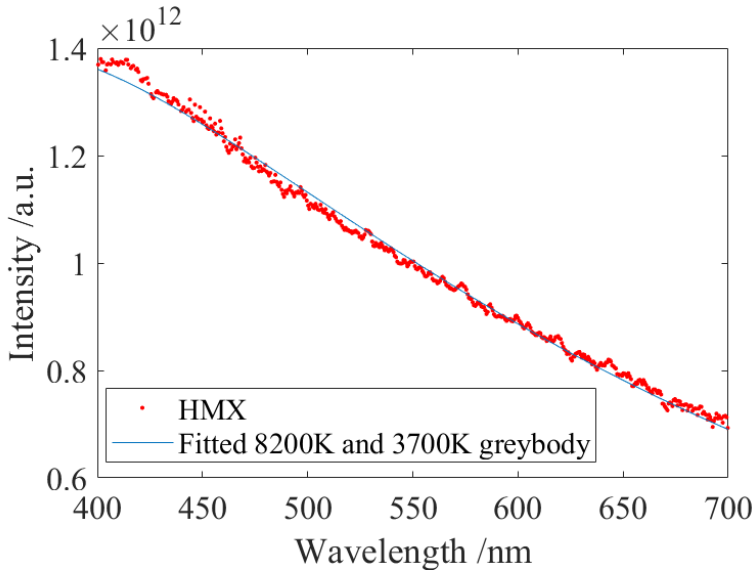

Fig. 6.23 The whole wavelength range of the previous data, but with both an 8000 K and a 3700 K greybody fit to the emission light.

The total intensity of greybody light is propertional to the fourth power of the temperature (eq. 1.14). In the fit shown in figure 6.23, the intensity of the 8200 K radiation was *circa* four times that of the 3700 K light. In order to produce this ratio of intensities, less than 15 % of the emitters would be at the higher 8200 K temperature. The majority of emitters being at the lower temperature is expected, as only the small hotspot volume reaches the high temperatures, whereas the bulk of the material would be reacting at deflagration temperatures. This result suggests that previous detonation emission spectra, whilst completely dominated by the higher 7000 K light temperatures, also contained a significant amount of emitters at 4000 K which could not be seen due to the lower intensity of lower temperature blackbody radiation. Therefore, it should be emphasised that the reported 'detonation temperature' measured in this research is not representative of the bulk temperature during detonation.

To avoid any bias, the same technique was applied to the pressed density detonation data. Calculating the temperature of the blue region of the light emission for these higher densities returned 7150 $\pm$ 200 K as the temperature, confirming the fit across all the wavelengths. This showed a significant difference between the temperatures of the pressed and tapped densities.

From the pyrometer measurements, the same overall temperature behaviour was seen (figure 6.24). However, there were a few observable differences. The lower densities had a slower detonation velocity, and so in the tapped densities the time over which there was high light emission was longer, as the front passed the fibres more slowly. Also, the same higher temperatures as seen in the spectrometer were observed in the tapped densities compared to the lower temperature pressed columns.

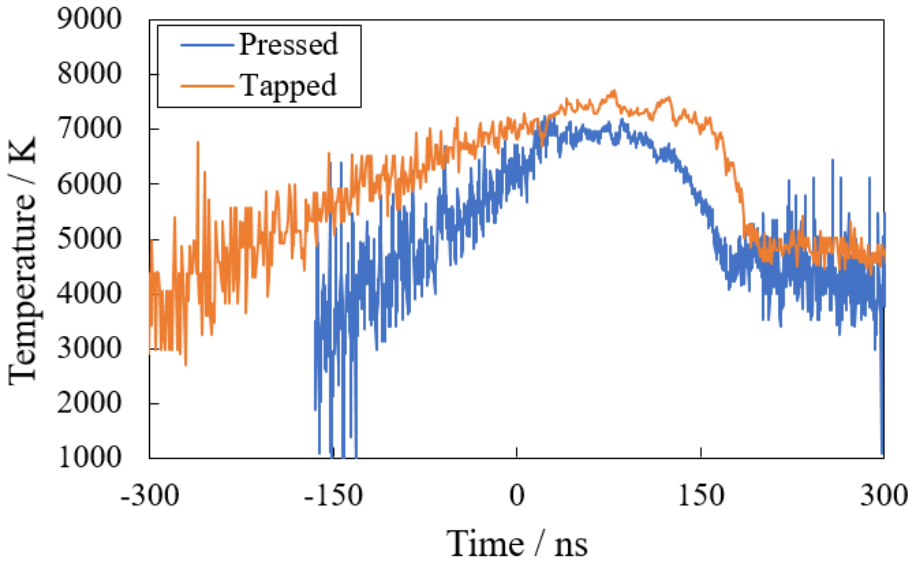

Fig. 6.24 The time evolution of the temperature for a pressed 74% TMD column and a tapped 58% TMD column.

The spectrometer and pyrometer measurements lead to two observations between the pressed and the tapped densities. Firstly, the detonation temperature itself was hotter in the tapped density, around 8000 K rather than 7000 K. Secondly, considerable deflagration-temperature emission (4000 K) was present within the detonation light for the tapped densities. These differences arose from the method of pressing, rather than the density itself. One explanation could be that in a tapped column there exist large voids that would be removed with the smallest force applied in the press. These large voids had a lower surface-to-volume ratio, so the cooling rates would decrease, meaning the potential temperature that could be reached would increase.

For the increase of the fraction of deflagration temperatures in the light emission, there were several reasons why such an increase was present. There were less of these larger voids present in the tapped densities compared to the higher distribution of smaller voids, so the total number of high-temperature emission sites was decreased. Also, with these larger particles, light could more easily shine through the sample (as there were less scattering particles).

Figure 6.25 shows the camera images of a tapped density alongside a pressed density detonation – the light more easily spreads through the column, meaning the deflagration light behind the front could be received by the fibre optic before the front hits. There was also the fact that the pressure was less in the tapped densities – so the fibre optic would survive longer and measure the deflagration light after the front had passed. Therefore, taking the hottest temperature in the spectrum as the ‘detonation-temperature’ for the tapped densities,

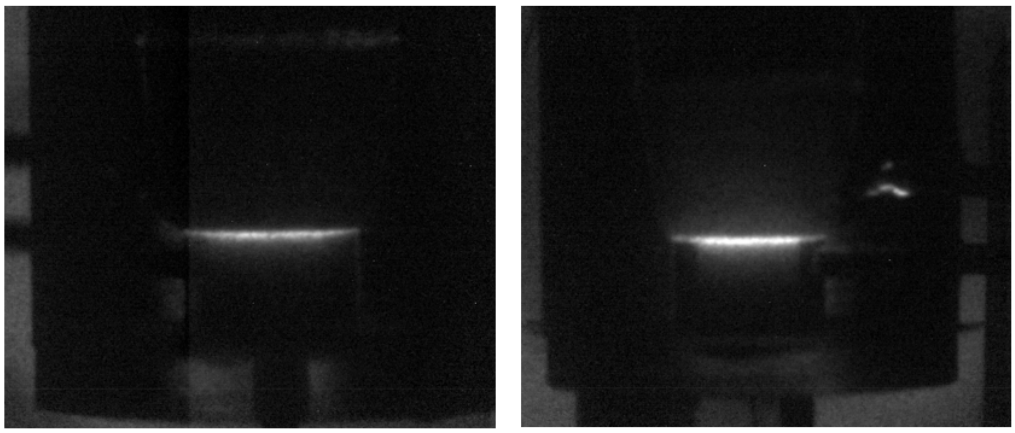

Fig. 6.25 Camera images comparing the pressed density column (left) to the tapped column (right). All the camera settings being the same, light could travel more easily through the tapped column, as small amounts of light emission away from the front can be seen as well as the fact the emission is brighter for the image on the right.

figure 6.26 shows the temperatures measured by the spectrometer and pyrometer for the experiments.

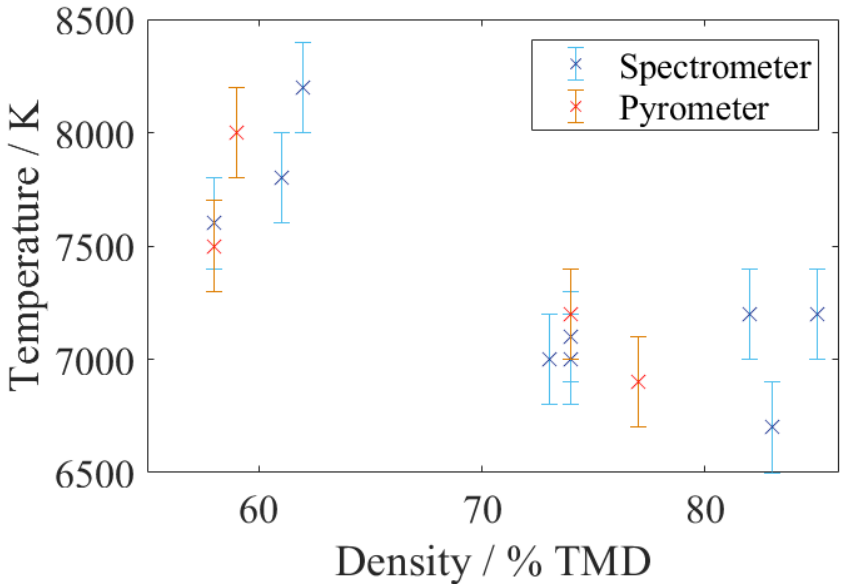

Fig. 6.26 The measured detonation temperatures from the spectrometer and pyrometer for both the pressed densities (70 – 85% TMD) and those that were tapped (60% TMD). There was a large difference due to the method of preparing the column, but the density itself – as seen for the pressed materials – did not significantly affect the temperature.

As can be seen, there was a consistent increase of temperature when the columns were tapped to a constant density rather than pressed. A noticeable gap of densities is present between 60 and 70% TMD, as the smallest easily repeatable force of 6 MPa in the press produced a column of 73% TMD. This sudden increase of density upon pressing reinforces the above hypothesis that a tapped column contains larger voids that are immediately pressed out upon application of a force, as the removal of these large voids would cause an immediate 'jump' increase in the density.

6.7.5 Summary on density series

In conclusion, the detonation temperature, pressure and velocity were measured for a series of densities in the 60 – 85% TMD range. The pressure and velocity exhibited the expected properties given the lowering density, with a roughly linear decrease that agreed with both previously measured quantities, as well as the theorised behaviour from two different models.

The temperature did not have any obvious density dependence for the pressed densities, however it did have a large change depending on the method used to prepare the column, with higher measured temperatures for a tapped column compared to a pressed one. This behaviour suggests that the *density* does not affect the measured temperature, but another variable is responsible, one that was changed due to the preparation method.

Such a variable could possibly be the size of the voids present in the HMX, with larger voids present in the tapped column producing higher temperatures. For the extreme case of a single crystal of HMX; no voids exist to collapse under the high pressure and so the expected measured temperature would be 4000 K.

Producing a large enough single crystal the correct shape to detonate was unfeasible for such research, however the size of the voids could be affected another way. The material used in these experiments was HMX Type-B, a mix of the larger Type-A particles and the smaller Type-C to create a polydisperse sample. Using larger particles would result in the same overall density (as the packing fraction of spheres does not depend on the size of the spheres), but would have larger voids present.

Therefore, comparing the detonation temperature of Type-A HMX, with fewer, larger voids, to Type-C, with more numerous smaller voids, would allow the theory of void size affecting temperature to be tested. This line of inquiry is shown in the next section.

6.8 Particle size

The aim was to measure the same detonation properties for Type-A and Type-C HMX in order to investigate whether particle size affects these values. The reasoning for doing so was linked to the size of the voids, with the assumption that larger particle sizes would have larger voids present. In order to preserve the monodispersity and size distribution of the material - to not crush or fracture the grains - the temperature of the tapped columns were compared for each type of HMX. These tapped densities were similar to those recorded for Type-B HMX, of *circa* 60% TMD.

6.8.1 Light emission

The first noticeable difference between the three types of HMX was the brightness of the detonation event. Type-B and Type-C HMX had similar amounts of light emission, which would be expected as Type-B is, by volume, composed of 75% Type-C. However, the detonation of Type-A HMX was significantly brighter. Keeping the same settings on the equipment led to every detector being saturated, and so the sensitivity had to be decreased before any measurements could be taken.

For the camera and spectrometer this was easily accomplished by lowering the amplified gain applied. For the pyrometer, two neutral density filters in front of each colour filter was used to drop the light to 5% of its original intensity.

This significant increase in light emission – *circa* 15 times brighter – for the larger particles could be explained by scattering theory. With the particles having a diameter of tens of microns, this was significantly larger than the wavelength of visible light at hundreds of nanometres. Therefore, the scattering could be described by Fraunhofer diffraction of light around a spherical particle. In this regime, the intensity of scattered light is proportional to the square of the particle diameter [180, 181]. However, with larger particles present, there are less of them present for the light to scatter from, and the volume occupied by each particle is proportional to the cube of the particle diameter. Therefore, despite each particle scattering more light, the number of scattering particles themselves decreases, so the overall light scatter is lessened. With less scattering, higher light intensity is therefore measured.

6.8.2 Results

The measured detonation velocity and pressure of both types fit onto the previously established linear fit with no significant difference to the pressed results (the data points were included in figures 6.19 and 6.20). This agreement indicated that for these properties it

was density, rather than particle size, that was the dominant factor. Such a conclusion was predicted by the theory – as only density was used in the calculations– however, it was important to verify this hypothesis.

The spectrometer wavelength emission spectra for the tapped columns had similar features as the previously measured Type-B, with a mix of high temperature detonation light and lower deflagration temperature light. Therefore, the same process of fitting a greybody to the blue region of the spectrum to gain a high temperature estimate was achieved. With the pyrometer, the temperature recorded during the main period of light emission was used as before.

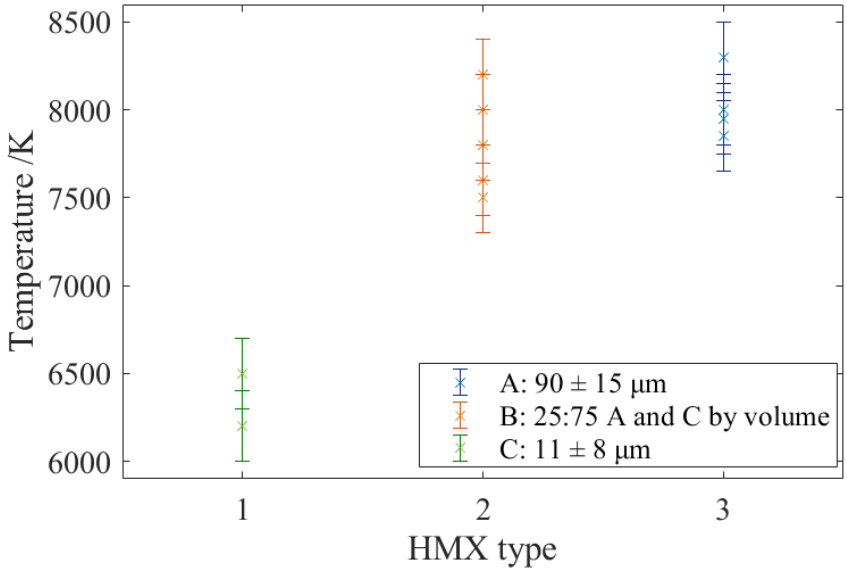

Fig. 6.27 The measured temperatures from the spectrometer and pyrometer comparing the tapped density temperatures of Type A, B and C HMX at *circa* 60% TMD. The temperature increases as particle, and void, size was increased. Despite Type-B HMX having a larger volume of the smaller particles, the light emission from the larger voids dominated the spectrum, and so the temperature was in agreement with that measured from Type-A.

The temperatures measured are shown in figure 6.27. These values clearly show that for tapped densities, Type-B and A had similar temperatures, whereas the smallest particle size (and therefore void size) Type-C had significantly lower temperatures. These temperatures were lower than even the pressed Type-B, at 6300 K rather than 7000 K. The smaller particles present in Type-C produced on average smaller voids, which in turn led to lower temperatures being recorded. In comparison, both Type-B and Type-A contained larger particles that produced large voids when tapped into the column, and when these collapsed produced a higher temperature light.

One more difference was observed between the detonation light from different HMX particle sizes. As well as the increased brightness as mentioned above, Type-A detonation also contained spectral features present in the detonation spectrum. Unlike every other detonation light emission (figure 6.15 and 6.23), sodium absorption was clearly present from all experiments conducted, with an example shown in figure 6.28. The absorption feature could easily be removed from the spectrometer temperature fits, and was narrow enough that it did not affect the 700 nm pyrometer channel, and therefore did not significantly affect the above temperature measurements.

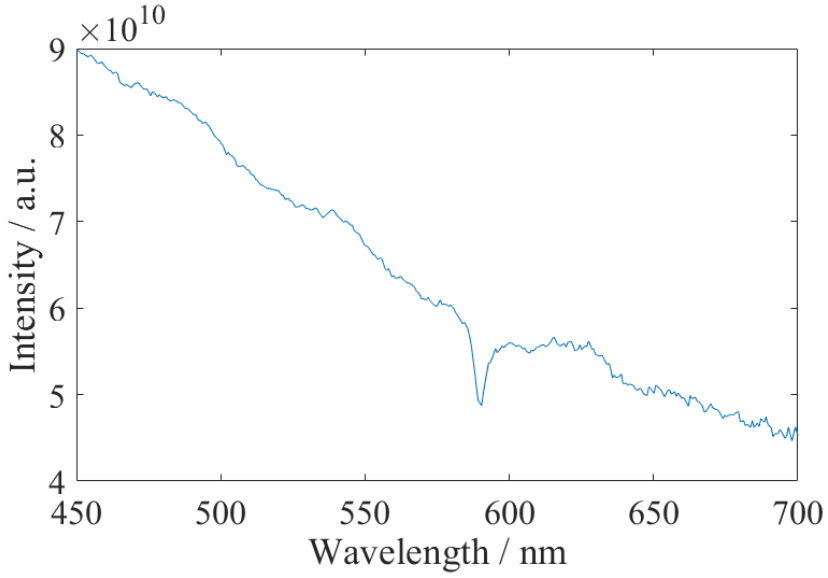

Fig. 6.28 The emission spectrum of 59% TMD Type-A HMX detonation. As well as the continuous greybody emission, a clear sodium absorption peak was also visible, at a wavelength of 590.4 nm.

Absorption features are present in spectra when unexcited atoms absorb photons, leading to an electron moving to a higher energy level, with the increase in energy corresponding to the energy delivered by the photon. Therefore, the presence of absorption in the detonation spectra indicates the presence of unexcited (or 'cold') sodium between the detonation light emission and the collecting fibre. These sodium atoms have to be in the vapour state in order to absorb the photons, and colder than the detonation light, otherwise thermal emission would be observed instead.

This absorption was slightly red-shifted from the 589.3 nm centre, indicating deflagration level pressures experienced by the sodium atoms. The first hypothesis for this sodium presence was that after the detonation front had passed, the light from the front shining back through the detonation products (and sodium vapour) led to the absorption seen. However, if

this was a post-detonation feature, the particle size of the HMX would no longer be affecting the reaction behaviour, as it would have started to react and decompose, losing its crystal structure. Therefore, in this deflagration region, the same features would be expected to be seen in the other detonation experiments.

The second hypothesis for the absorption was that the detonation light from the front passing through unreacted material, showing sodium absorption. The brighter reaction from Type-A would allow more light to pass through compared to the other materials investigated. However, sodium absorbs and emits in its vapour state, which it would not be in for unreacted HMX.

To better understand such a feature, the knowledge of when the sodium absorption occurred was important. Such a measurement could not be made with a single-shot spectrometer nor a pyrometer – a streak spectrometer, with both time and wavelength resolution would be required. However, there was another complication than just the apparatus used to measure the light emission. Similar to the measurements for time-dependent detonation temperature, the fibre would not be collecting light from just one detonation site, but from mutiple, all superimposed together. The sodium absorption is present in the dominating light from the shock front either passing backwards through detonation products, or forwards through unreacted HMX. However with the fibre collecting light from both events simultaneously, they cannot be easily separated.

6.8.3 Summary on particle size

From investigating the three types of HMX it was clear that some detonation properties depended on the density – such as the detonation pressure and velocity. Other properties, such as the brightness of the observed reaction and the light temperature, were more influenced by the particle/void size. Larger voids present in the material lead to higher temperatures, as well as other differences in the light emission, such as the sodium absorption. Therefore, brightness temperature in detonation is not a measurable function of detonation pressure nor velocity.

Studying the light emission from detonation would potentially reveal details of the internal structure that were not obvious. For example, if it had been damaged and had large voids inside, it would have a brighter measured detonation than if not. However, there are other techniques – such as x-ray tomography – that would allow such a measurement without needing to detonate the material.

Regardless, the dependence of detonation temperature has been linked to particle size. Given this data, hopefully more investigation can be done on the mechanisms of hotspot

collapse under detonation conditions, allowing for future model predictions of brightness temperature.

6.9 Streak spectrometer

Unlike deflagration, the detonation spectrum did not *often* show any spectral features. However, the curious sodium absorption present in Type-A detonation made it clear that simply assuming there would never be any spectral emission present in detonation was false. Therefore, the same spectrometer as assembled for deflagration (section 4.6.1) was attached onto the detonation reactions.

Both the usual Type-B as well as Type-A HMX detonation was measured. The aim was to investigate whether any spectral features would be observed in Type-B detonation - such as whether the reaction zone once the detonation front had passed could be detected. Also, as mentioned above, whether the mechanisms behind the sodium absorption seen in Type-A HMX could be understood.

The detonation reaction was initiated by a detonator, which in turn was initiated by a capacitor bank. There was a delay of 21.6 μs between firing the capacitor bank and detonation, and the time for the front to reach the optic fibre could be calculated from the known distance between the fibre and detonator and the detonation velocity at the specific density. Computing the triggers for the streak unit and camera was therefore more simple than in deflagration as everything - the streak, camera and capacitor bank - could be triggered from the same delay generator using the known timings.

6.9.1 Results

The temperature as a function of time was calculated for Type-B and Type-A of HMX, using the greybody fit across the spectrum at each point in time, with the results shown in figure 6.29.

The resultant temperature measurements were 7800 $\pm$ 200 K and 7600 $\pm$ 300 K for Type-B HMX and 7700 $\pm$ 300 K for Type-A. These temperatures were agreement with the previous measurements (presented in fig. 6.27), which showed a range of mean temperatures between 7500 and 8300 K for these materials and densities.

Agreement between the different diagnostic tools was important, and contributes to the reliability of the temperature measurements. However, the main reason for using the streak spectrometer was to observe whether any spectral features appeared in the light emission, and if so, whether they changed with time. In the mixed size Type-B HMX no such spectral

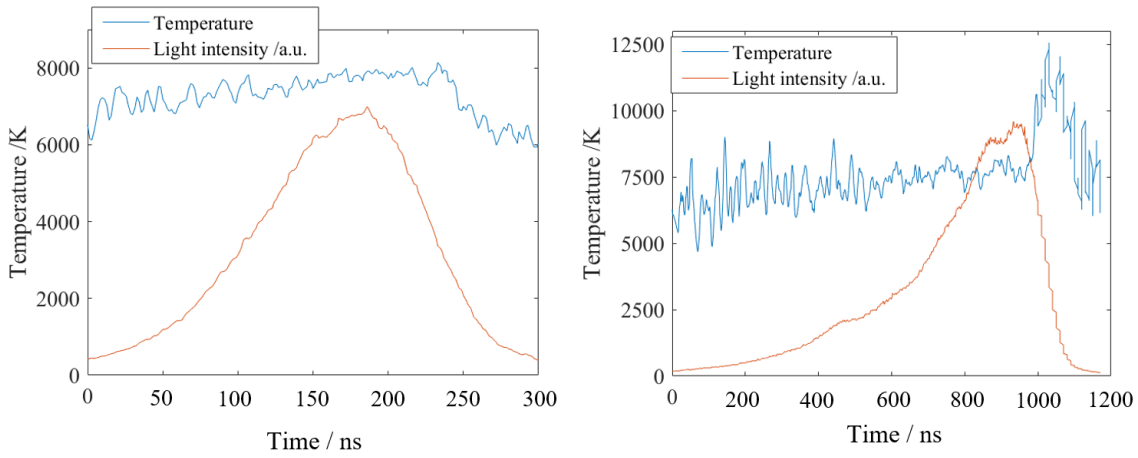

Fig. 6.29 The light intensity and temperature for the mixed Type-B HMX (left) and Type-A HMX (right). In agreement with the previous measurements, the temperature of the main light emission was equal to 7800 $\pm$ 200 K and 7700 $\pm$ 300 K. One main difference between these measurements is that, due to the higher scattering of Type-A, light emission was observed for a much longer period of time. Another is the spike of temperature in the Type-A measurements immediately after the main reaction period, likely due to the shock hitting the fibre (section 6.6), rather than any detonation effect.

features were ever recorded at any time. In contrast, the sodium absorption observed in Type-A HMX was present at all times in the light emission. This presence supports the conclusion that the collection angle of the fibre was large enough that it was detecting light from all parts of the reaction simultaneously, and so no discernable reaction zone separate from the detonation front could be resolved. Therefore, the light emission had similar features at each point in time.

In Type-A HMX detonation, the light scatters less, as observed from just measuring the brightness (section 6.8.1). Therefore, by scattering less, it is more likely to travel through multiple hotspot sites and vaporised sodium. Whereas in smaller particles, more scatter means the light does not travel as far (with a shorter mean-free-path) before hitting the fibre optic. Therefore, the measurements with Type-B HMX have both lower light intensity, and less spectral features, as the emission is only composed of light directly from front, without the addition of multiple scattering paths through the material.

The absorption peak, as shown in figure 6.28, had a nanometer order red-shift present, which meant the absorbing sodium had to be present at a large enough pressure in order to cause this shift. With the streak spectrometer, the position of the centre of absorption was known at different points in the reaction time. The resultant red-shift from sodium emission at 589.3 nm is shown in figure 6.30.

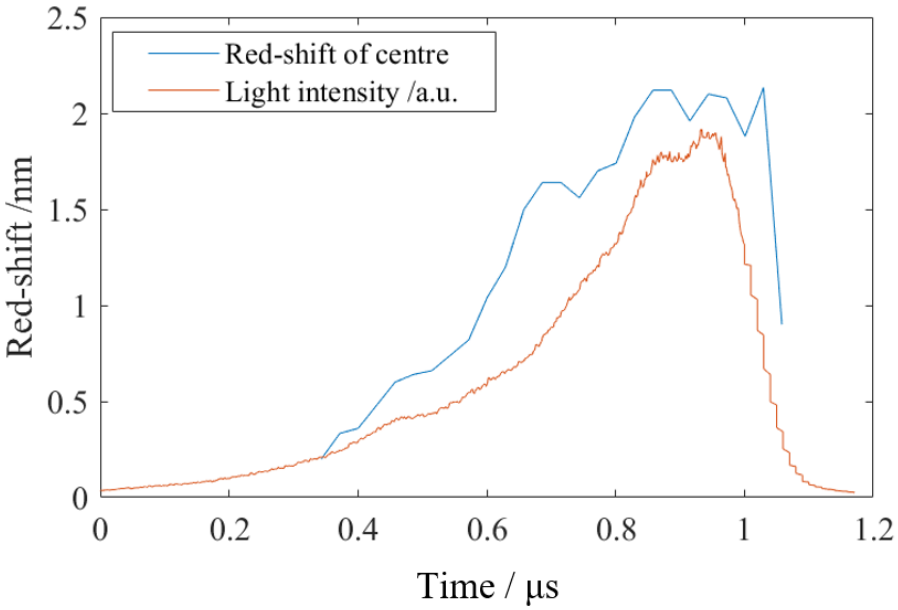

Fig. 6.30 The red-shift of the sodium absorption peak. The measurements were taken when a high enough signal was present to clearly identify the presence of the peak, and so there were no readings made for the low intensity early-time light. The red-shift increases as the front gets closer to the collecting fibre optic.

The red-shift is due to the change of energy levels due to the increased pressure, as discussed in Chapter 4. The shift is dependent on temperature and pressure, and by knowing one of these values, the other can be calculated. However, the absorbing sodium in the detonation experiment was located away from the detonation front, and so the measured temperature and pressure of the front cannot be assumed to be the same as what the sodium is experiencing. With two unknowns this means that the red-shift cannot be accurately linked back to the exact sodium properties. However, using certain assumptions and bounds in the data, the rough values of the sodium properties can be estimated.

One such assumption would be that all the absorbing sodium atoms are at the same pressure, and it was the temperature change that caused such a shift. However, it was clear that such an assumption was not true, as treating the system this way led to a completely unphysical result. For example, the small shifts present in the early-time light would be indicative of a much higher temperature than the larger shifts in the late-time light. The temperature of the sodium had to be less than the detonation temperature, and so choosing a low enough pressure that the temperature of the small-shift light was less than 8000 K led to the temperature of the large-shift light being less than 300 K for the same value of pressure. Therefore, the assumption of the shift being due to the change of temperature of the sodium was dropped.

The other assumption made was the opposite; that the sodium was absorbing at a constant temperature, and it was the pressure experienced by the atoms changing that caused the shift change. The highest probable temperature for the sodium to be present at was the temperature of the reaction zone, 4000 K, corresponding to sodium present during the reaction past the detonation front. The lowest temperature bound was chosen at 1156 K, the sodium vaporisation temperature. This value is correct only at ambient temperatures, and so would not equal the vaporisation temperature of the sodium in the experiment. However, it acts as a good lower bound for the temperature. Figure 6.31 details the resulting pressure values associated with the shift at these two constant temperature values, using the equation produced in Chapter 4.

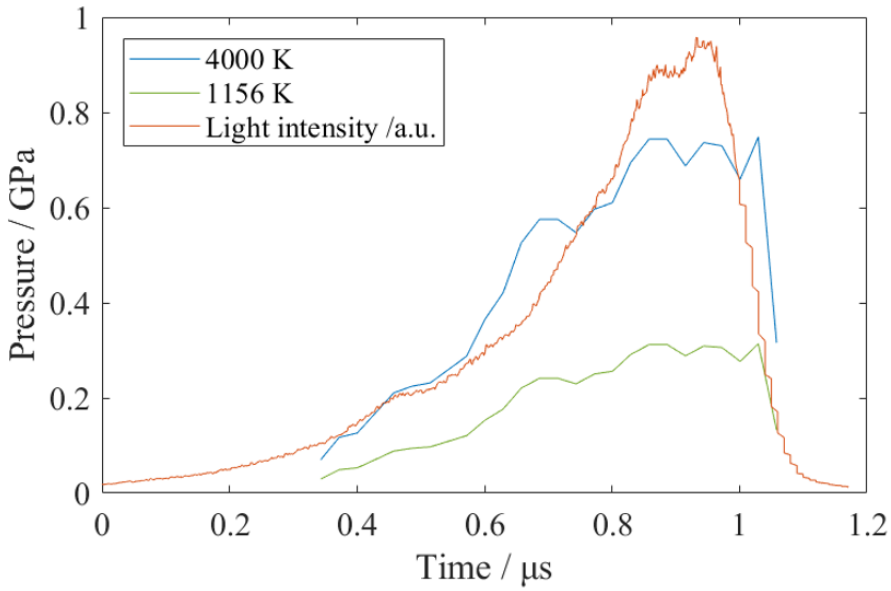

Fig. 6.31 The pressure associated with the observed red-shift in detonation, assuming a constant temperature of 4000 K and 1156 K. The pressure values between the 0.3 and 0.7 GPa range are of order to those observed in fallhammer deflagration, and are significantly less than the detonation pressure. This further establishes that the absorbing sodium was located away from the high pressure front.

The pressure values for the sodium atoms lie between 0.3 and 0.7 GPa, similar to the pressures observed in the fallhammer deflagration. The sodium atoms therefore exist far enough away from the reaction front to be at these lower (than detonation) pressures, however are still subject to a significant pressure environment. Indeed, with temperatures of 4000 K and pressure of 0.7 GPa, the higher bound suggests the sodium atoms are in exactly the same environment as deflagration. However, it is more likely the atoms exist in a lower temperature and/or pressure environment as the absorption width is reasonably narrow.

As discussed above, the decreased scattering with larger particles leads to a longer possible light path. The detonation front light is more likely, therefore, to travel from the hotspots, to old reaction sites where the pressure and temperature has lessened to deflagration conditions and sodium is still present.

The other result observed from the data shown in the above figures was the increase in the shift (and pressure) with time. With the decreased scatter of the Type-A detonation, more light from earlier times could be observed, and this early-time light had a smaller shift than the main period of light emission. It would be easy to theorise this increase could be the increase of detonation pressure along the reaction. However, the probable pressures of the reaction are much lower than detonation pressures, and the camera images show a prompt detonation (shock initiated rather than deflagration build up) at the detonator and a steady detonation front for the column - indicating a steady state at the same pressure throughout. Instead, this increasing red-shift is more likely due to the increased path the light travels.

The early-time light had a further distance to travel to reach the fibre, as the front was still millimetres away from the detection point. This longer path made it more probable that the light travelled through sodium existing further away from the front, and at a lower pressure. In contrast, at the front itself the majority (and dominating portion) of the detected light was straight from the front, travelling through only the nearby high-pressure sodium.

It is important to note that the light was from the greybody radiation produced by the high pressure detonation front, but the absorption (and the features of the peak, such as shift and width) were from colder sodium existing away from the front. Only through scattering less will the light reach both this sodium and the detecting fibre optic, and the less scattering that occurs, the further this light will travel.

6.9.2 Summary on streak spectrometer

With the use a streak-spectrometer, the previous time-dependent temperature measurements could be replicated, and the spectral features as a function of time were known. However, the streak system could not use light emission to distinguish different regimes suggested by ZND detonation model.

From the results, it was clear that adjusting the particle size of HMX in detonation had two main consequences. Firstly, with smaller particles - and smaller voids - the greybody temperatures were lower. Secondly, larger particles lead to less light scattering, with more light being detected and a sodium absorption peak due to more light travelling through areas away from the detonation front.

6.10 Conclusions

An experiment was designed which successfully measured the detonation velocity, pressure and detonation for a range of densities and different particle sizes. The results gained were in agreement with the theoretical model as well as past experiments. Detonation velocity and pressure showed the well-known almost linear relationship with density. The temperature had no obvious density dependence, instead was influenced by the size of the interstitial spaces inside the HMX column. At the lower tapped densities the emission spectra showed more of the deflagration temperature light, making temperature estimates more difficult as at least two different greybodies were present.

Other than increasing the measured temperature, increasing the particle size also led to decreased light scatter. This led to a much larger detected light emission for all measurements, as well as the presence of sodium absorption features.

6.10.1 Further research

Decreasing the collection angle of the fibre optic and utilising a high time-resolution streak-spectrometer would potentially measure when the sodium absorption occurs in the detonation process, and therefore give an indication of why and when such a feature might appear in other reactions.

Similar to the density series, a more complete ‘particle-size series’ could be undertaken to fully determine the relationship between the measured light temperature and particle size for a range of different sizes, rather than just two.

The high temperature detonation with its dependence on voids could also be investigated. Using a single crystal at 100% TMD would be ideal, however this would be difficult to produce and experiment with. Instead, a liquid explosive such as nitromethane could be investigated. Voids could be added artificially using carefully controlled glass beads to get exactly the required void size and distribution. This would allow the temperature of detonation to be measured up to 100% TMD, as well as any density needed, with any size void.

Chapter 7

Conclusions

The aim set out for this research was to measure and compare the light emission from different reactions of HMX, and to use the features and characteristics present in the emission to measure the properties of such reactions. To investigate the uses of optical spectroscopy as a tool in the field of energetics research, and to add to the knowledge of these complex reactions. The first goal was achieved by the successful measurement of the light emission from burning HMX, two different deflagration reactions and complete steady state denotation with a range of densities and particle sizes.

From burning HMX, the main spectral peaks were identified as belonging to the highly emissive alkali metal impurities that were naturally present in the material. In deflagration, the higher temperature leads to the presence of greybody emission alongside these spectral features, from which the temperature of deflagration was measured as 3900 ± 400 K. Using the knowledge of where the spectral features would be in the spectrum allowed a time-dependent 4-channel pyrometer to be built that avoided such features, which measured a constant temperature of 4000 ± 200 K over the main period of light emission.

A new technique for initiating energetics in a Hopkinson bar was developed, allowing further, more detailed, diagnostics and analysis on this regime. With the impedance matched bars accounting for all the energy in the system, the absorbed energy occurring before reaction was measured as 8.2 ± 0.8 J, calculated explicitly from a single experiment rather than relying on probability derived measurements that require multiple initiation events. The initial impact was also more repeatable, with the constant top-hat pulse leading to the determination of a clear pressure threshold at 1028 ± 18 MPa. However, unlike the fallhammer, which observed the reaction initiating mainly on the ring-up or ring-down of the pressure, the Hopkinson bar did not show initiation on ramping pressure pulses, even through the above mentioned pressure threshold, indicating a dependence on the pressure path history.

The decrease of the time to reaction in Hopkinson bar initiation with increasing initiating pressure was also evidence that an energy (or power) threshold was required for initiation. As long as the impact provided enough power so that the heat loss mechanisms were lower than the rate of energy accumulation, and the insult lasted long enough so the activation energy could be achieved, initiation would occur. Investigating RDX and PETN showed similar behaviour to HMX, with a clear pressure initiation threshold for each material, and the same sensitivity order for the three materials as had been previously established in the fallhammer. Therefore, despite not fully encompassing the physics of initiation, the SHPB pressure threshold for initiation could provide a good indication of sensitivity and allow easier and better comparison between materials than the fallhammer energy sensitivity, as the pressure is directly calculated and the threshold is very clear.

These two HMX deflagration regimes allowed for interesting comparison, and a more involved investigation into deflagration. The main difference in initiation was the pressure at which the reaction occurred - with the higher value of 1 GPa in the Hopkinson bar to 0.6 GPa in the fallhammer. A noticeable difference was also observed in the optical emission; both reactions showed a mix of greybody and spectral features, however the greybody emission was more dominant for the Hopkinson bar. Using the familiar method of measuring the temperature from the greybody emission showed another significant difference, that the Hopkinson bar deflagration was cooler by 1000 K, with temperatures of 2900 ± 200 K. By applying a mass spectrometer, it became clear that the chemical pathways for these two deflagration reactions were different enough that they could not be assumed variants on one overall 'ideal' deflagration reaction.

The presence of spectral features in both deflagrations was also important. The sodium emission had been red-shifted under the extreme pressures of the reaction, and using both the lower pressure fallhammer and the higher pressure Hopkinson bar initiation allowed this red-shift to be calibrated for a range of deflagration conditions. The behaviour was consistent with Lindholm-Foley collisional theory, and this new calibration into energetic conditions would allow optical based pressure measurements to be achieved in future experiments in this field. By assembling a streak-spectrometer, the technique of 'tracking' the sodium peak shift in order to measure the pressure evolution was achieved, measuring for the first time both the temperature and pressure of the deflagration reaction from the same light source.

Finally, the regime of detonation was examined. The detonation pressure and velocity as a function of density was recorded, and compared against both simple shock conservation models as well as more polymer based Group Interaction Modelling. The optical emission showed no spectral features for the majority of experiments. The resulting greybody allowed temperatures of *circa* 7000 K to be measured, confirming that the main source of light

emission in detonation was due to mechanical reasons - such as the voids in the material collapsing under the high shock pressures - rather than the exothermic chemical reaction.

The density of the granular bed of HMX did not have a significant effect on the temperature, however the particle size - or size of the voids - did, with the presence of larger voids leading the larger recorded temperatures. The use of larger particles also meant a decrease of light scattering, both increasing the brightness of the recorded measurements as well as the inclusion of absorption features from sodium atoms away from the detonation front.

In summary, a broad account of optical emission was achieved for HMX. The main optical characteristics of each regime were recorded and explained. The light emission measured was used to both verify previous measurements and methods, as well as develop new diagnostic techniques that would benefit future research. In particular, the now possible optical measurements of pressure from the sodium impurity spectral peak. Additionally, both the results achieved and the newly designed experiments inspired further useful findings, such as a better impact initiation sensitivity test in the Hopkinson bar, the identification of different thresholds required for initiation in deflagration and the effect initiation method has on the underlying chemistry.

References

[1] S. M. Walley, J. E. Field, R. A. Biers, W. G. Proud, D. M. Williamson, and A. P. Jardine. The use of glass anvils in drop-weight studies of energetic materials. *Propellants, Explosives, Pyrotechnics*, 40(3):351–365, 2015.

[2] D. M. Williamson, S. Gymer, N. E. Taylor, S. M. Walley, A. P. Jardine, A. Glauser, S. French, and S. Wortley. Characterisation of the impact response of energetic materials: observation of a low-level reaction in 2,6-diamino-3,5-dinitropyrazine-1-oxide (LLM-105). *RSC Adv.*, 6:27896–27900, 2016.

[3] N. Taylor. *Hotspots in ammonium nitrate*. PhD thesis, University of Cambridge, Department of Physics, 2011.

[4] J. Akhavan. *The chemistry of explosives*. Royal Society of Chemistry, 2004.

[5] C. M. Tarver. Jones–Wilkins–Lee unreacted and reaction product equations of state for overdriven detonations in octogen- and triaminotrinitrobenzene-based plastic-bonded explosives. *J. Phys. Chem. A*, 124(7):1399–1408, 2020.

[6] T. S. Bajpayee, T. R. Rehak, G. L. Mowrey, and D. K. Ingram. Blasting injuries in surface mining with emphasis on flyrock and blast area security. *Journal of Safety Research*, 35:47–57, 2004.

[7] W. E. Bachmann and J. C. Sheehan. A new method of preparing the high explosive RDX. *Journal of the American Chemical Society*, 71(5):1842–1845, 1949.

[8] T. R. Gibbs and A. Popolato. *LASL Explosive Property Data*. University of California Press, Berkeley, 1980.

[9] K. A. Fleming, R. Bird, M. W. G. Burt, and C. E. Whatmore. The influence of formulation variables on the growth of reaction in plastic bonded explosives. *Proceedings, Eighth Symposium (International) on Detonation*, 1985.

[10] D. L. Chapman. On the rate of explosion in gases. *The London, Edinburgh, and Dublin Philosophical Magazine and Journal of Science*, 47(284):90–104, 1899.

[11] E. Jouguet. Sur la propagation des réactions chimiques dans les gaz [On the propagation of chemical reactions in gases] (in French). *Journal de Mathématiques Pures et Appliquées*, 6:347–425, 1905.

[12] Y. B. Zel'dovich. On the theory of the propagation of detonation in gaseous systems (in Russian). *Journal of Experimental and Theoretical Physics*, 10:542–568, 1940.

[13] J. von Neumann. Theory of detonation waves. Progress report to the National Defense Research Committee div. b, OSRD-549 (PB 31090). *John von Neumann: Collected Works, 1903-1957. New York: Pergamon Press*, 6:178–218, 1963 [1942].

[14] W. Döring. Über Detonationsvorgang in Gasen [on detonation processes in gases] (in German). *Annalen der Physik*, 43:421–436, 1943.

[15] R. L. Gustavsen, B. D. Bartram, and N. J. Sanchez. Detonation wave profiles measured in plastic bonded explosives using 1550 nm photon doppler velocimetry. *AIP Conference Proceedings*, 1195(1):253–256, 2009.

[16] R. E. Duff and E. Houston. Measurement of the Chapman-Jouguet pressure and reaction zone length in a detonating high explosive. *J. Chem. Phys*, 23(1268), 1955.

[17] V. M. Zaitsev, P. F. Pokhil, and K. K. Shvedov. An electromagnetic method for measuring the speed of explosion products (in Russian). *Dokl. Akad. Nauk SSSR*, 132(6):1339–1340, 1960.

[18] W. C. Davis. Magnetic probe measurements of particle velocity profiles. *Proceedings, Sixth Symposium (International) on Detonation*, 1976.

[19] S. A. Sheffield, D. D. Bloomquist, and C. M. Tarver. Subnanosecond measurements of detonation fronts in solid high explosives. *J. Chem. Phys.*, 80(3831), 1984.

[20] V. Bouyer, M. Doucet, and L. Decaris. Experimental measurements of the detonation wave profile in a tatb based explosive. *EPJ Web of Conferences*, 10(00030), 2010.

[21] A. Sollier, V. Bouyer, P. Hébert, and M. Doucet. A novel method for the measurement of the von Neumann spike in detonating high explosives. *J. Appl. Phys.*, 119(245902), 2016.

[22] A. N. Dremin. *Toward detonation theory*. Springer, 1999.

[23] A. W. Campbell. Deflagration-to-detonation transition in granular HMX. *JANAF technical report, LASL*, 1:105–130, 1981.

[24] G. R. Parker, E. M. Heatwole, M. D. Holmes, B. W. Asay, P. M. Dickson, and J. M. McAfee. Deflagration-to-detonation transition in hot HMX and HMX-based polymer-bonded explosives. *Combustion and Flame*, 215:295 – 308, 2020.

[25] R. Meyer, J. Köhler, and A. Homburg. *Explosives*. Wiley-VCH, Weinheim, 2007.

[26] C. S. Coffey and E. T. Toton. A microscopic theory of compressive wave-induced reactions in solid explosives. *The Journal of Chemical Physics*, 76(2):949–954, 1982.

[27] F. J. Zerilli and E. T. Toton. Shock-induced molecular excitation in solids. *Phys. Rev. B*, 29:5891–5902, May 1984.

[28] H. Kim and D. D. Dlott. Theory of ultrahot molecular solids: Vibrational cooling and shock-induced multiphonon up pumping in crystalline naphthalene. *The Journal of Chemical Physics*, 93(3):1695–1709, 1990.

[29] A. A. L. Michalchuk, M. Trestman, S. Rudić, P. Portius, P. T. Fincham, C. R. Pulham, and C. A. Morrison. Predicting the reactivity of energetic materials: an ab initio multi-phonon approach. *J. Mater. Chem. A*, 7:19539–19553, 2019.

[30] F. P. Bowden and A. D. Yoffe. *The initiation and growth of explosions in liquids and solids*. Cambridge University Press, 1952.

[31] A. W. Campbell, W. C. Davis, J. B. Ramsay, and J. R. Travis. Shock initiation of solid explosives. *The Physics of Fluids*, 4(4):511–521, 1961.

[32] C. L. Mader. Shock and hot spot initiation of homogeneous explosives. *The Physics of Fluids*, 6(3):375–381, 1963.

[33] S. N. Heavens and J. E. Field. The ignition of a thin layer of explosive by impact. *Proc. R. Soc. Lond. A*, 338:77–93, 1974.

[34] N. K. Rai and H. S. Udaykumar. Void collapse generated meso-scale energy localization in shocked energetic materials: Non-dimensional parameters, regimes, and criticality of hotpsots. *The Physics of Fluids*, 31:016103, 2019.

[35] R. H. Perry, D. W. Greem, and J. O. Maloney. *Perry's Chemical Engineers' Handbook*. McGraw-Hill New York, 1997.

[36] J. Starkenberg. Ignition of solid high explosive by the rapid compression of an adjacent gas layer. *Proceedings, Seventhth Symposium (International) on Detonation*, 1981.

[37] N. K. Bourne and J. E. Field. Shock-induced collapse of single cavities in liquids. *Journal of Fluid Mechanics*, 244:225–240, 1992.

[38] A. K. Kapila, D. W. Schwendema, J. R. Gambino, and W. D. Henshaw. A numerical study of the dynamics of detonation initiated by cavity collapse. *Shock Waves*, 25(6):545–572, 2015.

[39] R. Menikoff and T. D. Sewell. Constituent properties of HMX needed for mesoscale simulations. *Combustion Theory and Modelling*, 6(1):103–125, 2002.

[40] M. M. Carroll and A. C. Holt. Static and dynamic pore-collapse relations for ductile porous materials. *Journal of Applied Physics*, 43:1626–1636, 1972.

[41] B. A. Khasainov, A. A. Borisov, B. S. Ermolaev, and A. I. Korotkov. Two phase viscoplastic model of shock initiation of detonation on high density pressed explosives. *Proceedings, Seventh Symposium (International) on Detonation*, 1981.

[42] P.C. Chou, Z. Ritman, and D. Liang. Viscosity and heat conduction effects in pore collapse. *Mechanics of Materials*, 17:295–305, 1994.

[43] R. Frey. Initiation of explosives by rapid shear. *Proceedings, Seventh Symposium (International) on Detonation*, 1981.

[44] F. P. Bowden and O. A. Gurton. Initiation of solid explosives by impact and friction: the influence of grit. *Proc. R. Soc. Lond. A*, 198:337–349, 1949.

[45] J. E. Field. Hot spot ignition mechanisms for explosives. *Acc. Chem. Res.*, 25(11):489–496, 1992.

[46] W. K. Lewis and C. G. Rumchik. Measurement of apparent temperature in post-detonation
105(5):056104, 2009.

[47] V. Bouyer, I. Ranc-Darbord, P. Hervé, G. Baudin, C. Le Gallic, F. Clément, and G. Chavent. Shock-to-detonation transition of nitromethane: Time-resolved emission spectroscopy measurements. *Combustion and Flame, Elsevier*, 144(1-2):139 – 150, 2006.

[48] W. P. Bassett and D. D. Dlott. High dynamic range emission measurements of shocked energetic materials: Octahydro-1,3,5,7-tetranitro-1,3,5,7-tetrazocine (HMX). *Journal of Applied Physics*, 119(22):225103, 2016.

[49] J. Schneider, R. Pflieger, S. I. Nikitenko, D. Shchukin, and H. Möhwald. Line emission of sodium and hydroxyl radicals in single-bubble sonoluminescence. *The Journal of Physical Chemistry A*, 115(2):136–140, 2011.

[50] C. H. Johansson and T. Sjölin. Emission and absorption of light behind detonation front. *Nature*, 185(4712):523–524, 1960.

[51] T. Hikita, T. Asaba, and K. Yoneda. Study of shock waves from high explosives. *Proceedings, Sixth Symposium (International) on Combustion*, 1956.

[52] C. H. Johansson and P. A. Persson. *Detonics of high explosives*. London ; New York : Academic Press, 1970.

[53] S. Paterson. Source of the light recorded in photographs of detonating explosives. *Nature*, 167:479–481, 1951.

[54] M. D. Tarasov, I. I. Karpenko, V. A. Sudovtsov, and A. I. Tolshmyakov. Measuring the brightness temperature of a detonation front in a porous explosive. *Combustion, Explosion, and Shock Waves*, 43(4):465–467, 2007.

[55] W. P. Bassett, B. P. Johnson, N. K. Neelakantan, K. S. Suslick, and D. D. Dlott. Shock initiation of explosives: High temperature hot spots explained. *Appl. Phys. Lett*, 111(6), 2017.

[56] B. P. Johnson, X. Zhou, H. Ihara, and D. D. Dlott. Observing hot spot formation in individual explosive crystals under shock compression. *J. Phys. Chem. A*, 124(23):4646–4653, 2020.

[57] R. Frey. Cavity collapse in energetic materials. *Proceedings, Eighth Symposium (International) on Detonation*, 1985.

[58] M.M. Chaudhri, J. E. Field, and D. Tabor. The role of rapidly compressed gas pockets in the initiation of condensed explosives. *Proc. R. Soc. Lond. A*, 340(1620), 1974.

[59] J. H. Blackburn and L. B. Seely. Light intensity from detonating PETN pressings filled with butane. *Nature*, 202:382–383, 1964.

[60] J. H. Blackburn and L. B. Seely. Detonation light in granular explosives. *Trans. Faraday Soc*, 61:537–545, 1965.

[61] J. H. Blackburn and L. B. Seely. Light emitted from shocked granular sodium chloride in a vacuum. *Nature*, 202:276–277, 1964.

[62] H. Le Chatelier. Sur le development et la propagation de l'onde explosive, [on the development and propagation of the explosive wave] (in French). *C.R. Acad. Sci., Paris,*, 130(1755), 1900.

[63] C. Johansson and L. Sternhoff. Suppressed light emission of the reaction zone in detonation. *Nature*, 183:247–248, 1959.

[64] W. C. Prinse, R. van Esveld, R. Oostdam, M. van Rooijen, and R. Bouma. Fiber optic techniques for measuring various properties of shock waves. *23rd International Congress on High-Speed Photography and Photonics*, 3516:246 – 251, 1999.

[65] J. Lee and P. A. Persson. Detonation behavior of emulsion explosives. *Propellants, Explosives, Pyrotechnics*, 15(5):208–216, 1990.

[66] M. F. Gogulya, M. N. Makhov, and A. Y. Dolgoborodov. Mechanical sensitivity and detonation parameters of aluminized explosives. *Combustion, Explosion, and Shock Waves*, 40:445–457, 2004.

[67] C. Campbell, W.B. Littler, and C. Whitworth. The measurement of pressures developed in explosion waves. *Proc. R. Soc. London Ser. A*, 137:380–396, 1932.

[68] E. Henderson. Combustible gas mixtures in pipe lines. *Proc. Pacific Coast Gas Association*, 32, 1941.

[69] L.M. Barker and R.E. Hollenbach. Laser interferometer for measuring high velocities of any reflecting surface. *J. Appl. Phys.*, 43(4669), 1972.

[70] O. T. Strand, L. V. Berzins, D. R. Goosman, W. W. Kuhlow, P.D. Sargis, and T. L. Whitworth. Velocimetry using heterodyne techniques. *26th International Congress on High-Speed Photography and Photonics*, 5580:593 – 599, 2005.

[71] F.P. Bowden and O.A. Gurton. Initiation of explosion: birth and growth of explosion by impact and friction. *Proc. R. Soc. Lond. A*, 198(1054):350–372, 1949.

[72] J.D. Blackwood and F.P. Bowden. The initiation, burning and thermal decomposition of gunpowder. *Proc. R. Soc. Lond. A*, 213(1114):285–306, 1952.

[73] J.E. Field, G.M. Swallowe, and S.N. Heavens. Ignition mechanisms of explosives during mechanical deformation. *Proc. R. Soc. Lond. A*, 382(1782):231–244, 1982.

[74] G.M. Swallowe and J.E. Field. The ignition of a thin layer of explosive by impact; the effect of polymer particles. *Proc. R. Soc. Lond. A*, 379(1777):389–408, 1982.

[75] S.M. Walley, J.E. Field, and S.J.P. Palmer. Impact sensitivity of propellants. *Proc. R. Soc. Lond. A*, 438(1904):571–583, 1992.

[76] J.E. Field, N.K. Bourne, S.J.P. Palmer, and S.M. Walley. Hot-spot ignition mechanisms for explosives and propellants. *Proc. R. Soc. Lond. A*, 339(1654):269–283, 1992.

[77] H. Czerski, M. W. Greenaway, W. G. Proud, and J. E. Field. β-δ phase transition during dropweight impact on cyclotetramethylene-tetranitroamine. *Journal of Applied Physics*, 96(8):4131–4134, 2004.

[78] A. Kramida, Yu. Ralchenko, J. Reader, and NIST ASD Team. NIST atomic spectra database (version 5.7.1), 2019. [online] https://physics.nist.gov/asd.

[79] E. E. Pickett and S.R.Koirtyohann. The nitrous oxide-acetylene flame in emission analysis i: General characteristics. *Spectrochimica Acta Part B: Atomic Spectroscopy*, 23(4):235–244, 1968.

[80] N. Glumac. Early time spectroscopic measurements during high-explosive detonation breakout into air. *Shock Waves*, 23:131–138, 2013.

[81] T. Goyal, D. Trivedi, and O. Samimi Abianeh. Autoignition and flame spectroscopy of propane mixture in a rapid compression machine. *Fuel*, 233:56 – 67, 2018.

[82] M. K. Hudson K. L. Maxwell. Spectral study of metallic molecular bands in hybrid rocket plumes. *Journal of Pyrotechnics*, pages 59–69, 2005.

[83] B. P. Aduev, E. D. Aluker, A.G. Krechetov, and Y. P. Sakharchuk. Predetonation optical breakdown spectrum of silver azide. *Tech. Phys. Lett.*, 24:636–637, 1998.

[84] S. Poeuf, G. Baudin, M. Genetier, A. Lefrancois, L. Jacquet, , and A. Chinnayya. Emission spectroscopy for monitoring condensed carbon in detonation products of oxygen-deficient high explosives. *AIP Conference Proceedings*, 1979, 2018.

[85] W. Demtröder. *Widths and Profiles of Spectral Lines. In Laser Spectroscopy*. Springer, Berlin, Heidelberg, 2008.

[86] W. P. Bassett and D. D. Dlott. Shock initiation of explosives: Temperature spikes and growth spurts. *Applied Physics Letters*, 109(9):091903, 2016.

[87] J. C. Richley and J. W. Ferguson. Results from a high speed pyrometer measuring detonating explosive. *AIP Conference Proceedings*, 1979(1):160022, 2018.

[88] W. Xiao, K. Chen, H. D. Xing, and B. L. Wang. Effect of storage temperature on explosion characteristics of RDX-based thermobaric explosive. *Journal of Physics: Conference Series*, 1507:022010, mar 2020.

[89] A. G. Gaydon. *The Spectroscopy of flames*. Springer, Netherlands, 1974.

[90] A. G. Gaydon and H. G. Wolfhard. *Flames – Their Structure, Radiation and Temperature*. Chapman and Hall Ltd., London, 1979.

[91] R. Rekers and D. Villars. Flame zone spectroscopy of solid propellants. *Review of Scientific Instruments*, 25:424 – 429, 06 1954.

[92] L.E. Harris and M. McIlwain. Coherent anti-stokes raman spectroscopy in propellant flames. *Fast Reactions in Energetic Systems. Springer, Dordrecht*, 71:424 – 429, 1981.

[93] G.C. Baumann, W.Y. Cheung, and L.E. Harris. CARS spectroscopy of the reaction zone of nitramine propellants. *Proceedings, tenth International Pyrotechnics Seminar*, 1985.

[94] A. Kurtz, D. Brüggemann, U. Giesen, and S. Heshe. Quantitative nitric oxide CARS spectroscopy in propellant flames. *Non-Intrusive Combustion Diagnostics*, pages 160 – 166, 1994.

[95] J. Vanderhoff, M. Teague, and A. Kotlar. Absorption spectroscopy through the dark zone of solid propellant flames. page 51, 04 1992.

[96] J. Vanderhoff. Species profiles in solid propellant flames using absorption and emission spectroscopy. *Combustion and Flame*, 84:73–92, 03 1991.

[97] R. A. Pesce-Rodriguez and R. A. Fifer. Applications of fourier transform infrared photoacoustic spectroscopy to solid propellant characterization. *Applied Spectroscopy*, 45(3):417–419, 1991.

[98] N. Lamoureux, K. Marschallek-Watroba, P. Desgroux, J.-F. Pauwels, M. D. Sylla, and L. Gasnot. Measurements and modelling of nitrogen species in CH4/O2/N2 flames doped with NO, NH3, or NH3+NO. *Combustion and Flame*, 176:48 – 59, 2017.

[99] J. H. Blackburn and L. B. Seely. Source of the light recorded in photographs of shocked granular pressings. *Nature*, 194:370–371, 1962.

[100] J. R. Carney, J. S. Miller, J. C. Gump, and G. I. Pangilinan. Time-resolved optical measurements of the post-detonation combustion of aluminized explosives. *Review of Scientific Instruments*, 77(6):063103, 2006.

[101] J. Wilkinson, J. M. Lightstone, C. J. Boswell, and J. R. Carney. Emission spectroscopy of aluminum in post-detonation combustion. *AIP Conference Proceedings*, 955(1):1271–1274, 2007.

[102] X. L. Zhou, Y. Li, Z. L. Liu, C. X. Lu, J. D. Wang, and Y. Cao. Transient detonation temperature measurement of explosives using spectroscopic method. *Spectroscopy and spectral analysis*, 23(5):982–983, 2003.

[103] W. K. Lewis, C. G. Rumchik, and M. J. Smith. Emission spectroscopy of the interior of optically dense post-detonation fireballs. *Journal of Applied Physics*, 113(2):024903, 2013.

[104] J. R. Carney, J. Wilkinson, and J. M. Lightstone. Time-resolved optical measurements of detonation and combustion products. *AIP Conference Proceedings*, 955(1):1225–1228, 2007.

[105] W. P. Bassett and D. D. Dlott. 32-channel pyrometer with high dynamic range for studies of shocked nanothermites. *AIP Conference Proceedings*, 1793(1):060012, 2017.

[106] W. P. Bassett, B. P. Johnson, and D. D. Dlott. Hot spot chemistry in several polymer-bound explosives under nanosecond shock conditions. *Propellants, Explosives, Pyrotechnics*, 45(2):338–346, 2020.

[107] S. French. *Initiation and Growth of Reaction in LLM-105*. PhD thesis, University of Cambridge, Department of Physics, 2019.

[108] World Health Organization. *Guidelines for drinking-water quality, 2nd ed. Vol. 2. Health criteria and other supporting information.* World Health Organization, Geneva, 1996.

[109] Energetic materials testing and assessment policy committee (EMTAP) manual of tests, fourth edition, 2007.

[110] Eurenco. HMX property characteristics, 2010. [online] http://www.eurenco.com.

[111] C.B. Storm, J.R. Stine, and J.F. Kramer. *Sensitivity Relationships in Energetic Materials*. Kluwer Academic Publishers, Dordrecht, 1990.

[112] D. Braund. Personal communication.

[113] D.J. Finney. *Probit Analysis, 3rd ed.* Cambridge University Press, 1971.

[114] A.V. Yurlov, V.A. Pushkov, T.G. Naidanova, A. N. Tsibikov, and A. V. Bakanova. Response of an HMX based explosive to dynamic loading by the hopkinson split bar technique. *Combust Explos Shock Waves*, 52:493–496, 2016.

[115] H. J. John and M. F. Alamo. High-strain rate testing of HMX-based explosive. *American Institute of Physics Conference Series*, 505:679–682, 2000.

[116] H. Trumel, P. Lambert, and M. Biessy. Mechanical and microstructural characterization of a HMX-based pressed explosive: Effects of combined high pressure and strain rate. *EPJ Web of Conferences*, 26:02005–, 2012.

[117] B. Hopkinson. The effects of the detonation of gun-cotton. *Trans. North-East Coast Inst. Engineers Shipbuilders*, 30:199–217, 1914.

[118] B. Hopkinson. A method of measuring the pressure produced in the detonation of high explosives or by the impact of bullets. *Proceedings of the Royal Society of London. Series A, Containing Papers of a Mathematical and Physical Character*, 89(612):411–413, 1914.

[119] J. W. Landon, H. Quinney, and A. W. Ewing. Experiments with the hopkinson pressure bar. *Proceedings of the Royal Society of London. Series A, Containing Papers of a Mathematical and Physical Character*, 103(723):622–643, 1923.

[120] G. I. Taylor. The testing of materials at high rates of loading. *J.Inst. Civil Engrs*, 26:486–519, 1946.

[121] H. Kolsky. An investigation of the mechanical properties of materials at very high rates of loading. *Proceedings of the Physical Society. Section B*, 62(11):676–700, 1949.

[122] S. Walley. A history of Hopkinson bars in Europe, 2019. Unpublished presentation at DYMAT.

[123] L. J. Lea and A. P. Jardine. Application of photon doppler velocimetry to direct impact hopkinson pressure bars. *Review of Scientific Instruments*, 87(2):023101, 2016.

[124] S. Rigby, A. Barr, and M. Clayton. A review of pochhammer-chree dispersion in the hopkinson bar. *Proceedings of the Institution of Civil Engineers - Engineering and Computational Mechanics*, 171:1–21, 2017.

[125] M. Gruhne, M. Lommel, M. Wurzenberger, N. Szimhardt, T. Klapötke, and J. Stierstorfer. OZM ball drop impact tester (BIT-132) vs. BAM standard method-a comparative investigation. *Propellants, Explosives, Pyrotechnics*, 2019.

[126] J. Šelešovský and J. Pachman. Probit analysis – a promising tool for evaluation of explosive's sensitivity. *Central European Journal of Energetic Materials*, 7, 01 2010.

[127] O. J. Morley and D. M. Williamson. Pressure and temperature induced red-shift of the sodium D-line during HMX deflagration. *Commun. Chem.*, 3(13), 2020.

[128] D. G. Tasker, R. J. Lee, and P. K. Gustavson. The measurement of electrical conductivity in detonating condensed explosives. *Weapons research and technology department, Naval Surface Warfare Center, Virginia*, 1993.

[129] L. Windholz and M. Musso. Stark-effect investigations of the sodium D_2 line. *Phys. Rev. A*, 39:2472–2480, 1989.

[130] S. Sahal-Bréchot, M. S. Dimitrijević, and N. Moreau. Virtual laboratory astrophysics: the STARK-b database for spectral line broadening by collisions with charged particles and its link to the european project VAMDC. *Journal of Physics: Conference Series*, 397:012019, 2012.

[131] S. Sahal-Bréchot. Impact theory of the broadening and shift of spectral lines due to electrons and ions in a plasma. *Astron. and Astrophys.*, 1:91–123, 1969.

[132] S. Y. Chén and M. Takeo. Broadening and shift of spectral lines due to the presence of foreign gases. *Rev. Mod. Phys.*, 29:20–73, 1957.

[133] H. Margenau and W. W. Watson. Pressure effects of foreign gases on the sodium D-lines. *Phys. Rev*, 44(2):92–98, 1933.

[134] H. Margenau and W. W. Watson. Pressure effects on spectral lines. *Rev. Mod. Phys.*, 8:22–53, 1936.

[135] H. Margenau. Pressure shift and broadening of spectral lines. *Phys. Rev.*, 40:387–408, 1932.

[136] H. A. Lorentz. *The theory of electrons*. Leipzig : B.G. Teubner ; New York : G.E. Stechert, 1916.

[137] D. G. Fletcher and J. C. McDaniel. Collisional shift and broadening of iodine spectral lines in air near 543 nm. *J. Quant. Spectrosc. Radiat. Transfer*, 54(5):837–850, 1995.

[138] G. Traving. *Interpretation of line broadening and line shift*. W. Lochte-Holtgreven (Ed.), Plasma Diagnostics, North-Holland,, 1978.

[139] R. Pollice and P. Chen. A universal quantitative descriptor of the dispersion interaction potential. *Angewandte Chemie International Edition*, 58(29):9758–9769, 2019.

[140] A. K. Chijioke, W. J. Nellis, A. Soldatov, and I. F. Silvera. The ruby pressure standard at 150 GPa. *J. App. Phys*, 98(11):114905, 2005.

[141] D.W. Langer and R.N. Euwema. Pressure shift of the Cr levels in Al2O3. *Journal of Physics and Chemistry of Solids*, 28(3):463 – 465, 1967.

[142] Y. Tanabe and S. Sugano. On the absorption spectra of complex ions. *Journal of the Physical Society of Japan*, 9(5):753–766, 1954.

[143] R. A. Forman, G. J. Piermarini, J. D. Barnett, and S. Block. Pressure measurement made by the utilization of ruby sharp-line luminescence. *Science*, 176(4032):284–285, 1972.

[144] D Breshears. One dimensional time-to-explode (ODTX) in HMX spheres. *Los Alamos National Lab*, 1997.

[145] T. B. Brill and K. J. James. Kinetics and mechanisms of thermal decomposition of nitroaromatic explosives. *Chem. Rev.*, 93(8):2667–2692, 1993.

[146] N.E. Ermolin and V.E. Zarko. Mechanism and kinetics of the thermal decomposition of cyclic nitramines. *Combust Explos Shock Waves*, 33:251–269, 1997.

[147] A. J. B. Robertson and A. Yoffe. Gases liberated from explosions initiated by impact. *Nature*, (4099):806–807, 1948.

[148] Y. Oyumi and T. B. Brill. Thermal decomposition of energetic materials. A high-rate, in situ, FTIR study of the thermolysis of RDX and HMX with pressure and heating rate as variables. *Combust. Flame*, 62:213–224, 1985.

[149] N. R. Greiner and R. Hermes. Chemistry of detonation soot: Diamonds, graphite, and volatiles. *University of North Texas Libraries, UNT Digital Library, https://digital.library.unt.edu*, 1989.

[150] F. Volk. Analysis of the detonation products of insensitive high explosives. In Jehuda Yinon, editor, *Advances in Analysis and Detection of Explosives*, pages 223–239, Dordrecht, 1993. Springer Netherlands.

[151] Pengwan Chen, Fenglei Huang, and Shourong Yun. Characterization of the condensed carbon in detonation soot. *Carbon*, 41(11):2093–2099, 2003.

[152] D. Pantea, S. Brochu, S. Thiboutot, G. Ampleman, and G. Scholz. A morphological investigation of soot produced by the detonation of munitions. *Chemosphere*, 65(5):821–831, 2006.

[153] D. W. Podlesak, R. C. Huber, R. S. Amato, D. M. Dattelbaum, M. A. Firestone, R. L. Gustavsen, C. E. Johnson, J. T. Mang, and B. S. Ringstrand. Characterization of detonation soot produced during steady and overdriven conditions for three high explosive formulations. *AIP Conference Proceedings*, 1793(1):030006, 2017.

[154] N. P. Satonkina, A. P. Ershov, A. O. Kashkarov, and I. A. Rubtsov. Elongated conductive structures in detonation soot of high explosives. *RSC Adv.*, 10:17620–17626, 2020.

[155] V. Sinditskii, V. Y. Egorshev, M. Berezin, and V. Serushkin. Mechanism of HMX combustion in a wide range of pressures. *Combustion Explosion and Shock Waves*, 45:461–477, 07 2009.

[156] G. Lengelle, J. Duterque, and J. F. Trubert. "Physicochemical mechanisms of solid propellant combustion" in: V. Yang, T. B. Brill, and W. Z. Ren (eds.). *Progress in Astronautics and Aeronautics*, 185:287–334, 2000.

[157] N. Kubota and S. Sakamoto. Combustion mechanism of HMX. *Propellants, Explosives, Pyrotechnics*, 14(1):6–11, 1989.

[158] A. A. Zenin and S. V. Finjakov. Studying RDX and HMX combustion mechanisms by various experimental techniques. *Combust Explos Shock Waves*, 45:559–578, 2009.

[159] R.D. Johnson III. NIST computational chemistry comparison and benchmark database, August 2019. [online] http://cccbdb.nist.gov/.

[160] J. Hanson. Spectroscopy IR frequencies, 2002. [online] http://www2.ups.edu/faculty/hanson/Spectroscopy/IR/IRfrequencies.html.

[161] R.C. Weast. *Handbook of Chemistry and Physics 53rd Edition*. Chemical Rubber Pub., 1972.

[162] University of Wisconsin. WiSTL Wisconsin shock tube laboratory, 2008. [online] http://silver.neep.wisc.edu/~shock/tools/gdcalc.html.

[163] J. D. Anderson. *Modern Compressible Flow with Historical Perspective*. McGraw-Hill Higher Education, 2002.

[164] J. Kurrle. HMX detonation vs density, report 0SA0 No. 4148. *SANL*, 901-003, 1971.

[165] D. Porter. *Group Interaction Modelling of Polymer Properties*. Taylor & Francis, 1995.

[166] P. Gould, I. Cullis, and D. Porter. Personal communication.

[167] S. Zeman. Modified Evans–Polanyi–Semenov relationship in the study of chemical micromechanism governing detonation initiation of individual energetic materials. *Thermochimica Acta*, 384(1):137 – 154, 2002.

[168] M. J. Kamlet and S. J. Jacobs. Chemistry of detonations. A simple method for calculating detonation properties of C–H–N–O explosives. *The Journal of Chemical Physics*, 48(1):23–35, 1968.

[169] T. M. Klapötke. *Chemistry of high-energy materials*. De Gruyter, 2010.

[170] E. L. Lee and C. M. Tarver. Phenomenological model of shock initiation in heterogeneous explosives. *The Physics of Fluids*, 23(12):2362–2372, 1980.

[171] T. Hussain and Liu Yan. Single and double shock initiation modelling for high explosive materials in last three decades. *IOP Conference Series: Materials Science and Engineering*, 146:012041, aug 2016.

[172] C. Mader and C. Forest. Two-dimensional homogeneous and heterogeneous detonation wave propagation. *NASA STI/Recon Technical Report N*, pages 19366–, 02 1976.

[173] C. Handley, N. Whitworth, H. James, B. Lambourn, and M-A. Maheswaran. The CREST reactive-burn model for explosives. *EPJ Web of Conferences*, 10:00004, 2010.

[174] K. Kim. Particle-size-dependent reaction rate in shocked explosives. *Shock Waves in Condensed Matter*, pages 531–534, 1987.

[175] B. M. Dobratz. LLNL explosives handbook: properties of chemical explosives and explosives and explosive simulants. 1981.

[176] D. Chapman, D. Eakins, D. Williamson, and W. Proud. Index of refraction measurements and window corrections for PMMA under shock compression. *AIP Conference Proceedings*, 1426:1041–, 06 2011.

[177] J. Pachman, O. Němec M. Künzel, and J. Majzlík. A comparison of methods for detonation pressure measurement. *Shock Waves*, 28(2):217–225, 2018.

[178] M. Sućeska. *Test Methods for Explosives*. Springer, New York, 1995.

[179] C. D. Molek, E. J. Welle, R. R. Wixom, M. B. Ritchey, P. Samuels, and Y. Horie. Microstructural characterization of pressed HMX material sets at differing densities. *AIP Conference Proceedings*, 1793(1):040007, 2017.

[180] M. Bertero and R. Pike. Particle size distributions from Fraunhofer diffraction. *Journal of Modern Optics*, 30, 08 1983.

[181] Wang Nai-Ning, Zhang Hong-Jian, and Yu Xian-Huang. A versatile Fraunhofer diffraction and Mie scattering based laser particle sizer. *Advanced Powder Technology*, 3(1):7 – 14, 1992.